VT-Forschungsbericht 2018-02

Large Eddy Simulation of Turbulent Reacting Multi-Phase Flows

Dipl.-Ing. Georg Eckel

Deutsches Zentrum für Luft- und Raumfahrt
Institut für Verbrennungstechnik
Stuttgart

DLR
Deutsches Zentrum
für Luft- und Raumfahrt

Herausgeber
Deutsches Zentrum
für Luft- und Raumfahrt

Institut für
Verbrennungstechnik

Pfaffenwaldring 38-40
70569 Stuttgart

Telefon (0 7 11) 68 62 - 3 08
Telefax (0 7 11) 68 62 - 5 78

D93, Stuttgart

Large Eddy Simulation of Turbulent Reacting Multi-Phase Flows

A thesis accepted by the Faculty of Aerospace Engineering and Geodesy of the University of Stuttgart in partial fulfilment of the requirements for the degree of Doctor of Engineering Sciences (Dr.-Ing.)

by

Dipl.-Ing. Georg Eckel

born in Karlsruhe

Main referee:	Prof. Dr.-Ing. Manfred Aigner
Co-referee:	Prof. Dr.-Ing. Hans-Jörg Bauer
Date of defence:	4 May 2018

Institute of Combustion Technology for Aerospace Engineering
University of Stuttgart

2018

Danksagung

Die vorliegende Arbeit entstand während meiner Tätigkeit am Institut für Verbrennungstechnik des Deutschen Zentrums für Luft- und Raumfahrt e.V. (DLR) in Stuttgart.

Mein erster Dank gilt daher meinem Institutsleiter und dem Hauptberichter dieser Arbeit, Herrn Prof. Dr.-Ing. Manfred Aigner, für die Möglichkeit zur Durchführung dieser Arbeit und die guten Arbeitsbedingungen am Institut. Herrn Prof. Dr.-Ing. Hans-Jörg Bauer danke ich für das Interesse an meiner Arbeit und die Übernahme des Mitberichts sowie für die wertvollen Anmerkungen und Korrekturen des Manuskripts.

Mein besonderer Dank gilt meinen Abteilungsleitern Berhold Noll und Patrick Le Clercq für die umfassende Unterstützung, den Rückhalt weit über diese Arbeit hinaus und für das in mich gesetzte Vertrauen.

Allen Mitarbeitern des Instituts, sowie allen externen Beteiligten bin ich sehr dankbar für die tolle Unterstützung und die angenehme Zusammenarbeit. Besonders erwähnen möchte ich meine langjährigen Bürokollegen Elizaveta Ivanova und Zhiyao Yin sowie die Weggefährten Michel Lourier, Christian Eberle, Massimiliano Di Domenico, Francesca Rebosio, Bhavin Kapadia, Bastian Rauch, Christopher Edelmann und Uwe Bauder. Die zahlreichen fachlichen und persönlichen Gespräche, Ratschläge und Anmerkungen haben mir auf dem Weg zur fertigen Arbeit sehr geholfen und immer wieder neue Wege und Ansätze aufgezeigt. Ein besonders herzlicher Dank gilt diesbezüglich Michael Rachner. Ohne seine Vorarbeit und seine Ratschläge wäre diese Arbeit nicht möglich gewesen. Für ein besseres Verständnis der experimentellen Vergleichs- und Validierungsdaten, der Numerik sowie der Verbrennungskinetik danke ich den Kollegen Jasper Grohmann, Klaus-Peter Geigle, Thomas Mosbach, Peter Kutne und Wolfgang Meier aus der Verbrennungsdiagnostik, den Kollegen Felix Grimm, Andreas Fiolitakis, Peter Ess und Peter Gerlinger aus der Numerik-Abteilung sowie den Kollegen Torsten Methling, Trupti Kathrotia und Nadja Slavinskaya aus der Kinetik-Abteilung.

Da eine wissenschaftliche Arbeit ohne eine fundierte Literaturrecherche nicht entstehen kann, möchte ich mich auch ausdrücklich bei unserer Bibliothekarin Cornelia Ban für die Unterstützung bei der Literatursuche bedanken.

Abschließend möchte ich mich von ganzem Herzen bei meiner Frau Francesca, meiner Schwester Julia, meinen Eltern, Cousins, Onkel und Tanten sowie meinen Freunden insbesondere Markus, Dirk, Johanna, Arzu, Sebastian, Okan, Martin, Antje, Thomas, Nina und Simone für die unermüdliche Stärkung und Motivierung bedanken, sowie für das stets offene Ohr.

Contents

List of Figures

List of Tables

List of Acronyms and Symbols

Acronyms

ADM	Approximate Deconvolution Method
ALECSYS	Advanced Low Emission Combustion System
APDF	Assumed Probability Density Function
ASTM	American Society for Testing and Materials
ATF	Artificially Thickened Flame
ATJ-SPK	Alcohol to Jet SPK
BiCGSTAB	BiConjugate Gradient STABilized method
CAB	Cascade Atomization and drop Breakup
CAEP	Committee on Aviation Environmental Protection
CARS	Coherent Anti-Stokes Raman scattering Spectroscopy
CFD	Computational fluid dynamics
CH	Catalytic Hydrothermolysis
CMC	Conditional filtered Moment Closure
CTM	Continuous Thermodynamics Model
DNS	Direct Numerical Simulations
DSHC	Direct Sugar to HydroCarbon
ETAB	Enhanced Taylor Analogy Breakup
F-T	Fischer-Tropsch
FGM	Flamelet Generated Manifolds
FGMRES	Flexible Generalized Minimal RESidual method
FRC	Finite-Rate Chemistry
FSJF	Fully Synthetic Jet Fuel
GC	Gas Chromatograph
HEFA	Hydroprocessed Esters and Fatty Acids
ICAO	International Civil Aviation Organization
ISAT	In Situ Adaptive Tabulation
LEM	Linear-Eddy Mixing
LES	Large Eddy Simulation
MMD	Mass Mean Diameter
MPI	Message Passing Interface
MS	Mass Spectrometer
ODE	Ordinary Differential Equation
OEM	Original Equipment Manufacturer
PDA	Phase Doppler Anemometry
PDF	Probability Density Function
PIV	Particle Image Velocimetry
PM	Particulate Matter
PVC	Precessing vortex core
RANS	Reynolds-Averaged Navier-Stokes equations
RHS	Right-Hand Side
RQL	Rich burn-Quick quench-Lean burn

SGS	Sub-Grid Scale
SIP	Synthetic Iso-Paraffin from Fermented Hydroprocessed Sugar
SKA	Synthetic Kerosene with Aromatics
SMD	Sauter Mean Diameter
SPH	Smoothed Particle Hydrodynamics
SPK	Synthetic Paraffinic Kerosene
TAB	Taylor Analogy Breakup
TAPS	Twin Annular Premixing Swirler
TPB	Three Point Backward
TPDF	Transported Probability Density Function
UHC	Unburned HydroCarbons
VOF	Volume-of-fluid
XTL	X to liquid

Non-dimensional Numbers

Da	Damköhler number
Le	Lewis number
Nu	Nusselt number
Oh	Ohnesorge number
Pr	Prandtl number
Re	Reynolds number
Sc	Schmidt number
Sh	Sherwood number
We	Weber number

Calligraphic symbols

$\mathcal{D}_p$	Deformation of a parcel	$[-]$
$\mathcal{D}_{end,parent}$	End deformation of a parent parcel	$[-]$
$\mathcal{D}_{ini,child}$	Initial deformation of a child parcel	$[-]$
$\mathcal{D}_{p,max}$	Maximum deformation of a parcel	$[-]$
$\mathcal{E}$	Axial ratio	$[-]$
$\mathcal{F}$	Fresnel sine integral	$[-]$
$\mathcal{G}$	Mathematical term	$[-]$
$\mathcal{M}_\alpha$	Reactant	$[-]$
$\mathcal{O}$	Order of magnitude	$[-]$
$\mathcal{R}$	Specific gas constant	$[\frac{J}{kgK}]$
$\mathcal{S}_{ij}^d$	Traceless symmetric part of the square of the velocity gradient tensor	$[\frac{1}{s^2}]$
$\mathcal{T}_p$	Current lifetime of a parcel	$[s]$

Greek letters without a diacritical mark

α_g	Exponential factor	$[\sqrt{m}]$
α_g^0	Value of α_g without vaporization	$[\sqrt{m}]$
α_l	Exponential factor	$[\sqrt{m}]$
α_T	Heat transfer coefficient	$[\frac{W}{m^2K}]$
δ_L^0	Flame thickness	$[m]$
Δh_{vap}	Specific enthalpy of vaporization	$[\frac{J}{kg}]$
Δ	Filter width	$[m]$
δ	Damping coefficient	$[\frac{kg}{s}]$
δ_{ij}	Kronecker delta	$[-]$
δ_{vort}	Vorticity thickness	$[m]$
ϵ	Mathematical term	$[-]$

η_s	Dynamic viscosity ratio at the surface	$[-]$
$\mathit{\Gamma}$	Diffusion coefficient	$[-]$
$\mathit{\Gamma}$	Mathematical function	$[-]$
λ_{span}	Wave length of the spanwise instability	$[m]$
$\lambda_{\mathrm{stream}}$	Wave length of the streamwise instability	$[m]$
μ	Dynamic viscosity	$[\frac{kg}{ms}]$
$\mu_{g,s}$	Dynamic gas viscosity at the surface	$[\frac{kg}{ms}]$
$\mu_{l,s}$	Dynamic liquid viscosity at the surface	$[\frac{kg}{ms}]$
ν_g	Kinematic viscosity of the gas	$[\frac{m^2}{s}]$
ν_l	Kinematic viscosity of the liquid	$[\frac{m^2}{s}]$
ν_t	Kinematic turbulent viscosity	$[\frac{m^2}{s}]$
$\mathit{\Omega}$	Volume of the domain	$[m^3]$
ω	Angular frequency of the drop oscillation	$[\frac{1}{s}]$
ω_0	Angular frequency of the undamped system in the drop oscillation	$[\frac{1}{s}]$
ϕ	Angle	$[rad]$
ρ_g	Gas density	$[\frac{kg}{m^3}]$
ρ_l	Liquid density	$[\frac{kg}{m^3}]$
σ	Surface tension	$[\frac{kg}{s^2}]$
σ	Variance of a random variable	$[-]$
τ_{ij}	Stress tensor	$[\frac{N}{m^2}]$
τ_{sgs}	Turbulent time scale of the sub-grid scale fluctuations	$[s]$
τ_t	Turbulent time scale	$[s]$
ξ_{Gauss}	Normally distributed random number	$[-]$
ζ_α	Ratio between the species and total vapor mass flux	$[-]$
τ_p	Particle response time	$[s]$

Greek letters with a diacritical mark

$\bar{\mathit{\Psi}}$	Filtered value of a quantity $\mathit{\Psi}$	$[-]$
$\bar{\tau}_{ij}$	Filtered stress tensor	$[\frac{N}{m^2}]$
$\hat{\beta}$	Average density ratio in the boundary layer	$[-]$
$\hat{\rho}_g$	Average gas density in the boundary layer	$[\frac{kg}{m^3}]$
$\hat{\rho}_l$	Average liquid density in the boundary layer	$[\frac{kg}{m^3}]$
$\nu'_{\alpha,r}$	Stoichiometric coefficient of the reactant α in reaction r	$[-]$
$\nu''_{\alpha,r}$	Stoichiometric coefficient of the product α in reaction r	$[-]$
$\tilde{\mathit{\Psi}}$	Density weighted filtered value of a quantity $\mathit{\Psi}$	$[-]$

Roman letters without a diacritical mark

A	Surface area	$[m^2]$
a	Thermal diffusivity	$[\frac{m^2}{s}]$
A_r	Constant in the pre-exponential factor in the Arrhenius equation	$[-]$
b	Axis of a spheroid	$[m]$
B_M	Spalding mass transfer number	$[-]$
b_r	Temperature exponent in the Arrhenius equation	$[-]$
B_T	Spalding heat transfer number	$[-]$
B_{ij}	Diffusion coefficient tensor in the stochastic dispersion model	$[\frac{m}{s^{3/2}}]$
c_d	Drag coefficient	$[-]$
$c_{d,\parallel}$	Drag coefficient parallel to the axis	$[-]$
$c_{d,\perp}$	Drag coefficient perpendicular to the axis	$[-]$
c_{p_l}	Specific isobaric heat capacity of the liquid	$[\frac{J}{kgK}]$

C_{sgs}	Model constant in the WALE model	$[-]$
D_α	Diffusion coefficient of species α	$[\frac{m^2}{s}]$
d_p	Particle diameter	$[m]$
d_{cyl}	Cylinder diameter	$[m]$
d_{jet}	Jet diameter	$[m]$
$d_{p,cross}$	Particle diameter in cross-flow direction	$[m]$
E	Efficiency funtion in the artificially thickened flame model	$[-]$
e^α	Specific internal energy associated with species α	$[\frac{J}{kg}]$
$E_{a,r}$	Activation energy of the reaction r	$[J]$
F	Flame thickening factor in the artificially thickened flame model	$[-]$
f	specific volume forces	$[\frac{m}{s^2}]$
f_{stream}	Frequency of the streamwise instability	$[\frac{1}{s}]$
G	Filter function	$[-]$
g_{ij}	Velocity gradient tensor	$[\frac{1}{s}]$
H	Channel height	$[m]$
h	Specific enthalpy	$[\frac{J}{kg}]$
h_l	Specific enthalpy of the liquid	$[\frac{J}{kg}]$
j	Mass flux due to diffusion	$[\frac{kg}{m^2 s}]$
j_m	Mass flux	$[\frac{kg}{m^2 s}]$
K	Kernel function	$[-]$
k	Turbulent kinetic energy	$[J]$
k_r	Reaction rate of reaction r	$[-]$
k_{sgs}	Turbulent kinetic energy in the sub-grid scales	$[J]$
L	Characteristic length scale	$[m]$
l	Length	$[m]$
l_{eddy}	Eddy size	$[m]$
m_p	Mass of parcel p	$[kg]$
m_p	Particle mass	$[kg]$
M_α	Molar mass of species α	$[\frac{kg}{mol}]$
N_A	Avogadro constant	$[\frac{1}{mol}]$
N_p	Number of parcels in the cell	$[-]$
N_{sp}	Number of species	$[-]$
p	pressure	$[\frac{N}{m^2}]$
$p_{g,\alpha}$	Partial pressure of species α in the gas	$[\frac{N}{m^2}]$
$p_{vap,\alpha}$	Vapor pressure of species α in a mixture	$[\frac{N}{m^2}]$
$p^*_{vap,\alpha}$	Vapor pressure of the pure species α	$[\frac{N}{m^2}]$
q	Heat flux	$[\frac{J}{m^2 s}]$
q	Momentum flux ratio	$[-]$
R	Radius	$[m]$
r	Radial distance	$[m]$
r^∞	Radial position of the farfield	$[m]$
S_α	Chemical source term	$[\frac{kg}{m^3 s}]$
S_h^d	Enthalpy source term due to spray	$[\frac{J}{m^3 s}]$
S_r	Enthalpy source term due to radiation	$[\frac{J}{m^3 s}]$
S_α^d	Species source term due to spray	$[\frac{kg}{m^3 s}]$
$S_{\rho u}^d$	Momentum source term due to spray	$[\frac{kg}{m^2 s^2}]$
s_L^0	Laminar flame speed	$[\frac{m}{s}]$
T	Temperature	$[K]$

t	Time	$[s]$
t^*	Characteristic timescale	$[s]$
t_b	Breakup time	$[s]$
T_g	Gas temperature	$[K]$
T_p	Particle temperature	$[K]$
t_{bag}	Breakup time of the bag	$[s]$
t_{base}	Breakup time of the basal ring	$[s]$
t_{eddy}	Eddy lifetime in the interaction time dispersion model	$[s]$
T_g^∞	Gas temperature in the farfield	$[K]$
T_g^S	Gas temperature at the droplet surface	$[K]$
t_{ini}	Initiation time	$[s]$
t_{trans}	Transit time in the interaction time dispersion model	$[s]$
u	Tangential velocity in the bounary layer equations	$[\frac{m}{s}]$
u_c	Group velocity	$[\frac{m}{s}]$
U_g	Gas velocity outside the boundary layer	$[\frac{m}{s}]$
u_i	Velocity component	$[\frac{m}{s}]$
$U_{\infty,rel}$	Relative freestream velocity	$[\frac{m}{s}]$
u_g	Tangential gas velocity	$[\frac{m}{s}]$
u_l	Tangential liquid velocity	$[\frac{m}{s}]$
v	Radial velocity in the bounary layer equations	$[\frac{m}{s}]$
V_f	Filter volume	$[m^3]$
V_0	Liquid volume undergoing bag breakup	$[m^3]$
v_g	Radial gas velocity	$[\frac{m}{s}]$
v_l	Radial liquid velocity	$[\frac{m}{s}]$
$v_{w,g}$	Local blowing velocity	$[\frac{m}{s}]$
W	Wiener process	$[-]$
w	Width of the wetted surface	$[m]$
x	Tangential coordinate	$[m]$
$X_{\alpha,l}$	Molar fraction of species α in the liquid	$[-]$
X_α^S	Molar fraction of species α at the surface	$[-]$
y	Radial coordinate	$[m]$
Y_α	Mass fraction of species α	$[-]$
Y_α^∞	Species mass fraction in the farfield	$[-]$
Y_α^S	Species mass fraction at the droplet surface	$[-]$
$\jmath_{m,shed}$	Mass flux due to shedding	$[\frac{kg}{m^2s}]$
$\jmath_{m,vap}$	Mass flux due to vaporization	$[\frac{kg}{m^2s}]$

Roman letters with a diacritical mark

$\bar{M}$	Mean molar mass	$[\frac{kg}{mol}]$
$\bar{v}_{w,g}$	Average blowing velocity	$[\frac{m}{s}]$
$\ddot{y}$	Second time derivative of y	$[\frac{m}{s^2}]$
$\dot{H}$	Enthalpy flow rate	$[\frac{J}{s}]$
$\dot{m}$	Mass flow rate	$[\frac{kg}{s}]$
$\dot{m}_l$	Liquid mass flow rate	$[\frac{kg}{s}]$
$\dot{m}_{shed}$	Mass flow rate due to shedding	$[\frac{kg}{s}]$
$\dot{m}_{vap}$	Mass flow rate due to vaporization	$[\frac{kg}{s}]$
$\dot{Q}$	Surface heat flow rate	$[\frac{J}{s}]$
$\dot{q}$	Surface heat flux	$[\frac{J}{m^2s}]$
$\dot{y}$	First time derivative of y	$[\frac{m}{s}]$

$\overline{t^*}$	Time-averaged value of t^*	$[s]$
$\tilde{S}_{ij}$	Strain rate tensor of the resolved scales	$[\frac{1}{s}]$
$\vec{a}_d$	Acceleration vector due to drag	$[\frac{m}{s^2}]$
$\vec{F}$	External forces	$[N]$
$\vec{F}_d$	Drag force	$[N]$
$\vec{g}$	Acceleration vector due to gravity	$[\frac{m}{s^2}]$
$\vec{u}_p$	Particle velocity vector	$[\frac{m}{s}]$
$\vec{u}_{child,mean}$	Mean velocity of the child parcel	$[\frac{m}{s}]$
$\vec{u}_{child,rms}$	Rms velocity of the child parcel	$[\frac{m}{s}]$
$\vec{u}_{child}$	Velocity of the child parcel	$[\frac{m}{s}]$
$\vec{u}_g$	Gas velocity vector	$[\frac{m}{s}]$
$\vec{u}_{parent}$	Velocity of the parent parcel	$[\frac{m}{s}]$
$\vec{u}_{rel,\parallel}$	Relative velocity parallel to the axis	$[\frac{m}{s}]$
$\vec{u}_{rel,\perp}$	Relative velocity perpendicular to the axis	$[\frac{m}{s}]$
$\vec{u}_{rel}$	Relative velocity vector	$[\frac{m}{s}]$
$\vec{x}_p$	Particle position vector	$[m]$

Zusammenfassung

Die vorliegenden Arbeit zielt darauf ab, modernste Modelle für einzelne Sub-Prozesse, welche zuvor meist isoliert eingesetzt wurden, in einer numerischen Plattform für die Simulation turbulenter, reagierender Mehrphasenströmungen zu vereinen. Da die Brennstoffflexibilität in modernen Gasturbinen eine große Herausforderung darstellt, liegt ein spezieller Fokus der Modellierung auf der Abbildung von Brennstoffabhängigkeiten. Diesbezüglich wird eine Kopplung von Größen in der LES, welche nicht mit dem Gitter aufgelöst werden und in Feinstrukturmodellen modelliert werden müssen, mit den Tropfentransportgleichungen im Lagrange-Löser vorgestellt. Dies schließt LES-Feinstrukturmodelle für die turbulente Tropfendispersion und die Tropfenverdampfung mit ein. Hierbei wird insbesondere der Kopplung eines Modelles für die Verdampfung bei komplexen Treibstoffzusammensetzungen mit einem detaillierten Chemie-Löser eine besondere Bedeutung beigemessen. Überdies hinaus werden zwei semi-empirische Zerstäubungsmodelle präsentiert. Diese Modelle zielen jedoch nicht darauf ab, die Grenzfläche zwischen Gas und Flüssigkeit detailliert aufzulösen. Sie basieren zu Teilen auf Empirie und können demzufolge nur charakteristische Merkmale des Zerstäubungsvorganges unter sehr spezifischen Bedingungen abbilden. Die im Rahmen dieser Arbeit durchgeführten Simulationen zeigen, dass isotherme, turbulente, eingeschlossene Strömungen mit einer hohen Genauigkeit vorhergesagt werden können, vorausgesetzt die Gitterauflösung ist ausreichend hoch. Large Eddy Simulationen mit dem WALE-Feinstrukturmodell für die Schließung der nicht aufgelösten Reynoldsspannungen ermöglichen genaue Vorhersagen nicht nur der mittleren Geschwindigkeiten sondern auch der Geschwindigkeitsfluktuationen. Die Untersuchungen bezüglich der turbulenten Partikeldispersion in diesen isothermen, turbulenten, eingeschlossenen Strömungen zeigen, dass auch die turbulente Dispersion sphärischer Feststoffteilchen in Drallströmungen gut vorhergesagt werden kann. In diesem Zusammenhang wurden zwei Feinstrukturmodelle für die turbulente Dispersion getestet, ein Interaktionszeit-Dispersionsmodell sowie ein stochastisches Dispersionsmodell. Beide Modelle sind in der Lage, die experimentellen Daten im Hinblick auf Massenströme sowie Gas- und Partikelgeschwindigkeiten (inklusive Fluktuationen) zu reproduzieren. In Simulationen der Verbrennung von fünf monodispersen Tropfenketten konnte gezeigt werden, dass die Kopplung eines Mehrkomponentenverdampfungsmodelles mit einem detaillierten Verbrennungsmodell vorteilhaft ist, um den Einfluss verschiedener Treibstoffzusammensetzungen auf die Verdampfung und Verbrennung abbilden zu können. Zusätzlich wurde mit Hilfe der entwickelten numerischen Plattform ein Flugstromvergaser untersucht. Im Zuge des Wandels hin zu nachhaltigen Flugzeugtreibstoffen stellt die Flugstromvergasung einen vielversprechenden Prozess dar, Biomasse oder andere Ausgangsmaterialien minderer Qualität,

z.B. hochviskose Schlämme und Suspensionen mit einem erheblichen Anteil an Feststoffpartikeln, in Brenn- und Treibstoffe höherer Qualität zu überführen. Eine große, wissenschaftliche Herausforderung besteht in der Vorhersage der physikalischen und chemischen Phänomene, welche in solchen Hochtemperatur-Hochdruck-Mehrphasenströmungssystemen stattfinden. Um die Komplexität zu reduzieren, fokussiert sich die Studie im Rahmen dieser Arbeit auf ein System bestehend aus einer Zweiphasenströmung (gasförmig und flüssig) und einem Modellbrennstoff (Ethylenglykol) unter atmosphärischen Bedingungen. Die Vergleiche der numerischen Simulation mit experimentellen Daten an verschiedenen Positionen stromab des Injektors zeigen sinnvolle Ergebnisse bezüglich der Temperatur- und Speziesprofile. Die Analyse des Nahbereichs des Injektors lässt erkennen, dass die Hochtemperatur-Reaktionszone nahe des Injektors nicht durch eine direkte Reaktion des Brennstoffes mit dem Oxidator erklärt werden kann. Stattdessen werden Kohlenstoffmonoxid und Wasserstoff, welche auf der Achse gebildet werden, durch Rezirkulationszonen stromauf transportiert. Die Reaktionen des Kohlenstoffmonoxids und Wasserstoffs mit dem Sauerstoff des Vergasungsmediums stabilisieren die Flamme. Die Wärmefreisetzung dieser Reaktionen stellt die Wärme für die Verdampfung und Zersetzung des Brennstoffes sowie für die Vergasungsreaktionen stromab bereit. Des Weiteren wurde ein drallstabilisierter Laborspraybrenner analysiert, welcher einige wichtige Merkmale derzeitiger Fluggasturbinenbrennkammern aufweist. Globale Eigenschaften, wie die Sprayverteilung und die Position der Reaktionszone, konnten durch die Simulation gut wiedergegeben werden. Auch der quantitative Vergleich der Tropfengröße, Tropfengeschwindigkeiten und des Flüssigvolumenstromes zeigt eine gute Übereinstimmung. Dagegen weisen die Temperaturprofile eine signifikante Diskrepanz in der zentralen Mischzone auf. In der LES zeigt sich der Temperaturanstieg auf der zentralen Achse weiter in Richtung des Brennkammerauslasses verschoben. Es konnte nicht abschließend geklärt werden, ob die Diskrepanzen auf unterschiedliche Randbedingungen oder noch existierende Mängel in den Submodellen zurückzuführen sind. Nichtsdestotrotz zeigen die Simulationen des drallstabilisierten Spraybrenners das große Potenzial von LES-Sprayverbrennungssimulationen. Im Vergleich zu Messungen steht ein großer Datensatz simultan aufgenommener Daten mit einer hohen zeitlichen wie räumlichen, dreidimensionalen Auflösung zur Verfügung. Dadurch können LES-Simulationen einen wertvollen Beitrag zum Verständnis und der Interpretation von komplexen Phänomenen leisten. In diesem Zusammenhang zeigen die Simulationen, dass Verdampfung und Mischung die limitierenden Schritte in der Flammenzone darstellen, so dass die Chemie in dieser Zone als unendlich schnell angenommen werden kann. Dies bedeutet, dass Verdampfungs- und Mischungszeiten eine inhärente Dämpfung in der Verbrennung darstellen. Diese Erkenntnis steht in direktem Zusammenhang mit modernsten Verbrennungskonzepten, da sie erklärt, warum diese auf Grund des Trends zu höheren Vorverdampfungs- und Vormischgraden anfälliger für Instabilitäten sind. Darüber hinaus, offenbart der Testfall die Vorteile eines Finite-Raten-Chemieansatzes in Kombination mit einer direkten Berechnung der Elementarreaktionen. Es konnte gezeigt werden, dass mehrere Zustände in der Brennkammer vorherrschen, welche von einer Finiten-Raten-Chemie abhängen.

Abstract

The thesis at hand aims at combining state-of-the-art sub-models, which were previously used for isolated individual sub-processes, to obtain a computational platform for the simulation of turbulent reacting multi-phase flows. Due to the new challenges related to fuel flexibility of modern gas turbine combustors, a special focus is on fuel dependencies in the modeling. A coupling of LES sub-grid scale quantities with the droplet equations in Lagrangian particle tracking is presented. This involves LES sub-grid scale models for (turbulent) dispersion and vaporization and a coupling of a multi-component vaporization model with a detailed chemistry solver. Furthermore, two semi-empirical atomization models are presented. These atomization models do not aim at resolving the gas-liquid interface in detail. Partly depending on empiricism, they represent key features of the atomization process at specific conditions. The simulations performed within this work show that iso-thermal, turbulent, confined flows can be predicted with a high level of accuracy given that the mesh resolution is sufficiently high. Large Eddy Simulations with the WALE sub-grid scale closure for the unresolved sub-grid Reynolds stresses provide accurate predictions of not only the average velocities but also the velocity fluctuations. Investigations concerning the turbulent dispersion of solid particles in these iso-thermal, turbulent, confined flows, demonstrate that the turbulent dispersion of solid spherical particles in swirling flows can also be well predicted. Two sub-grid scale models for turbulent dispersion are tested, i.e. an interaction time dispersion model and a stochastic dispersion model. Both are capable of reproducing the experimental data concerning the mass fluxes as well as the gas and particle velocities (including fluctuations). In simulations of the combustion around five mono-dispersed droplet chains, it is shown that the coupling of evaporation models to detailed chemistry solvers is beneficial to reflect the influence of different fuel compositions on evaporation and combustion. By means of the developed computational platform, an entrained-flow gasifier is investigated. With the switch to sustainable aviation fuels, the source of the energy and the medium used to store the energy on the aircraft have to be distinguished. In this context, entrained flow gasification is a promising process for the conversion of biomass and other low-grade feedstock, e.g. highly viscous slurries and suspensions with a significant content of solid particles, to high quality fuels. A major scientific challenge is the prediction of the physical and chemical phenomena occurring in such high-temperature and high-pressure multi-phase flow systems. In order to reduce the complexity, the study within this thesis focuses on a two-phase (gas and liquid) flow system with a model fuel (mono-ethylene glycol) under atmospheric conditions. Downstream comparisons of the simulation with experimental data show a reasonable agreement concerning temperature and species profiles. The analysis of the injector near-field reveals that the high temperature reaction zone close to the injector cannot be explained by a direct reaction of the fuel with the oxidizer. Instead, carbon monoxide and hydrogen mainly formed on the axis are transported upstream by the recirculation zone. The reactions of CO and H_2 with the oxygen stabilize the flame. The heat release from this reactions supports the vaporization and decomposition of fuel as well as the downstream gasification reactions. Furthermore, a lab-scale, swirl-stabilized spray burner is analyzed, which exhibits some of the key features of current aero-engines combustors. Global features like the spray distribution and the position of the reaction zone are well reproduced by the LES. The quantitative comparison of droplet size, droplet velocity and liquid volume flux profiles show a good agreement as well. However, the temperature profiles reveal a significant discrepancy in the central mixing zone. In the LES, the temperature rise on the central axis is observed further towards the outlet. It could not be finally clarified, if the discrepancies are related to differences in boundary conditions or still existing deficiencies in the sub-models. However, the simulations of the swirl-stabilized spray burner show the great potential of spray combustion LES. In comparison to measurements, a large set of simultaneously taken three-dimensional data with a high temporal and spatial resolution is available. Therefore, LES can help in the understanding and interpretation of complex phenomena. In this context, the simulations show that evaporation and mixing are the rate-controlling steps in the flame zone, so that chemistry can be assumed to be infinitely fast in this zone. This means that evaporation and mixing times introduce an inherent damping to combustion. These findings directly relate to modern combustion concepts explaining why the trend towards a higher degree of prevaporization and premixing makes these combustion systems more susceptible to instabilities. Furthermore, the test case shows the benefits of the finite rate chemistry approach and the direct computation of the elementary reactions. It is demonstrated that several states in the combustion chamber are present which depend on a finite rate chemistry.

1. Introduction

The introductory chapter will start with some fundamentals of spray combustion in aero-engines (section 1.1). The requirements for a modern aero-engine combustor (section 1.1.1) as well as the state-of-the-art in combustor design will be covered (section 1.1.2). On the basis of these fundamentals, the scope of this thesis will be defined in section 1.2.

1.1. Spray combustion in aero-engines

1.1.1. Requirements for combustor design

The liquid-fueled gas turbine is the predominant power plant on aircrafts. As an essential part of the gas turbine, the combustor has to meet a range of requirements governed by size and weight constraints, operability and safety as well as emission regulations (Epstein, 2012). In the design phase, it is important to keep the complex interplay between these requirements in mind. A light, short and compact combustor is desired. However, the combustor needs to be large enough to ensure satisfactory fuel burn-out and reliable relight in high altitudes in case of a flameout (Doerr, 2013). If the flame in the combustor extinguishes, the turbo-components of the engine are not driven anymore so that the engine windmills. The pressure and temperature inside the combustor reach values close to the outside ambience (Lefebvre and Ballal, 2010). Especially at high altitudes, the conditions are unfavorable for atomization, vaporization and ignition. Hence, the residence time in the combustor needs to be long enough to ensure a successful and reliable relight. A reduction of the combustor volume reduces the residence time, which in consequence deteriorates the relight capability (Doerr, 2013). Generally speaking, combustor-related safety and operability implies a high durability and that the combustor stays lit or reliably relights in case of a flame extinction. This includes stable operation over a wide range of air/fuel ratios without combustion-induced instabilities like pressure pulsations, which can lead to severe damage.

The performance of the combustor, i.e. high combustion efficiency with low pressure loss, is strongly linked to pollutant emissions. Inefficient combustion is not only a waste of fuel but also leads to the formation of undesirable pollutants. Although combustors in modern engines convert more than 99 % of the chemical energy of the fuel into heat over a large part of the operating range with a combustion efficiency of nearly 100 % at take-off, the remainder is emitted in the form of carbon monoxide (CO), unburned hydrocarbons (UHC) and particulate matter (PM) (Lefebvre and Ballal, 2010). Additionally, aircraft gas turbines emit carbon dioxide (CO_2), water vapor (H_2O), oxides of nitrogen (NO_x) and, if sulfur is present in the fuel, oxides of sulfur (SO_x). The first two have not always been considered as pollutants. But due to their contribution to global warming as greenhouse gases, they have recently attracted attention (Lee *et al.*, 2010). Being the natural products of complete hydrocarbon combustion, CO_2 and H_2O emissions can only be reduced by cutting down the overall fuel consumption by the development of more efficient engines. CO, UHC, and PM (mostly soot) are associated with respiratory diseases and atmospheric pollution (Barrett *et al.*, 2010). They result from incomplete combustion so that they can be consumed in regions of the combustor with excess oxygen and sufficiently high temperatures. Unfortunately, this is conflicting with the NO_x formation, which occurs in near-stoichiometric, high temperature regions. NO_x is a precursor of photo-chemical smog and can harm the respiratory system at ground level (Monks *et al.*, 2009), e.g. in the vicinity of airports. At cruise in high altitudes, NO_x contributes to the depletion of the ozone layer, which protects us from ultra-violet radiation (Lee *et al.*, 2010). Furthermore, NO_x and SO_x produce nitric and sulfuric acid in conjunction with atmospheric moisture harming plants, animals and infrastructure in the form of acid rain (Lee *et al.*, 2010). The toxic and corrosive SO_x are formed in reactions of sulfur-containing compounds in the fuel with oxygen. They can be avoided by removing sulfur from the fuel prior to combustion. Hence, the content of sulfur in aviation fuels is regulated and limited to a total percentage by mass of 0.30 % (ASTM D1655, 2016). On the other hand, the sulfur content has implications on the fuel lubricity (Moses and Roets, 2009; Hileman *et al.*, 2010). For ultra-low sulfur jet fuels, a sufficiently high lubricity has to be guaranteed, e.g. by adding lubricity improving additives. The International Civil Aviation Organization's (ICAO) Committee on Aviation Environmental Protection (CAEP) sets standards for emissions of aero-engines (ICAO, 2008). Driven by concerns about local air quality and global climate, these legal requirements for engines tend to become more stringent with time. In the U.S., mandatory emissions reporting for all engines sold to U.S. airlines was initiated (ICAO, 2016). In Europe, airports have started to introduce landing charges based on emissions (Zurich Airport, 2010).

1.1.2. State of the art in combustor design

The original equipment manufacturers (OEMs) needed to react on the more stringent emission regulations and introduced (new) lean-burn technologies, e.g. Rolls-Royce Advanced Low Emission Combustion System (ALECSYS) (Haselbach *et al.*, 2015) or GE Twin Annular Premixing Swirler (TAPS) (Mongia, 2003; Foust *et al.*, 2012; Stickles and Barrett, 2013). The concepts of these technologies are similar and will be explained on the basis of the latter, which is depicted in Fig. 1.1. The TAPS is a staged combustor. Each burner consists of a central pilot and a concentric outer main stage. Generally, the same sub-processes can be identified in both stages. Liquid is introduced via an injector. During the atomization sub-process, the bulk liquid disintegrates into droplets. As a high volume fraction is occupied by the liquid phase, collisions, agglomeration and break-up phenomena are of importance. Subsequently, the resulting fuel droplets disperse and interact with turbulent structures in the gas phase. During the turbulent

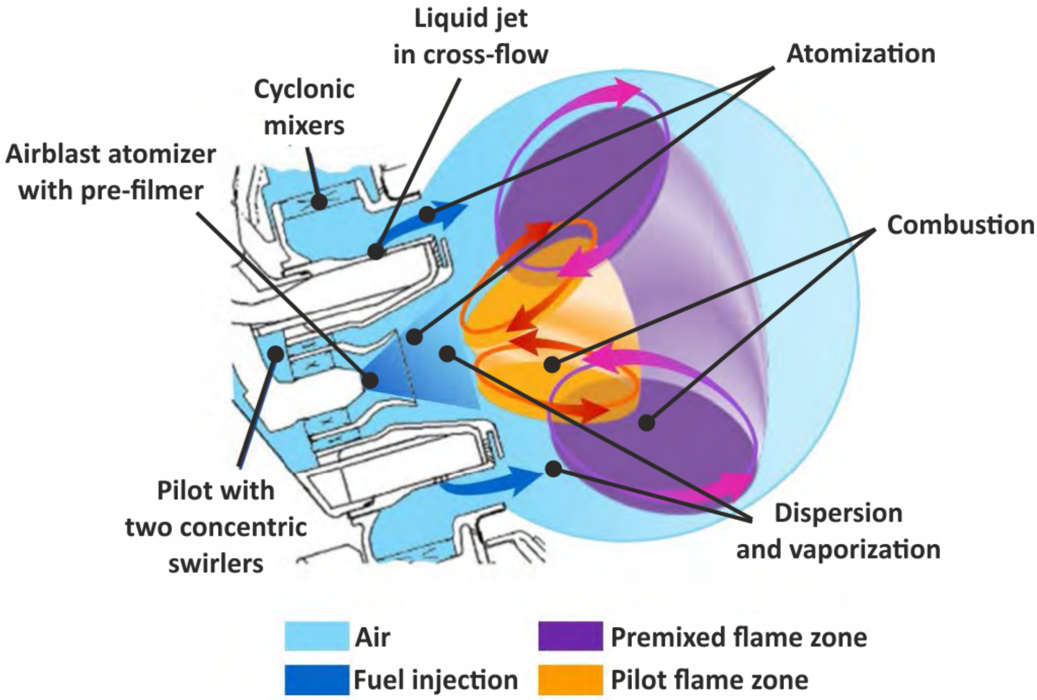

Figure 1.1.: Concept of the GE Twin Annular Premixing Swirler (TAPS) lean burn combustion system (adapted from Foust *et al.* (2012); Stickles and Barrett (2013))

dispersion, the droplets heat up and vaporize. Finally, the fuel vapor reacts with the oxygen in the air. The flame is stabilized by means of large-scale flow recirculations. These recirculations aim at generating a low-velocity region where the flame is able to anchor. Additionally, the recirculatory flow transports hot combustion products upstream to continuously ignite the fresh fuel-air mixture. These mixing processes determine the conversion rates and emissions. Details and modeling aspects of the atomization, turbulent dispersion, vaporization and combustion sub-processes will be explained in section 2.3.1, 2.3.2, 2.3.3 and 2.2.2.2, respectively.

After this general description of the fundamental phenomena, a closer look at the two individual stages will be taken. The central pilot resembles traditional Rich burn-Quick quench-Lean burn (RQL) burners with a pre-filming airblast atomizer (Mongia, 2003). In this type of atomizer, a central pressure-swirl atomizer sprays droplets onto a concentric surface leading to the formation of a thin liquid film. This film is subsequently sandwiched between two swirling air streams until it is disintegrated by the shear at the gas-liquid interface. The mass flow rates of the pilot are set to produce a rich fuel-air mixture. A modeling approach for pre-filming airblast atomization will be presented in section 2.3.1.2 of this work. The main stage relies on multi-point fuel injection via discrete jets. These jets are transversely injected into air coming from a larger main swirler (modeling aspects see section 2.3.1.1). The fuel is finely atomized and uniformly distributed to achieve a significant premixing and prevaporization. In regions of low velocity and long residence times, e.g. in wakes, the resulting combustible mixture is prone to autoignition if it is sufficiently hot and caution has to be taken for flashback, i.e. an undesired upstream propagation of flame kernels (Foust *et al.*, 2012). The mass flow rates of the main stage are chosen to sustain a lean fuel-air ratio in the main reaction zone. The combination of premixing, prevaporization and lean conditions ensures low NO_x formation rates, as near-stoichiometric hot spots are avoided. Additionally, soot formation is prevented by avoiding rich burn around droplet clusters. At high power, e.g. at take-off and climb, the main stage is operated with the majority of the fuel. As the likelihood of combustion instabilities increases the leaner the flame is, there is a trade-off between minimum NO_x and maintaining stable combustion (Foust *et al.*, 2012). As a consequence, the fuel split between pilot and main has to be carefully chosen. At low power, e.g. taxi and approach, as well as at start-up and relight, the entire fuel enters the combustor via the pilot in order to ensure ignition and a stable operation. Due to the fact that no quench region is necessary in lean burn concepts compared to RQL systems, about 70 % of the combustor's total air flow enters the combustor via the pilot and main mixers. The entire rest can be used for liner and dome cooling as well as for the adjustment of the temperature profile (pattern factor) at the exit of the combustor in order to maximize the life cycle of turbine blades and nozzle guide vanes. Improved pattern factors allow for a reduction of cooling air for these components increasing the overall engine efficiency (Epstein, 2012).

During the development process of the TAPS combustor, the design optimization largely relied on computational fluid dynamics (CFD). With the rise in computing power, CFD is increasingly used to complement existing industrial knowledge, conception rules, and hardware tests. But, as the sub-processes in a combustor, i.e. fuel atomization, vaporization, mixing and chemical reaction, are highly interdependent, complex flow dynamics and combustion responses develop. Unfortunately, current computer models still struggle with the prediction of these coupled unsteady phenomena.

Furthermore, new challenges arise due to the introduction of alternative fuels. Modern combustors need to guarantee fuel-flexibility, i.e. the capability to run with petroleum-based, synthetic and biomass-based fuels. Since the first jet engines, the design of combustors has relied on experiences with petroleum-based fuels. New methods and models need to have the capability to predict the performance of combustors dependent on the fuel composition.

1.2. Scope of this work

To solve the challenges described in the previous section, the thesis at hand aims at combining state-of-the-art sub-models, which were previously used for isolated individual sub-processes, to obtain a computational platform for the simulation of turbulent reacting multi-phase flows. The simulation tool targets not only the capability to reproduce a well-known data set but rather the prediction of physical and chemical phenomena in a combustor. Concerning unsteady phenomena and instabilities, a gain in accuracy and predictive capability can be achieved by the transition from modeling the entire spectrum of turbulent scales (RANS) to resolving parts of it (LES). In this context, the coupling of a gas phase LES with a Lagrangian description of the liquid phase will be shown. Due to the new challenges related to fuel flexibility, a special focus will be on fuel dependencies in the modeling. In this regard, the coupling of a multi-component vaporization model with a direct, detailed chemistry solver based on Arrhenius equations will be established. Only few research groups in the world showed this combination allowing for a detailed description of chemical reaction kinetics in multi-phase flows.

During the course of this thesis, the simulation platform for turbulent reactive, multi-phase flows (THETA-SPRAYSIM) of the DLR Institute of Combustion Technology was upgraded to Eulerian-Lagrangian Large Eddy Simulations. This included the coupling of LES sub-grid scale quantities in THETA with the droplet equations in SPRAYSIM. Furthermore, LES sub-grid scale models for (turbulent) dispersion and vaporization were implemented and tested. In this context, the vaporization model for complex mixtures in SPRAYSIM was coupled to the detailed chemistry solver in THETA. Additionally, the steady versions of the jet in cross-flow breakup model and the secondary breakup models were upgraded to unsteady flows. An empirical approach for the derivation of spray initial/boundary conditions resulting from the breakup of liquid films was deduced. The complete platform was subsequently validated by means of non-reactive and reactive test cases. The non-reactive test cases comprised sub-model tests for the atomization models (see section 3.1 and 3.2) and the dispersion models (see section 3.3). The reactive test cases included the combustion around droplet chains (see section 4.1), a swirl-stabilized lab-scale spray burner (see section 4.3) and a reactor related to fuel processing technology (see section 4.2). With the switch to sustainable aviation fuels, the source of the energy and the medium used to store the energy on the aircraft have to be distinguished. In this context, the investigated reactor presents a promising pathway to produce fuel from biomass. Furthermore, it shows the wide applicability of the numerical tools developed in the framework of this thesis. As Large Eddy Simulations are very costly, the speed-up of computations was a necessary requirement.

2. Theory and modeling of spray combustion

This chapter describes the underlying theory and modeling aspects concerning the sub-processes occurring in turbulent reacting multi-phase flows. As the name suggests, the term multi-phase flows refers to flows involving different phases (gas, liquid or solid). In these flows, the interaction and interchange between the phases is of particular interest. Gas-solid multi-phase flows can be encountered, inter alia, in porous media, flutter of aircraft wings, aerodynamic loads on bridges, sediment transport, and rocket engines. Among many others, gas-liquid multi-phase flows are present in rain, ocean waves, medical sprays, fire suppression, and the combustion of liquid fuel. The multi-phase flows examined within this thesis are related to spray combustion so that the term "multi-phase flows" will refer to separated and dispersed flows in the following.

Within this chapter, an overview over numerical approaches for the simulation of multi-phase flows will be given (section 2.1). This is followed by modeling aspects concerning the gaseous phase (section 2.2). The emphasis in this subsection will be placed on the numerical description of turbulence (section 2.2.1) and chemical reactions (section 2.2.2). Afterwards, the modeling of the dispersed liquid phase will be specified (section 2.3) covering the most relevant sub-processes, namely atomization (section 2.3.1), dispersion (section 2.3.2) and vaporization (2.3.3). The scope of this thesis was the upgrade of the DLR-VT simulation platform for the numerical analysis of turbulent reacting multi-phase flows in lab scale configurations. Nevertheless, the models were chosen targeting the applicability to real scale problems. This implies that not only the accuracy but also the numerical costs have to be kept at reasonable levels. In general, it is important to scientifically identify pros and cons of the individual models. In some cases, simple models may be favored but their limits have to be well understood. In this context, spatial accuracy and detailed modeling sometimes have to be sacrificed to ensure robustness and performance, e.g. several LES sub-grid scale closure models proposed in the literature showed great potential in a priori studies but they were insufficiently dissipative and prone to numerical instabilities in more realistic test cases (Gicquel *et al.*, 2012).

2.1. Numerical approaches

Turbulence, chemical kinetics, and multi-phase flows are themselves, i.e. isolated from each other, complex areas of research. But the combination of these three topics still is a major scientific challenge. The interaction between the turbulent eddies with the gas-liquid interface leads to a dynamic system of complicated flow structures and changing phase boundaries (Kuo and Acharya, 2012). The complexity is further increased by the interdependence of the fluid properties, the phase change, and the exothermic reactions of the combustion process. Moreover, reacting multi-phase flow systems exhibit different spacial and time scales, which results in a multi-scale problem. Macroscale, large flow structures in the order of magnitude of the geometrical scale of the apparatus are present among mesoscale phenomena like breakup and coalescence and microscale phenomena like chemical reactions, micro-mixing and turbulent dissipation. As a consequence, the strong coupling between chemistry, turbulence and the multiple phases poses a considerable challenge to both experimental diagnostics (Tropea, 2011) and numerical simulations (Jenny *et al.*, 2012). For instance, fully resolved measurements at the scale of single droplets in a turbulent reacting flow or in the dense spray regime remain difficult. On the other hand, numerical approaches usually rely on a direct computation of phenomena at the macroscale while the details at the microscale, i.e. of the order of a particle diameter, are modeled (Balachandar and Eaton, 2010). It is possible to reduce the complexity of these microscale models by cutting down the field of view. But this usually involves the modeling of macroscale phenomena in terms of boundary conditions.

In the literature, many different numerical approaches can be distinguished. In the following only numerical approaches based on continuum mechanics will be considered. This is due to the fact that clusters of already a couple thousands of molecules exhibit the behavior of a continuum as shown by direct molecular dynamics simulations (Koplik and Banavar, 1993). The dependence of the number of molecules on the droplet diameter displayed in Fig. 2.1 is

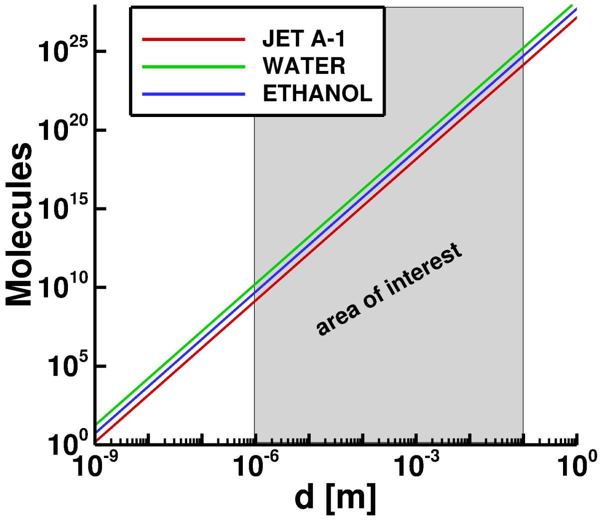

Figure 2.1.: Number of molecules over droplet diameter

given by:

$$N = \frac{m_p \cdot N_A}{\bar{M}} = \frac{\rho_l \, \pi \, d_p^3 \cdot N_A}{6 \cdot \bar{M}} \tag{2.1.1}$$

with the Avogadro constant N_A, the mean molar mass $\bar{M}$ and the mass of the droplet m_p which is dependent on the density of the liquid ρ_l and the droplet diameter d_p. Most atomizers in thermal turbomachinery generate droplets in the order of magnitude of 1 μm to 1 mm as well as bigger structures like sheets, threads and ligaments justifying the applicability of continuum mechanics. In continuum mechanics two spatial reference systems can be distinguished, namely the Eulerian and Lagrangian framework. In the Eulerian framework, a space-fixed reference system is employed, i.e. the problem is observed from an exterior point of view. Most finite volume solvers commonly used for the gaseous phase in computational fluid dynamics rely on this framework. In contrast, the Lagrangian framework is based on a reference system located on the fluid particle, i.e. the observer moves with the fluid and experiences changes in the surroundings (e.g. of density, velocity and temperature) relative to the particle. Mixed methodologies combine both approaches and use them to solve parts of the considered problem.

For separated flows with a detailed description of the gas-liquid interface, pure Lagrangian formulations can be found for example within the meshless smoothed particle hydrodynamics (SPH) method. In the SPH method, the fluids are represented by numerous Lagrangian particles interacting with each other within a certain influence area around each particle. Promising results were shown by Höfler (2013) for non-reacting isothermal flows. But due to the immense computational costs, the SPH method is restricted to a small field of view, up to now. Pure Eulerian descriptions appear in interface capturing methods (Gorokhovski and Herrmann, 2008) like Volume-of-fluid (VOF) and Level-set. In the VOF method, an additional transport equation for the volume fraction of liquid in the gaseous media is solved. Mass is implicitly conserved via the conservative formulation of the transport equation. The volume fraction f yields $f = 0$ in cells fully filled with gas and $f = 1$ in cells fully occupied by liquid. The gas-liquid interface is located in cells with $0 < f < 1$, i.e. partially filled with gas and liquid, and needs to be reconstructed. This can lead to problems with surface tension as it depends on the local curvature. Therefore, the surface reconstruction model is crucial (Ashgriz, 2011). In the Level-set method, an additional transport equation for the shortest distance to the gas-liquid interface is solved (Sethian and Smereka, 2003). The interface location is described by a level set scalar G with $G = 0$ at the interface, $G > 0$ in the liquid and $G < 0$ in the gas. Consequently, the gas-liquid interface can be easily reconstructed. Unfortunately, mass conservation is not automatically satisfied by the method. As the benefits and drawbacks of the VOF and the Level-set method are partly complementary, combinations of both methods exist, e.g. Sussman (2003); Sussman *et al.* (2007) and Ménard *et al.* (2007). Similar to the SPH method, the interface capturing Eulerian methods come along with high computational costs limiting the field of view. Phase change and reactions were usually neglected. For example, Gomaa (2014) performed VOF simulations of the interaction of a single droplet with a wall. Successful applications of the VOF and the Level-set method in the field of primary atomization can be found in Tomar *et al.* (2010); Ling and Zaleski (2015); Ertl *et al.* (2016) and Herrmann (2011), respectively. The most sophisticated mixed Eulerian-Lagrangian approach with a detailed description of the gas-liquid interface is the Front-tracking method (Tryggvason *et al.*, 2001). Tryggvason *et al.* introduced an additional mesh following the interface in a Lagrangian framework. The velocities on both sides of the interface are calculated by a standard Eulerian finite volume solver. Large deformation or wrinkling leads to a huge computational effort for re-meshing. Collision and other significant changes in fluid topology can even lead to nonphysical solutions. As a consequence, disintegration and coalescence needs to be modeled (Thomas *et al.*, 2010). Again, the high computational costs limit the field of view. Generally speaking, all high-resolution techniques described above are very useful to describe isolated sub-processes like atomization or to develop sub-models but still are far from applicability to combustion problems. In order to enlarge the field of view, the interface reconstruction has to be neglected, up to now.

For dispersed flows, e.g. particle-laden flows or reactive sprays in combustion chambers, the two prevalent methods in the literature are the Eulerian-Eulerian method (e.g. Boileau *et al.* (2008) and Moreau *et al.* (2010)) and the Eulerian-Lagrangian method (e.g. Chrigui *et al.* (2012); Sacomano Filho *et al.* (2014) and Jones *et al.* (2015)). While the former is based on an Eulerian reference system for both phases, the latter uses an Eulerian and Lagrangian reference system for the gaseous and dispersed liquid phase, respectively. Comparisons of the two methods can be found in de Chaisemartin *et al.* (2007); Riber *et al.* (2009); Jaegle *et al.* (2011), and Sanjosé *et al.* (2011). The Eulerian-Eulerian method rests upon the assumption that all phases are interpenetrating continuous fluids and behave like a continuum with averaged state variables ($\vec{u}_p$, T_p,...). In the Eulerian-Lagrangian method, the gaseous phase is described as a continuum in an Eulerian framework while each discrete particle of the dispersed phase is tracked using a Lagrangian reference system. In order to obtain meaningful statistics, a sufficiently high number of particles is necessary. The state variables of the droplets are individually determined making Lagrangian particle tracking more expensive than the Eulerian-Eulerian method. Both phases are coupled by boundary conditions provided from the Eulerian to the Lagrangian phase as well as source terms handed over from the Lagrangian to the Eulerian phase. Fig. 2.2 schematically shows the resulting gas (blue arrows) and particle (red arrows) velocities for both numerical approaches. The biggest advantage of Eulerian-Eulerian methods is that all equations have the form of standard transport equations, i.e. the same algorithms and solution methods can be applied for both the gaseous and the dispersed phase. As a consequence, they are less

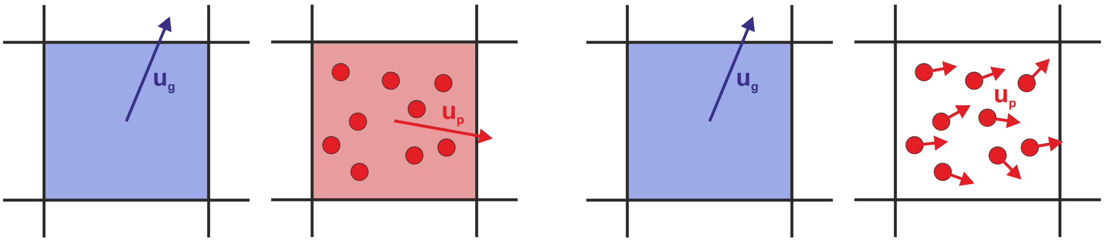

(a) Eulerian-Eulerian (b) Eulerian-Lagrangian

Figure 2.2.: Numerical approaches for spray computations (adapted from Koch (2011))

(a) Eulerian-Eulerian (b) Eulerian-Lagrangian

Figure 2.3.: Numerical result of crossing trajectories of mono-disperse droplets (adapted from Koch (2011))

computationally intensive and can be easily implemented in common finite volume solvers. The disadvantage of the Eulerian-Eulerian method is that the individuality of a droplet, particle or bubble is not accounted for. Information on the motion of individual particles is not available resulting for example in wrong particle trajectories in case of dilute sprays (Fig. 2.3). A sufficiently high volume fraction of the single phases in a control volume is necessary to get meaningful average properties. In other words, the average particle distance needs to be significantly smaller than the spatial discretization (Frank, 2002). Furthermore, the phases have to be well mixed to justify the application of transport equations for a continuum. Another drawback is that characteristic diameters (representative of diameter classes) have to be predefined and kept fixed during run-time. As a consequence, a discretization error related to the number of diameter classes is introduced for continuous processes like evaporation. In contrast, in the Eulerian-Lagrangian approach the modeling of physical and chemical processes, e.g. evaporation, condensation, droplet breakup, particle-wall interaction and surface reactions, is eased and more accurate due to the consideration of individual particles and the Lagrangian reference system. Nevertheless, the detailed flow around each individual particle cannot be resolved as the computational costs have to be kept at reasonable levels. Hence, models are commonly based on empirical correlations. Besides, particles with the same properties are summed up to so-called parcels. A limited applicability of the Eulerian-Lagrangian method exists in regions of high liquid volume fractions due to large liquid structures, high particle densities or small grid cells. This is due to the fact that the volume fraction of the dispersed phase is commonly neglected in the continuous phase. Nevertheless, in thermal turbomachinery the dense spray region is confined to a small area close to the fuel injector so that a dilute spray prevails in the major part of the combustion chamber (Faeth, 1983). The physical system consists of discrete liquid droplets with a spectrum of diameters being dispersed in a turbulent, continuous gaseous phase. Due to the very large number of droplets involved, resolving the detailed evolution of the gas-liquid interface as well as the flow on both sides of the interface will not be feasible in the foreseeable future.

Accounting for all the considerations above, the Eulerian-Lagrangian approach is chosen as a good compromise between accuracy and numerical costs. The gaseous phase is calculated by a finite volume solver in the Eulerian reference frame while the liquid phase is computed by means of Lagrangian particle tracking using a point source approximation, i.e. droplets are assumed to be mathematical points providing point sources and point forces to the gas field.

2.2. Gas Flow Solver

The gaseous phase is calculated by the pressure-based DLR in-house code THETA (Turbulent Heat Release Extension of the TAU Code). THETA is a 3D finite volume solver for unstructured dual grids. The underlying equations are the conservation of mass, species mass, momentum and enthalpy (Gerlinger, 2005; Kuo and Acharya, 2012):

$$\frac{\partial \rho_g}{\partial t} + \frac{\partial}{\partial x_i}\left(\rho_g u_i\right) = S^d_\rho \tag{2.2.1}$$

$$\frac{\partial}{\partial t}(\rho_g Y_\alpha) + \frac{\partial}{\partial x_i}(\rho_g u_i Y_\alpha) + \frac{\partial j_{\alpha i}}{\partial x_i} = S_\alpha + S^d_\alpha \tag{2.2.2}$$

$$\frac{\partial}{\partial t}(\rho_g u_i) + \frac{\partial}{\partial x_j}(\rho_g u_i u_j) - \frac{\partial \tau_{ij}}{\partial x_j} = -\frac{\partial p}{\partial x_i} + \rho_g f_i + S^d_{\rho u} \tag{2.2.3}$$

$$\frac{\partial}{\partial t}(\rho_g h) + \frac{\partial}{\partial x_i}(\rho_g u_i h) + \frac{\partial q_i}{\partial x_i} - \tau_{ij}\frac{\partial u_i}{\partial x_j} = \frac{Dp}{dt} + \rho_g f_i u_i + S_r + S^d_h \tag{2.2.4}$$

The convective and diffusive fluxes are discretized using second-order central differencing schemes. The time discretization is based on a second-order Three-Point Backward (TPB) or second-order Crank-Nicolson scheme. A projection method is applied to couple velocity and pressure. The Poisson equation for the pressure correction is solved by the FGMRES method preconditioned by a single multigrid V-cycle. The other transport equations are computed by the BiCGStab method with Jacobi preconditioning. For details on the numerical methods, the reader is referred to Ferziger and Peric (2008). In order to reduce memory requirements, a matrix-free formulation for all linear equations is used (Löwe *et al.*, 2015).

2.2.1. Turbulence model

2.2.1.1. Modeling approaches for turbulence

Depending on the resolution of the flow and turbulent structures, three general modeling approaches can be distinguished, namely Reynolds-averaged Navier-Stokes (RANS) simulations, large eddy simulations (LES) and direct numerical simulations (DNS) (Pope, 2000). In RANS simulations, all flow scales are modeled and computations usually rely on calibration. The computational effort of these simulations is rather small allowing for short turnaround times and parameter variations so that they were extensively used in industry in the last decades. However, unsteady phenomena and inhomogeneities, which are present in modern gas turbine combustors, e.g. turbulent mixing, ignition and extinction sequences, are very difficult to model within the RANS context. Hence, the precision of such computations is limited (Gicquel *et al.*, 2012). Furthermore, the local transient processes can have an impact on global phenomena like flame stabilization and emissions. Consequently, the main objective of alternative approaches is to relax the modeling constraints. In DNS strictly speaking all scales, i.e. flow scales of both phases as well as chemical scales, are resolved and no modeling is required. With this strict definition aeronautical multi-phase, reactive flows remain out of reach for DNS. Besides the resolution requirements due to the high Reynolds numbers inducing very small turbulent structures, the highly energetic fuels lead to very thin reaction zones which can hardly be resolved. Furthermore, a resolution of the highly distributed and numerous gas-liquid interfaces and the flow on both sides are beyond the capabilities of current supercomputers. In practice, DNS is usually only referred to the resolution of turbulent structures while the descriptions of chemistry and the dispersed phase rely on modeling. Despite this simplification, computational costs remain very high restricting the method to only simple configurations, which are used for model derivation and validation as well as understanding of fundamental phenomena. Very few computations of test cases with increased complexity exist, as for example in Luo *et al.* (2011), who analyzed a three-dimensional n-heptane spray flame in a model swirl combustor by means of DNS (for the continuous phase only) with a point-droplet assumption for the dispersed phase. Large Eddy Simulation is a compromise between DNS and RANS relying on on a scale separation, i.e. large scale structures are resolved while small scales structures and their feedback to the large structures are modeled (Sagaut, 2006). If the models for the small scales are correctly defined, the LES solution approaches the DNS solution in regions of high resolution. Thanks to the increase in computing power, LES has become a clear scientific alternative to RANS. Especially for the specific application within this thesis, i.e. highly unsteady enclosed flows in complex geometries, the advantages of LES computations outweigh the disadvantages. As a consequence, LES will be used within the work at hand (details see section 2.2.1.2).

2.2.1.2. Large Eddy Simulation

The simulation of turbulence is a multi-scale problem in time and space (Sagaut *et al.*, 2006) and the characteristics of large and small scales are very different (Pope, 2000). The energy-rich, inhomogeneous, large scales have a longer life span and depend on the geometry. In contrast, the small scales are short-lived, dissipative and have a more isotropic, universal character (Fröhlich, 2006). Due to this fact, the basic idea of Large Eddy Simulations (LES) is to separate the large scales from the small ones by a filtering operation. The spatially filtered value $\bar{\Psi}$ of a local, instantaneous quantity $\Psi(\vec{x},t)$ results from the convolution with the filter function G and is defined as:

$$\bar{\Psi}(\vec{x},t) = \int_{\Omega} \Psi(\vec{y},t)\; G(\vec{x}-\vec{y};\Delta\vec{x})\; d\vec{y} \tag{2.2.5}$$

wherein Ω and Δ represent the entire domain and the filter width, respectively. In a finite volume formulation an implicit filtering by the discretization is often adopted (Gicquel *et al.*, 2012) and also used within this work. This leads to the following spatially varying filter width:

$$\Delta = (\Delta x \Delta y \Delta z)^{1/3} \tag{2.2.6}$$

Advantages and drawbacks of this method can be found in Fröhlich (2006) and Poinsot and Veynante (2011). In case of density variations due to temperature changes, chemical reactions or compressibility, it is widely accepted to introduce a density weighted (Favre) filtering (Noll, 1992; Gerlinger, 2005; Poinsot and Veynante, 2011). The density weighted filtered value $\tilde{\Psi}$ of a quantity Ψ is defined as:

$$\tilde{\Psi} = \frac{\overline{\rho_g \Psi}}{\bar{\rho}_g} \tag{2.2.7}$$

Mass conservation equation Filtering the mass conservation equation (Eq. 2.2.1) for a reacting gas-liquid mixture gives:

$$\frac{\partial \bar{\rho}_g}{\partial t} + \frac{\partial}{\partial x_i}\left(\bar{\rho}_g \tilde{u}_i\right) = \bar{S}^d_\rho \tag{2.2.8}$$

with the filtered mass source term $\bar{S}^d_\rho$ due to the presence of the liquid droplets.

Momentum conservation equation Filtering the momentum conservation equation (Eq. 2.2.3) for a reacting gas mixture yields:

$$\frac{\partial}{\partial t}(\bar{\rho}_g \tilde{u}_i) + \frac{\partial}{\partial x_j}(\bar{\rho}_g \tilde{u}_i \tilde{u}_j) - \frac{\partial}{\partial x_j}\left(\bar{\tau}_{ij} - \bar{\rho}_g\left(\widetilde{u_i u_j} - \tilde{u}_i \tilde{u}_j\right)\right) = -\frac{\partial \bar{p}}{\partial x_i} + \bar{\rho}_g f_i + \bar{S}^d_{\rho u} \tag{2.2.9}$$

with the filtered momentum source term $\bar{S}^d_{\rho u}$ due to the presence of the liquid droplets. Assuming a Newtonian fluid (linear dependence of the stresses on the shear) and replacing the volume viscosity according to the Stokes hypothesis, the filtered stress tensor in Eq. 2.2.9 has the form:

$$\bar{\tau}_{ij} = \bar{\rho}_g \nu_g \left(\frac{\partial \tilde{u}_i}{\partial x_j} + \frac{\partial \tilde{u}_j}{\partial x_i} - \frac{2}{3}\delta_{ij}\frac{\partial \tilde{u}_k}{\partial x_k}\right) \tag{2.2.10}$$

The unresolved sub-grid Reynolds stresses $\bar{\rho}_g\left(\widetilde{u_i u_j} - \tilde{u}_i \tilde{u}_j\right)$ require modeling and several approaches were proposed in the literature (Smagorinsky, 1963; Germano *et al.*, 1991; Lilly, 1992; Ghosal and Moin, 1995; Nicoud and Ducros, 1999; Stolz *et al.*, 2001). For a review, the reader is referred to Gicquel *et al.* (2012). Within this work, the unresolved sub-grid Reynolds stresses $\bar{\rho}_g\left(\widetilde{u_i u_j} - \tilde{u}_i \tilde{u}_j\right)$ are calculated by the WALE (Wall-Adapting Local Eddy-viscosity) model (Ducros *et al.*, 1998; Nicoud and Ducros, 1999). As the name of the model indicates, it follows the tradition of classical RANS approaches relying on the eddy viscosity concept proposed by Boussinesq (1877). By analogy with the resolved stresses caused by molecular viscosity (Eq. 2.2.10), the eddy viscosity concept introduces a turbulent viscosity relating the unresolved sub-grid Reynolds stresses to the resolved flow:

$$\bar{\rho}_g\left(\widetilde{u_i u_j} - \tilde{u}_i \tilde{u}_j\right) = -\bar{\rho}_g \nu_t \left(\frac{\partial \tilde{u}_i}{\partial x_j} + \frac{\partial \tilde{u}_j}{\partial x_i} - \frac{2}{3}\delta_{ij}\frac{\partial \tilde{u}_k}{\partial x_k}\right) + \frac{2}{3}\delta_{ij}\bar{\rho}_g k_{sgs} \tag{2.2.11}$$

In case of an incompressible flow, the dilatational term (last term in the brackets) of Eq. 2.2.10 and Eq. 2.2.11 is zero. The very last term on the right hand side of Eq. 2.2.11 is added to ensure that the sum of the normal stresses equals $2k_{sgs}$. The eddy viscosity is modeled by:

$$\nu_t = (C_{sgs}\Delta)^2 \frac{\left(\mathcal{S}^d_{ij}\mathcal{S}^d_{ij}\right)^{\frac{3}{2}}}{\left(\tilde{S}_{ij}\tilde{S}_{ij}\right)^{\frac{5}{2}} + \left(\mathcal{S}^d_{ij}\mathcal{S}^d_{ij}\right)^{\frac{5}{4}}} \tag{2.2.12}$$

This formulation results in a proper near-wall behavior and is based on the traceless symmetric part of the square of the velocity gradient tensor:

$$\mathcal{S}^d_{ij} = \frac{1}{2}\left(\tilde{g}^2_{ij} + \tilde{g}^2_{ji}\right) - \frac{1}{3}\delta_{ij}\tilde{g}^2_{kk} \tag{2.2.13}$$

with

$$\tilde{g}^2_{ij} = \tilde{g}_{ik}\tilde{g}_{kj} \tag{2.2.14}$$

and the velocity gradient tensor:

$$\tilde{g}_{ij} = \frac{\partial \tilde{u}_i}{\partial x_j} \tag{2.2.15}$$

$\tilde{S}_{ij}$ represents the strain rate tensor of the resolved scales:

$$\tilde{S}_{ij} = \frac{1}{2}\left(\frac{\partial \tilde{u}_i}{\partial x_j} + \frac{\partial \tilde{u}_j}{\partial x_i}\right) \tag{2.2.16}$$

Within the work at hand a model constant of $C_{sgs} = 0.325$ was used (Probst *et al.*, 2015).

Enthalpy conservation equation In low Mach number flows the viscous dissipation $\tau_{ij}\frac{\partial u_i}{\partial x_j}$ in the enthalpy equation (Eq. 2.2.4) can be neglected and the substantial pressure derivative approximated by $\frac{Dp}{dt} = \frac{\partial p}{\partial t} + u_i\frac{\partial p}{\partial x_i} \approx \frac{dp}{dt}$ (Gerlinger, 2005). In addition, radiation is neglected within this study. This leads to the filtered enthalpy conservation equation:

$$\frac{\partial}{\partial t}(\bar{\rho}_g\tilde{h}) + \frac{\partial}{\partial x_i}(\bar{\rho}_g\tilde{u}_i\tilde{h}) + \frac{\partial}{\partial x_i}\left(\bar{q}_i - \bar{\rho}_g\left(\widetilde{u_i h} - \tilde{u}_i\tilde{h}\right)\right) = \frac{d\bar{p}}{dt} + \bar{\rho}_g f_i\tilde{u}_i + \bar{S}^d_h \tag{2.2.17}$$

wherein $\bar{S}^d_h$ is the enthalpy source term due to the presence of the droplets and h the specific enthalpy of a gas mixture defined as:

$$h = \sum_{\alpha=1}^{N_{sp}} h_\alpha Y_\alpha \tag{2.2.18}$$

with the specific enthalpy h_α of species α:

$$h_\alpha = \Delta h^0_{f,\alpha} + \int_{T_0}^{T} c_{p,\alpha}dT \tag{2.2.19}$$

In Eq. 2.2.19, $h^0_{f,\alpha}$ represents the heat of formation and $c_{p,\alpha}$ the specific isobaric heat capacity of species α. The filtered energy flux $\bar{q}_i$ in Eq. 2.2.17 is assumed to be only composed of thermal conduction (Fourier's law) and energy fluxes due to species diffusion and is modeled by:

$$\bar{q}_i = -\bar{\lambda}\frac{\partial \tilde{T}}{\partial x_i} + \sum_{\alpha=1}^{N_{sp}} \tilde{h}_\alpha \bar{j}_{\alpha i} \tag{2.2.20}$$

The thermal diffusion by conduction is related to the viscous diffusion via the non-dimensional Prandtl number:

$$Pr_g = \frac{\nu_g}{a} = \nu_g \cdot \frac{\rho_g c_p}{\lambda_g} = \frac{\text{Viscous diffusion}}{\text{Thermal diffusion}} \tag{2.2.21}$$

Species conservation equation Filtering the species conservation equation (Eq. 2.2.2) for a reacting gas mixture results in:

$$\frac{\partial}{\partial t}(\bar{\rho}_g \tilde{Y}_\alpha) + \frac{\partial}{\partial x_i}(\bar{\rho}_g \tilde{u}_i \tilde{Y}_\alpha) + \frac{\partial}{\partial x_i}\left(\bar{j}_{\alpha i} - \bar{\rho}_g\left(\widetilde{u_i Y_\alpha} - \tilde{u}_i \tilde{Y}_\alpha\right)\right) = \bar{S}_{Y_\alpha} + \bar{S}^d_{Y_\alpha} \tag{2.2.22}$$

The filtered species diffusion fluxes $\bar{j}_{\alpha i}$ were approximated by a formulation based on Fick's law neglecting species diffusion due to temperature gradients (thermophoresis or Soret effect) and pressure gradients as well as species diffusion induced by external forces:

$$\bar{j}_{\alpha i} = -\bar{\rho}_g \bar{D}_\alpha \frac{\partial \tilde{Y}_\alpha}{\partial x_i} \tag{2.2.23}$$

The diffusion coefficient D_α of species α into the mixture is determined from the binary diffusion coefficients according to Di Domenico (2008). The species diffusion is related to the viscous diffusion via the non-dimensional Schmidt number and to the thermal diffusion through the non-dimensional Lewis number:

$$Sc_\alpha = \frac{\nu_g}{D_\alpha} = \frac{\text{Viscous diffusion}}{\text{Species diffusion}} \tag{2.2.24}$$

$$Le_\alpha = \frac{\lambda_g}{\rho_g c_p D_\alpha} = \frac{Sc_{\alpha,g}}{Pr_g} = \frac{\text{Thermal diffusion}}{\text{Species diffusion}} \tag{2.2.25}$$

The filtered species source term $\bar{S}_{Y_\alpha}$ due to chemical reactions will be addressed in section 2.2.2.3.

Closure of the unresolved scalar fluxes In analogy to the resolved scalar fluxes, the widely-used gradient diffusion hypothesis, i.e. the scalar transport follows the main scalar gradient (Pope, 2000), is applied for the closure of the unresolved scalar fluxes $\bar{\rho}_g\left(\widetilde{u_i\phi} - \tilde{u}_i\tilde{\phi}\right)$ with $\phi = h, Y_1, ..., Y_{sp-1}$:

$$\bar{\rho}_g\left(\widetilde{u_i\phi} - \tilde{u}_i\tilde{\phi}\right) = \bar{\rho}_g \mathit{\Gamma}_{t,\phi}\frac{\partial \tilde{\phi}}{\partial x_i} \tag{2.2.26}$$

The diffusion coefficient $\mathit{\Gamma}_{t,\phi}$ is determined by means of a turbulent Prandtl number and a turbulent Schmidt number for the enthalpy and species equations, respectively (Gicquel *et al.*, 2012). For the enthalpy equation ($\phi = h$) this leads to:

$$\mathit{\Gamma}_{t,h} = \frac{\nu_t}{Pr_t} \tag{2.2.27}$$

For the species equations ($\phi = Y_1, ..., Y_{sp-1}$) the diffusion coefficients yield:

$$\mathit{\Gamma}_{t,Y_\alpha} = \frac{\nu_t}{Sc_{\alpha,t}} \tag{2.2.28}$$

Eq. 2.2.27 and 2.2.28 illustrate that the accuracy strongly depends on the turbulent viscosity closure. Both the turbulent Prandtl number and the turbulent Schmidt number were set to a constant value of one. Ivanova *et al.* (2010) showed that the choice of the constants had a minor influence on results.

Resulting set of equations In total, Eq. 2.2.8, Eq. 2.2.9, Eq. 2.2.17 and Eq. 2.2.22 result in a set of $N_{sp} + 4$ transport equations to be solved. The last species is calculated by:

$$\sum_{\alpha=1}^{N_{sp}} Y_\alpha = 1 \tag{2.2.29}$$

The gas density ρ_g can be calculated by the ideal gas law for a gaseous mixture:

$$\rho_g = \frac{p_g}{\mathcal{R} T_g \sum_{\alpha=1}^{N_{sp}} (Y_\alpha / M_\alpha)} \tag{2.2.30}$$

2.2.2. Chemical reaction model

2.2.2.1. Modeling approaches for chemical reactions

Chemical reaction kinetics can be described by Arrhenius laws for the rate constants (Kuo, 1986). The finite-rate chemistry model (FRC), which is used within this work (details see section 2.2.2.2), relies on a direct computation of these terms but comes along with the necessity of solving a transport equation for each species. Detailed chemical mechanisms, however, involve thousands of species (Warnatz *et al.*, 2006). For CFD, these detailed schemes need to be significantly cut down by identifying the most important species and reactions. The reduced chemical mechanisms aim at reproducing target variables, e.g. laminar flame speed, adiabatic flame temperature and ignition delay times, or even profiles of intermediate species for the most complex ones, at specific conditions. The more general a mechanism ought to be, the more species and reactions have to be considered. Unfortunately, the chemical reactions in a reduced mechanism can exhibit very different chemical time scales leading to so-called stiff sets of ordinary partial differential equations. The Eulerian solver for the gaseous phase has to be able to cope with such stiff chemistry.

In contrast to a direct computation of the chemical reactions, tabulated chemistry approaches, e.g. Flamelet Generated Manifolds (FGM), aim at accelerating the calculation by using look-up tables which consist of solutions for pre-computed laminar flames. Reaction rates and species mass fractions are tabulated as functions of a limited set of coordinates (Poinsot and Veynante, 2011). Franzelli *et al.* (2013) proposed a three-dimensional look-up table parametrized as a function of the progress variable describing the extent in which the reaction proceeded, the mixture fraction describing the local mixing of fuel and oxidizer, and the scalar dissipation, which identifies the combustion regime. The information for the table was obtained by pre-computing premixed, partially-premixed and diffusion flames. Look-up tables with two or more variables can become costly due to multi-linear interpolations. Besides, they can become fairly large which leads to high memory requirements if duplication is necessary on massively-parallel systems. On shared memories, proper and efficient memory access has to be taken care off. As a consequence and as usually only small portions of the table are used, several techniques (see Gicquel *et al.* (2012) for details) exist to generate look-up tables during run-time, e.g. in situ adaptive tabulation (ISAT). At the start of the computation, the table is empty and it is continuously filled as the computation proceeds. Besides these numerical aspects, special modeling is necessary to account for heat losses due to wall heat fluxes, radiation or spray evaporation (Olguin and Gutheil, 2014).

In recent years, LES research mainly focused on the modeling of second-order correlations, e.g. sub-grid scale Reynolds stresses and scalar fluxes in the gas phase as well as their implications on the liquid phase, and the highly non-linear filtered chemical source term controlling the production and consumption of species. The necessity of models is associated with the loss of information due to the filtering. Following Gicquel *et al.* (2012), sub-grid scale models for combustion can be subdivided in geometric and statistical models as well as the linear-eddy mixing (LEM) model. The artificially thickened flame (ATF) model (Butler and O'Rourke, 1977; Colin *et al.*, 2000) belongs to the first category. Its basic idea is to artificially increase the flame thickness until the flame front can be resolved by the computational grid. The laminar flame speed s_L^0 and the flame thickness δ_L^0 are related to the thermal diffusivity a and the pre-exponential factor A_r in the Arrhenius expression (Eq. 2.2.34) by:

$$s_L^0 \propto \sqrt{aA_r} \tag{2.2.31}$$

$$\delta_L^0 \propto \frac{a}{s_L^0} = \sqrt{\frac{a}{A_r}} \tag{2.2.32}$$

If the thermal diffusivity a is increased by a factor F while the pre-exponential factor A_r is decreased by F, the flame thickness is increased by F while the flame speed is maintained. However, the Damköhler number $Da = \tau_t/\tau_c$, i.e. the ratio of turbulent time scale $\tau_t = l_t/|\vec{u'}_g|$ to chemical time scale $\tau_c = \delta_L^0/s_L^0$ is decreased by F. As a consequence, the flame is less sensitive to turbulent fluctuations. Hence, a correction factor called efficiency function E is introduced ($a \rightarrow EFa$ and $A_r \rightarrow E/FA_r$). The efficiency function corresponds to a sub-grid scale wrinkling factor depending on sub-grid scale properties, e.g u'_g/s_L and $\mathit{\Delta}/(F\delta_L^0)$ and is derived from DNS. Applications to spray combustion of the artificially thickened flame model can be found in Boileau *et al.* (2008) and Ghani *et al.* (2016). Boileau *et al.* (2008) simulated a laminar, one-dimensional JP10/air flame combining a one-step global reaction with the ATF model. Ghani *et al.* (2016) computed acoustic instabilities in a swirl-stabilized kerosene/air flame combining a two-step, six species FRC model with the ATF model.

In statistical models, the SGS terms are determined by means of probability density functions (PDFs). The PDF specifies the relative likelihood that a variable takes a certain value. The transported probability density function (TPDF) approach (Pope, 1981), assumed probability density function (APDF) approach (Girimaji, 1991a,b; Gaffney *et al.*, 1992; Gerlinger *et al.*, 2001), the Eulerian stochastic fields method (Valiño, 1998) and the conditional filtered moment closure (CMC) (Klimenko and Bilger, 1999) belong to this class of models. In the transported PDF approach, the joint PDF is computed at each point and time by an ensemble of notional particles following a set of stochastic differential equations (SDEs). The SDEs are solved by a Lagrangian Monte-Carlo solver (Pope, 1981). Heye *et al.* (2013, 2015) successfully calculated ethanol and methanol spray flames combining the flamelet generated manifold (FGM) combustion model with the TPDF approach. But, with respect to Eulerian-Lagrangian simulations, a third solver is necessary increasing the degree of complexity. In order to overcome this issue, instead of determining the joint PDF via Lagrangian stochastic particles, an ensemble of stochastic Eulerian fields for each scalar is used in the Eulerian stochastic fields method (Jones *et al.*, 2011). The sub-grid scale contributions to the scalar equations can then be obtained from averaging over these stochastic fields. Applications of the Eulerian stochastic fields methods to swirl-stabilized kerosene flames as well as to spray flames with co-axial injection of methanol and air can be found in Jones *et al.* (2011, 2012, 2014) and Jones *et al.* (2015), respectively. Both the TPDF approach and the Eulerian stochastic fields method belong to the most accurate methods, but they come along with immense computational costs. As a consequence, their application is limited to academic test cases, up to now. In contrast, computational costs can be significantly reduced by using assumed probability density functions, which were adopted in this work (details see section 2.2.2.3). Within both the APDF methods and the CMC approach, the shape of the PDF is fixed a priori. Unfortunately, this is accompanied with a loss of generality. In the APDF method, the PDF is usually parametrized by the local value of the filtered quantity and its variance (Gicquel *et al.*, 2012). Combinations of the FGM combustion model with the APDF approach can be found in Chrigui *et al.* (2012) simulating the partially pre-vaporized acetone spray flame of Gounder (2009); Gounder *et al.* (2012) as well as in Sacomano Filho *et al.* (2014) computing the partially pre-vaporized n-heptane spray flame of Pichard *et al.* (2002). In the CMC approach, transport equations for the conditional moments of species mass fractions and enthalpy are solved. The conditioning variable is usually the mixture fraction. The cell filtered value is obtained by integrating the conditional moment across mixture fraction space assuming a PDF for the distribution of the scalar. A computation of the partially pre-vaporized acetone spray flame of Gounder (2009); Gounder *et al.* (2012) by means of the CMC approach can be found in Ukai *et al.* (2013). Ukai *et al.*, however, also highlight some limitations associated with mixture fraction as a single conditioning variable for spray combustion.

In linear-eddy mixing (LEM) models (Menon and Kerstein, 2011), sub-grid processes, e.g. subgrid scale mixing, reaction kinetics and phase change of the liquid fuel, are modeled on a one-dimensional domain embedded inside each LES grid cell. The 1-D domain is aligned in the direction of the maximum scalar gradient and discretized with a certain number of points. The number of points is chosen so that all the relevant scales are resolved. In practical applications, the optimum number of points can strongly vary in time and space depending on the local turbulence. As a consequence, dynamic load balancing is required in massively-parallel computations. By means of this accurate but very costly method, Patel and Menon (2008) simulated spray-turbulence-flame interactions in a lean direct injection combustor. As already mentioned during the course of this section, the FRC model in combination with the APDF approach for turbulence-chemistry interaction was used within this thesis. They will be shortly described in the following.

2.2.2.2. Finite-rate chemistry model

A reduced chemical reaction mechanism consists of $N_{sp} = 40 - 150$ species and a set of $N_r = 300 - 1000$ elementary reactions. These elementary reactions describe the conversion of a reactant $\mathcal{M}_\alpha$ into a product and can be generalized by the following formulation (Gerlinger, 2005):

$$\sum_{\alpha}^{N_{sp}} \nu'_{\alpha,r}\mathcal{M}_\alpha \underset{k_{b,r}}{\overset{k_{f,r}}{\rightleftharpoons}} \sum_{\alpha}^{N_{sp}} \nu''_{\alpha,r}\mathcal{M}_\alpha \tag{2.2.33}$$

with $\nu'_{\alpha,r}$ representing the stoichiometric coefficient of the reactant α in reaction r. Accordingly, $\nu''_{\alpha,r}$ represents the stoichiometric coefficient on the product side. The forward and backward reaction rate $k_{f,r}$ and $k_{b,r}$ can be calculated by the modified Arrhenius equation (Kuo, 1986):

$$k_r = A_r T^{b_r} exp\left(-\frac{E_{a,r}}{\mathcal{R}T}\right) \tag{2.2.34}$$

The pre-exponential factor incorporates the constant A_r and the temperature exponent b_r. $E_{a,r}$ is the activation energy of the reaction r.

By summing over all reactions in the chemical kinetics mechanism, the source term on the right hand side of the equation for mass conservation of species $\alpha = 1, ..., N_{sp} - 1$ can be calculated for laminar (or fully resolved) reactive flows (Gerlinger, 2005):

$$S_\alpha = M_\alpha \sum_{r=1}^{N_r} \left(\left(\nu''_{\alpha,r} - \nu'_{\alpha,r}\right) \left(k_f \prod_{\beta=1}^{N_{sp}+1} [\mathcal{M}_\alpha]^{\nu'_{\beta,r}} - k_b \prod_{\beta=1}^{N_{sp}+1} [\mathcal{M}_\alpha]^{\nu''_{\beta,r}} \right)\right) \tag{2.2.35}$$

with the concentration $[\mathcal{M}_\alpha]$ of a species named $\mathcal{M}_\alpha$:

$$[\mathcal{M}_\alpha] = \frac{\rho_g Y_\alpha}{M_\alpha} \tag{2.2.36}$$

2.2.2.3. Assumed PDF model for turbulence-chemistry interaction

As chemical processes take place on a molecular level with characteristic length scales below the grid size and hence the filter width, the interaction between unresolved turbulent fluctuations and chemistry has to be accounted for by a so called sub-grid scale model for turbulence-chemistry interaction. The chemical source term $\bar{S}_\alpha$ is given by the integration over the one-point one-time joint PDF of temperature and composition:

$$\bar{S}_\alpha = \int S_\alpha(T, Y_1, Y_2 \ldots Y_{sp})\; f(T, Y_1, Y_2 \ldots Y_{sp})\; dT dY_1 dY_2 \ldots dY_{sp} \tag{2.2.37}$$

In the work at hand, the filtered chemical source term was determined by an assumed probability density function approach, i.e. the shape of the PDF was a priori set to a fixed mathematical form. The approach of Gerlinger *et al.* (2001); Di Domenico (2008); Blacha (2012) was adopted presuming statistical independence of temperature and composition. Hence, the filtered chemical source term was approximated by:

$$\bar{S}_\alpha \approx M_\alpha \sum_{r=1}^{N_r} \left(\left(\nu''_{\alpha,r} - \nu'_{\alpha,r}\right) \left(\bar{k}_f \overline{\prod_{\beta=1}^{N_{sp}+1} [\mathcal{M}_\alpha]^{\nu'_{\beta,r}}} - \bar{k}_b \overline{\prod_{\beta=1}^{N_{sp}+1} [\mathcal{M}_\alpha]^{\nu''_{\beta,r}}} \right) \right) \tag{2.2.38}$$

The filtered forward and backward reaction rates were determined by:

$$\bar{k}_r = \int_{T=0}^{T=\infty} k_r(T) f_T(T) dT \tag{2.2.39}$$

It was assumed that the temperature in the sub-grid scale followed a clipped Gaussian PDF:

$$f_T(T) = \frac{1}{\sqrt{2\pi\sigma_{T_0}}} exp\left(-\frac{(T-\bar{T}_0)^2}{2\sigma_{T_0}}\right) + C_{min}\delta(T - T_{min}) + C_{max}\delta(T - T_{max}) \tag{2.2.40}$$

The temperature PDF was clipped by introducing Dirac functions due to the fact that the temperature cannot fall below a minimum temperature T_{min}, e.g. the inflow temperature, and exceed a maximum temperature T_{max}, e.g. adiabatic flame temperature. The coefficients C_{min} and C_{max} were determined by the normalization condition:

$$\int_{T=0}^{T=\infty} f_T(T)\; dT = 1 \tag{2.2.41}$$

$\bar{T}_0$ and σ_{T_0} were calculated such that the mean (first moment) and the variance (second central moment) of the PDF equaled the filtered temperature $\bar{T}$ and the temperature variance σ_T, respectively:

$$\bar{T} = \int_{T=0}^{T=\infty} T f_T(T)\, dT \tag{2.2.42}$$

$$\sigma_T = \int_{T=0}^{T=\infty} \left(T - \bar{T}_0\right)^2 f_T(T)\, dT \tag{2.2.43}$$

The filtered species production terms were calculated by:

$$\overline{\prod_{\beta=1}^{N_{sp}+1} [\mathcal{M}_\alpha]^{\nu'_{\beta,r}}} = \int_Y \left(\prod_{\beta=1}^{N_{sp}+1} [\mathcal{M}_\alpha]\, (\tilde{T})^{\nu'_{\beta,r}} \right) f_Y(Y)\, dY \tag{2.2.44}$$

It was assumed that the species follow a multivariate β-PDF in the sub-grid scale:

$$f_Y(Y) = \frac{\mathit{\Gamma}\left(\sum_{\alpha=1}^{N_{sp}} \beta_\alpha\right)}{\prod_{\alpha=1}^{N_{sp}} \mathit{\Gamma}(\beta_\alpha)} \delta \left(1 - \sum_{\alpha=1}^{N_{sp}} Y_\alpha\right) \prod_{\alpha=1}^{N_{sp}} Y_\alpha^{\beta_\alpha - 1} \tag{2.2.45}$$

with

$$\mathit{\Gamma}(\beta) = \int_{t=0}^{t=\infty} t^{\beta-1} exp(-t) dt \tag{2.2.46}$$

and

$$\beta_\alpha = Y_\alpha \left(\frac{\sum_{\beta=1}^{N_{sp}} Y_\beta (1 - Y_\beta)}{\sigma_Y} - 1 \right) \tag{2.2.47}$$

The sum of the sub-grid scale species variances σ_Y resulted from:

$$\sigma_Y = \sum_{\alpha=1}^{N_{sp}} \int_{Y=0}^{Y=1} \left(Y_\alpha - \bar{Y}_\alpha\right)^2 f_Y(Y)\, dY \tag{2.2.48}$$

with $\bar{Y}_\alpha$ being the filtered value of the species mass fraction. Both the sub-grid scale temperature variance σ_T and the sum of the sub-grid scale species variances σ_Y were calculated by an additional transport equations of the form (Gerlinger *et al.*, 2001):

$$\frac{\partial}{\partial t}(\bar{\rho}_g \tilde{\phi}) + \frac{\partial}{\partial x_i}(\bar{\rho}_g \tilde{u}_i \tilde{\phi}) + \frac{\partial}{\partial x_i}\left(\bar{j}_\phi - \bar{\rho}_g \left(\widetilde{u_i \phi} - \tilde{u}_i \tilde{\phi}\right)\right) = \bar{S}_\phi \tag{2.2.49}$$

For the diffusive flux $\bar{j}_\phi$ and the closure of the unresolved fluxes $\bar{\rho}_g \left(\widetilde{u_i \phi} - \tilde{u}_i \tilde{\phi}\right)$ with $\phi = \sigma_T, \sigma_Y$, the gradient diffusion hypothesis was applied yielding:

$$\bar{j}_\phi - \bar{\rho}_g \left(\widetilde{u_i \phi} - \tilde{u}_i \tilde{\phi}\right) = \bar{\rho}_g \left(\mathit{\Gamma}_\phi + \mathit{\Gamma}_{t,\phi}\right) \frac{\partial \tilde{\phi}}{\partial x_i} \tag{2.2.50}$$

The diffusion coefficient $\mathit{\Gamma}_\phi$ and $\mathit{\Gamma}_{t,\phi}$ were set analogously to the enthalpy and species transport equations to:

$$\mathit{\Gamma}_{\sigma_T} = \frac{\nu_g}{Pr_g} \ ; \ \mathit{\Gamma}_{t,\sigma_T} = \frac{\nu_t}{Pr_t} \tag{2.2.51}$$

$$\varGamma_{\sigma_Y} = \frac{\nu_g}{Sc_g} \; ; \; \varGamma_{t,\sigma_Y} = \frac{\nu_t}{Sc_t} \tag{2.2.52}$$

The source terms on the right hand side follow from a balance of production (first term on the RHS) and dissipation (second term on the RHS):

$$S_{\sigma_T} = 2\rho_g \frac{\nu_t}{Pr_t} \left(\frac{\partial \tilde{T}}{\partial x_i} \right)^2 - C_{\sigma_T} \frac{\bar{\rho}_g \sigma_T}{\tau_{sgs}} \tag{2.2.53}$$

$$S_{\sigma_Y} = 2\rho_g \frac{\nu_t}{Sc_t} \sum_{\alpha=1}^{N_{sp}} \left(\frac{\partial \tilde{Y}_\alpha}{\partial x_i} \right)^2 - C_{\sigma_Y} \frac{\bar{\rho}_g \sigma_Y}{\tau_{sgs}} \tag{2.2.54}$$

Following Blacha (2012), the modeling constants were set to $C_{\sigma_T} = 1$ and $C_{\sigma_Y} = 2$. The turbulent time scale τ_t resulted from the sub-grid scale model for turbulence in section 2.2.1.2:

$$\tau_{sgs} = \frac{(C_{sgs} \varDelta)^2}{\nu_t} \tag{2.2.55}$$

For a detailed description on the derivation of the equations and the integration into the solver, the reader is referred to Gerlinger *et al.* (2001); Gerlinger (2005); Di Domenico (2008); Blacha (2012).

2.3. Liquid phase solver

The dispersed liquid phase is computed by the DLR in-house code SPRAYSIM, which is based on a Lagrangian particle tracking method using a point source approximation, i.e. droplets are assumed to be mathematical points providing point sources and point forces to the gas field. Lagrangian particle tracking requires solving the coupled ordinary differential equations (ODE) for $\vec{x}_p$, $\vec{u}_p$, d_p, $Y_{\alpha,l}$, and T_p along the trajectory of each computational parcel. These ordinary differential equations describe the change of the particle location, velocity, diameter, composition, and temperature with time (Noll, 1992).

Particle position The particle position is directly linked to the particle velocity and can be described by:

$$\frac{d\vec{x}_p}{dt} = \vec{u}_p \tag{2.3.1}$$

Particle velocity The change in particle velocity is calculated by Newton's second law summing accelerations acting on the particle (Mashayek and Ashgriz, 2011):

$$\frac{d\vec{u}_p}{dt} = \vec{a}_d + \left(1 - \frac{\rho_g}{\rho_l} \right) \vec{g} \tag{2.3.2}$$

with the acceleration vector due to drag $\vec{a}_d$ and due to gravity $\vec{g}$. In Eq. 2.3.2, Faxen force, Saffman force, virtual mass force, Basset force, Magnus effect, electromagnetic forces and forces due to non-uniform evaporation were neglected. Faxen forces due to a non-uniformity in the incoming flow velocity as well as Saffman forces, which are related to lift in high-shear regions, can be omitted if the particle diameter is small compared to the integral flow scales. The virtual mass force, which emerges as surrounding fluid has to be deflected, and the Basset force related to the history of the surrounding boundary layer are negligible in case of high particle to fluid density (Jenny *et al.*, 2012). Within the study at hand, both conditions are satisfied. For a spherical shape the acceleration vector due to drag can be calculated by:

$$\vec{a}_d = \frac{\vec{F}_d}{m_p} = \underbrace{\frac{3}{4}\frac{c_d}{d_p}\frac{\rho_g}{\rho_l}|\vec{u}_{rel}|}_{\tau_p^{-1}} \cdot \vec{u}_{rel} \tag{2.3.3}$$

including the drag force $\vec{F}_d$, the particle mass m_p,the drag coefficient c_d and the relative velocity $\vec{u}_{rel}$ defined as:

$$\vec{u}_{rel} = \vec{u}_g - \vec{u}_p \tag{2.3.4}$$

The reciprocal of the first term in Eq. 2.3.3 is referred to as particle response time or particle relaxation time:

$$\tau_p = \frac{4}{3}\frac{d_p}{c_d}\frac{\rho_l}{\rho_g}\frac{1}{|\vec{u}_{rel}|} \tag{2.3.5}$$

Particle diameter The change in diameter d_p can be derived from a mass balance:

$$\frac{dm_p}{dt} + \dot{m} = 0 \tag{2.3.6}$$

with the mass flow rate $\dot{m}$ from the droplet surface to the surroundings. The mass flow rate can be further subdivided in a mass flow rate $\dot{m}_{shed}$ (see section 2.3.1) related to the shedding of mass and a mass flow rate $\dot{m}_{vap}$ due to vaporization (see section 2.3.3):

$$\dot{m} = \dot{m}_{shed} + \dot{m}_{vap} \tag{2.3.7}$$

The mass of a spherical particle is given by:

$$m_p = \rho_l \frac{\pi d_p^3}{6} \tag{2.3.8}$$

Inserting Eq. 2.3.8 into Eq. 2.3.6 leads to:

$$\frac{d}{dt}\left(\rho_l \frac{\pi d_p^3}{6}\right) + \dot{m} = 0 \tag{2.3.9}$$

Applying the product rule, Eq. 2.3.9 is equivalent to:

$$\frac{\pi d_p^3}{6}\frac{d\rho_l}{dt} + \rho_l \frac{\pi d_p^2}{2}\frac{d(d_p)}{dt} + \dot{m} = 0 \tag{2.3.10}$$

Rearranging gives the ODE for the change in diameter d_p:

$$\frac{d(d_p)}{dt} = -\frac{d_p}{3}\frac{1}{\rho_l}\frac{d\rho_l}{dt} - \frac{2}{\rho_l}j_m \tag{2.3.11}$$

In Eq. 2.3.11 the mass flux j_m leaving the particle's surface was introduced, which is defined as:

$$j_m = \frac{\dot{m}}{A} \tag{2.3.12}$$

with the mass flow rate $\dot{m}$ and the droplet surface area $A = \pi d_p^2$. Assuming the parcel consists of a medium of low compressibility, the change in density can be approximated by:

$$\frac{d\rho_l}{dt} = \left(\frac{\partial \rho_l}{\partial T_p}\right)_p \frac{dT_p}{dt} + \left(\frac{\partial \rho_l}{\partial p}\right)_T \frac{dp}{dt} \approx \left(\frac{\partial \rho_l}{\partial T_p}\right)_p \frac{dT_p}{dt} \tag{2.3.13}$$

$()_p$ and $()_T$ denote derivatives keeping pressure constant and temperature constant, respectively.

Particle composition The change in droplet composition is calculated from the species mass balance:

$$\frac{d}{dt}\left(m_p Y_{\alpha,l}\right) + \dot{m}_\alpha = 0 \tag{2.3.14}$$

Applying the product rule yields:

$$m_p \frac{dY_{\alpha,l}}{dt} + Y_{\alpha,l}\frac{dm_p}{dt} + \dot{m}_\alpha = 0 \tag{2.3.15}$$

The species mass flux $\dot{m}_\alpha$ can be sub-divided into a species mass flux related to shedding and a species mass flux $\dot{m}_{\alpha,vap}$ due to vaporization:

$$\dot{m}_\alpha = \dot{m}_{shed} Y_{\alpha,l} + \dot{m}_{\alpha,vap} \tag{2.3.16}$$

Inserting Eq. 2.3.6 and Eq. 2.3.16 in Eq. 2.3.15, results in:

$$m_p \frac{dY_{\alpha,l}}{dt} + \left(\dot{m}_{shed} - \dot{m}\right) Y_{\alpha,l} + \dot{m}_{\alpha,vap} = 0 \tag{2.3.17}$$

Rearranging yields:

$$\frac{dY_{\alpha,l}}{dt} = \frac{1}{m_p}\left(\dot{m}_{vap} Y_{\alpha,l} - \dot{m}_{\alpha,vap}\right) \tag{2.3.18}$$

Finally, inserting Eq. 2.3.8 into Eq. 2.3.18 results in the ODE for the change in liquid composition:

$$\frac{dY_{\alpha,l}}{dt} = \frac{6}{\rho_l \pi d_p^3}\,\dot{m}_{vap}\left(Y_{\alpha,l} - \zeta_\alpha\right) \tag{2.3.19}$$

with the ratio between the species and total vapor mass flux defined as:

$$\zeta_\alpha = \frac{\dot{m}_{\alpha,vap}}{\dot{m}_{vap}} \tag{2.3.20}$$

Particle temperature The change in particle temperature T_p can be deduced from an energy balance:

$$\frac{d}{dt}\left(m_p h_l\right) + \dot{H} + \dot{Q} + V_p \frac{dp}{dt} = 0 \tag{2.3.21}$$

wherein $\dot{Q}$ represents the heat flow rate. The enthalpy flow $\dot{H}$ leaving the particle is due to shedding and vaporization:

$$\dot{H} = \dot{m}_{shed} h_l + \dot{m}_{vap} h_{vap} \tag{2.3.22}$$

with h_l and h_{vap} being the specific enthalpy of the liquid and the vapor, respectively. Applying the product rule as well as introducing Eq. 2.3.6 and Eq. 2.3.7, the first term in Eq. 2.3.21 is equivalent to:

$$\frac{d}{dt}\left(m_p h_l\right) = m_p \frac{dh_l}{dt} + h_l \frac{dm_p}{dt} = m_p \frac{dh_l}{dt} - \left(\dot{m}_{shed} + \dot{m}_{vap}\right) h_l \tag{2.3.23}$$

Inserting Eq. 2.3.22 and Eq. 2.3.23 into Eq. 2.3.21 yields:

$$m_p \frac{dh_l}{dt} + \dot{m}_{vap}\left(h_{vap} - h_l\right) + \dot{Q} + V_p \frac{dp}{dt} = 0 \tag{2.3.24}$$

The specific enthalpy of vaporization Δh_{vap} of the mixture is given by:

$$\Delta h_{vap} = h_{vap} - h_l \tag{2.3.25}$$

Inserting Eq. 2.3.25 into Eq. 2.3.24 results in:

$$m_p \frac{dh_l}{dt} + \dot{m}_{vap} \Delta h_{vap} + \dot{Q} + V_p \frac{dp}{dt} = 0 \tag{2.3.26}$$

Writing the total differential of the specific enthalpy of the liquid and neglecting the pressure dependence yields:

$$dh_l = \left(\frac{\partial h_l}{\partial T}\right)_p dT + \left(\frac{\partial h_l}{\partial p}\right)_T dp \approx c_{p_l} dT \tag{2.3.27}$$

with the specific isobaric heat capacity of the liquid mixture c_{p_l} calculated from the isobaric heat capacity of the pure species $c_{p_l,\alpha}$:

$$c_{p_l} = \sum_{\alpha=1}^{N_{sp}} Y_{\alpha,l}\; c_{p_l,\alpha} \tag{2.3.28}$$

Neglecting the last term in Eq. 2.3.26, which is small compared to the others, as well as inserting Eq. 2.3.27 into Eq. 2.3.26 leads to:

$$m_p c_{p_l} \frac{dT_p}{dt} + \dot{m}_{vap} \Delta h_{vap} + \dot{Q} = 0 \tag{2.3.29}$$

Replacing the particle mass by Eq. 2.3.8 and rearranging yields the ODE for the change in temperature for a spherical particle:

$$\frac{dT_p}{dt} = -\frac{6}{d_p}\frac{j_{m,vap}\varDelta h_{vap} + \dot{q}}{\rho_l c_{p_l}} \tag{2.3.30}$$

wherein $\dot{q}$ is the surface heat flux defined as:

$$\dot{q} = \frac{\dot{Q}}{A} \tag{2.3.31}$$

The specific enthalpy of vaporization $\varDelta h_{vap}$ of the mixture is calculated from the specific enthalpy of vaporization $\varDelta h_{vap,\alpha}$ of the pure species by:

$$\varDelta h_{vap} = \sum_{\alpha=1}^{N_{sp}} \zeta_\alpha \varDelta h_{vap,\alpha} \tag{2.3.32}$$

2.3.1. Atomization models

Atomization is referred to as the process of a liquid continuum disintegrating into small droplets, so called sprays (Lefebvre, 1989). It occurs if internal or external forces exceed cohesion forces among liquid molecules. These cohesion forces are evident in phenomena like viscosity and surface tension. Viscosity reflects a fluid's internal resistance to distortion and can be interpreted as internal friction opposing velocity gradients and the growth of instabilities. Surface tension acts on interfaces between different fluids, e.g. at the surface between gas and liquid. In contrast to molecules in the bulk of the liquid having neighboring liquid molecules in each direction, molecules at the interface encounter a net force in direction of the liquid's inside. The liquid tends to form a sphere in order to minimize surface energy. In equilibrium, normal stress at a free surface is balanced by the surface tension which is related to the local curvature. If aerodynamic forces act on the gas-liquid interface, the liquid's surface is distorted until surface tension is overcome and the liquid disintegrates. In thermal turbomachinery, the disintegration is mainly enhanced by high relative velocity between the liquid and the surrounding gas. High relative velocities can be achieved either by injecting the liquid at high velocity into slow-moving gas or by exposing slow-moving liquid to high velocity air streams. The disintegration process can be subdivided into an initial phase, the so called primary atomization comprising the breakup of bulk liquid into large drops, and a subsequent stage of so called secondary breakup involving the collapse of the large drops into smaller droplets. The disintegration finishes when a critical drop size is reached with disruptive and cohesive forces being in balance. This is due to the fact that a smaller diameter leads to a higher local curvature and hence increased surface tension forces.

High resolution interface tracking techniques, e.g. volume-of-fluid (Tomar *et al.*, 2010), level-set (Herrmann, 2011) or front-tracking methods (Tryggvason *et al.*, 2001), coupled with DNS or

LES are promising approaches to simulate primary atomization. However, due to their immense computational costs, they are not yet applicable to industrial computations. Unfortunately, the accuracy of spray simulations depends strongly on initial and boundary conditions imposed on both the gaseous and the liquid phase. To make matters worse, the droplet size distribution and droplet velocities close to the atomizer cannot be measured in many applications. Therefore, less intensive numerical models for the atomization process are necessary to provide initial and boundary conditions for the spray computation. In this context, section 2.3.1.1 and 2.3.1.2 focus on initial and boundary conditions for Lagrangian particle tracking of the dispersed phase in Euler-Lagrange simulations by means of empirical and semi-empirical primary atomization modeling. The examined atomization concepts of a liquid jet in cross-flow and a liquid sheet subjected to a high velocity air stream are configurations typical of industrial gas turbine applications. Subsequently, section 2.3.1.3 covers the modeling of secondary breakup.

2.3.1.1. Liquid jet in cross-flow

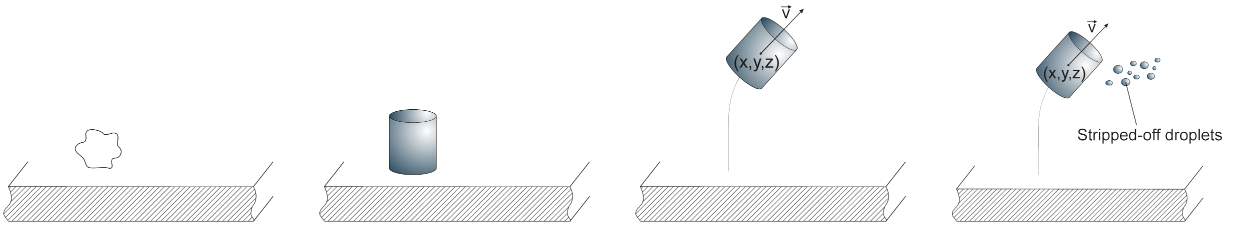

(a) Inject a universal computational parcel

(b) Assign attributes to the parcel

(c) Tracing of parcel in Lagrangian framework

(d) Parcel's attributes can interact with the surroundings and change (e.g. mass loss due to shear stresses)

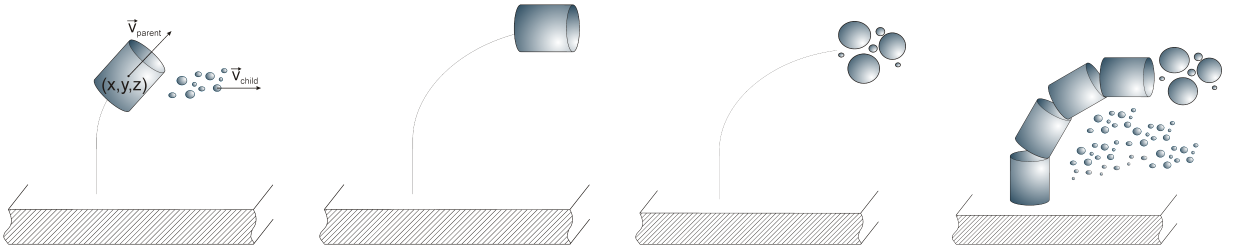

(e) Tracing of new child parcels created with attributes according to specified heredity rules

(f) Reaching a characteristic time scale → Break-up into fragments → Finish tracing of old parcel

(g) Start tracing of new fragment parcels

(h) Continuous sequence of computational parcels → Representation of liquid continuum

Figure 2.4.: Modeling strategy for liquid jet breakup in high velocity cross-flow (from Eckel *et al.* (2016))

Fragmentation of liquid jets in an unsteady cross-flow is modeled by the shear stripping breakup model of Eckel *et al.* (2016). Fig. 2.4 displays the modeling strategy. After injecting a universal computational parcel, attributes like shape, mass and drag of the represented real particles are assigned. Then, the parcel is tracked in a Lagrangian framework and is able to interact with its surroundings. The model calculates the deflection and distortion of the jet from its initially circular cross-section into an elliptic one caused by the high cross-flow momentum. Along with the deformation, a liquid boundary layer flow adjacent to the gas-liquid interface is driven by the high velocity gas. As a consequence, droplets are continuously stripped off from the surface whereby the tracing of new child parcels is initiated. The child parcels are created with attributes according to specified heredity rules. For instance, the initial position of the newly created child parcel is determined in relation to the position of the parent jet parcel. When the jet reaches a characteristic timescale, the column of remaining liquid finally breaks up into several large fragments due to a growing Kelvin-Helmholtz instability (Arienti and Soteriou, 2009). These large fragments are then individually tracked while they also undergo a stripping process releasing a large amount of small droplets. Both the surface stripping from the jet and from the jet fragments involve the creation of new parcels for the particle tracking. As there is de facto a persistent emission of a large number of particles from the surface, the quantity of created computational parcels has to be restricted in the simulation to keep the computational costs at a reasonable level. Thus, the stripped-off mass is accumulated until a fixed fraction of the parcel's initial mass is reached. The accumulated mass is then released by creating a fixed number of parcels following a root normal distribution for the diameter. This approximation introduces two numerical discretization errors: a spatial discretization error caused by the distinct events of releasing sheared-off droplets and a discretization error related to a limited representation of the presumed size distribution by taking only a few random samples of this distribution. Both discretization errors decrease with smaller integration time step and a higher number of newly created computational parcels per event. Before a parcel undergoes its column breakup a final stripping event is performed to shed the mass not yet released.

Differential equations for non-spherical particles Within the solution algorithm, different parcel types are distinguished. Parcels which undergo primary breakup are called primary parcels. They can have a cylindrical or a spherical shape. All parcels which are an outcome of the atomization process are treated as spherical particles. For a spherical shape the ordinary differential equations of section 2.3 are solved. For a cylindrical shape the acceleration due to drag (Eq. 2.3.3) is modified to the following expression:

$$\vec{a}_d = \frac{2}{\pi\, d_p} \frac{\rho_g}{\rho_l} \left(c_{d,\parallel}\, |\vec{u}_{rel,\parallel}| \cdot \vec{u}_{rel,\parallel} + c_{d,\perp} |\vec{u}_{rel,\perp}| \cdot \vec{u}_{rel,\perp} \right) \tag{2.3.33}$$

with the drag coefficient parallel to the cylinder surface $c_{d,\parallel}$ and in the cross-flow direction (perpendicular to the surface) $c_{d,\perp}$. The relative velocity parallel to the parcel $\vec{u}_{rel,\parallel}$ and perpendicular to the parcel $\vec{u}_{rel,\perp}$ can be written as:

$$\vec{u}_{rel,\parallel} = \frac{\vec{u}_p \cdot \vec{u}_{rel}}{|\vec{u}_p|^2} \cdot \vec{u}_p \tag{2.3.34}$$

$$\vec{u}_{rel,\perp} = \vec{u}_{rel} - \vec{u}_{rel,\parallel} \tag{2.3.35}$$

It is assumed that the entire liquid column moves with its local bulk velocity. Therefore, no velocity distribution inside the liquid jet is calculated. The change in diameter for a liquid jet parcel can be derived from a mass balance and be written as follows:

$$\frac{d(d_p)}{dt} = -\frac{d_p}{2}\frac{1}{\rho_l}\frac{d\rho_l}{dt} - \frac{d_p}{2}\frac{1}{|\vec{u}_p|}\frac{d|\vec{u}_p|}{dt} - \frac{2}{\rho_l}\dot{j}_m \tag{2.3.36}$$

Compared to Eq. 2.3.11 the coefficients are different because of the cylindrical shape and an additional term arises, which is responsible for the thinning or thickening of the liquid jet in case of an acceleration and deceleration, respectively. The change in particle temperature for a cylindrical shape can be calculated by:

$$\frac{dT_p}{dt} = -\frac{4}{d_p}\frac{\dot{j}_{m,vap}\Delta h_{vap}(T_p) + \dot{q}}{\rho_l c_{p_p}} \tag{2.3.37}$$

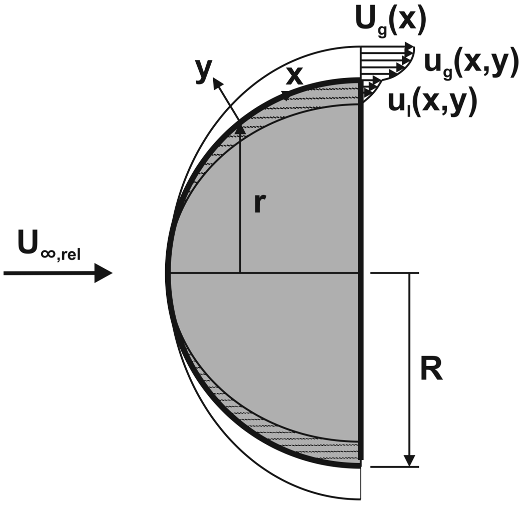

Figure 2.5.: Sketch of the boundary layer development on both sides of the gas-liquid interface (from Eckel *et al.* (2016) following Ranger and Nicholls (1969))

Shear stripping breakup model The shear stripping breakup model was originally developed for spherical droplets by Ranger and Nicholls (1969) and later refined by Delplanque and Sirignano (1994) to include evaporation. Rachner *et al.* (2002) and Eckel *et al.* (2011, 2016) extended the model to shear breakup of ellipsoids and flattened liquid jets in steady and unsteady cross-flow, respectively. The shear stripping breakup model is applied to all primary parcels, i.e cylindrical jet parcels and spherical jet fragment parcels after column breakup. It relies on the assumption that a boundary layer flow inside the liquid is driven by the high velocity air. Fig. 2.5 shows schematically a section through the liquid exposed to the free stream velocity (here the magnitude not the vector):

$$U_{\infty,rel} = |\vec{u}_g - \vec{u}_p| \tag{2.3.38}$$

The grey shaded area represents the liquid. In the vicinity of the gas-liquid interface, a gaseous and a liquid boundary layer evolve. The mass contained in the liquid boundary layer detaches from the liquid body at the radial extremities. The mass flux $j_{m,shed}$ $[kg/(m^2 s)]$ for a spherical parcel can be expressed by:

$$j_{m,shed} = \frac{2}{\pi d_p} \int_0^\infty \rho_l u_l \, dy \tag{2.3.39}$$

For a cylindrical parcel the mass flux can be evaluated by:

$$j_{m,shed} = \frac{1}{d_p} \int_0^\infty \rho_l u_l \, dy \tag{2.3.40}$$

The velocity profiles in both boundary layers can be approximated by profiles proposed by G.I. Taylor (Delplanque and Sirignano, 1994):

$$\begin{aligned} \frac{u_g(x,y)}{U_g(x)} &= 1 - (1 - A_T) e^{-\frac{y}{\alpha_g \sqrt{x}}} \\ \frac{u_l(x,y)}{U_g(x)} &= A_T \, e^{-\frac{y_l}{\alpha_l \sqrt{x}}} \end{aligned} \tag{2.3.41}$$

The gas velocity outside the boundary layer $U_g(x)$ depends on the shape of the liquid body and will be addressed later in this section. Equations for the parameters A_T, α_g and α_l can be derived by means of the boundary layer equations. A detailed analysis can be found in Delplanque (1992). The boundary layer equations for both phases are (Schlichting, 1965):

$$\frac{\partial (\rho u r)}{\partial x} + \frac{\partial (\rho v r)}{\partial y} = 0 \tag{2.3.42}$$

$$\rho u \frac{\partial u}{\partial x} + \rho v \frac{\partial u}{\partial y} = -\frac{\partial p}{\partial x} + \frac{\partial}{\partial y} \left(\mu \frac{\partial u}{\partial y} \right) \tag{2.3.43}$$

With the local interface velocity $A_T \, U_g(x)$ and the local radial gas velocity $v_{w,g}(x)$, the boundary conditions for the gas in the local coordinate system (x,y) depicted in Fig. 2.5 yield:

$$\begin{aligned} u_g(y=0) &= A_T \, U_g(x) \\ v_g(y=0) &= v_{w,g}(x) \\ u_g(y=\infty) &= U_g(x) \\ v_g(y=\infty) &= 0 \end{aligned} \tag{2.3.44}$$

Assuming a quiescent liquid core, the boundary conditions for the liquid are:

$$\begin{aligned} u_l(y=0) &= A_T \, U_g(x) \\ v_l(y=0) &= v_{w,l}(x) \\ u_l(y=\infty) &= 0 \\ v_l(y=\infty) &= 0 \end{aligned} \tag{2.3.45}$$

with the radial liquid velocity at the surface:

$$v_{w,l}(x) = -\frac{\rho_g}{\rho_l} v_{w,g}(x) \tag{2.3.46}$$

Furthermore, the condition of continuous shear stress at the interface between the two fluids has to be fulfilled:

$$-\mu_{l,s} \left(\frac{\partial u_l}{\partial y} \right)_s = \mu_{g,s} \left(\frac{\partial u_g}{\partial y} \right)_s \tag{2.3.47}$$

$(\partial/\partial y)_s$ in Eq. 2.3.47 indicates the gradient at the surface. Combining the velocity profiles (Eq. 2.3.41), the boundary layer equations (Eq. 2.3.42, Eq.2.3.43), the condition of continuous shear stress (Eq. 2.3.47) and the assumption $A_T << 1$ the parameters α_g, A_T and α_l can be deduced:

$$\alpha_g = \frac{\alpha_g^0}{\mathcal{G}(\epsilon)} \tag{2.3.48}$$

$${A_T}^3 = \eta_s \hat{\beta} \mathcal{G}(\epsilon) \left(\mathcal{G}(\epsilon) - 2\epsilon A_T \right) \tag{2.3.49}$$

$$\alpha_l = \alpha_g \frac{A_T}{\eta_s} \tag{2.3.50}$$

where α_g^0 is the value of α_g without any vaporization:

$$\alpha_g^0 = \sqrt{\frac{\nu_{g,s} \rho_{g,s}}{\hat{\rho}_g U_g}} \tag{2.3.51}$$

$\mathcal{G}(\epsilon)$ and ϵ are substitutions defined as:

$$\mathcal{G}(\epsilon) = \frac{1}{\epsilon + \sqrt{1+\epsilon^2}} \tag{2.3.52}$$

$$\epsilon = \frac{4}{\sqrt{2\pi}\ \mathcal{F}_s(\sqrt{2})} \frac{\sqrt{R}}{\alpha_g^0} \frac{\rho_{g,s}}{\hat{\rho}_g} \frac{\bar{v}_{w,g}}{U_g} \tag{2.3.53}$$

with $\mathcal{F}_s(x)$ being the Fresnel sine integral:

$$\mathcal{F}_s(x) = \int_0^x sin \left(\frac{\pi}{2} t^2 \right) dt \tag{2.3.54}$$

The average blowing velocity at the liquid surface $\bar{v}_{w,g}$ associated to the Stefan flow around the particle can be evaluated from the vapor mass flux at the surface:

$$\bar{v}_{w,g} = \frac{\dot{m}_{vap}}{\rho_{g,s}} \tag{2.3.55}$$

The local blowing velocity $v_{w,g}$ is related to the average blowing velocity $\bar{v}_{w,g}$ via:

$$v_{w,g}(x) = \frac{2}{\sqrt{2\pi}\ \mathcal{F}_s(\sqrt{2})} \sqrt{\frac{R}{x}} \bar{v}_{w,g} \tag{2.3.56}$$

The average density ratio in the boundary layer $\hat{\beta}$ and the viscosity ratio at the surface η_s used in Eq. 2.3.49 are defined as:

$$\hat{\beta} = \frac{\hat{\rho}_g}{\hat{\rho}_l} \tag{2.3.57}$$

$$\eta_s = \frac{\mu_{g,s}}{\mu_{l,s}} = \frac{\nu_{g,s}\rho_{g,s}}{\nu_{l,s}\rho_{g,s}} \tag{2.3.58}$$

Onset and end of breakup The experiments of Becker and Hassa (2002) indicate no time delay between the moment of injection and the first shedding of droplets. This yields:

$$\left(\frac{t_{ini}}{t^*}\right)_{jet} = 0 \tag{2.3.59}$$

wherein t^* represents the characteristic timescale introduced by Ranger and Nicholls (1969):

$$t^* = \frac{L}{|\vec{u}_{rel}|}\sqrt{\frac{\rho_l}{\rho_g}} \tag{2.3.60}$$

with the characteristic length scale L and the relative velocity $\vec{u}_{rel}$ between gas and liquid (Eq. 2.3.4). For a jet parcel, the characteristic length scale L in Eq. 2.3.60 is replaced by the initial jet diameter. The breakup time, at which the remaining liquid column disintegrates into fragments, is calibrated to match the experiments of Becker and Hassa (2002) at baseline conditions:

$$\left(\frac{t_b}{\overline{t^*}}\right)_{jet} = 5.35 \tag{2.3.61}$$

$\overline{t^*}$ is an average value of t^* over the current lifetime $\mathcal{T}_p$ of the parcel. Accounting for the history of the parcel, this is an extension of the breakup timescale of Ranger and Nicholls (1969) for drops in gaseous environments with varying density and free stream velocity. The definition of $\overline{t^*}$ is as follows:

$$\overline{t^*} = \frac{1}{\mathcal{T}_p}\int_0^{\mathcal{T}_p} t^* dt \tag{2.3.62}$$

The onset of mass shedding from the jet fragments is assumed to happen immediately after column breakup:

$$\left(\frac{t_{ini}}{t^*}\right)_{frag} = 0 \tag{2.3.63}$$

wherein the characteristic length scale L in Eq. 2.3.60 is replaced by the initial fragment drop diameter. The time span between the initiation of droplet stripping and the final breakup of the jet fragments is taken from Chou *et al.* (1997):

$$\left(\frac{t_b}{\overline{t^*}}\right)_{frag} = 5.5 - 1.6 = 3.9 \tag{2.3.64}$$

Deformation of the liquid body A jet parcel is initially started with an undistorted circular cross-section. The diameter of the parcel corresponds to the diameter of the injection orifice.

Along the trajectory, the cross-section is deformed by the aerodynamic forces. The deformation $\mathcal{D}_p$ is defined as:

$$\mathcal{D}_p = \frac{d_{p,cross}}{d_p} \tag{2.3.65}$$

with the cross-stream diameter $d_{p,cross}$ and the diameter of a sphere or a circular cylinder d_p, which results in the same volume. This definition is related to the fact that the Lagrangian tracking algorithm considers particles to have an ideal, round shape. In analogy to the breakup of drops investigated by Hsiang and Faeth (1992), a jet parcel is assumed to deform linearly with t/t^* until a maximum value of $\mathcal{D}_{p,max}$ is reached at $(t/t^*)_{max}$. After the distortion reaches the maximum, it remains constant. From literature the following values for $(t/t^*)_{max}$ and $\mathcal{D}_{p,max}$ are taken and kept constant:

$$\left(\frac{t}{t^*}\right)_{max} = 1.25 \tag{2.3.66}$$

$$\mathcal{D}_{p,max} = 2.5 \tag{2.3.67}$$

The drag coefficient perpendicular to the axis $c_{d,\perp}$ of the jet parcel increases linearly with deformation. The minimum of $c_{d,\perp}$ is defined by the drag coefficient of an infinite cylinder. The maximum is calibrated to meet the jet penetration observed in the baseline case of Brandt *et al.* (1998).

The initial distortion of a child jet fragment parcel, released after column breakup of a jet parcel, is assumed to be inherited from the final deformation of the parent jet parcel. This means that the semi-axis ratio of the child drop, considered as an oblate ellipsoid, at its birth ($t/t^* = 0$) is set equal to the semi-axis ratio of the elliptic cross section of the parent jet parcel at the end of its lifetime. This yields:

$$\mathcal{D}_{ini,child} = \mathcal{D}_{end,parent}^{2/3} \tag{2.3.68}$$

Hsiang and Faeth (1992) observed that the drop distortion $\mathcal{D}_p$ correlates linearly with the characteristic time t/t^*. Furthermore, the drag coefficient shows a linear dependence on the drop distortion with a maximum roughly at:

$$\left(\frac{t}{t^*}\right)_{max} = 1.6 \tag{2.3.69}$$

After the distortion reaches the maximum $\mathcal{D}_{p,max}$, it remains constant. Hsiang and Faeth (1992) give the following correlation for the maximum distortion:

$$\mathcal{D}_{p,max} = 1 + 0.19\sqrt{min(We_{d_p}, 100)} \tag{2.3.70}$$

The Weber number We_L in Eq. 2.3.70 is a dimensionless number describing the ratio of inertia and surface tension forces:

$$We_L = \frac{\rho_g |\vec{u}_g|^2 L}{\sigma} \tag{2.3.71}$$

In Eq. 2.3.70 the characteristic length scale L is replaced by the diameter d_p of the drop. Finally, the drop deformation for $t/\overline{t^*} < (t/\overline{t^*})_{max}$ can be described by:

$$\mathcal{D}_p \left(\frac{t}{\overline{t^*}} \right) = \mathcal{D}_{p,ini} + \frac{t/\overline{t^*}}{(t/\overline{t^*})_{max}} \left(\mathcal{D}_{p,max} - 1 \right) \tag{2.3.72}$$

wherein $\overline{t^*}$ is the average of t^* calculated according to Eq. 2.3.62. For $t/\overline{t^*} \geq (t/\overline{t^*})_{max}$, it yields:

$$\mathcal{D}_p \left(t/\overline{t^*} \geq (t/\overline{t^*})_{max} \right) = \mathcal{D}_{p,max} \tag{2.3.73}$$

Via the deformation, the drag coefficient of the jet fragment parcel, assumed to be an oblate spheroid, can be determined. Following Hsiang and Faeth (1992) Fig.5, the drag coefficient can be approximated by blending between a round solid sphere and a circular solid disk. The drag coefficient of a disk is reached at a distortion of $\mathcal{D}_p = 1.77$. The values used for the drag coefficient can be found in Clift *et al.* (1978).

The influence of the deformation on the gas velocity outside the boundary layer $U_g(x)$, which is needed in the shear stripping breakup model of subsection 2.3.1.1, is described in the following. Ranger and Nicholls (1969) as well as Delplanque and Sirignano (1994) determined $U_g(x)$ from the inviscid potential flow solution around a sphere. The potential flow around a sphere yields:

$$U_g(\phi) = \frac{3}{2}\, U_{\infty,rel}\ sin\left(\phi\right) \tag{2.3.74}$$

At the radial extremities of the sphere the gas velocity outside the boundary layer gives:

$$U_g \left(\frac{\pi}{2} \right) = \frac{3}{2} U_{\infty,rel} \tag{2.3.75}$$

As a jet fragment drop is deformed into a spheroid and the jet flattens to an elliptic cylinder, it seems reasonable to take the potential flow solution for an oblate spheroid and an elliptic cylinder. At the radial extremities of an oblate spheroid, this yields (Fishburn, 1974):

$$U_g \left(\frac{\pi}{2} \right) = - \frac{1 - \mathcal{E}^2}{\mathcal{E}^2} \left(1 - \frac{arcsin\left(\sqrt{1 - \mathcal{E}^2}\right)}{\mathcal{E}\sqrt{1 - \mathcal{E}^2}} \right) U_{\infty,rel} \tag{2.3.76}$$

with the axial ratio:

$$\mathcal{E} = \frac{a}{b} \tag{2.3.77}$$

wherein a is the short and b the long semi-axis of the spheroid. Typically, the cross-stream deformation is used in the literature to determine the drag coefficient. The ratio of a and b can be related to the deformation $\mathcal{D}_p$ by mass conservation:

$$\rho_l \frac{4}{3}\pi a b^2 = \rho_l \frac{\pi}{6} {d_p}^3 \tag{2.3.78}$$

The long semi-axis b can be written as:

$$b = \frac{d_{p,cross}}{2} \tag{2.3.79}$$

Rewriting Eq. 2.3.78 leads to the relation between the semi-axes of the spheroid and its deformation:

$$\frac{b}{a} = {\mathcal{D}_p}^3 \tag{2.3.80}$$

According to the potential flow theory, the velocity around an elliptic cylinder in cross-flow is given by (Schlichting, 1965):

$$U_g(\phi) = \frac{1 + \frac{b}{a}}{\sqrt{1 + \left(\frac{b}{a}\right)^2 cot^2(\phi)}} \tag{2.3.81}$$

with a and b being the short and the long semi-axis of an elliptic cylinder, respectively. At the radial extremities $\phi = \pi/2$ it follows:

$$U_g\left(\frac{\pi}{2}\right) = \left(1 + \frac{b}{a}\right) U_{\infty,rel} \tag{2.3.82}$$

Analogously to the spheroid, the ratio of a and b can be related to the deformation $\mathcal{D}_p$ of the elliptic cylinder by mass conservation:

$$\rho_l \pi a b l = \rho_l \frac{\pi}{4} {d_p}^2 l \tag{2.3.83}$$

By using Eq. 2.3.79, Eq. 2.3.83 can be rewritten leading to an equivalent formulation to Eq. 2.3.80 for an elliptic cylinder:

$$\frac{b}{a} = {\mathcal{D}_p}^2 \tag{2.3.84}$$

However, for high Reynolds numbers or high b/a-ratio, the potential flow solutions delivers unrealistically high velocity values at the radial extremities. This is due to the fact that the separation region behind the liquid body is not accounted for. In order to overcome the issue of unrealistically high velocities, $U_g(\pi/2)$ is obtained by linear interpolation between numerical results of CFD simulations. Simulations of the flow past a sphere and a spheroid ($d_{p,cross}/d_{p,0} = 2.5$) at a freestream Reynolds number of $Re_{d_{p,0}} = 3000$ were carried out to evaluate the flow around spherical parcels. The numerical results of a flow at a freestream Reynolds number of $Re_{d_{p,0}} = 10000$ around an infinite circular cylinder and an elliptic cylinder with $d_{p,cross}/d_{p,0} = 2.5$ served as basis for the approximation of a distorted jet. The Reynolds numbers were chosen to be of the order of typical values in the shear breakup regime. As the stripping model exhibited only a moderate dependence on the value of $U_g(\pi/2)$, this approach can be seen as a reasonable approximation for high Reynolds numbers.

Initial conditions of the stripped-off droplets The Sauter mean diameter of the stripped-off droplets is obtained by multiplying the displacement thickness of the boundary layer, calculated by the shear stripping breakup model, by an empirical calibration factor. Following Rachner *et al.* (2002), the calibration factors are set to 1.0 and 1.68 for a jet parcel and a jet fragment parcel being the parent parcel, respectively. The size of the starting droplets is randomly picked from a root-normal distribution with constant width parameter MMD/SMD=1.04. Chou *et al.* (1997), who investigated drops in the shear breakup regime, experimentally determined the mean and rms velocity of the stripped-off droplets. Their correlations result in:

$$\vec{u}_{child,mean} = \vec{u}_{parent} + 0.37\,(\vec{u}_g - \vec{u}_{parent}) \tag{2.3.85}$$

$$\vec{u}_{child,rms} = 0.34\,(\vec{u}_g - \vec{u}_{parent}) \tag{2.3.86}$$

Assuming the velocity of the starting child parcels follows a Gaussian distribution curve, it can be calculated by:

$$\vec{u}_{child} = \vec{u}_{child,mean} + \xi_{Gauss}\vec{u}_{child,rms} \tag{2.3.87}$$

wherein ξ_{Gauss} is a normally distributed random number. In reality, a large number of droplets are continuously stripped off from the jet surface. However, in the simulation the number of newly created computational parcels has to be limited in order to keep the computational cost at a reasonable level. This is done by discretizing the continuous release in so-called stripping events. A stripping event occurs if the mass accumulated since the previous stripping event reaches a certain fraction of the parcel's initial mass. The accumulated mass is then released by creating new child parcels.

Limits of applicability The primary atomization model for liquid jets in cross-flow is limited to the shear breakup (sheet stripping) regime, i.e. $\mathcal{O}(100) < We_{d_{jet}} < \mathcal{O}(1000)$. $We_{d_{jet}}$ corresponds to the Weber number (Eq. 2.3.71) based on the jet diameter as characteristic length scale L. At higher Weber numbers, the breakup mechanism changes to a sudden catastrophic breakup of the liquid body, whereas at lower Weber numbers bag breakup and Rayleigh breakup can be observed. Furthermore, the model is not suited for simulation of coaxial injectors, high pressure injection of liquid jets and impingement on a wall.

2.3.1.2. Pre-filming airblast atomization

The second atomization principle examined in the work at hand deals with the concept of airblast atomization involving a pre-filming surface. Although airblast atomization has been extensively studied in the last decades, there are still open questions concerning the disintegration of liquid sheets. Recent investigations focusing on film breakup without a pre-filming surface can be found in Fernandez *et al.* (2011a,b); Park *et al.* (2004); Lozano *et al.* (2011); Sirignano and Mehring (2000) and Senecal *et al.* (1999). Concerning the fragmentation of liquid sheets involving pre-filmers with planar and more realistic, conical configurations the reader is

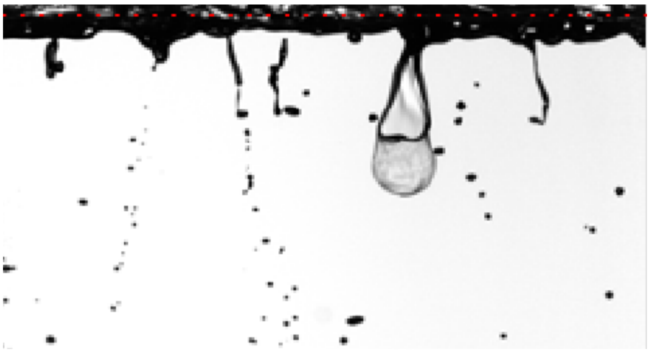

Figure 2.6.: Film break-up of Shellsol D70 at 50 m/s (from Gepperth *et al.* (2012))

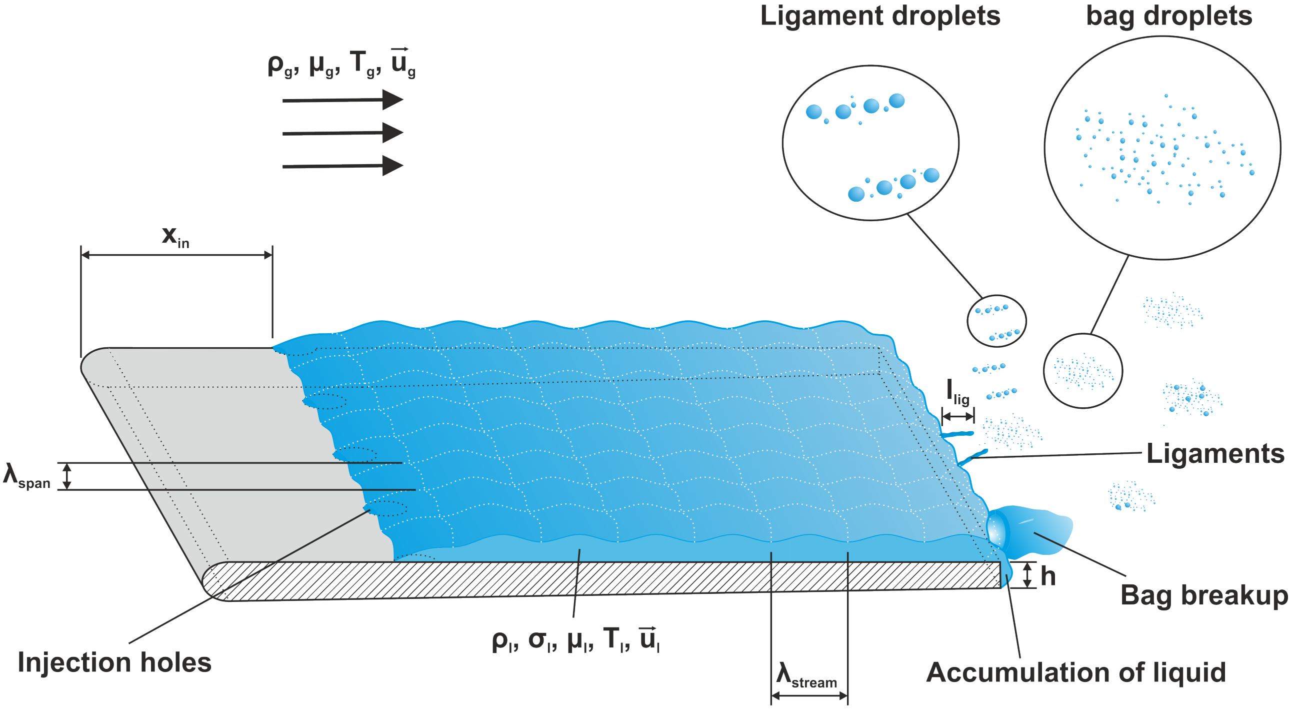

Figure 2.7.: Sketch of the atomization process of a liquid flat sheet subjected to a high velocity gaseous co-flow (from Eckel *et al.* (2013))

referred to publications of Chaussonnet *et al.* (2016); Gepperth *et al.* (2012); Batarseh *et al.* (2010); Bhayaraju and Hassa (2009); Yule and Vamvakoglou (1999); Villermaux (1998) and Holz *et al.* (2016); Bärow *et al.* (2015); Gepperth *et al.* (2014); Aigner (1986); Sattelmayer (1985), respectively. Despite this variety of publications, mechanisms inducing the disintegration of liquid sheets are still not fully understood. Lately, studies of Gepperth *et al.* (2010, 2012, 2014) and Bärow *et al.* (2015) indicate a breakup scenario of the liquid sheet resembling secondary atomization of droplets in the bag breakup regime (Fig. 2.6). A sketch of the breakup scenario of the liquid sheet is depicted in Fig. 2.7. The liquid is usually introduced via a set of small orifices. A liquid film forms on top of the pre-filmer surface. The gas-liquid interface is disturbed by the high velocity gaseous co-flow and shows small undulations. These waves reach the atomizer edge and fill a liquid reservoir behind the trailing edge of the pre-filmer. Originating from this liquid accumulation, balloon like bags are formed which stay attached to the trailing edge. The thin liquid membrane at the far end hemisphere of the bag bursts and forms a number of small droplets. The elongated, cylindrical part attached to the basal torus retracts to the basal volume. Subsequently, the basal torus splits up to form ligaments which disintegrate afterwards into several larger fragments. The outcome of such a bag breakup is typically a bimodal drop size distribution (Opfer *et al.*, 2012).

The modeling presented here is based on the empirical work of Raynal *et al.* (1997); Villermaux (1998); Gepperth *et al.* (2010) and Eckel *et al.* (2013). Due to the high complexity of the sheet disintegration, the atomization model was divided into a sequence of sub-models representing the single sub-processes of the entire fragmentation. This modular approach has the advantage that the sub-processes can be individually evaluated, improved and extended or adapted to upcoming experimental findings. The sub-models comprise the injection of liquid, film flow, evaluation of the interface instability, accumulation of liquid at the pre-filmer trailing edge, and film breakup.

Film flow and interface instability In order to estimate the interface instability and the frequency of waves reaching the pre-filmer edge, the approach of Raynal *et al.* (1997) and Villermaux (1998) was followed, which had also been adopted by Gepperth *et al.* (2010). They postulated the following condition to estimate the dominating wave length:

$$We_L \sqrt{\frac{\rho_l}{\rho_g}} > 1 \tag{2.3.88}$$

with the Weber number We_L based on a characteristic length scale L of the gas flow adjacent to the liquid, e.g. the boundary layer or vorticity thickness. In case of a high liquid to gas density ratio $\rho_l/\rho_g > 10$ and if the condition of Eq. 2.3.88 was fulfilled, Villermaux (1998) suggested that the dominating wave length λ_{stream} leading to the destabilization of the liquid film could be estimated by:

$$\lambda_{\text{stream}} \sim L \sqrt{\frac{\rho_l}{\rho_g}} \tag{2.3.89}$$

Unfortunately, the length scale L relies on the global flow conditions and not on the local flow. Implemented into a CFD platform, a model dependence on local conditions, i.e. conditions in each grid cell, would be desirable for a universally valid model. The dependence on global flow conditions makes the model less general and introduces a test case dependence. Due to this fact, prior to an application of the model, the proper length scale has to be identified (see section 3.2). Furthermore, another simplification was introduced by Raynal *et al.* (1997) and Villermaux (1998). They showed that the viscosity of the liquid can be neglected in the case of:

$$\frac{\nu_g}{\nu_l} \frac{|\vec{u}_g| L}{\nu_g} \gg 1 \tag{2.3.90}$$

Author	$\mathbf{V_{bag}/V_0}$	$\mathbf{V_{base}/V_0}$
Lane (1951)	0.25	0.75
Wert (1995)	0.20	0.80
Chou and Faeth (1998)	0.44 ± 0.04	0.56±0.04
Dai and Faeth (2001)	0.25	0.75
Zhao *et al.* (2011)	0.15±0.04	0.85±0.04

Table 2.1.: Volume ratios in the bag breakup regime

It can be demonstrated that the constraints of Eq. 2.3.88 and Eq. 2.3.90 are met for all laboratory conditions investigated in this study. Beyond that, high-pressure combustion systems operate in the majority of cases at conditions which comply with these restrictions. The group velocity u_c can be approximated by:

$$\vec{u}_c = \vec{u}_g \sqrt{\frac{\rho_g}{\rho_l}} \tag{2.3.91}$$

leading to the following frequency of the streamwise instability:

$$f_{\text{stream}} = \frac{|\vec{u}_c|}{\lambda_{\text{stream}}} \tag{2.3.92}$$

Assuming the spanwise undulation with a wave length λ_{span} is caused mainly by capillary forces, the findings of Rayleigh (1878) describing the destabilization of liquid cylinders of diameter d_{cyl} can be adopted:

$$\lambda_{\text{span}} = 4.508 \cdot d_{cyl} \tag{2.3.93}$$

The corresponding diameter d_{cyl} was estimated by mass conservation (Gepperth *et al.*, 2010):

$$\dot{m}_l = \rho_l \cdot \frac{\pi}{4} d_{cyl}^2 w \cdot f_{\text{stream}} \tag{2.3.94}$$

and rewriting Eq. 2.3.94:

$$d_{cyl} = \sqrt{\frac{4}{\pi} \frac{\dot{m}_l}{\rho_l w f_{\text{stream}}}} \tag{2.3.95}$$

with the width w of the wetted surface in spanwise direction and the liquid mass flux $\dot{m}_l$. A cellular structure with the dimensions $\lambda_{\text{stream}} \times \lambda_{\text{span}}$ forms the liquid volume V_0 undergoing bag breakup. Postulating mass conservation this volume can be evaluated:

$$\rho_l \cdot V_0 \cdot f_{\text{stream}} = \dot{m}_l \cdot \frac{\lambda_{\text{span}}}{w} \tag{2.3.96}$$

Rewriting yields:

$$V_0 = \frac{\dot{m}_l}{\rho_l} \frac{\lambda_{\text{span}}}{w} \frac{1}{f_{\text{stream}}} \tag{2.3.97}$$

Film breakup A portion of liquid shapes the thin bag membrane, whose burst eventually leads to a number of small droplets. The rest of the mass is embodied in the basal ring which later forms the ligament-like structures. In the literature, the ratio of the volume comprised in the bag to the one within the basal ring strongly varies depending on the research group (see table 2.1). For the following investigation the volume ratios of Wert (1995) recommended by Gepperth *et al.* (2010) are used. Additional uncertainties are related to the temporal evolution of the bag breakup process. Ambiguities exist concerning the period of time t_{ini} between the first exposure of the droplet to the dynamic air pressure and the initiation of bag breakup. The same applies to the time span t_{bag} until the rupture of the bag membrane and the time span t_{base} until the disintegration of the basal ring, which signifies the end of bag breakup. Pilch and Erdman (1987) derived the following correlation for the initiation time:

$$\frac{t_{ini}}{t^*} = 1.9 \cdot (We_{d_0} - 12)^{-0.25} \tag{2.3.98}$$

wherein t^* represents the characteristic timescale of Eq. 2.3.60 and We_{d_0} the Weber number defined in Eq. 2.3.71 substituting the initial diameter of the droplet d_0 for the characteristic length scale L:

$$d_0 = \sqrt[3]{\frac{6}{\pi} V_0} \tag{2.3.99}$$

Furthermore, Pilch and Erdman specified the total breakup time depending on the Weber number in order to distinguish between different breakup mechanisms. This yields:

$$\frac{t_{base}}{t^*} = \begin{cases} 6.00 \cdot (We_{d_0} - 12)^{-0.25} & \text{, for} \quad 12 \leq We_{d_0} \leq 18 \\ 2.45 \cdot (We_{d_0} - 12)^{0.25} & \text{, for} \quad 18 < We_{d_0} \leq 45 \\ 14.10 \cdot (We_{d_0} - 12)^{-0.25} & \text{, for} \quad 45 < We_{d_0} \leq 351 \end{cases} \tag{2.3.100}$$

Hsiang and Faeth (1992) as well as Chou and Faeth (1998) proposed for fluids with $Oh < 0.1$:

$$\frac{t_{ini}}{t^*} = 1.6 \tag{2.3.101}$$

$$\frac{t_{bag}}{t^*} = 3.5 \tag{2.3.102}$$

$$\frac{t_{base}}{t^*} = 5.0 \tag{2.3.103}$$

The Ohnesorge number Oh_L is a dimensionless quantity describing the importance of viscous forces relative to inertial and surface tension forces:

$$Oh_L = \frac{\mu_l}{\sqrt{\rho_l \sigma L}} \tag{2.3.104}$$

It consists of the dynamic liquid viscosity μ_l, the density of the liquid ρ_l, the surface tension σ and the characteristic length scale L. The sizes of droplets arising from the fragmentation of the bag membrane are evaluated following Chou and Faeth (1998) to yield on average $\mathrm{SMD_{bag}} = 0.044 \cdot d_0$. Being almost mono-disperse, the droplet sizes can be described by a narrow root normal distribution (Tate and Marshall Jr., 1953) with MMD/SMD=1.04. The breakup of the basal torus left after the fragmentation of the bag is assumed to form ligaments. The ligament length is taken to be half the perimeter of the torus with the small diameter of the cross-section $d_{torus,1}$ and the large diameter $d_{torus,2}$:

$$l_{lig} = \frac{\pi}{2} d_{torus,2} \tag{2.3.105}$$

The sizes of droplets d_{base} resulting from the breakup of the ligaments are estimated by the approach of Wert (1995) as suggested by Gepperth *et al.* (2012):

$$\mathrm{SMD}_{base} = 0.32 \frac{\sigma}{\rho_g |\vec{u}_{rel}|^2} \left(We_{d_0} \frac{t_{base} - t_{ini}}{t^*} \right)^{\frac{2}{3}} \tag{2.3.106}$$

The measurements of droplet sizes resulting from the disintegration of the ligaments (Gepperth *et al.*, 2012) indicated a monotonically decreasing value of the Sauter mean diameter with increasing Weber number. As a consequence, the correlations for the breakup times of Hsiang and Faeth (1992) as well as Chou and Faeth (1998) are used within the sheet atomization model. Furthermore, the experiments did not indicate the existence of a distinct droplet size but rather a distribution of droplet sizes. Consequently, the value obtained by Eq. 2.3.106 is used in conjunction with a root normal distribution (Tate and Marshall Jr., 1953) which has already been successfully applied for secondary atomization of droplets by Simmons (1977a,b); Hsiang and Faeth (1992) as well as Chou and Faeth (1998). With a constant MMD/SMD value the root normal distribution is unambiguously specified by the SMD. In order to include the chaotic nature of the atomization process, droplet sizes are randomly chosen from the individual root normal distributions for the bag and ligament droplets.

Limits of applicability The primary atomization model for pre-filming airblast atomization is limited to moderate Weber numbers. At ambient pressures of 6 bar and $100 < We < 380$, a transition from a break-up scenario at the pre-filmer edge to atomization via surface stripping can be observed (Bhayaraju and Hassa, 2009). Furthermore, it is limited to conditions where adhesion dominates convection at the tip of the pre-filmer leading to an accumulation of liquid at the pre-filmer edge. Bhayaraju and Hassa (2009) suggest a dependence on the ratio between film thickness and pre-filmer edge height, which has to be further investigated. Besides, only films originating from orifices or slits were considered. Films forming from the impingement of jets or droplets on a surface like in hybrid airblast atomizers (i.e. pressure-swirl atomizer spraying on a concentric surface) cannot be reflected, up to now.

2.3.1.3. Secondary atomization

The breakup of initially spherical drops in relative movement to a gaseous flow field is referred to as secondary atomization. The aerodynamic forces acting on the surface of the liquid drop lead to a deformation which is resisted by surface tension and viscous forces. In case the disruptive forces overcome the cohesive forces fragmentation is caused. Experimental investigations (Bartz

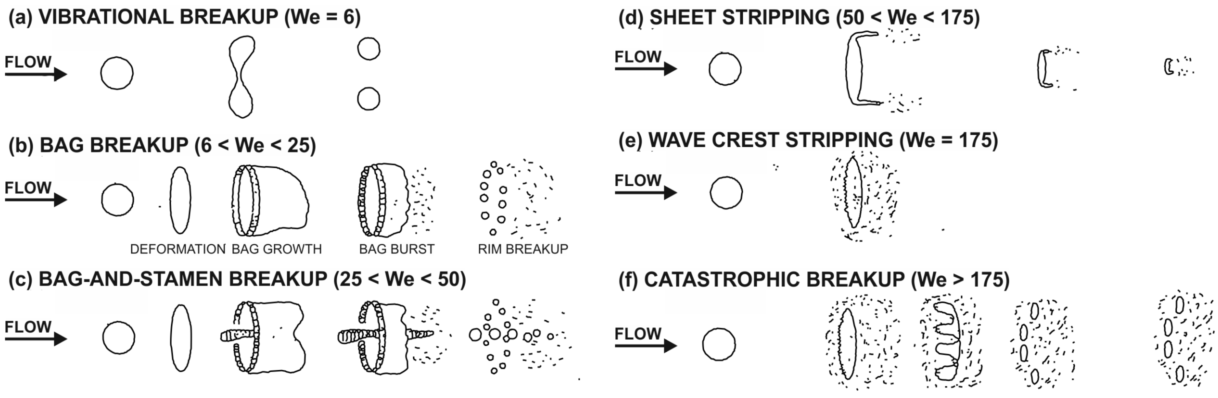

Figure 2.8.: Secondary breakup regimes (adapted from Pilch and Erdman (1987))

et al., 2010, 2011) suggest that the temporal evolution of the breakup process is important for the breakup time as well as the trajectories and sizes of both the parent and child droplets. Interestingly, the smallest fragment sizes are not necessarily obtained at the highest relative velocities. Hence, in order to determine conditions leading to the desired final droplet sizes, secondary breakup has been extensively studied (Guildenbecher *et al.*, 2009). Fig. 2.8 shows

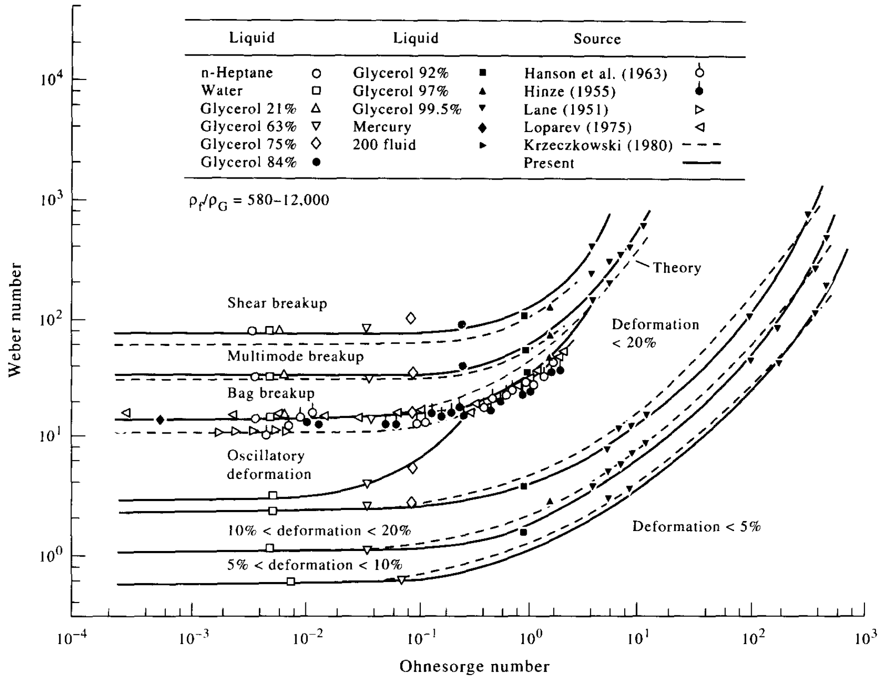

Figure 2.9.: Breakup regime map for shock wave disturbances (from Hsiang and Faeth (1995))

the various breakup modes depending on the incoming flow. The disruptive forces increase from (a) to (f). Different numerical values of the Weber number limits describing the transition between the breakup modes can be found in the literature. The ones given in Fig. 2.8 are based on the droplet radius and taken from Pilch and Erdman (1987). A comparison of various data sets from shock wave experiments of secondary breakup is depicted in Fig. 2.9 (Hsiang and Faeth, 1995). It shows that the Weber number limits are constant and independent of Oh for an Ohnesorge number Oh < 0.1, i.e. breakup is mainly resisted by surface tension forces and less by viscosity. In case of a higher Ohnesorge number, the breakup regimes are shifted towards larger Weber numbers. At low disruptive forces, the drop oscillates with its eigenfrequency. When the deformation becomes large enough the drop breaks up into fragments in the order of magnitude of the original drop size (Fig. 2.8a). This process is called vibrational breakup. In bag breakup mode (Fig. 2.8b), a soap bubble like structure is formed attached to a toroidal ring. The basal ring comprises 50-80% of the drop's original volume. Firstly, the bag disintegrates into small droplets resulting in droplet diameters of approximately 4% of the parent diameter. Subsequently, the basal ring continues to grow before it gets unstable and breaks up into a small amount of larger droplets (ca. 30% of the parent diameter). Multi-mode breakup or often also called bag-and-stamen breakup (Fig. 2.8c) shows a similar behavior to bag breakup with the difference that a ligament like structure forms in the middle of the bag. Fragmentation occurs starting with the bag, succeeded by the stamen and the basal ring. In the breakup regime of sheet-stripping or sheet-thinning (Fig. 2.8d), liquid is continuously shorn off the drop's surface leading to a huge amount of small droplets. Occasionally, a core remains in the order of magnitude of the original drop size. For very large disruptive forces, catastrophic breakup (sometimes sub-divided into wave-crest stripping depicted in Fig. 2.8e and catastrophic breakup shown in Fig. 2.8f) occurs resulting in a small number of large fragments subsequently undergoing rapid atomization. Initiated by surface disturbances with high amplitude and small wavelengths, liquid is eroded from the fragments' surface.

Up to now, many models have been proposed in the literature but none of them is able to comprehensively capture all aspects of secondary atomization (Guildenbecher *et al.*, 2009). In the work at hand, the cascade atomization and drop breakup (CAB) model of Tanner (2004) is used in conjunction with the droplet deformation law of Schmehl (2004) and drag formulae from Clift *et al.* (1978). The CAB model is an extension of the Taylor analogy breakup (TAB) (O'Rourke and Amsden, 1987) and the enhanced Taylor analogy breakup (ETAB) (Tanner, 1997) model. In analogy to a spring-mass system, the droplet is considered to undergo a forced and damped harmonic oscillation. During this oscillation, the droplet is thought to change from an oblate to prolate spheroid. Introducing the displacement Δr_p from the undistorted

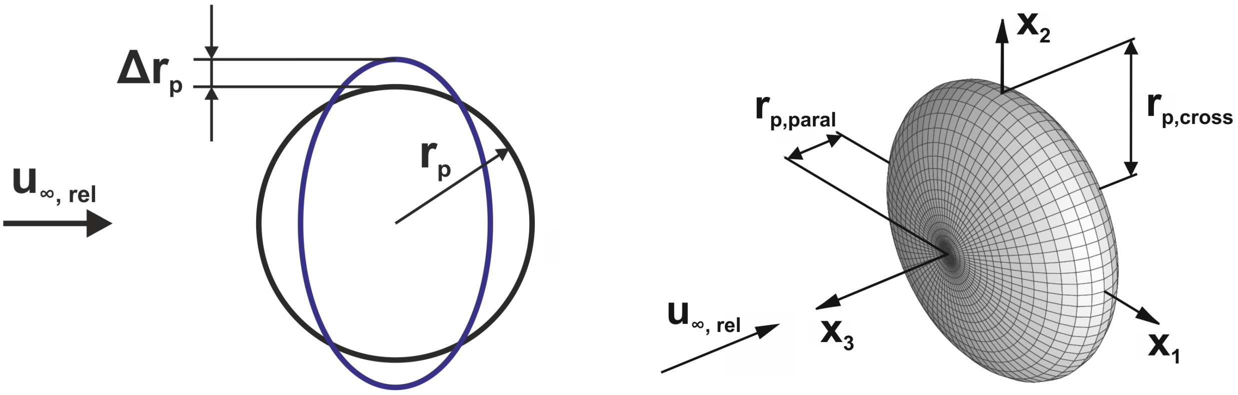

Figure 2.10.: Sketch of the droplet deformation (adapted from Schmehl (2004))

state depicted in Fig. 2.10, the oscillation can be described by:

$$\ddot{\Delta r}_p + \frac{d}{m}\dot{\Delta r}_p + \frac{k}{m}\Delta r_p = \frac{F}{m} \tag{2.3.107}$$

The damping is due to liquid viscosity:

$$\frac{d}{m} = C_d \frac{\mu_l}{\rho_l r_p^2} \tag{2.3.108}$$

The restoring force (spring constant) is a result of surface tension:

$$\frac{k}{m} = C_k \frac{\sigma_l}{\rho_l r_p^3} \tag{2.3.109}$$

The forcing term is given by the aerodynamic forces acting on the droplet:

$$\frac{F}{m} = C_F \frac{\rho_g |\vec{u}_{rel}|^2}{\rho_l r_p} \tag{2.3.110}$$

Before solving, Eq. 2.3.107 is non-dimensionalized by introducing:

$$y = \frac{2\Delta r_p}{r_p} \tag{2.3.111}$$

This leads to:

$$\ddot{y} + \frac{C_d \mu_l}{\rho_l r_p^2}\dot{y} + \frac{C_k \sigma_l}{\rho_l r_p^3} y = \frac{2 C_F \rho_g |\vec{u}_{rel}|^2}{\rho_l r_p^2} \tag{2.3.112}$$

With the boundary condition $y_0 = y(0)$ and $\dot{y}_0 = \frac{dy}{dt}(0)$, the solution of the second order ODE (Eq. 2.3.112) is:

$$y(t) = \frac{2C_F}{C_k} We_{r_p} + e^{-\delta t}\left(\left(y_0 - \frac{2C_F}{C_k} We_{r_p}\right) cos(\omega t) + \left(\dot{y}_0 + \delta\left(y_0 - \frac{2C_F}{C_k} We_{r_p}\right)\right)\frac{sin(\omega t)}{\omega}\right) \tag{2.3.113}$$

Droplet breakup is assumed in case the deformation exceeds a critical value of:

$$y > 1 \tag{2.3.114}$$

The drop oscillation angular frequency ω can be calculated by:

$$\omega = \sqrt{\omega_0^2 - \delta^2} = \sqrt{C_k \frac{\sigma_l}{\rho_l r_p^3} - C_d^2 \frac{\mu_l^2}{4 \rho_l^2 r_p^4}} \tag{2.3.115}$$

with ω_0 being the angular frequency of the undamped system:

$$\omega_0 = \sqrt{\frac{k}{m}} \tag{2.3.116}$$

The damping coefficient δ is given by:

$$\delta = \frac{d}{2m} \tag{2.3.117}$$

The constants $C_d = 5$, $C_k = 8$ and $C_F = 1/3$ were determined by comparisons to the theoretical fundamental oscillation mode and the experimental data for the initiation of breakup at $We_{r_p} = 6$ for $Oh = 0$, i.e. $d/m = 0$ (O'Rourke and Amsden, 1987). The number and size of child droplets are calculated based on an analogy to population dynamics assuming a uniform, mono-disperse size distribution. This gives:

$$\frac{r_{child}}{r_{parent}} = e^{-K_{bu} t_{bu}} \tag{2.3.118}$$

with K_{bu} and t_{bu} being the breakup frequency and the breakup time, respectively. The breakup time is the moment when Eq. 2.3.114 is fulfilled. In the CAB model, three breakup regimes are distinguished: bag breakup, stripping breakup and catastrophic breakup. The breakup frequency is dependent on these regimes and is given by:

$$K_{bu} = \begin{cases} k_1\ \omega & \text{, for} \quad 6 < We_{r_p} \leq 80 \quad \text{(bag breakup)} \\ k_2\ \omega\ We_{r_p}^{1/2} & \text{, for} \quad 80 < We_{r_p} \leq 350 \quad \text{(stripping breakup)} \\ k_3\ \omega\ We_{r_p}^{3/4} & \text{, for} \quad 350 < We_{r_p} \quad \text{(catastrophic breakup)} \end{cases} \tag{2.3.119}$$

The Weber number limits were taken from Liu and Reitz (1993). In this thesis, for the sake of numerical stability, smooth transitions between the regimes were ensured by setting the constants k_1, k_2 and k_3 to the following values:

$$\begin{aligned} k_1 &= 0.2 \\ k_2 &= \frac{k_1}{80^{1/2}} \\ k_3 &= \frac{k_2}{350^{1/4}} \end{aligned} \tag{2.3.120}$$

In Tanner (2004), the initial drop deformation of the child droplets is expected to be zero, i.e $y(0) = \dot{y}(0) = 0$. The velocity of the child droplets is assumed to be:

$$\vec{u}_{child} = \vec{u}_{parent} + \vec{u}_{drift} \tag{2.3.121}$$

with the drift velocity $\vec{u}_{drift}$ being perpendicular to the relative velocity $\vec{u}_{rel}$ defined in Eq. 2.3.4. The magnitude of the drift velocity is calculated from the oscillation velocity at the time of breakup:

$$|\vec{u}_{drift}| = A_{drift}\ \dot{\varDelta r}_p(t_{bu}) \tag{2.3.122}$$

The constant A_{drift} in Eq. 2.3.122 is derived from an energy balance between parent and child droplets (details see Tanner (2004)). This yields:

$$A_{drift} = \sqrt{3\left(1 - \frac{r_{parent}}{r_{child}} + \frac{5}{72} c_d We_{r_p}\right)\left(\frac{\omega_0}{\dot{y}(t_{bu})}\right)^2} \tag{2.3.123}$$

The influence of the deformation on the droplet trajectory is accounted for following Hsiang and Faeth (1992), who showed that the drag coefficient prior to breakup evolves from the drag coefficient of a solid sphere to the one of a thin disk perpendicular to the relative velocity vector.

$$c_{d,spheroid} = (1 - f_{spheroid}) \cdot c_{d,sphere} + f_{spheroid} \cdot c_{d,disk} \tag{2.3.124}$$

The transition between these drag coefficients is modeled according to the dynamic drag law of Schmehl (2004) who proposed the blending factor $f_{spheroid}$:

$$f_{spheroid} = 1 - e^2_{spheroid} \tag{2.3.125}$$

with the eccentricity of the oblate spheroid $e_{spheroid}$ (see Fig. 2.10) defined by:

$$e_{spheroid} = \frac{r_{p,paral}}{r_{p,cross}} = \left(\frac{d_p}{d_{p,cross}}\right)^3 \tag{2.3.126}$$

The term on the right hand side of Eq. 2.3.126 results from mass conservation. The drag coefficients of a solid sphere and the one of a disk perpendicular to the relative velocity vector were taken from Clift *et al.* (1978, p. 112 and p. 145).

2.3.1.4. Remarks on atomization modeling

The atomization models presented in the previous sections are not designed to solve break-up in detail. Omitting a detailed resolution of the gas-liquid interface, the semi-empirical models can only represent key features of the atomization at specific conditions. As a consequence, the models cannot be universally valid and are restricted to a limited applicability range. Still, the representation of atomization in combustion simulations is a major scientific challenge and involves high uncertainties. More research is needed to universally predict atomization and to embed accurate and efficient models into simulation tools.

2.3.2. Dispersion models

2.3.2.1. Modeling approaches for dispersion

After the stage of atomization, the physical system consists of discrete liquid droplets with a spectrum of diameters being dispersed in a turbulent, continuous gaseous phase (Balachandar and Eaton, 2010). As can be seen from Eq. 2.3.2, 2.3.3 and 2.3.4, the droplet trajectory depends on the relative velocity between the droplet and the surrounding gas. Due to droplet sizes being generally smaller than the grid size and hence the filter width, the gas velocity seen by the droplet is composed of resolved and unresolved (sub-grid) scales. Many examples can be found in the literature, e.g. Wang and Squires (1996); Apte *et al.* (2003); Boileau *et al.* (2008); Vreman *et al.* (2009); Vuorinen *et al.* (2010); Sacomano Filho *et al.* (2014) and Chrigui *et al.* (2014), solving the droplet velocity only with the filtered gas velocity without any model for the sub-grid scales. Armenio *et al.* (1999); Kuerten (2006); Marchioli *et al.* (2008) as well as Pozorski and Apte (2009) investigated the effect of disregarding unresolved velocity fluctuations on particle trajectories. They came to the conclusion that sub-grid scale models for turbulence-droplet interaction became important in case of a large amount of turbulent kinetic energy in the sub-grid scales, e.g. in areas of low grid resolution, as well as for small particle response times (Eq. 2.3.5) compared to sub-grid turbulent time scales. But it should be pointed out that the particle response time itself depends on the absolute value of the relative velocity and hence on resolved and unresolved velocity fluctuations. In contrast to laminar flows where a clear definition of the particle relaxation time exists, this fact complicates both the a priori and the a posteriori analysis. Furthermore, the authors pointed out that a sub-grid scale model was necessary for accurate predictions of preferential segregation and concentration, particularly in near-wall regions.

Numerous sub-grid models for the turbulence-droplet interaction were proposed both for the Euler-Euler and the Euler-Lagrange framework (Balachandar and Eaton, 2010; Fox, 2012). As this study relies on an Eulerian description of the gas phase and a Lagrangian description of the dispersed phase, the focus will be on models in the Euler-Lagrange framework in the following. Segura (2004) as well as Patel and Menon (2008) used an approach originally developed by Gosman and Ioannides (1983) in the context of RANS simulations (see section 2.3.2.2). Although the system of differential equations looks very similar between RANS and LES, there is a fundamental difference between averaged and filtered quantities, e.g. in contrast to RANS averaging, the filtered value of a sub-grid fluctuation in the LES is not zero (Poinsot and Veynante, 2011). Furthermore, in RANS the entire spectrum from the energy-containing range over the inertial range until the dissipation range is modeled. In LES, the spectrum is incorporated to some extent in the resolved scales and partly in the unresolved sub-grid scales. Underlying assumptions which are valid in the RANS context might not be conclusive in the LES context. Hence, a different formalism for LES sub-grid scale models is advisable (Minier, 2015). One approach is to reconstruct the velocity field by a deconvolution of the filtered equations, i.e. applying an inverse filter. These so called approximate deconvolution methods (ADM) (Kuerten, 2006; Shotorban *et al.*, 2007) are extensions for multi-phase flows of the single-phase formulation of Stolz *et al.* (2001) and show promising results (Cernick *et al.*, 2014). Nevertheless, this method is not consistent with the LES sub-grid scale model for turbulence of section 2.2.1.2 as the deconvoluted velocity should be used in both the gaseous and the liquid phase. Other approaches introduce stochastic terms based on a Langevin equation. The generalized Langevin equation was originally introduced by Pope and co-workers (Pope, 2000) for RANS of single phase turbulent reacting flows and later extended to RANS of particle-laden flows by Minier and co-workers (Minier and Peirano, 2001; Minier *et al.*, 2004; Chibbaro and Minier, 2008; Minier *et al.*, 2014; Minier, 2015). Two types of sub-grid scale models of this category can be distinguished. In the first type, the Langevin equation is used to determine the gas velocity seen by the droplet. Shotorban and Mashayek (2006); Berrouk *et al.* (2007); Oefelein *et al.* (2007) and Pozorski and Apte (2009) came up with Lagrangian formulations for particle-laden LES. A combination of ADM and a Langevin equation for the gas velocity seen by the droplet can be found in Michalek *et al.* (2013). In the second type of stochastic models, the influence of the sub-grid scale fluctuations is considered by adding a stochastic acceleration term in analogy to Brownian motion to the right hand side of the ordinary differential equation of the droplet velocity (Eq. 2.3.2). Examples of this type were developed by Fukagata *et al.* (2004) and Bini and Jones (2008). Many applications of the latter can be found in the literature, e.g. Franchetti *et al.* (2013); Stein *et al.* (2013); Jones *et al.* (2010a,b, 2011, 2012, 2014), and Jones *et al.* (2015). Within this work, the sub-grid scale models for turbulence-droplet interaction based on the work of Gosman and Ioannides (1983) (representative of classical RANS models) as well as Bini and Jones (2008) (representative of widely-used stochastic LES models) are applied. These models will be shortly introduced in the following.

2.3.2.2. Interaction time dispersion model

Gosman and loannides (1981; 1983) suggested that the particle dispersion depended on a distinct interaction time between the turbulent structures and the particle. In their model, the turbulent structures are assumed to be represented by a characteristic eddy. The interaction time is limited by either the lifetime of the turbulent eddy in case the particle is slow enough to stay within the eddy until it decays or the transit time, i.e. the time the particle needs to cross the eddy:

$$t_{int} = min(t_{eddy}, t_{trans}) \tag{2.3.127}$$

The characteristic length and time scale of the eddy were estimated drawing an analogy to the Kolmogorov microscale. The Kolmogorov microscale, being the scale of the smallest, dissipative eddies in a turbulent flow, is defined as (Pope, 2000):

$$\eta = \left(\frac{\nu_g^3}{\epsilon}\right)^{\frac{1}{4}} \tag{2.3.128}$$

As already mentioned in section 2.3.2, the model of Gosman and Ioannides was developed in a RANS context. The equations for the turbulent length and time scale were derived based on the $k-\epsilon$ model. In the $k-\epsilon$ model, the turbulent viscosity is modeled by:

$$\nu_t = C_\mu \frac{k^2}{\epsilon} \tag{2.3.129}$$

with the turbulent kinetic energy:

$$k = \frac{1}{2}\left(u'^2_g + v'^2_g + w'^2_g\right) \tag{2.3.130}$$

C_μ represents a modeling constant amounting to 0.09. Inserting Eq. 2.3.129 into Eq. 2.3.128 yields the characteristic eddy size proposed by Gosman and loannides (1981):

$$l_{eddy} = \frac{C_\mu^{\frac{3}{4}} k^{\frac{3}{2}}}{\epsilon} \tag{2.3.131}$$

The eddy lifetime was estimated by:

$$t_{eddy} = \frac{l_{eddy}}{|\vec{u'}_g|} \tag{2.3.132}$$

with

$$|\vec{u'}_g| = \sqrt{u'^2_g + v'^2_g + w'^2_g} \tag{2.3.133}$$

In homogeneous isotropic turbulence, i.e $u'_g = v'_g = w'_g = \sqrt{2/3k}$, the eddy life time yields:

$$t_{eddy} = \frac{l_{eddy}}{\sqrt{2k}} \tag{2.3.134}$$

Shuen *et al.* (1983) found a better agreement with measurements applying:

$$t_{eddy} = \frac{l_{eddy}}{u'_g} = \frac{l_{eddy}}{\sqrt{2/3k}} \tag{2.3.135}$$

For the transit time, Gosman and loannides(1981; 1983) proposed the following formulation:

$$t_{trans} = \tau_p \, ln \left(1 - \frac{l_{eddy}}{\tau_p |\vec{u}_{rel}|} \right) \tag{2.3.136}$$

In contrast, in the work at hand a linear relationship for the transit time proposed by Amsden *et al.* (1989) is adopted:

$$t_{trans} = \frac{l_{eddy}}{|\vec{u}_{rel}|} \tag{2.3.137}$$

In order to apply the interaction time dispersion model in the framework of Large Eddy Simulations, the eddy lifetime and characteristic eddy size have to be related to the sub-grid scale quantities of the Eulerian gas phase. Therefore, in this work the following formulations are used:

$$t_{eddy} = C_t \, \tau_{sgs} \tag{2.3.138}$$

$$l_{eddy} = C_l \, t_{eddy} \sqrt{\frac{2}{3} k_{sgs}} \tag{2.3.139}$$

The characteristic turbulent time scale τ_{sgs} and the turbulent kinetic energy in the sub-grid scales k_{sgs} result from the sub-grid scale model for turbulence in section 2.2.1.2:

$$\tau_{sgs} = \frac{\left(C_{sgs}\varDelta\right)^2}{\nu_t} \tag{2.3.140}$$

$$k_{sgs} = \left(\frac{\nu_t}{C_{sgs}\varDelta}\right)^2 \tag{2.3.141}$$

The modeling constants C_t and C_l are set to:

$$C_t = 1.0 \tag{2.3.142}$$

$$C_l = 0.3 \tag{2.3.143}$$

2.3.2.3. Stochastic dispersion model of Bini and Jones

In the model of Bini and Jones (2008), the droplet acceleration due to the resolved scales is equivalent to Eq. 2.3.2. Besides this deterministic part, an additional stochastic term is added to account for the unresolved sub-grid scales. Introducing the particle response time described in Eq. 2.3.5, this leads to:

$$\frac{d\vec{u}_p}{dt} = \underbrace{\frac{\tilde{\vec{u}}_g - \vec{u}_p}{\tau_p}}_{\text{resolved scales}} + \left(1 - \frac{\rho_g}{\rho_l}\right)\vec{g} + \underbrace{\chi}_{\text{unresolved scales}} \tag{2.3.144}$$

Assuming the effect of the sub-grid scale fluctuations on the particle trajectory resembles a diffusion-like process similar to Brownian motion, the diffusion process can be expressed in terms of a Wiener process (Gardiner, 2004). Thus, an infinitely small particle velocity increment yields:

$$d\vec{u}_p = \underbrace{\frac{\vec{u}_g - \vec{u}_p}{\tau_p}\,dt + \left(1 - \frac{\rho_g}{\rho_l}\right)\vec{g}\,dt}_{\text{deterministic terms}} + \underbrace{\mathbf{B}\cdot d\vec{W}}_{\text{stochastic term}} \tag{2.3.145}$$

The stochastic part on the right hand side of Eq. 2.3.145 is composed of a diffusion coefficient tensor $\mathbf{B}$ multiplied by a three-dimensional Wiener process. A time discretized Wiener process can be approximated by a series of random walks:

$$W(t_n) \approx \sqrt{\delta t}\,\sum_{i=1}^{n} \xi_i \tag{2.3.146}$$

with the accumulated time $t_n = n\ \delta t$ after n time steps δt as well as a random variable ξ with zero mean and a variance of unity. The diffusion coefficient tensor $\mathbf{B}$ depends on the unresolved gas velocity fluctuations $\widetilde{u_i u_j} - \tilde{u}_i\tilde{u}_j$ (Eq. 2.2.11) and on a characteristic time scale τ_t describing the interaction between the droplet and these turbulent structures:

$$B_{ij} = \frac{\widetilde{u_i u_j} - \tilde{u}_i \tilde{u}_j}{2/3\, k_{sgs}} \cdot \sqrt{\frac{C_0}{\tau_t} k_{sgs}} \tag{2.3.147}$$

wherein C_0 is a model constant with a value of unity in the work at hand. In contrast to the original work of Bini and Jones (2008), the denominator in the pre-factor of the diffusion coefficient tensor $\mathbf{B}$ is changed from k_{sgs} to $2/3\ k_{sgs}$ in order to recover their simplified form in case of isotropic turbulence:

$$B_{ij} = \delta_{ij} \sqrt{\frac{C_0}{\tau_t} k_{sgs}} \tag{2.3.148}$$

The turbulent kinetic energy in the sub-grid scales k_{sgs} results from the sub-grid scale model for turbulence in section 2.2.1.2:

$$k_{sgs} = \left(\frac{\nu_t}{C_{sgs} \Delta} \right)^2 \tag{2.3.149}$$

The characteristic time scale τ_t is modeled by:

$$\tau_t = \tau_p^{2\alpha} \left(\frac{\sqrt{k_{sgs}}}{\Delta} \right)^{2\alpha - 1} \tag{2.3.150}$$

with $\alpha = 0.8$ as well as Δ and τ_p being the filter width of Eq. 2.2.6 and the particle response time of Eq. 2.3.5, respectively.

2.3.3. Vaporization models

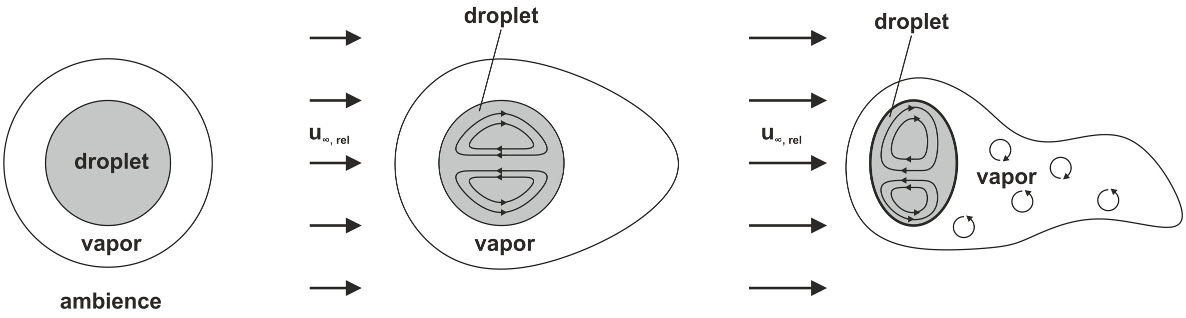

(a) quiescent (b) moderate Re (c) high Re

Figure 2.11.: Schematic of droplet evaporation for different freestream velocities (adapted from Rauch (2017))

Besides the momentum transfer between the phases described in section 2.3.2, the droplets and the gaseous phase also exchange heat, mass and species. The phase change from liquid to vapor and vice versa is referred to as vaporization and condensation, respectively. The vaporization increases if the liquid is heated up or the pressure of the surrounding gas phase decreases, e.g. via expansion. The liquid molecules transition into the vapor phase in case their kinetic energy is high enough to overcome the intermolecular forces in the liquid and the adverse partial pressure in the gas phase (Tanner, 2011). The liquid phase vaporizes as long as the vapor pressure at the surface $p_{vap,\alpha}$, which results from the transitioning molecules, is higher than the local partial pressure $p_{g,\alpha}$ in the gas phase. The higher the vapor pressure of a species, the more volatile it is. In case the vapor pressure exceeds the environmental pressure p_g the boiling point is reached. The vaporization changes from a surface phenomenon (evaporation) to a bulk phenomenon (boiling). Vapor bubbles are formed below the surface. In equilibrium, the vapor pressure at the surface $p_{vap,\alpha}$ equals the local partial pressure $p_{g,\alpha}$ in the gas phase. Condensation occurs if the vapor is cooled down or compressed so that the local partial pressure in the gas phase is higher than the vapor pressure at the surface.

Apart from the local conditions close to the gas-liquid interface, the gaseous flow around the droplet influences the exchange of mass, momentum and energy. In general, the coupling between both phases gets stronger, the higher the vaporization/condensation rates are, e.g. because of high ambient gas temperatures as a result of combustion (Sirignano, 2010). This is due to the fact that the time scale of vaporization/condensation approaches characteristic time scales of the flow in the surroundings. The flow can be characterized by means of the Reynolds number based on the gas phase properties, relative velocity and the droplet diameter. In a quiescent environment (Fig. 2.11a), vaporization and condensation are governed by diffusion. A spherically symmetric vapor shell surrounds the droplet. The resulting flow is called Stefan flow. At moderate Reynolds numbers (Fig. 2.11b), a gaseous boundary layer develops and a shear-driven internal circulation arises (Mashayek and Ashgriz, 2011). The vapor shell is deformed shaping a tail behind the droplet. At high Reynolds numbers (Fig. 2.11c), the vapor wake becomes unsteady with strong interactions between the droplet and turbulent vortices. As a consequence, the internal circulation gets asymmetric (Sugioka and Komori, 2007). Additional flow modifications appear in dense sprays due to other droplets in the vicinity.

2.3.3.1. Modeling approaches for vaporization

A variety of droplet vaporization models can be found in the literature. Following Sirignano (2010), six types of models can be distinguished based on the complexity of resolving the droplet internal transport phenomena. In the following, the model types will be introduced starting from a 0-D approximation and ending with a full 3-D solution. Assuming spherical symmetry as well as steady-state vaporization with constant droplet temperature and species distribution results in the well-known *d^2-law* of Spalding (1953), i.e. a linear decrease of the square of the droplet diameter with time. An extension to multi-component vaporization can be found in Law and Law (1982). Increasing the complexity by allowing for a time-dependent but uniform droplet temperature and species distribution gives the so-called *infinite-liquid-conductivity model*, also referred to as *rapid mixing model*. Abramzon and Sirignano (1989) extended the rapid mixing model to account for the radial Stefan flow and forced convection. In order to allow for transient heating inside the droplet, a one-dimensional radial profile can be solved, which results in the so-called *conduction limit model*. In the classical formulation, both the rapid mixing and conduction limit model rely on analogies to the analytical solution of a species profile in a steady 1-D diffusion-governed vapor film combined with empirical corrections. For both models, Miller *et al.* (1998) proposed a different formulation for the heat transfer correction based on the analytical solution of a species profile around a spherically symmetric droplet. Furthermore, Miller *et al.* (1998) incorporated non-equilibrium effects at the droplet surface. The *conduction limit model* turns into the *effective conductivity model* in case the thermal diffusivity is corrected by an algebraic function reflecting the enhanced transport by the internal flow. The algebraic function is usually derived from DNS. Two-dimensional representations of the droplet can be found in *vortex models.* The heat and mass transfer in these models is calculated by means of a potential flow solution for the external flow and the solution of a vorticity equation (curl of the momentum equation) for the internal flow, e.g. Hill's vortex in the inviscid limit (Sirignano, 2010). In the last type of models the Navier-Stokes equations (2-D or 3-D) are directly solved.

Liquid fuels usually consist of a mixture of multiple components. Wahl and Kapernaum (2003) identified 410 different species in Jet A-1 by means of a gas chromatograph coupled to a mass spectrometer (GC-MS). The computational costs for solving for each of these species with a discrete species evaporation model (see section 2.3.3.2) are too high, up to now. As a consequence, several models can be found in the literature which aim at reducing the number of variables and hence the computational expenses (Dagaut and Cathonnet, 2006). In the so-called surrogate models, the fuel is represented by one or a few surrogate species. Two types of surrogates can be distinguished, namely physical and chemical surrogates (Edwards and Maurice, 2001). A physical surrogate mimics the physical properties of the fuel (e.g. density, viscosity, surface tension, thermal conductivity). These physical properties are important for atomization, dispersion and heat transfer. Chemical surrogates aim at matching chemical properties (e.g. laminar flame speed, ignition delay time, adiabatic flame temperature and chemical-class composition, i.e. right proportion of n-alkanes, iso-alkanes, cyclo-alkanes and aromatics). These chemical properties are important for chemical reaction kinetics, i.e. ignition, combustion and pollutant emissions. In the early days of combustion simulation, researchers tried to incorporate both physical and chemical properties into a single component surrogate. For example, the automotive industry used iso-octane (C_8H_{18}) and tetra-decane ($C_{14}H_{30}$) to represent gasoline and diesel, respectively (Rauch, 2017). In the aerospace industry, n-decane ($C_{10}H_{22}$) represented Jet A-1 (Dagaut and Cathonnet, 2006). Instead of using a single n-alkane species, Rachner *et al.* (1996) proposed a single component surrogate exhibiting the average properties of real multi-component Jet A-1 based on an extensive literature study (Rachner, 1998). This single-component surrogate fuel yielded a good agreement of numerical results and experimental data concerning global features of evaporation, mixing (Rachner *et al.*, 1996) and combustion (Jones *et al.*, 2012). However, in real fuel blends, species with a high volatility vaporize earlier than species with a low one. This difference in volatility cannot be accounted for using single-component surrogates. Edwards and Maurice (2001) recommended to match the distillation curve to describe fuel vaporization without reaction. Burger *et al.* (2003) came up with a model reflecting the distillation curve of aviation fuels by means of a single progress variable, i.e. the mean molar weight. Only depending on this progress variable, the fuel properties were derived from the properties of n-alkanes. The change in mean molar weight during evaporation is described by algebraic functions and polynomials fitted to distillation data from the American Society for Testing and Materials (ASTM). Although Burger *et al.* (2003) obtained good results for the vaporization of different multi-component fuels, the model relies on a single-component chemical surrogate in the chemical kinetics mechanism of the gaseous phase. In order to correctly describe fuel ignition, heat release, flame speed and emission, Edwards and Maurice (2001) recommended a multi-component surrogate matching the important chemical classes. In aviation fuels, these classes are the n-alkane, iso-alkane, cyclo-alkane and aromatics families. The average composition of 55 jet fuels collected worldwide in the framework of a world fuel survey (Shafer *et al.*, 2006) yielded 20 % n-alkanes, 40 % iso-alkanes, 20 % cyclo-alkanes and 20 % aromatics. Table 2.2 lists these four chemical classes together with their general formula and an example species. In the very right column, the chemical structure of the example species is depicted. Alkanes are saturated hydrocarbons, i.e. the compounds of hydrogen and carbon have only single bonds. They can be sub-divided according to their chemical structure. Straight chains are called n-alkanes or n-paraffins. Branched chains are entitled iso-alkanes or iso-paraffins and ringlike structures are named cyclo-alkanes or naphtenes. Alkanes possess a relatively high gravimetric heat of combustion and relatively low density compared to other hydrocarbons due to the high H/C-ratio. They exhibit a high thermal stability as well as low coke deposition and soot-forming tendencies (Lefebvre and Ballal, 2010). The structure of aromatics is based on rings with six carbon atoms and three double bonds (six electrons floating around). These so-called benzene rings are named after the simplest aromatic hydrocarbon, i.e. benzene C_6H_6. Replacing a hydrogen atom by a hydrocarbon group, more complex structures are obtained, e.g. toluene with one H-atom being replaced by a CH_3-group. Aromatics are hygroscopic, which can lead to the formation of ice crystals at low temperatures (Lefebvre and Ballal, 2010). Furthermore, they show strong soot formation tendencies (Eberle *et al.*, 2015). Hence, from a combustion standpoint it is desirable to keep the aromatics content at a low level. Unfortunately, nitrile rubber o-rings, commonly used in

Chemical class	General formula	Representative	Formula	Chemical structure
n-alkanes	C_nH_{2n+2}	n-dodecane	$C_{12}H_{26}$	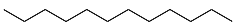
iso-alkanes	C_nH_{2n+2}	iso-octane	C_8H_{18}	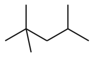
cyclo-alkanes	C_nH_{2n}	cyclo-hexane	C_6H_{12}	
aromatics	C_nH_{2n-6}	toluene	C_7H_8	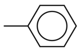

Table 2.2.: Fuel families and their chemical structure (Kuo, 1986)

aircraft systems (especially in legacy hardware), are sensitive to the aromatics content of the fuel. Currently investigated alternative fuels with a low aromatic content showed significantly lower swelling of these elastomers risking fuel leaks in aircraft systems (Corporan *et al.*, 2011). As a consequence, alternative fuel blend specifications prescribe a minimum aromatics content of 8 % (ASTM D7566, 2016).

For Jet A-1, Violi *et al.* (2002) proposed three multi-component (physical and chemical) surrogates composed of 5 to 6 surrogate species (depending on the actual composition of the fuel batch). The surrogate species came from the n-alkane, iso-alkane, cyclo-alkane and aromatics classes and had to have known detailed kinetic mechanisms. Furthermore, the surrogate composition was required to match both physical properties (e.g. the distillation curve) and chemical properties (e.g. sooting tendency, calorific value) of practical fuels. For gasoline and diesel fuels, Ra and Reitz (2009, 2011, 2015) suggested a multi-component physical surrogate coupled to a multi-component chemical surrogate for the vaporization and oxidation, respectively. In the latest version, Ra and Reitz (2015) used a 22-component physical surrogate to describe the thermo-physical properties, such as the distillation curve, specific gravity, lower heating value and hydrogen-to-carbon (H/C) ratio. The chemical surrogate consisted of 43 components out of 6 chemical classes, i.e. n-alkanes, iso-alkanes, alkenes, aromatics and oxygenates (alcohols and ethers). Despite a significant reduction in the number of species, still a fairly large set of surrogate species remains. If the vaporization of these species is calculated by means of a discrete species vaporization model, the computational costs still remain high. Tamim and Hallett (1995); Hallett (2000) proposed a vaporization model in which the composition of mixtures with a large number of components is described by means of probability density functions rather than as a series of discrete components. The number of variables is reduced to a few distribution parameters while the entire spectrum from light to heavier components in the mixture is considered. Hence, vaporization can be accurately described and the computational costs kept at reasonable levels. By means of this model, Le Clercq and Bellan (2004, 2005) performed direct numerical simulations of the evaporation of gasoline, diesel and three types of kerosene (Jet A, RP-1, JP-7) in gaseous mixing layers laden with liquid drops.

As the simulation of sprays in combustion chambers involves a large number of droplets, the resolution of the internal flow as well as the temperature and species distribution within the droplet involves high computational costs. Hence, the focus is put on the uniform temperature model of Abramzon and Sirignano (1989) within this work. Formulations of this model for liquid mixtures consisting of discrete species (see section 2.3.3.2) and for liquid mixtures represented by probability density functions (see section 2.3.3.3) are used. Droplet-droplet interactions are neglected as the spacing between droplets in combustion chambers of aero-engines is rather large, besides in the primary atomization zone (Faeth, 1983).

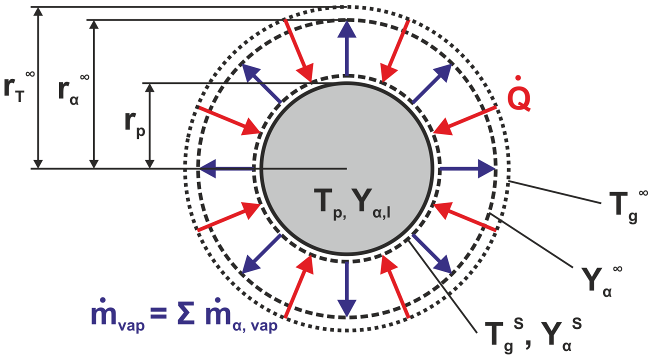

Figure 2.12.: Sketch of the evaporation in quiescent ambience (spherically symmetric solution)

2.3.3.2. Evaporation model for discrete species

Derivation of the vapor mass flow rate Writing the mass and species mass conservation equations (Eq. 2.2.1 and 2.2.2) in spherical coordinates (r, θ, ϕ) yields (Kuo and Acharya, 2012):

$$\frac{\partial \rho}{\partial t} + \frac{1}{r^2}\frac{\partial}{\partial r}\left(\rho u_r r^2\right) + \frac{1}{r sin\theta}\frac{\partial}{\partial \theta}\left(\rho u_\theta sin\theta\right) + \frac{1}{r sin\theta}\frac{\partial}{\partial \phi}\left(\rho u_\phi\right) = 0 \tag{2.3.151}$$

$$\begin{aligned} &\frac{\partial}{\partial t}\left(\rho Y_\alpha\right) + \frac{1}{r^2}\frac{\partial}{\partial r}\left(\rho u_r Y_\alpha r^2\right) + \frac{1}{r sin\theta}\frac{\partial}{\partial \theta}\left(\rho u_\theta Y_\alpha sin\theta\right) + \frac{1}{r sin\theta}\frac{\partial}{\partial \phi}\left(\rho u_\phi Y_\alpha\right) \\ &\quad + \frac{1}{r^2}\frac{\partial}{\partial r}\left(j_{\alpha r} r^2\right) + \frac{1}{r sin\theta}\frac{\partial}{\partial \theta}\left(j_{\alpha\theta} sin\theta\right) + \frac{1}{r sin\theta}\frac{\partial j_{\alpha\phi}}{\partial \phi} = S_{Y_\alpha} \end{aligned} \tag{2.3.152}$$

with $r \geq 0$, $0 \leq \theta \leq \pi$ and $0 \leq \phi \leq 2\pi$. In the limiting case of zero relative velocity, the solution is spherically symmetric and a so-called Stefan flow exclusively in radial direction evolves. Furthermore, as the heating of the liquid is much slower than the one of the gas, a quasi-steadiness in the gas phase can be assumed. Omitting time derivatives as well as gradients in the direction of θ and ϕ, Eq. 2.3.151 and 2.3.152 reduce to:

$$\frac{1}{r^2}\frac{\partial}{\partial r}\left(\rho u_r r^2\right) = 0 \tag{2.3.153}$$

$$\frac{1}{r^2}\frac{\partial}{\partial r}\left(\rho u_r Y_\alpha r^2 + j_{\alpha r} r^2\right) = 0 \tag{2.3.154}$$

Integrating both equations gives:

$$\rho u_r r^2 = const. \tag{2.3.155}$$

$$\rho u_r Y_\alpha r^2 + j_{\alpha r} r^2 = const. \tag{2.3.156}$$

The constants can be determined from a mass and species mass balance at the droplet surface:

$$4\pi r^2 \rho u_r = \dot{m}_{vap} \tag{2.3.157}$$

$$4\pi r^2 \rho u_r Y_\alpha + 4\pi r^2 j_{\alpha r} = \dot{m}_{\alpha,vap} \tag{2.3.158}$$

with the vapor mass flux $\dot{m}_{\alpha,vap}$ of species α. Inserting Eq. 2.3.157, 2.3.158, 2.3.20 and Fick's law $j_{\alpha r} = -\rho_g D_\alpha \frac{\partial Y_\alpha}{\partial r}$ into 2.3.156 yields:

$$\dot{m}_{vap}\left(Y_\alpha - \zeta_\alpha\right) = 4\pi r^2 \rho_g D_\alpha \frac{\partial Y_\alpha}{\partial r} \tag{2.3.159}$$

Separating variables results in:

$$\frac{\dot{m}_{vap}}{4\pi\rho_g D_\alpha}\int_{r_p}^{r_\alpha^\infty}\frac{\partial r}{r^2} = \int_{Y_\alpha^S}^{Y_\alpha^\infty}\frac{\partial Y_\alpha}{Y_\alpha - \zeta_\alpha} \tag{2.3.160}$$

Integrating over the intervals $[r_p, r_\alpha^\infty]$ and $[Y_\alpha^S, Y_\alpha^\infty]$ yields:

$$\dot{m}_{vap} = 4\pi\frac{r_p r_\alpha^\infty}{r_\alpha^\infty - r_p}\rho_g D_\alpha ln\left(1 + \frac{Y_\alpha^S - Y_\alpha^\infty}{\zeta_\alpha - Y_\alpha^S}\right) \tag{2.3.161}$$

with Y_α^S and Y_α^∞ being the species mass fraction at the positions of the droplet surface r_p and in the surrounding gas phase with r^∞, respectively. The non-dimensional species mass transfer rate is called Sherwood number $Sh_{\alpha,L}$ of species α with respect to the characteristic length scale L and defined as (Sirignano, 2010):

$$Sh_{\alpha,L} = \frac{\left(\frac{\partial Y_\alpha}{\partial r}\right)^S}{\frac{Y_\alpha^S - Y_\alpha^\infty}{L}} \tag{2.3.162}$$

In analogy to the Sherwood number in a steady, diffusion-governed thin vapor film (Bird *et al.*, 2002) (see Appendix A), Abramzon and Sirignano (1989) defined a modified Sherwood number Sh_α of species α:

$$Sh_\alpha = 2\frac{r_\alpha^\infty}{r_\alpha^\infty - r_p} \tag{2.3.163}$$

with a characteristic length scale of $L = 2r_\alpha^\infty$. In order to account for the radial Stefan flow, they proposed a correction term for the empirical Sherwood number Sh_0:

$$Sh_\alpha = 2 + \frac{Sh_0 - 2}{F(B_M)} \tag{2.3.164}$$

with

$$F(B) = (1 + B)^{0.7}\frac{ln(1 + B)}{B} \tag{2.3.165}$$

and a limitation of B to the range $0 \leq B \leq 20$. B_M is the Spalding mass transfer number given by:

$$B_M = \frac{Y_\alpha^S - Y_\alpha^\infty}{\zeta_\alpha - Y_\alpha^S} = \frac{\sum_{\alpha=1}^{N_{sp}^S} Y_\alpha^S - \sum_{\alpha=1}^{N_{sp}^\infty} Y_\alpha^\infty}{1 - \sum_{\alpha=1}^{N_{sp}^S} Y_\alpha^S} \tag{2.3.166}$$

The equality in Eq. 2.3.166 can be shown by Eq. 2.3.20:

$$\sum_{\alpha=1}^{N_{sp}^S} \zeta_\alpha = \sum_{\alpha=1}^{N_{sp}^S} \left(Y_\alpha^S + \frac{Y_\alpha^S - Y_\alpha^\infty}{B_M} \right) = \sum_{\alpha=1}^{N_{sp}^S} Y_\alpha^S + \frac{\sum_{\alpha=1}^{N_{sp}^S} Y_\alpha^S - \sum_{\alpha=1}^{N_{sp}^\infty} Y_\alpha^\infty}{B_M} = 1 \tag{2.3.167}$$

For the Sherwood number Sh_0 the empirical correlations of Clift *et al.* (1978, pp. 121-124) are used:

$$Sh_0 = 1 + (1 + Re_{d_p} Sc_\alpha)^{\frac{1}{3}} \, f(Re_{d_p}) \tag{2.3.168}$$

with:

$$f(Re_{d_p}) = \begin{cases} 1 & \text{, for} \quad 0 \leq Re_{d_p} \leq 1 \\ Re_{d_p}^{0.41-\frac{1}{3}} & \text{, for} \quad 1 < Re_{d_p} \leq 100 \\ 0.752 Re_{d_p}^{0.472-\frac{1}{3}} & \text{, for} \quad 100 < Re_{d_p} \leq 2000 \\ 0.44 Re_{d_p}^{\frac{1}{2}-\frac{1}{3}} + 0.034 Re_{d_p}^{0.71-\frac{1}{3}} & \text{, for} \quad 2000 < Re_{d_p} \end{cases} \tag{2.3.169}$$

In Eq. 2.3.168, Sc_α is the non-dimensional Schmidt number (Eq. 2.2.24) and Re_L represents the non-dimensional Reynolds number, i.e. the ratio of inertial forces to viscous forces acting on the particle:

$$Re_L = \frac{|\vec{u}| L}{\nu_g} = \frac{\text{Inertial forces}}{\text{Viscous forces}} \tag{2.3.170}$$

with L and u being a characteristic length scale and velocity, respectively. In the equations above, L is replaced by the droplet diameter d_p and u by the relative velocity u_{rel} from Eq. 2.3.4. Substituting Eq. 2.3.163 and Eq. 2.3.166 in Eq. 2.3.161 yields the equation for the vapor mass flow rate:

$$\dot{m}_{vap} = 2\pi r_p Sh_\alpha \rho_g D_\alpha ln \left(1 + B_M\right) \tag{2.3.171}$$

The mass flow rate ratio is obtained by reorganizing Eq. 2.3.166:

$$\zeta_\alpha = Y_\alpha^S + \frac{Y_\alpha^S - Y_\alpha^\infty}{B_M} = \frac{Y_\alpha^S (1 + B_M) - Y_\alpha^\infty}{B_M} \tag{2.3.172}$$

Ambient and surface value of the species mass fraction The species mass fraction Y_α^∞ is provided by the gas flow solver while Y_α^S is calculated assuming thermodynamic equilibrium at the surface. In thermodynamic equilibrium, the partial pressure $p_{g,\alpha}$ equals the vapor pressure $p_{vap,\alpha}$ of species α in the mixture:

$$p_{g,\alpha} = p_{vap,\alpha} \tag{2.3.173}$$

Replacing the left hand side of Eq. 2.3.173 by Dalton's law of partial pressures and the right hand side by Raoult's law for partial vapor pressures in ideal mixtures (Poling *et al.*, 2001, chap. 8.4) results in:

$$X_\alpha^S \, p_g = X_{\alpha,l} \, p_{vap,\alpha}^* \tag{2.3.174}$$

with the species molar fraction at the surface X_α^S and in the liquid $X_{\alpha,l}$ as well as the vapor pressure $p^*_{\alpha,vap}$ of the pure component. The vapor pressure of the pure component is obtained from the Wagner equation (Poling *et al.*, 2001, chap. 7.3). Rearranging Eq. 2.3.174 yields:

$$X_\alpha^S = \frac{p^*_{vap,\alpha}}{p_g} X_{\alpha,l} \tag{2.3.175}$$

The species mass fraction Y_α can be obtained from the species molar fraction X_α by:

$$Y_\alpha = X_\alpha \frac{M_\alpha}{\bar{M}} = X_\alpha \frac{M_\alpha}{\sum_{\alpha=1}^{N_{sp}} (X_\alpha M_\alpha)} \tag{2.3.176}$$

Derivation of the heat flow rate In the following, the equation for the heat flow rate $\dot{Q}$ will be derived. Writing the energy conservation equation (Eq. 2.2.4) in spherical coordinates (r, θ, ϕ) yields (Bird *et al.*, 2002):

$$\begin{aligned}
&\frac{\partial \rho h}{\partial t} + \frac{1}{r^2}\frac{\partial}{\partial r}\left(\rho u_r h r^2\right) + \frac{1}{rsin\theta}\frac{\partial}{\partial \theta}\left(\rho u_\theta h sin\theta\right) + \frac{1}{rsin\theta}\frac{\partial}{\partial \phi}\left(\rho u_\phi h\right) \\
&+ \frac{1}{r^2}\frac{\partial}{\partial r}\left(q_r r^2\right) + \frac{1}{rsin\theta}\frac{\partial}{\partial \theta}\left(q_\theta sin\theta\right) + \frac{1}{rsin\theta}\frac{\partial q_\phi}{\partial \phi} \\
&- \tau_{rr}\frac{\partial u_r}{\partial r} - \tau_{r\theta}\left(\frac{1}{r}\frac{\partial u_r}{\partial \theta} - \frac{u_\theta}{r}\right) - \tau_{r\theta}\left(\frac{1}{rsin\theta}\frac{\partial u_r}{\partial \phi} - \frac{u_\phi}{r}\right) \\
&- \tau_{\theta r}\frac{\partial u_\theta}{\partial r} - \tau_{\theta\theta}\left(\frac{1}{r}\frac{\partial u_\theta}{\partial \theta} - \frac{u_r}{r}\right) - \tau_{\theta\phi}\left(\frac{1}{rsin\theta}\frac{\partial u_\theta}{\partial \phi} - \frac{u_\phi}{r}cot(\theta)\right) \\
&- \tau_{\phi r}\frac{\partial u_\phi}{\partial r} - \tau_{\phi\theta}\left(\frac{1}{r}\frac{\partial u_\theta}{\partial \theta}\right) - \tau_{\phi\phi}\left(\frac{1}{rsin\theta}\frac{\partial u_\phi}{\partial \phi} + \frac{u_r}{r} + \frac{u_\theta}{r}cot(\theta)\right) \\
&= \frac{Dp}{dt} + S_r
\end{aligned} \tag{2.3.177}$$

Neglecting pressure gradients, viscous dissipation, radiation and assuming quasi-steadiness and spherical symmetry, Eq. 2.3.177 reduces to (Sirignano and Mehring, 2000):

$$\frac{1}{r^2}\frac{\partial}{\partial r}\left(\rho u_r h r^2 + q_r r^2\right) = 0 \tag{2.3.178}$$

Replacing the enthalpy by Eq. 2.2.18 and the energy flux q_r by Eq. 2.2.20 leads to:

$$\frac{1}{r^2}\frac{\partial}{\partial r}\left(\rho u_r r^2 \sum_{\alpha=1}^{N_{sp}} h_\alpha Y_\alpha - r^2 \lambda_g \frac{\partial T}{\partial r} + r^2 \sum_{\alpha=1}^{N_{sp}} h_\alpha j_{\alpha r}\right) = 0 \tag{2.3.179}$$

Rearranging gives:

$$\frac{1}{r^2}\frac{\partial}{\partial r}\left(\sum_{\alpha=1}^{N_{sp}} h_\alpha \left(\rho u_r r^2 Y_\alpha + r^2 j_{\alpha r}\right) - r^2 \lambda_g \frac{\partial T}{\partial r}\right) = 0 \tag{2.3.180}$$

Inserting Eq. 2.3.158 results in:

$$\frac{1}{r^2}\frac{\partial}{\partial r}\left(\frac{1}{4\pi}\sum_{\alpha=1}^{N_{sp}}\dot{m}_{\alpha,vap}h_\alpha - r^2\lambda_g\frac{\partial T}{\partial r}\right)=0 \tag{2.3.181}$$

Integrating yields:

$$\frac{1}{4\pi}\sum_{\alpha=1}^{N_{sp}}\dot{m}_{\alpha,vap}h_\alpha - r^2\lambda_g\frac{\partial T}{\partial r}=const. \tag{2.3.182}$$

At the droplet surface, the previous equation becomes:

$$\frac{1}{4\pi}\sum_{\alpha=1}^{N_{sp}}\dot{m}_{\alpha,vap}h_\alpha^S - r^2\lambda_g\left.\frac{\partial T}{\partial r}\right|_{r=r_p}=const. \tag{2.3.183}$$

with the conductive fluxes balancing the droplet heating and vaporization:

$$4\pi r^2\lambda_g\left.\frac{\partial T}{\partial r}\right|_{r=r_p}=\sum_{\alpha=1}^{N_{sp}}\dot{m}_{\alpha,vap}\mathit{\Delta} h_{vap,\alpha}+\dot{Q}_l \tag{2.3.184}$$

wherein $\mathit{\Delta} h_{vap,\alpha}$ is the specific enthalpy of vaporization and $\dot{Q}_l$ the droplet heating rate. Combining Eq. 2.3.183 and Eq. 2.3.184 the integration constant yields:

$$const.=\frac{1}{4\pi}\left(\sum_{\alpha=1}^{N_{sp}}\dot{m}_{\alpha,vap}h_\alpha^S-\sum_{\alpha=1}^{N_{sp}}\dot{m}_{\alpha,vap}\mathit{\Delta} h_{vap,\alpha}-\dot{Q}_l\right) \tag{2.3.185}$$

Inserting the constant into Eq. 2.3.182 and replacing the specific enthalpies h_α and h_α^S by Eq. 2.2.19 gives:

$$\sum_{\alpha=1}^{N_{sp}}\dot{m}_{\alpha,vap}c_{p,\alpha}\left(T_g-T_g^S\right)+\sum_{\alpha=1}^{N_{sp}}\dot{m}_{\alpha,vap}\mathit{\Delta} h_{vap,\alpha}+\dot{Q}_l=4\pi r^2\lambda_g\frac{\partial T}{\partial r} \tag{2.3.186}$$

Separating variables and introducing Eq. 2.3.20 results in:

$$\int_{r_p}^{r_T^\infty}\frac{\partial r}{4\pi r^2\lambda_g}=\int_{T_g^S}^{T_g^\infty}\frac{\partial T}{\dot{m}_{vap}\left(\sum_{\alpha=1}^{N_{sp}}\zeta_\alpha c_{p,\alpha}\left(T_g-T_g^S\right)+\sum_{\alpha=1}^{N_{sp}}\zeta_\alpha\mathit{\Delta} h_{vap,\alpha}+\frac{\dot{Q}_l}{\dot{m}_{vap}}\right)} \tag{2.3.187}$$

The integration over the intervals $[r_p, r_T^\infty]$ and $[T_g^S, T_g^\infty]$ yields:

$$\dot{m}_{vap}=4\pi\,\frac{r_p r_T^\infty}{r_T^\infty-r_p}\,\frac{\lambda_g}{\sum_{\alpha=1}^{N_{sp}}\zeta_\alpha c_{p,\alpha}}ln\left(1+\frac{\sum_{\alpha=1}^{N_{sp}}\zeta_\alpha c_{p,\alpha}\left(T_g^\infty-T_g^S\right)}{\sum_{\alpha=1}^{N_{sp}}\zeta_\alpha\mathit{\Delta} h_{vap,\alpha}+\frac{\dot{Q}_l}{\dot{m}_{vap}}}\right) \tag{2.3.188}$$

In analogy to the Sherwood number, the modified Nusselt number Nu accounting for the Stefan flow, as stated in Abramzon and Sirignano (1989), is used:

$$Nu = 2\frac{r_p r_T^{\infty}}{r_T^{\infty} - r_p} = 2 + \frac{Nu_0 - 2}{F(B_T)} \tag{2.3.189}$$

with $F(B_T)$ according to Eq. 2.3.165. The Nusselt number is the non-dimensional heat transfer rate (Baehr and Stephan, 2006) defined as:

$$Nu = \frac{\alpha_T L}{\lambda} \tag{2.3.190}$$

wherein L is a characteristic length scale and α_T represents the heat transfer coefficient:

$$\alpha_T = -\lambda \frac{\left(\frac{\partial T}{\partial r}\right)^S}{T^S - T^{\infty}} \tag{2.3.191}$$

The Spalding heat transfer number B_T for a multi-component fuel droplet is defined by:

$$B_T = \frac{\sum_{\alpha=1}^{N_{sp}} \zeta_\alpha c_{p,\alpha} \left(T_g^{\infty} - T_g^S\right)}{\sum_{\alpha=1}^{N_{sp}} \zeta_\alpha \Delta h_{vap,\alpha} + \frac{\dot{Q}_l}{\dot{m}_{vap}}} \tag{2.3.192}$$

The Nusselt number Nu_0 without Stefan flow is determined according to the empirical correlations of Clift *et al.* (1978):

$$Nu_0 = 1 + \left(1 + \left(Re_{d_p} Pr_g\right)^{\frac{1}{3}}\right) \cdot f(Re_{d_p}) \tag{2.3.193}$$

with $f(Re_{d_p})$ according to Eq. 2.3.169. In Eq. 2.3.193, Pr_g is the non-dimensional Prandtl number defined in Eq. 2.2.21. With Eq. 2.3.189 and Eq. 2.3.192, Eq. 2.3.188 can be written as:

$$\dot{m}_{vap} = 2\pi r_p Nu \; \frac{\lambda_g}{\sum_{\alpha=1}^{N_{sp}} \zeta_\alpha c_{p,\alpha}} ln\left(1 + B_T\right) \tag{2.3.194}$$

Equating the two equations for the surface mass flux (Eq. 2.3.171 and Eq. 2.3.194), a relationship between the Spalding mass transfer number B_M and the Spalding heat transfer number B_T can be derived:

$$B_T = \left(1 + B_M\right)^{\phi} - 1 \tag{2.3.195}$$

with the exponent ϕ being:

$$\phi = \frac{Sh_\alpha}{Nu} \frac{\rho_g D_\alpha}{\lambda_g} \sum_{\alpha=1}^{N_{sp}} \zeta_\alpha c_{p,\alpha} \tag{2.3.196}$$

As the value of B_T is needed to calculate Nu, an iterative method is used to determine B_T and Nu. Computational costs were reduced by means of lookup tables. Finally, the droplet heating rate $\dot{Q}_l$ can be calculated by rearranging Eq. 2.3.192:

$$\dot{Q}_l = \dot{m}_{vap} \left(\frac{\sum_{\alpha=1}^{N_{sp}} \zeta_\alpha c_{p,\alpha} \left(T_g^\infty - T_g^S \right)}{B_T} - \sum_{\alpha=1}^{N_{sp}} \zeta_\alpha \Delta h_{vap,\alpha} \right) \tag{2.3.197}$$

The entire heat flow rate $\dot{Q}$ as defined in the ODE for the change in droplet temperature (Eq. 2.3.30) is then given by:

$$\dot{Q} = \dot{m}_{vap} \frac{\sum_{\alpha=1}^{N_{sp}} \zeta_\alpha c_{p,\alpha} \left(T_g^\infty - T_g^S \right)}{B_T} \tag{2.3.198}$$

Physical properties In the derivations of the equations above, the physical properties were assumed to be constant and independent of location and temperature. In order to compensate for this shortcoming, it is commonly accepted (Miller *et al.*, 1998) to evaluate the physical properties at a characteristic reference state. The physical properties of the vapor are calculated at the reference conditions known as the "1/3 rule" originally proposed by Hubbard *et al.* (1975) and recommended by Yuen and Chen (1976); Abramzon and Sirignano (1989); Miller *et al.* (1998) and Chrigui *et al.* (2014):

$$T_{ref} = T_g^S + \frac{1}{3} \left(T_g^\infty - T_g^S \right) \tag{2.3.199}$$

$$Y_{\alpha,ref} = Y_\alpha^S + \frac{1}{3} \left(Y_\alpha^\infty - Y_\alpha^S \right) \tag{2.3.200}$$

Effect of sub-grid scale fluctuations on heat and mass transfer Besides the effect of velocity modulation described in section 2.3.2, the enhanced mixing due to the turbulent fluctuations around the droplet increase the heat and mass transfer. In order to incorporate the influence of the unresolved, sub-grid scale fluctuations on the heat and mass transfer, empirical correlations describing the effect of turbulence intensity Tu on the average Nusselt number Nu from Clift *et al.* (1978, pp. 266-271) were used. While the local Nusselt number in the experiments for spheres and cylinders varied, the average Nusselt number increased with turbulence intensity for all Reynolds numbers. A fit to the experimental data gave a linear relationship between Nu and Tu (Clift *et al.*, 1978, p. 270) at a fixed Reynolds number:

$$Nu = Nu_0 \cdot \left(1.0 + 4.8 \cdot 10^{-4} Re_{d_p}^{0.57} \frac{Tu}{Tu_c} \right) \tag{2.3.201}$$

The turbulence intensity is calculated from the turbulent kinetic energy in the sub-grid scales following Clift *et al.* (1978, p. 266):

$$Tu = \frac{2k_{sgs}}{|\vec{u}_{rel}|} \tag{2.3.202}$$

The critical turbulence intensity is given by (Clift *et al.*, 1978, p. 267):

$$Tu_c = \begin{cases} \frac{5.562 - log(Re_{d_p})}{16.4} & \text{for} \quad Tu_c \leq 0.15 \\ \frac{3.371 - log(Re_{d_p})}{1.75} & \text{for} \quad Tu_c > 0.15 \end{cases}$$

2.3.3.3. Evaporation model for multi-component mixtures

The evaporation model for multi-component mixtures used within this study approximates the discrete species distribution by a continuous description via probability density functions. Typical distribution parameters are the molar mass, carbon atom number or normal boiling point, depending on accurate and available experimental data. According to their molecular structure, the components ranging from C_6 to C_{17} are grouped into a PDF f_j for each of the four main fuel families, i.e. chemical-classes (n-alkanes, iso-alkanes, cyclo-alkanes, and mono-aromatics). Figure 2.13 shows the chemical composition of the fuel as measured by a GCxGC system (bars) and the approximation by the PDFs (lines). The molar mass is used as distribution parameter. In the following, the concept of the continuous thermodynamics model (CTM) will be explained using the molar mass as distribution parameter. The total molar mass X_j of a family j results from the sum over the molar masses X_i of species i contained in j:

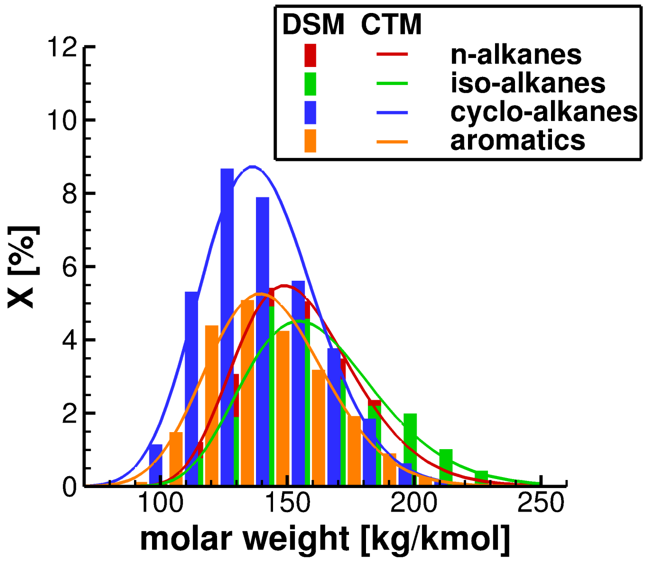

Figure 2.13.: Discrete species distribution from GCxGC measurement (bars) and the approximation by the continuous thermodynamics model (lines) for Jet A-1

$$X_j = \sum_{i \in j} X_i \tag{2.3.203}$$

Vice versa, the molar mass of an individual species is obtained by:

$$X_i = X_j f_j(I) \mathit{\Delta} I \approx X_j f_j(I) dI \tag{2.3.204}$$

The PDF of each family needs to follow the normalization condition:

$$\int_0^\infty f_j(I) dI = 1 \tag{2.3.205}$$

Whitson (1983) showed that mixtures of hydrocarbons can be accurately described by:

$$f_j(I) = \frac{(I - \gamma_j)^{\alpha_j - 1}}{\beta_j^{\alpha_j} \Gamma(\alpha_j)} e^{\frac{I - \gamma_j}{\beta_j}} \tag{2.3.206}$$

with the origin of the PDF γ_j as well as the parameters α_j and β_j describing the shape of the distribution. $\Gamma(\alpha_j)$ represents the Γ-function given by:

$$\Gamma(\alpha_j) = \int_0^\infty t^{\alpha_j - 1} e^{-t} dt \tag{2.3.207}$$

The n-th moment of a function $f(x)$ about a value c is defined as:

$$\mu_n = \int_{-\infty}^{\infty} (x - c)^n f(x)\, dx \tag{2.3.208}$$

The mean θ_j for a family j is given by the first moment with $c = 0$:

$$\theta_j = \int_\gamma^\infty I f(I)\, dI \tag{2.3.209}$$

The second moment ψ_j for a family j yields:

$$\psi_j = \int_\gamma^\infty I^2 f(I)\, dI \tag{2.3.210}$$

The variance σ_j^2 is given by the second central moment (central moments are moments about the mean, i.e. $c = \theta_j$):

$$\sigma_j^2 = \int_\gamma^\infty (I - \theta_j)^2 f(I)\, dI \tag{2.3.211}$$

With these definitions, the following relations between the parameters θ_j, ψ_j and σ_j^2 and the distribution parameters α_j and β_j can be inferred:

$$\begin{aligned} \theta_j &= \alpha_j \beta_j + \gamma_j \\ \sigma_j^2 &= \alpha_j \beta_j^2 \\ \psi_j &= \theta_j^2 + \sigma_j^2 \end{aligned} \tag{2.3.212}$$

A drawback of presuming a distribution function is that the shape is a priori fixed and cannot change during run-time. Alternatively, the PDF can be described by a Fourier series as shown by Doué *et al.* (2006); Le Clercq *et al.* (2009) allowing for complexly shaped PDFs. This is especially advantageous in case of condensation. Unfortunately, the description by Fourier series is prone to oscillations tending to under- and overshoot the mole or mass fraction boundaries of $[0; 1]$. Due to this fact and due to lower computational costs (3-6 Fourier coefficients needed in the Fourier approach), the presumed PDF approach was preferred within the work at hand.

Gas phase analysis Subsequent to the basic definitions above, the equation for the vaporizing mass flow rate will be derived following Rachner and Doué (2009). Replacing ζ_α by Eq. 2.3.172 in Eq. 2.3.159 yields:

$$\dot{m}_{vap}\left(Y_{\alpha,g}-\frac{Y_{\alpha,g}^{\infty}-Y_{\alpha,g}^{S}\left(1+B_M\right)}{B_M}\right)=4\pi r^2\rho_g D_\alpha\frac{\partial Y_\alpha}{\partial r} \tag{2.3.213}$$

Inserting Eq. 2.3.176 and Eq. 2.3.204 into Eq. 2.3.213 gives:

$$\dot{m}_{vap}\left(\frac{X_{j,g}f_{j,g}(I)}{\bar{M}_g}-\frac{\frac{X_{j,g}^{\infty}f_{j,g}^{\infty}(I)}{\bar{M}_g^{\infty}}-\frac{X_{j,g}^{S}f_{j,g}^{S}(I)}{\bar{M}_g^{S}}\left(1+B_M\right)}{B_M}\right)M_i(I)dI=4\pi r^2\rho_g D_\alpha\frac{\partial}{\partial r}\left(\frac{X_{j,g}f_{j,g}(I)}{\bar{M}_g}\right) \tag{2.3.214}$$

Integrating over the interval $I\in[\gamma;\infty]$ yields:

$$\dot{m}_{vap}\left(\frac{X_{j,g}\bar{M}_{j,g}}{\bar{M}_g}-\frac{\frac{X_{j,g}^{\infty}\bar{M}_{j,g}^{\infty}}{\bar{M}_g^{\infty}}-\frac{X_{j,g}^{S}\bar{M}_{j,g}^{S}}{\bar{M}_g^{S}}\left(1+B_M\right)}{B_M}\right)=4\pi r^2\rho_g D_\alpha\frac{\partial}{\partial r}\left(\frac{X_{j,g}\bar{M}_{j,g}}{\bar{M}_g}\right) \tag{2.3.215}$$

with the mean molar weight $\bar{M}_{j,g}$ of family j in the gas phase. Inserting $Y_{j,g}=X_{j,g}\bar{M}_{j,g}/\bar{M}_g$ into Eq. 2.3.215 results in:

$$\dot{m}_{vap}\left(Y_{j,g}-\frac{Y_{j,g}^{\infty}-Y_{j,g}^{S}\left(1+B_M\right)}{B_M}\right)=4\pi r^2\rho_g D_\alpha\frac{\partial Y_j}{\partial r} \tag{2.3.216}$$

As Eq. 2.3.216 is equivalent to Eq. 2.3.213, the vaporizing mass flow rate follows the same equation as derived for discrete species (section 2.3.3.2) replacing the index α for the species by j for the family:

$$\dot{m}_{vap}=2\pi r_p Sh_\alpha\rho_g D_\alpha ln\left(1+B_M\right) \tag{2.3.217}$$

with

$$B_M=\frac{Y_j^S-Y_j^{\infty}}{\zeta_j-Y_j^S}=\frac{\sum_{j=1}^{N_j^S}Y_j^S-\sum_{j=1}^{N_j^{\infty}}Y_j^{\infty}}{1-\sum_{\alpha=1}^{N_j^S}Y_j^S} \tag{2.3.218}$$

and

$$\zeta_j=\sum_{i\in j}\zeta_i=\frac{\dot{m}_{j,vap}}{\dot{m}_{vap}} \tag{2.3.219}$$

Droplet composition With the analysis of the gaseous phase being concluded, the ordinary differential equations for the change in composition of the liquid mixture will be derived following Rachner and Doué (2009). The starting point is Eq. 2.3.166 inserted into Eq. 2.3.19. This yields:

$$\frac{dY_{\alpha,l}}{dt}=\frac{6\ \dot{m}_{vap}}{\rho_l\pi d_p^3}\left(Y_{\alpha,l}+\frac{Y_{\alpha,l}^{\infty}-Y_{\alpha,l}^{S}\left(1+B_M\right)}{B_M}\right) \tag{2.3.220}$$

Inserting Eq. 2.3.176 and Eq. 2.3.204 into Eq. 2.3.220 gives:

$$\frac{d}{dt}\left(\frac{X_{j,l}f_{j,l}(I)M_i dI}{\bar{M}_l}\right)=\frac{6\,\dot{m}_{vap}}{\rho_l\pi d_p^3}\left(\frac{X_{j,l}f_{j,l}(I)}{\bar{M}_l}+\frac{\frac{X_{j,g}^{\infty}f_{j,g}^{\infty}(I)}{\bar{M}_g^{\infty}}-\frac{X_{j,g}^{S}f_{j,g}^{S}(I)}{\bar{M}_g^{S}}(1+B_M)}{B_M}\right)M_i(I)dI \tag{2.3.221}$$

Integrating over the interval $I\in[\gamma;\infty]$ with a weighting function w results in:

$$\begin{aligned}&\frac{d}{dt}\left(\frac{X_{j,l}\int_{\gamma}^{\infty}f_{j,l}(I)M_i w_j dI}{\bar{M}_l}\right)\\ =&\frac{6\,\dot{m}_{vap}}{\rho_l\pi d_p^3}\int_{\gamma}^{\infty}\left(\frac{X_{j,l}f_{j,l}(I)}{\bar{M}_l}+\frac{\frac{X_{j,g}^{\infty}f_{j,g}^{\infty}(I)}{\bar{M}_g^{\infty}}-\frac{X_{j,g}^{S}f_{j,g}^{S}(I)}{\bar{M}_g^{S}}(1+B_M)}{B_M}\right)M_i(I)w_j dI\end{aligned} \tag{2.3.222}$$

For $w_j=1$ and with $\int_{\gamma}^{\infty}f_{j,l}(I)M_i dI=\bar{M}_j$ and $Y_i=X_j\bar{M}_j/\bar{M}$, a formulation identical to Eq. 2.3.220 is obtained for the change in composition of family j:

$$\frac{dY_{j,l}}{dt}=\frac{6\,\dot{m}_{vap}}{\rho_l\pi d_p^3}\left(Y_{j,l}+\frac{Y_{j,l}^{\infty}-Y_{j,l}^{S}(1+B_M)}{B_M}\right) \tag{2.3.223}$$

Analogously, for $w=1/M_j(I)$, $w=I/M_j(I)$ and $w=I^2/M_j(I)$ the integration of Eq. 2.3.222 yields :

$$\frac{d}{dt}\left(\frac{Y_{j,l}}{\bar{M}_{j,l}}\right)=\frac{6\,\dot{m}_{vap}}{\rho_l\pi d_p^3}\left(\frac{Y_{j,l}}{\bar{M}_{j,l}}+\frac{\frac{Y_{j,g}^{\infty}}{\bar{M}_{g,l}^{\infty}}-\frac{Y_{j,g}^{S}}{\bar{M}_{j,g}^{S}}(1+B_M)}{B_M}\right) \tag{2.3.224}$$

$$\frac{d}{dt}\left(\frac{Y_{j,l}\theta_{j,l}}{\bar{M}_{j,l}}\right)=\frac{6\,\dot{m}_{vap}}{\rho_l\pi d_p^3}\left(\frac{Y_{j,l}\theta_{j,l}}{\bar{M}_{j,l}}+\frac{\frac{Y_{j,g}^{\infty}\theta_{j,g}^{\infty}}{\bar{M}_{g,l}^{\infty}}-\frac{Y_{j,g}^{S}\theta_{j,g}^{S}}{\bar{M}_{j,g}^{S}}(1+B_M)}{B_M}\right) \tag{2.3.225}$$

$$\frac{d}{dt}\left(\frac{Y_{j,l}\psi_{j,l}}{\bar{M}_{j,l}}\right)=\frac{6\,\dot{m}_{vap}}{\rho_l\pi d_p^3}\left(\frac{Y_{j,l}\psi_{j,l}}{\bar{M}_{j,l}}+\frac{\frac{Y_{j,g}^{\infty}\psi_{j,g}^{\infty}}{\bar{M}_{g,l}^{\infty}}-\frac{Y_{j,g}^{S}\psi_{j,g}^{S}}{\bar{M}_{j,g}^{S}}(1+B_M)}{B_M}\right) \tag{2.3.226}$$

Expanding the left hand side of Eq. 2.3.225 and Eq. 2.3.226, inserting Eq. 2.3.224 and rearranging yields the ODEs for the distribution parameters:

$$\frac{d\theta_{j,l}}{dt}=\frac{6\,\dot{m}_{vap}}{\rho_l\pi d_p^3}\frac{\bar{M}_{j,l}}{Y_{j,l}B_M}\left(\frac{Y_{j,g}^{\infty}\left(\theta_{j,g}^{\infty}-\theta_{j,l}\right)}{\bar{M}_{j,g}^{\infty}}-\frac{Y_{j,g}^{S}\left(\theta_{j,g}^{S}-\theta_{j,l}\right)}{\bar{M}_{j,g}^{S}}(1+B_M)\right) \tag{2.3.227}$$

$$\frac{d\psi_{j,l}}{dt}=\frac{6\,\dot{m}_{vap}}{\rho_l\pi d_p^3}\frac{\bar{M}_{j,l}}{Y_{j,l}B_M}\left(\frac{Y_{j,g}^{\infty}\left(\psi_{j,g}^{\infty}-\psi_{j,l}\right)}{\bar{M}_{j,g}^{\infty}}-\frac{Y_{j,g}^{S}\left(\psi_{j,g}^{S}-\psi_{j,l}\right)}{\bar{M}_{j,g}^{S}}(1+B_M)\right) \tag{2.3.228}$$

With the above relations, the composition can now be computed by the first and second moments and the (N_j-1) mass fractions (Eq. 2.3.223) of the j families.

Droplet temperature The change in droplet temperature for a mixture is derived starting from Eq. 2.3.30:

$$\frac{dT_p}{dt} = -\frac{1}{c_{p_l}} \frac{6}{\rho_l \pi d_p^3} \left(\dot{m}_{vap} \sum_{\alpha=1}^{N_{sp}} \zeta_\alpha \Delta h_{vap,\alpha} + \dot{Q} \right) \tag{2.3.229}$$

Replacing ζ_α by Eq. 2.3.172, $\dot{Q}$ by Eq. 2.3.198 and the mass fractions by the mole fractions (Eq. 2.3.176) yields:

$$\frac{dT_p}{dt} = -\frac{1}{c_{p_l}} \frac{6\dot{m}_{vap}}{\rho_l \pi d_p^3} \left(\sum_{\alpha=1}^{N_{sp}} \left(\frac{X_{\alpha,g}^S M_\alpha}{\bar{M}_g^S B_M}(1+B_M) - \frac{X_{\alpha,g}^\infty M_\alpha}{\bar{M}_g^\infty B_M} \right) \left(\Delta h_{vap,\alpha} - \frac{c_{p,\alpha}\left(T_g^\infty - T_g^S\right)}{B_T} \right) \right) \tag{2.3.230}$$

In the next step, the continuous representation for the mole fraction (Eq. 2.3.204) is inserted. The specific heat of evaporation and the specific isobaric heat capacities are replaced by their molar PDF-representation $\Delta h_{vap,\alpha} = \Delta H_{vap,\alpha}(T_l, I_i)/M_j(I_i)$ and $c_{p,\alpha} = C_{p,\alpha}(T_{ref}, I_i)/M_j(I_i)$, respectively:

$$\begin{aligned} \frac{dT_p}{dt} = -\frac{1}{c_{p_l}} \frac{6\dot{m}_{vap}}{\rho_l \pi d_p^3} \sum_j \sum_{i\in j} & \left(\frac{X_{j,g}^S f_{j,g}^S(I_i)(1+B_M)}{\bar{M}_g^S B_M} - \frac{X_{j,g}^\infty f_{j,g}^\infty(I_i)}{\bar{M}_g^\infty B_M} \right) \\ & \cdot \left(\Delta H_{vap,j}(T_l, I_i)\Delta I_i - \frac{C_{p,j}(T_{ref}, I_i)\Delta I_i \left(T_g^\infty - T_g^S\right)}{B_T} \right) \end{aligned} \tag{2.3.231}$$

The following abbreviations are brought in:

$$\begin{aligned} \Delta\hat{h}_{vap,j} &= \sum_{i\in j} \left(\frac{X_{j,g}^S f_{j,g}^S(I_i)(1+B_M)}{\bar{M}_g^S B_M} - \frac{X_{j,g}^\infty f_{j,g}^\infty(I_i)}{\bar{M}_g^\infty B_M} \right) \Delta H_{vap,j}(T_l, I_i)\Delta I_i \\ &\approx \int_{\gamma_j}^\infty \left(\frac{X_{j,g}^S f_{j,g}^S(I_i)(1+B_M)}{\bar{M}_g^S B_M} - \frac{X_{j,g}^\infty f_{j,g}^\infty(I_i)}{\bar{M}_g^\infty B_M} \right) \Delta H_{vap,j}(T_l, I_i) dI \end{aligned} \tag{2.3.232}$$

$$\begin{aligned} \hat{c}_{p,j} &= \sum_{i\in j} \left(\frac{X_{j,g}^S f_{j,g}^S(I_i)(1+B_M)}{\bar{M}_g^S B_M} - \frac{X_{j,g}^\infty f_{j,g}^\infty(I_i)}{\bar{M}_g^\infty B_M} \right) C_{p,j}(T_{ref}, I_i)\Delta I_i \\ &\approx \int_{\gamma_j}^\infty \left(\frac{X_{j,g}^S f_{j,g}^S(I_i)(1+B_M)}{\bar{M}_g^S B_M} - \frac{X_{j,g}^\infty f_{j,g}^\infty(I_i)}{\bar{M}_g^\infty B_M} \right) C_{p,j}(T_{ref}, I_i) dI \end{aligned} \tag{2.3.233}$$

With the above abbreviations Eq. 2.3.231 reduces to the ODE for the change in liquid temperature:

$$\frac{dT_p}{dt} = -\frac{1}{c_{p_l}} \frac{6\dot{m}_{vap}}{\rho_l \pi d_p^3} \sum_j \left(\Delta\hat{h}_{vap,j} - \frac{\hat{c}_{p,j}\left(T_g^\infty - T_g^S\right)}{B_T} \right) \tag{2.3.234}$$

In the equations derived above, several physical properties are needed in a continuous form. The used correlations can be found in appendix B.

2.3.4. Spray source terms

Due to the presence of the spray, additional source terms for mass, momentum, energy and species arise on the right hand side of Eq. 2.2.8, Eq. 2.2.9, Eq. 2.2.17 and Eq.2.2.22, respectively. The filtered source terms result from the contribution S^p_ϕ of each individual parcel p located at $\vec{x}_p$ (Leboissetier *et al.*, 2005):

$$\bar{S}^d_\phi(\vec{x},t) = \int_\Omega S^p_\phi(\vec{x},t)\ \delta(\vec{x}_p - \vec{x})\ G(\vec{x} - \vec{y}; \Delta\vec{x})\ d\vec{y} \tag{2.3.235}$$

with the Dirac delta function $\delta(\vec{x}_p - \vec{x})$ limiting the source term to the parcel's position $\vec{x}_p$. For a top-hat or box filter like the implicit filtering by the discretization used within this work, the exact solution for the filtered source terms can be stated as:

$$\bar{S}^d_\phi(\vec{x},t) = \frac{1}{V_f}\sum_{p=1}^{N_p} S^p_\phi(\vec{x},t) \tag{2.3.236}$$

This represents the volume-average of N_p parcels in the filter volume V_f. In case of implicit filtering by the discretization, the filter volume V_f is equivalent to the cell volume V_{cell}.

Mass source terms The mass change of the particles due to evaporation or condensation leads to a mass source or sink term in the gas field equations:

$$\bar{S}^d_\rho(\vec{x},t) = -\frac{1}{V_f}\sum_{p=1}^{N_p} \frac{dm_p}{dt} \tag{2.3.237}$$

$$\bar{S}^d_\alpha(\vec{x},t) = -\frac{1}{V_f}\sum_{p=1}^{N_p} \frac{d(m_p Y_{\alpha,p})}{dt} \tag{2.3.238}$$

with the mass m_p of the parcel p and the liquid mass fraction $Y_{\alpha,p}$ of species α.

Momentum source term A momentum source term arises due to changes in the parcel's momentum along its trajectory and due to forces acting on the parcel during a gas flow time step:

$$\bar{S}^d_{\rho u}(\vec{x},t) = -\frac{1}{V_f}\sum_{p=1}^{N_p} \left(\frac{d(m_p\vec{u}_p)}{dt} - \vec{F}\right) \tag{2.3.239}$$

wherein $\vec{u_p}$ represents the particle velocity vector and the second term in Eq. 2.3.239 accounts for external forces $\vec{F}$ affecting the particle, e.g. the gravity force $\vec{F}_g = m_p\vec{g}$.

Energy source term The energy source term S^d_E yields:

$$\bar{S}^d_h(\vec{x},t) = -\frac{1}{V_f}\sum_{p=1}^{N_p} \left(\sum_{\alpha=1}^{N_{sp}} \frac{d(m_p Y_{\alpha,p} e^\alpha)}{dt} + \frac{d(\frac{1}{2}m_p|\vec{u}_p|^2)}{dt} - \vec{F}\cdot\vec{u}_p\right) \tag{2.3.240}$$

The first term on the right hand side of Eq. 2.3.240 is the change of internal energy e, the second term the change of kinetic energy and the third one the work of external forces acting on the particle. The data are exchanged online between the gaseous Eulerian phase and the liquid Lagrangian phase via an iterative two-way-coupling procedure.

3. Non-reactive test cases

The non-reactive test cases comprise sub-model tests for the atomization and dispersion models. In section 3.1, the liquid jet in cross-flow model described in section 2.3.1.1 is tested in a premixing duct. Section 3.2 covers the examination of the pre-filming airblast atomization model described in section 2.3.1.2 checked against measurements at the KIT-ITS. Chapter 3 is concluded in section 3.3 by a comparison of the dispersion models, which were specified in section 2.3.2, with experimental data in a particle-laden swirling flow.

3.1. Atomization of a liquid jet in cross-flow

Calibration and validation of the jet breakup model described in section 2.3.1.1 is based on a comparison to experiments carried out at the facilities of DLR Cologne (Becker and Hassa, 2002). In order to cover a large parameter range, the test case is computed with an unsteady RANS method on a coarse grid allowing for short turnaround times. The primary goal is to test the model in an unsteady environment before applying it to a rather costly LES. Besides these considerations, the author has no concerns related to the applicability to LES.

3.1.1. Test case description

The test rig shown in Fig. 3.1 consists of a medium pressure, high temperature test cell designed for three-way optical access. The dimensions of the rectangular channel are 180 mm x 25 mm x 40 mm. Medium pressure conditions up to 15 bars, air temperatures of 850 K and air velocities of about 120 m/s can be achieved. For a detailed description of the test rig the reader is referred to Brandt *et al.* (1998). The fuel jet composed of Jet A-1 enters the duct via a plain jet nozzle of 0.45 mm in diameter at a downstream distance of 155 mm from the main air inlet. The measurement techniques, which were applied, include time-resolved shadowgraphy, Mie-scattering laser techniques and Phase Doppler Anemometry (PDA). Fig. 3.2 shows shadowgraph images of the disintegrating jet corresponding to approximately 10 mm by 7.0 mm in reality. Associated test conditions are listed in Table 3.1.

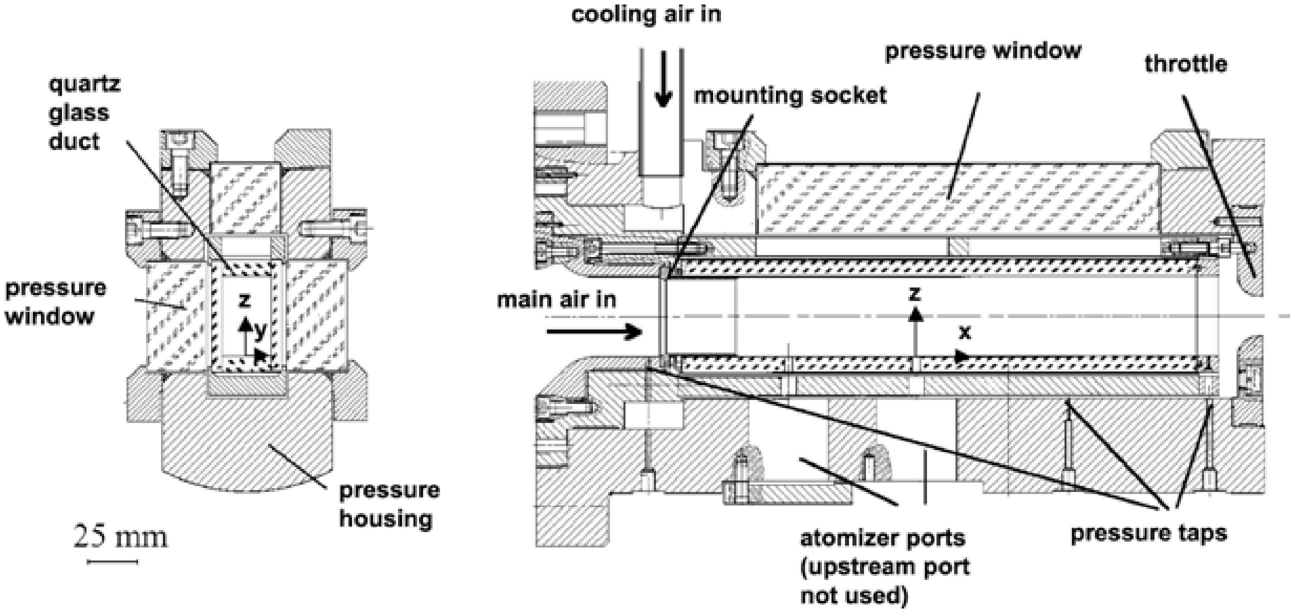

Figure 3.1.: Premix duct for spray measurements at DLR Cologne (from Brandt *et al.* (1998))

Test case id	**Air pressure** p_{air} $[bar]$	**Air temperature** T_{air} $[K]$	**Air density** ρ_{air} $[kg/m^3]$	**Air velocity** u_{air} $[m/s]$	**Momentum flux ratio** q [-]
baseline	5.8	280	7.19	100	6
q2	5.8	280	7.19	100	2
q18	5.8	280	7.19	100	18
p9	8.7	280	10.78	100	6
u75	5.9	285	7.18	75	6
u75q2	5.9	285	7.18	75	2

Table 3.1.: Boundary conditions of the jet in cross-flow experiment

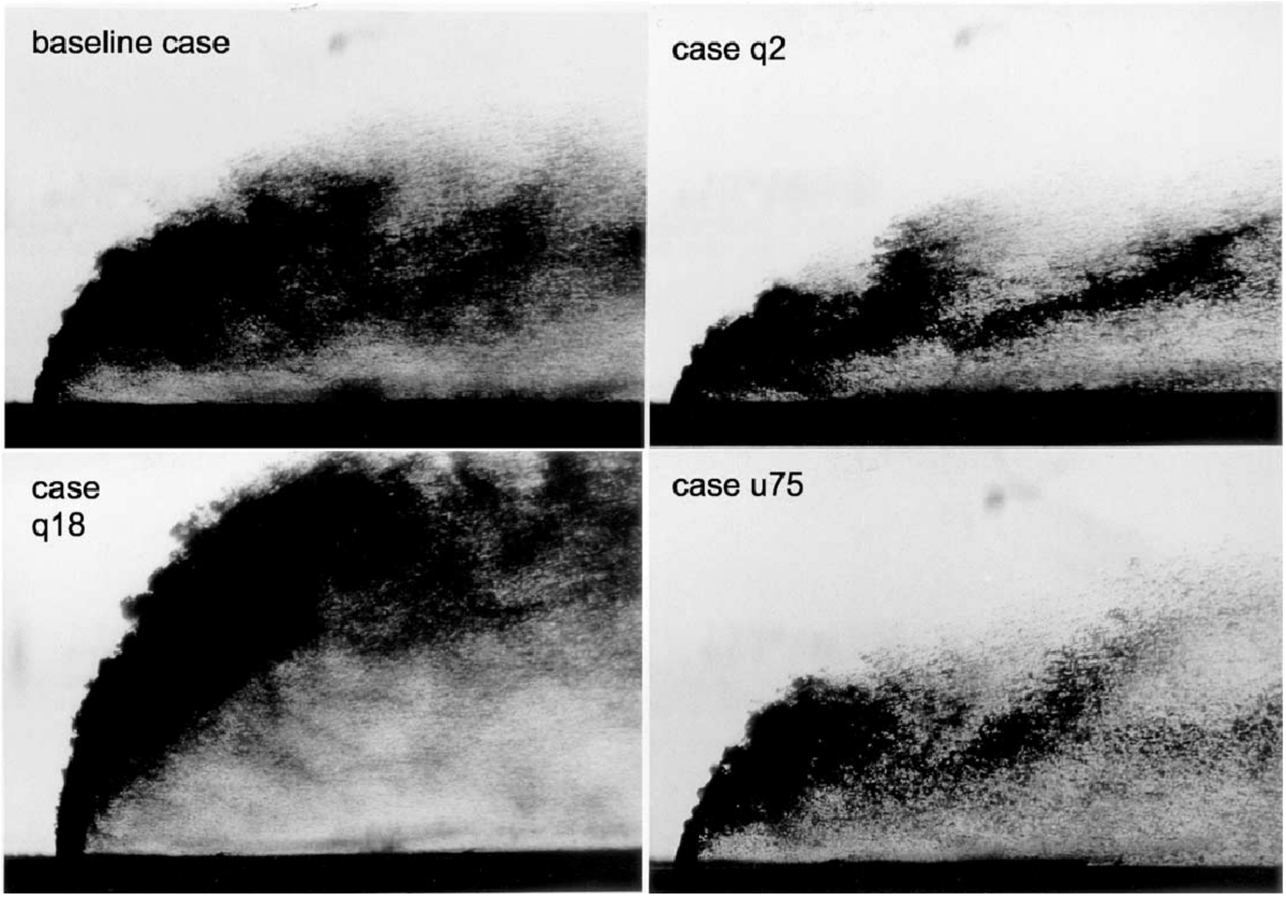

Figure 3.2.: Shadowgraph images of the disintegrating jet (from Rachner *et al.* (2002) and Eckel *et al.* (2016))

3.1.2. Numerical Setup

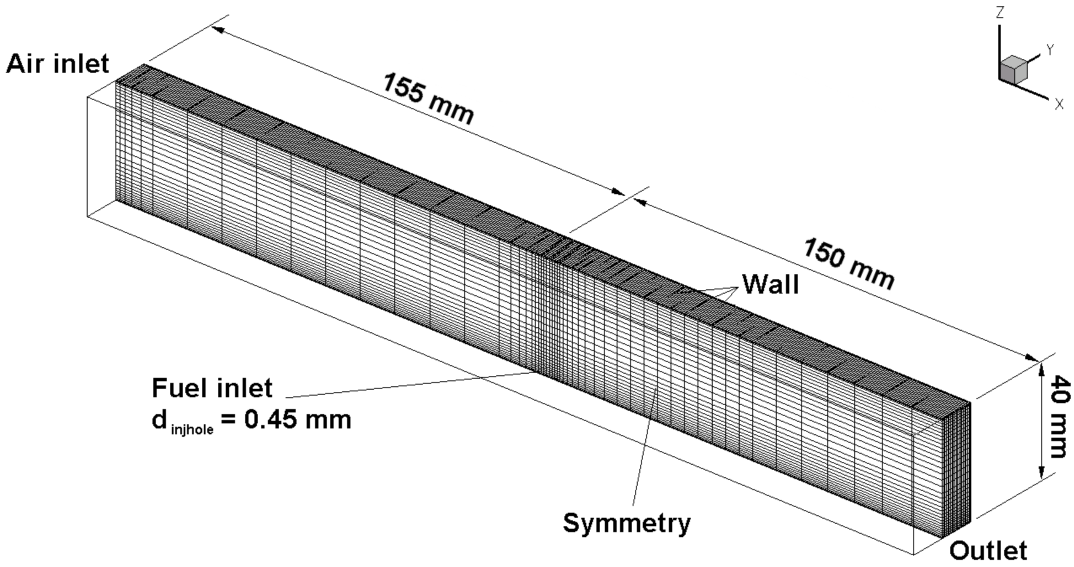

Figure 3.3.: Numerical discretization of the premix duct with boundary conditions (from Eckel *et al.* (2016))

The rectangular duct is discretized by structured, hexahedral mesh elements (Fig. 3.3). The mesh density is increased in the vicinity of the fuel injection orifice, which is located at the lower wall. In order to reduce computational costs, a symmetry condition is applied at the center plane (normal to the y-direction) of the duct. The gas phase (air) enters the domain at the air inlet 155 mm upstream of the plain jet nozzle with a constant velocity. At $x = 0$, the liquid phase (Jet A-1) issues from the fuel nozzle in the center plane. At the outlet an outflow boundary condition is applied. The dispersed phase solver SPRAYSIM described in subsection 2.3 is coupled to the gas phase solver THETA presented in subsection 2.2 by an iterative two-way-coupling procedure. A projection method is used to couple pressure and velocity. For the spatial discretization, second-order upwind and central schemes are used for convective and diffusive terms, respectively. A second-order three point backward method is applied for the temporal evolution. Turbulence is modeled by a standard $k - \epsilon$ turbulence model (Wilcox, 1994). The dispersion model of Gosman and Ioannides (1983) is applied for the droplet dispersion.

3.1.3. Results

The jet breakup model is calibrated by means of comparisons between the experiments and the computational results at baseline conditions. Subsequently, it is applied with the same set of model parameters to a diversity of test conditions, i.e. a variation in air pressure p_{air} and hence air density ρ_{air}, air velocity u_{air} as well as the momentum flux ratio q (see Table 3.1). The momentum flux ratio, which is the main parameter controlling the breakup of liquid jets

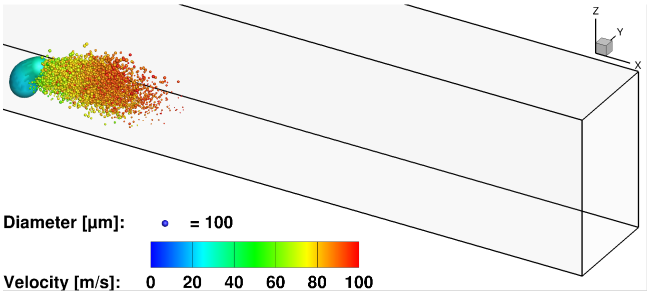

(a) after Δt=0.5 ms

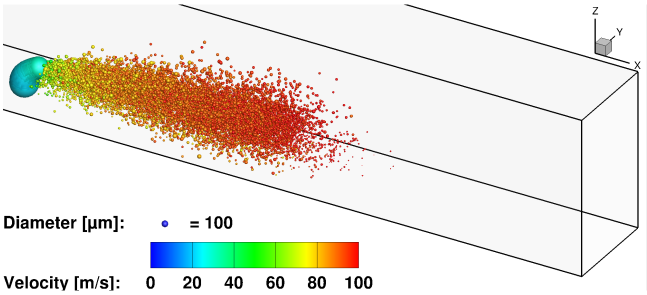

(b) after Δt=1 ms

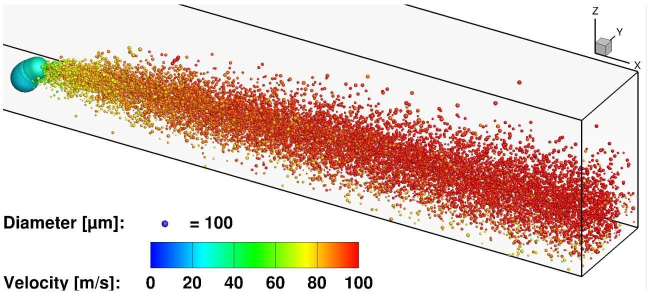

(c) quasi-steady state

Figure 3.4.: Simulation of liquid jet break-up in cross-flow at baseline conditions (from Eckel *et al.* (2016))

in cross-flow, is defined as:

$$q = \frac{\rho_l |\vec{u}_l|}{\rho_g |\vec{u}_g|} \tag{3.1.1}$$

Results of the simulation at baseline conditions at different time spans after the beginning of liquid injection are depicted in Fig. 3.4. Illustrated droplet sizes are proportional to their physical dimensions. The jet diameter corresponds to 450 μm, jet fragments have typical sizes of 100 - 150 μm and initial spray droplets are on the scale of 40 - 80 μm. The jet diameter decreases along its trajectory due to the acceleration and the loss of mass. At the position of column breakup, the remaining jet mass collapses and forms large jet fragments. A high percentage of small droplets is now generated due to erosion from this fragments. As the fragment drops are accelerated and the relative velocity between gas and drop decreases, the rupture of liquid from the surface finally stops. The little droplets, which are ripped out of the surface of both the liquid jet and the fragment drops, are immediately transported with the gas flow due to their small Stokes numbers. Highly accelerated by the co-flowing air, they reach the freestream velocity on very short path lengths. In contrast, the bigger drops with high inertia

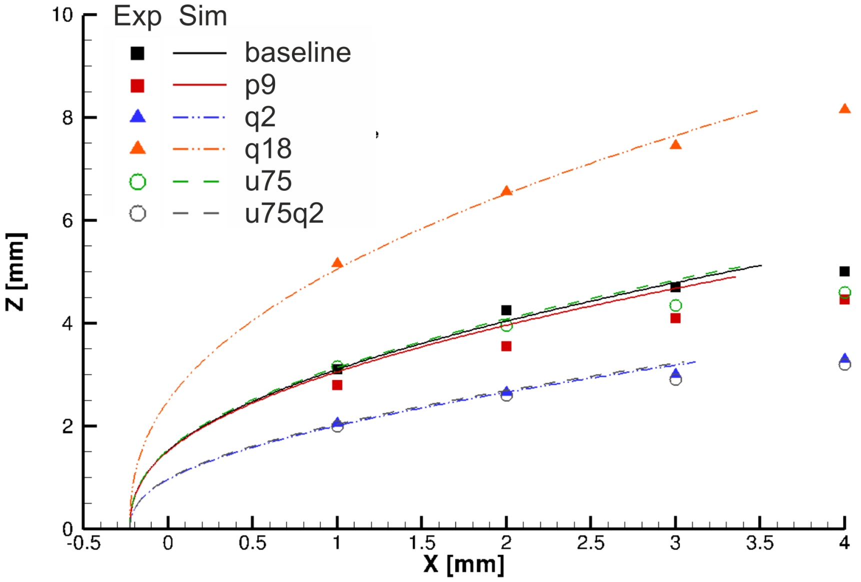

Figure 3.5.: Liquid jet trajectory for experimental conditions of Table 3.1 (from Eckel *et al.* (2016))

(high Stokes numbers) approach the freestream velocity towards the end of the duct. With respect to spray spread, the bigger drops are able to penetrate deeper into the duct because of their higher momentum.

Fig. 3.5 illustrates a comparison of the jet trajectory between the experimental findings and the computed results. The jet trajectory is based on the outer contour. The position of column breakup in the simulation is given by the end of the lines. In the experiment, the position of column breakup at baseline conditions was determined to be at $x \approx 3.3\,mm$, which matches well with the simulation. However, this only verifies the calibration of the breakup time criterion of Eq. 2.3.61. Comparing the trajectory for all conditions, an overall good agreement can be observed except for a slightly higher slope of the numerical computation at the location of column breakup. For the case of elevated pressure (case p9) as well as for the case of reduced velocity (case u75), a small overestimation of the jet penetration is visible.

The comparison of fuel fluxes in a plane 80 mm downstream of the injection orifice shows strong similarities between experiment (Fig. 3.6a) and simulation (Fig. 3.6b). However, the center of maximum volumetric fuel flow rate is measured to be at a distance of $\Delta z = 8\,mm$ from the bottom of the duct. The simulation shows a maximum at $\Delta z = 9\,mm$. From Table 3.2, it can be seen that the diameters are slightly overpredicted in the simulation. This leads to an overestimation of the penetration due to a higher inertia. The extent of regions of high fuel flux is moderately underestimated indicating an underprediction of spray spread. However, it should be noted that PDA measurements of fuel fluxes are known to have large uncertainties with respect to the quantitative information (Tropea, 2011). Nevertheless, they give a good qualitative impression. The jet atomization model is capable of predicting the

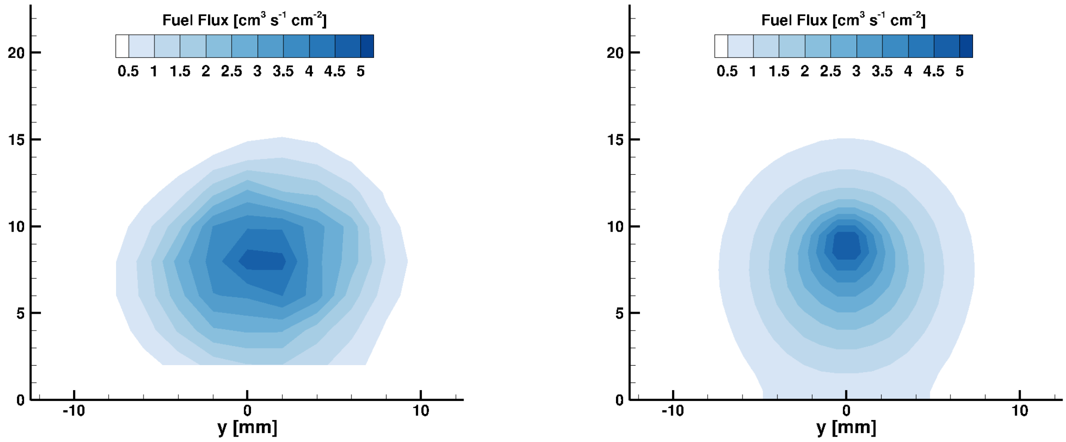

(a) Measurement at DLR Cologne (Rachner *et al.*, 2002)

(b) THETA-SPRAYSIM Simulation

Figure 3.6.: Comparison of liquid fuel fluxes for baseline conditions in plane x=80 mm (from Eckel *et al.* (2016))

	Experiment	Simulation
SMD	31.0 μm	32.7 μm
$D_{0.1}$	21.8 μm	24.2 μm
$D_{0.5}$	32.6 μm	33.6 μm
$D_{0.9}$	47.2 μm	46.6 μm

Table 3.2.: Comparison of droplet diameters for baseline conditions in plane x=80 mm

location of droplet detachment from the liquid body as well as the collapse of the remaining liquid column producing large droplets. In combination with the calculation of diameters and velocities of the resulting droplets, the model improves the accuracy of initial and boundary conditions for the Lagrangian particle tracking algorithm. As a consequence the quality of spray computations involving transverse jets can be enhanced, in particular with respect to droplet sizes (covering the whole size spectrum), spray spread, penetration length and liquid volume flux. Furthermore, breakup is modeled without the necessity of resolving the interface. Hence, initial and boundary conditions can be imposed for industrial spray computations of complex geometries in which a resolution of the gas-liquid interface is impossible, up to now.

3.2. Pre-filming airblast atomization

The empirical sheet breakup model described in section 2.3.1.2 is tested based on a comparison to experiments carried out by Gepperth *et al.* (2010, 2012).

3.2.1. Test case description

The test case is a simplified two-dimensional version of a pre-filming airblast atomizer. Perspex was used as material for the pre-filmer and the walls. This and the 2D configuration ensure a good optical accessibility. After passing an upstream mixer, a flow straightener and a convergent

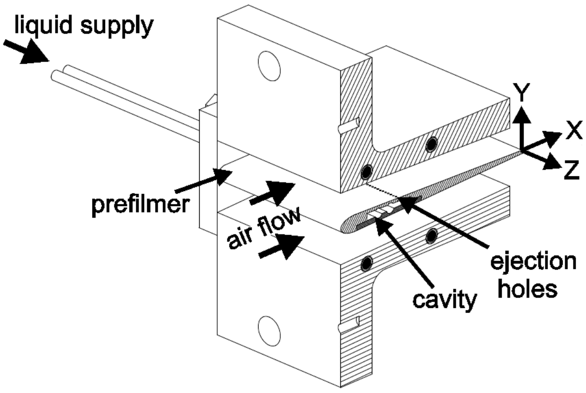

Figure 3.7.: Test section of the pre-filming airblast atomization experiment conducted at KIT-ITS (adapted from Gepperth *et al.* (2012))

Liquid	**Density** ρ_l $[kg/m^3]$	**Kin. viscosity** ν_l $[m^2/s]$	**Surface tension** σ $[kg/s^2]$
$C_3H_8O_2$-H_2O	1004.3	$6.25 \cdot 10^{-6}$	0.0454
Shellsol D100	797.0	$3.20 \cdot 10^{-6}$	0.0380
Shellsol D70	792.0	$1.97 \cdot 10^{-6}$	0.0260
Shellsol D40	780.0	$1.14 \cdot 10^{-6}$	0.0250

Table 3.3.: Physical properties of liquids from Gepperth *et al.* (2010)

nozzle, the air enters the test section from the left of Fig. 3.7. At a downstream distance of 25 mm the liquid is injected via a row of small holes and forms a thin film. The high velocity gas flow causes waves at the liquid surface until the atomizer edge is reached and the liquid is atomized. The experimental data was obtained by a laser-based shadowgraphy technique directly after the atomizer edge. The atomizer was operated at ambient pressure and temperature ($T = 298K$). For details of the experimental setup and the measurement technique the reader is referred to Gepperth *et al.* (2010, 2012).

3.2.2. Numerical setup

The empirical correlations derived in section 2.3.1.2 were implemented into a MATLAB® (The MathWorks Inc., 2013) code with sub-routines for the individual sub-processes. No secondary breakup model is applied as the experimental data were taken directly after the atomizer edge. The investigated liquids comprise a propanediol-water mix ($C_3H_8O_2 - H_2O$), Shellsol D100, Shellsol D70 and Shellsol D40. The properties of these liquids relevant for atomization are listed in table 3.3.

3.2.3. Results

A comparison of wave frequencies obtained via the breakup model (Eq. 2.3.92) to the shedding frequency experimentally measured can be found in Fig. 3.8a. As mentioned in section 2.3.1.2, the length scale L in the break-up model depends on the global flow conditions and not on the local flow, which would be desirable for a universally valid model. Hence, different length scales

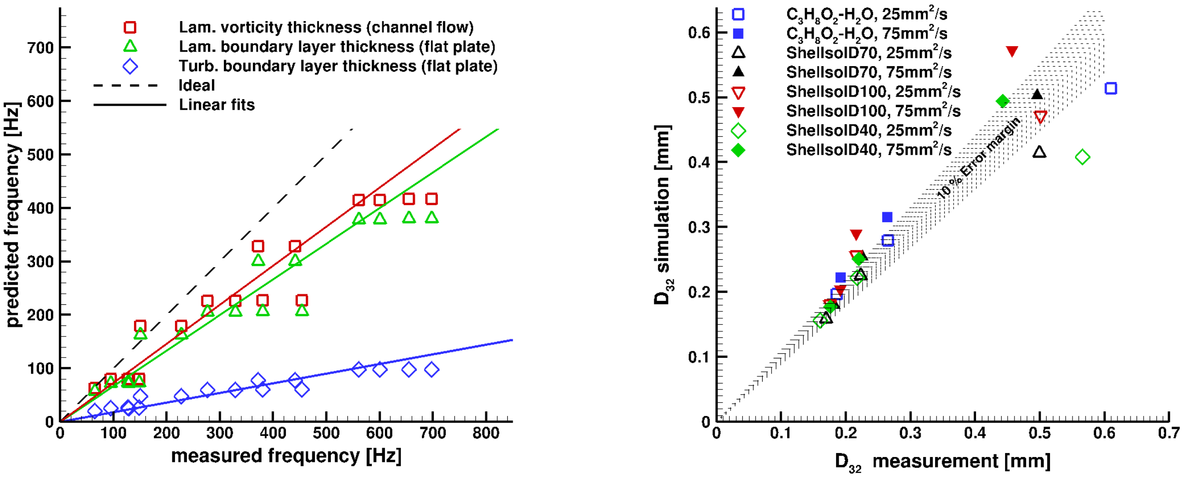

(a) Wave frequencies (b) Sauter Mean Diameter

Figure 3.8.: Comparison of the measurement and the model prediction (from Eckel *et al.* (2013))

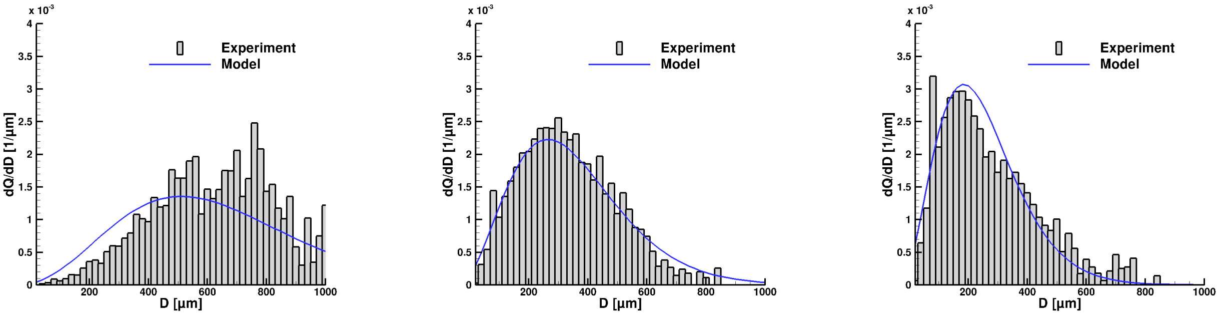

(a) Gas velocity $u_g = 20\,m/s$ (b) Gas velocity $u_g = 40\,m/s$ (c) Gas velocity $u_g = 60\,m/s$

Figure 3.9.: Volume distributions of Shellsol D70 with a volume flux of $\dot{V}/w = 25mm^2/s$ dependent on the gas velocity (from Eckel *et al.* (2013), experimental data of Gepperth (2013))

are tested as the flow conditions inside the channel above the pre-filmer were not known. The length scales tested are the laminar vorticity thickness in a channel flow as well as the laminar and turbulent boundary layer thicknesses on a flat plate. For the vorticity thickness δ_{vort}, the correlation for laminar channel flows measured by Raynal *et al.* (1997) is used:

$$\delta_{vort} = 8.5H \left(\frac{|\vec{u}_g| x}{\nu_g} \right)^{-\frac{1}{2}} \tag{3.2.1}$$

with x being the distance along which the boundary layer evolves and H the channel height. The lines in Fig. 3.8a are obtained by linear regression. The dashed line represents the perfect match between measured and predicted frequencies. The results obtained with the vorticity thickness show the smallest deviation from this ideal line. Because of the particular inflow conditions, i.e. a flow contraction caused by a convergent nozzle, the boundary layer seems to stay

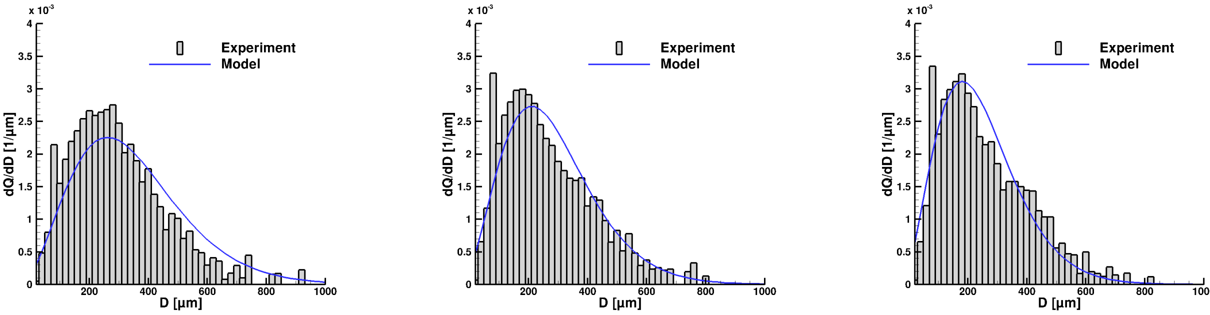

(a) Propanediol-water mix (b) Shellsol D100 (c) Shellsol D40

Figure 3.10.: Volume distributions at a gas velocity $u_g = 60\,m/s$ with a volume flux of $\dot{V}/w = 25\,mm^2/s$ dependent on the liquid properties (from Eckel *et al.* (2013), experimental data of Gepperth (2013))

laminar. The deviations from the straight line might be due to the disregard of liquid viscosity and surface tension in the approximations of Raynal *et al.* (1997) and Villermaux (1998). On the basis of this results, a constant correction factor is introduced in Eq. 2.3.92.

As mentioned earlier, the outcome of bag breakup, which was observed in the experiments of Gepperth *et al.* (2010, 2012, 2014) and Bärow *et al.* (2015) (see Fig. 2.7) is typically a bimodal drop size distribution (Opfer *et al.*, 2012). But the data of Gepperth (2013) (Fig. 3.9 and 3.10) does not show this bimodal behavior, besides a small peak around 50 μm. This peak was ascribed to a systematic measurement error by the authors (Gepperth, 2013). The absence of a bimodal distribution could be due to the fact that the volume ratios given in table 2.1 might not be representative for bag breakup in primary atomization of liquid films. For primary atomization, the majority of the volume is possibly comprised in the basal ring structure, while only a small portion of the volume ends up in the thin bubble-like film. Furthermore, as the experimental apparatus of Gepperth *et al.* (2010, 2012) was optimized for diameters larger than 50 μm, droplets stemming from the disintegration of the bag membrane having smaller diameters might have been rejected from the data acquisition system. Due to the above considerations, the confrontation of experimental data with results calculated with the breakup model will focus only on the fragments originating from ligament breakup in the following. In Fig. 3.8b, the SMD of ligament droplets calculated by the breakup model is compared with the one measured experimentally. A general good agreement can be seen. However, as mentioned earlier, the experiments show the existence of rather a distribution of droplet sizes than a distinct single droplet size. Thus, beside integral values like the SMD, the whole volume distribution ought to be compared. Fig. 3.9 shows a juxtaposition of volume distributions of Shellsol D70 at different gas velocities. The experimental data are illustrated by grey bars while the results of the atomization model are displayed by blue lines. The agreement at gas velocities of 40 m/s and higher is excellent while it slightly deteriorates towards the lower velocity of 20 m/s. But it has to be noted that the measurement accuracy also falls off towards lower velocities due to the low number of counts and hence higher statistical errors. Nevertheless, the trend is correctly predicted. Fig. 3.9c and Fig. 3.10 combined show the influence of the liquid properties on the atomization outcome. The confrontation reveals good correspondence for Shellsol D40, Shellsol D70 and Shellsol D100 as well as a satisfactory one for the Propanediol-water mixture. Nonetheless, it should be mentioned again that the results were obtained with the same set of parameters without any tuning of constants.

3.3. Particle dispersion in a particle-laden swirling flow

The particle dispersion models described in section 2.3.2 are tested on the particle-laden swirling flow test case of Sommerfeld and Qiu (1991, 1993). As very few test cases for particle-laden swirling flows exist, which separate the dispersion from vaporization and combustion, it is well-known and was also simulated by Apte *et al.* (2003); Cuenot *et al.* (2006); Oefelein *et al.* (2007); Boileau *et al.* (2008).

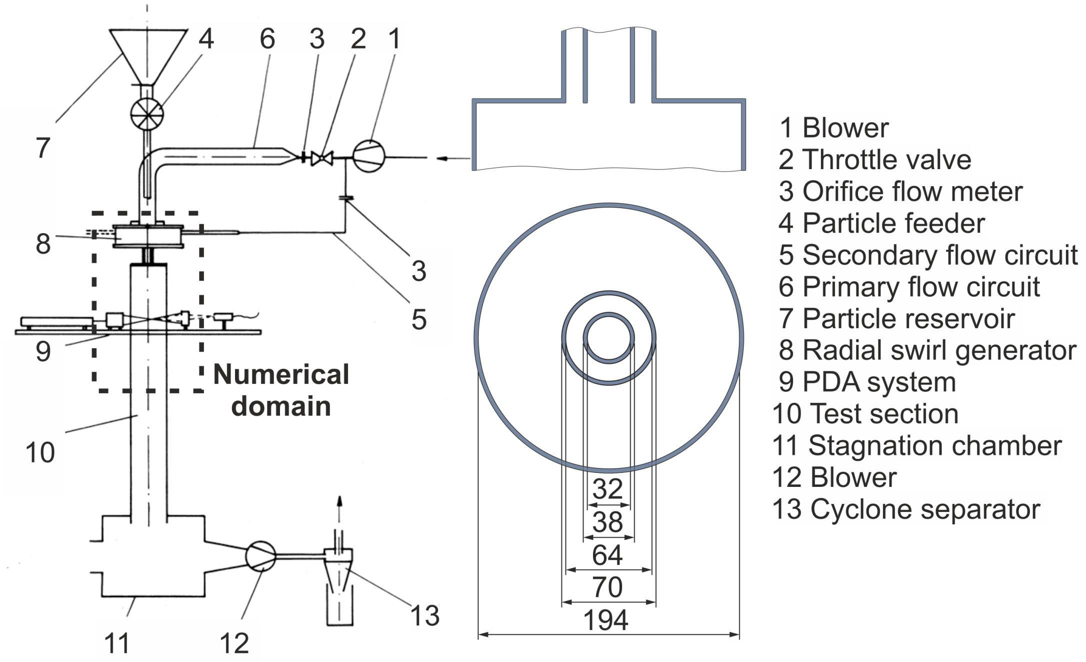

Figure 3.11.: Setup of the particle-laden swirling flow experiment (adapted from Sommerfeld and Qiu (1991, 1993))

3.3.1. Test case description

The experimental setup is shown in Fig. 3.11. The test section made of Plexiglas, which guaranteed good optical accessibility, is the central part in the setup. The system comprised two flow circuits. The first one was used for the central tube, in which the particles (spherical glass beads) were injected. In the second flow circuit, the air passed a swirl generator and entered a concentric annulus. Both the inner tube and the concentric annulus ended in the test section with a sudden expansion. Particle sizes and velocities were measured at several downstream positions by means of a PDA system. Simultaneously, the gas phase velocity was determined using tracer particles with a mean diameter of about $1.5\,\mu m$. Due to the

Gas phase		
Temperature	$[K]$	300
Density	$[kg/m^3]$	1.18
Dyn. viscosity	$[kg/(ms)]$	$1.84 \cdot 10^{-5}$
Mass flow rate central jet	$[kg/s]$	$6.0 \cdot 10^{-3}$
Mass flow rate concentric jet	$[kg/s]$	$4.46 \cdot 10^{-3}$
Dispersed phase		
Material		Glass
Shape		Spherical
Density	$[kg/m^3]$	2500.0
Size distribution		see Fig. 3.12
Sauter Mean Diameter	$[m]$	$58.56 \cdot 10^{-6}$
Mass flow rate central jet	$[kg/s]$	$1.0 \cdot 10^{-3}$
Mass flow rate concentric jet	$[kg/s]$	0.0

Table 3.4.: Boundary conditions for the swirling flow test case

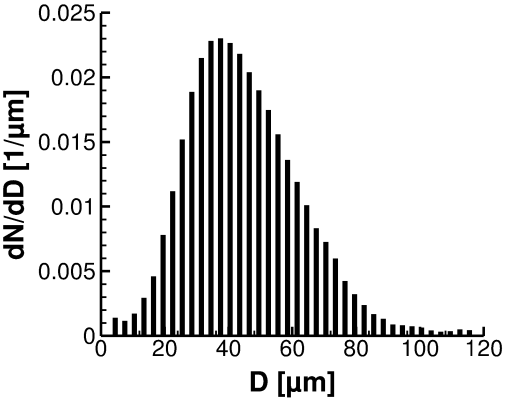

Figure 3.12.: Particle size distribution in the swirling flow test case

uncertainties in mass flux determination, the particle mass flux values were corrected using the global particle mass balance. The boundary conditions of the full swirling flow test case are listed in Table 3.4. The particle size distribution is depicted in Fig. 3.12 with particle sizes ranging from a few to 120 microns and a Sauter mean diameter of 58.56 μm.

3.3.2. Numerical setup

In comparison to prior investigations by Apte *et al.* (2003); Cuenot *et al.* (2006); Oefelein *et al.* (2007); Boileau *et al.* (2008), the inlet velocities of the concentric inlet in this work are not provided by an inflow generator. Instead, the swirler is integrated into the computational domain (see dashed box in Fig. 3.11). Thereby, the inflow conditions into the test section are directly computed in the LES avoiding uncertainties related to synthetic turbulence generators. A fully unstructured tetrahedral mesh with refinements in the swirler vanes, in the proximity of walls, and in the mixing zone is used. The resulting grid shown in Fig. 3.13 consists of 10.9 million mesh points, i.e. 60.0 million mesh elements. Using a proportional-integral (PI) mass flow controller, a pre-calculation of an infinite pipe flow was performed. A time-series of

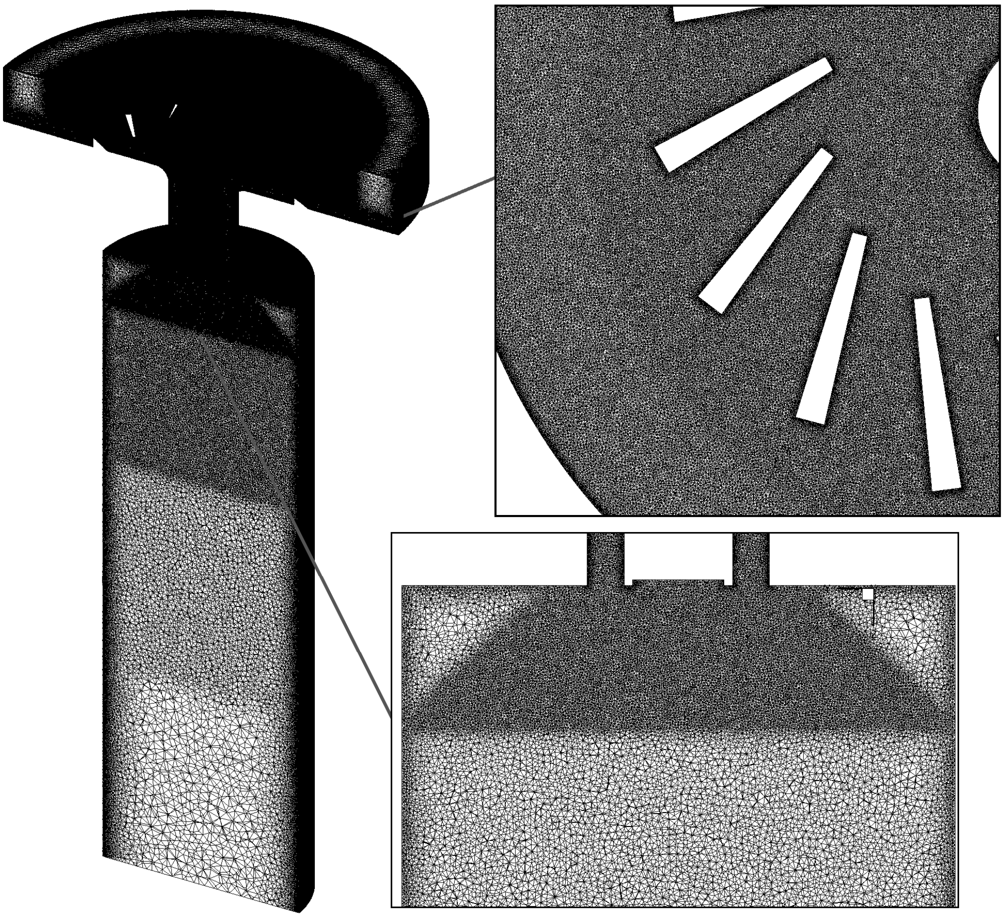

Figure 3.13.: Computational grid of the swirling flow test case

instant velocities in a cross-section of this pipe flow serves as boundary condition for the central flow. The particles are randomly introduced at the central inflow boundary, following the size distribution depicted in Fig. 3.12.

3.3.3. Results

3.3.3.1. Qualitative description of phenomena

Fig. 3.14 demonstrates the general flow features of the test case. The axial gas velocity is shown in the center plane. It is characterized by the high velocity (red) swirling jets entering the test section from the concentric annulus. The swirl generates an inner and outer recirculation zone (blue) with a relatively short re-attachment length. Vortices are visualized by the widely-used λ_2-criterion (Jeong and Hussain, 1995). λ_2 is the second eigenvalue of the tensor:

$$q_{ij} = \Omega_{ik}\Omega_{kj} + S_{ik}S_{kj} \tag{3.3.1}$$

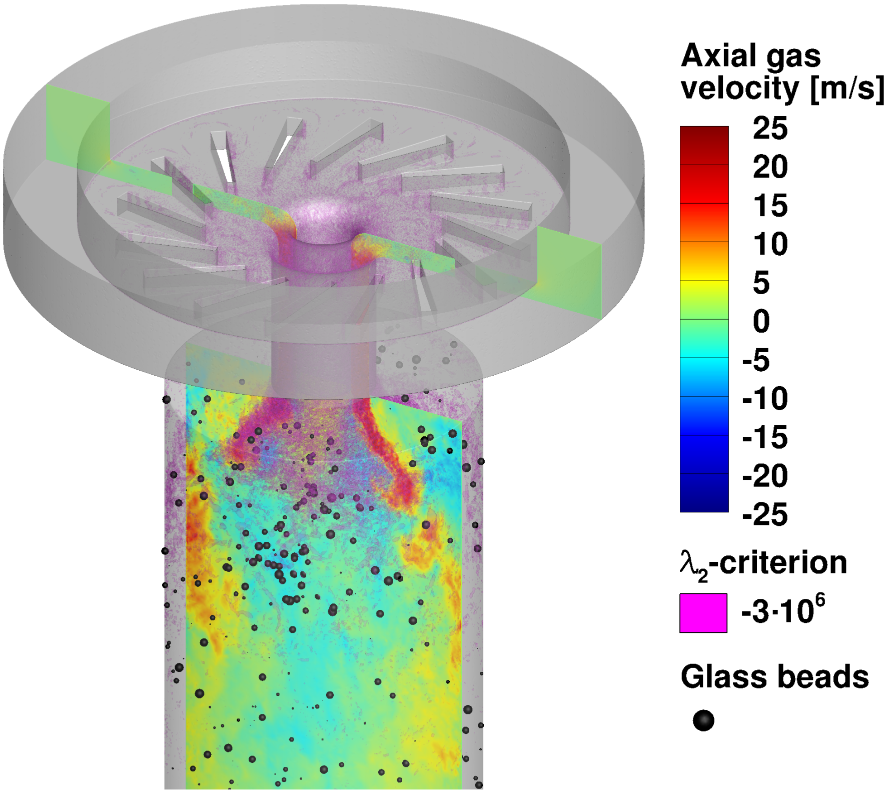

Figure 3.14.: Instantaneous snapshot of the computation

with S and Ω being the symmetric and asymmetric parts of the velocity gradient tensor:

$$S = \frac{1}{2}\left(\frac{\partial u_i}{\partial x_j} + \frac{\partial u_j}{\partial x_i}\right) \tag{3.3.2}$$

$$\Omega = \frac{1}{2}\left(\frac{\partial u_i}{\partial x_j} - \frac{\partial u_j}{\partial x_i}\right) \tag{3.3.3}$$

The vortical structures (pink) originate from the sharp edges of the swirler and the high-shear regions in the test section. They are flushed downstream in the high velocity regions and sucked back in the recirculation zones. The little black spheres represent the glass beads injected trough the inlet of the inner pipe. The size of the spheres corresponds to the actual size of the glass particles scaled by a constant factor for the sake of visualization.

3.3.3.2. Gas phase

After this qualitative description of the physical phenomena, the results of the computation will be quantitatively compared to the experimental findings. The values of the simulation were time-averaged during run-time. Then, they were extracted at the downstream positions of the measurement planes and averaged in angular direction. Fig. 3.15, 3.16 and 3.17 display the axial, radial and tangential mean velocities, respectively. The continuous lines reflect the results obtained with the stochastic dispersion model while the ones calculated with the interaction time dispersion model are given by the dashed lines. The experimental data is represented by squares. The agreement between simulation and experiment concerning the mean gas velocities is excellent. No differences between the stochastic and the interaction time dispersion model can be observed. The juxtaposition of the gas velocity fluctuations in axial direction (Fig. 3.18) shows identical behavior. The radial (Fig. 3.19) and tangential (Fig. 3.20) direction reveal small discrepancies. While the stochastic model performs better in the radial direction in contrast to a more dissipative behavior of the interaction time model, the interaction time model shows a slightly better agreement in the tangential direction with the stochastic model exhibiting some overshoots.

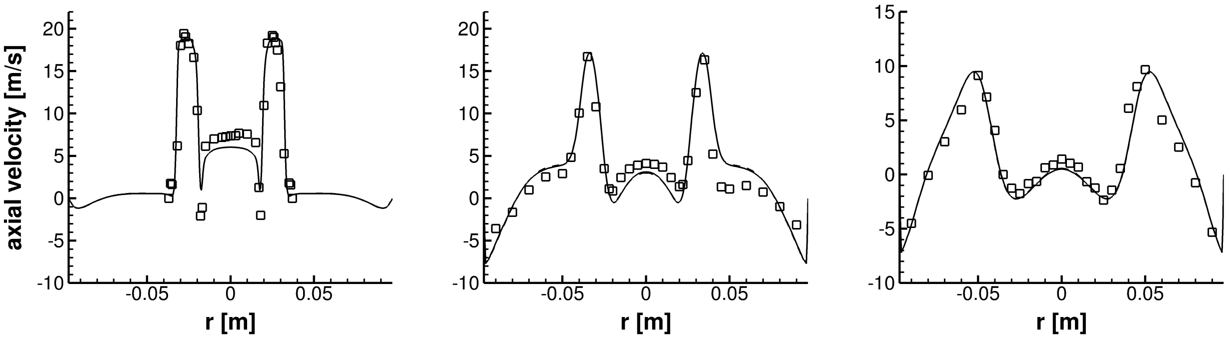

(a) z = 0.003 m (b) z = 0.025 m (c) z = 0.052 m

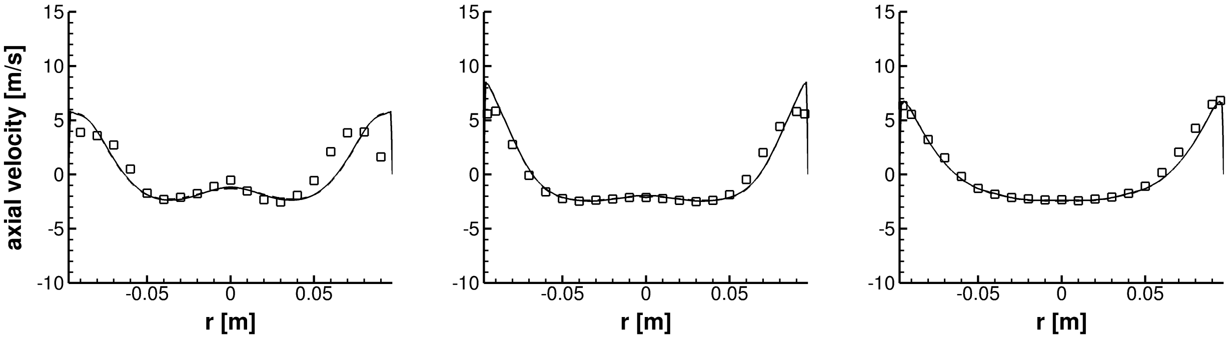

(d) z = 0.085 m (e) z = 0.112 m (f) z = 0.155 m

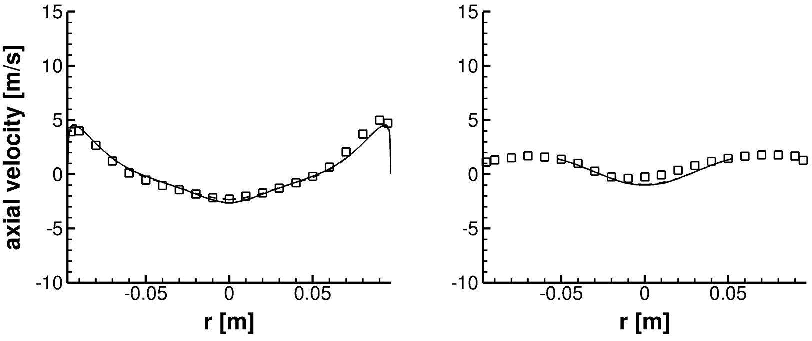

(g) z = 0.195 m (h) z = 0.315 m

Figure 3.15.: Time- and angular-averaged mean axial gas velocity at different downstream positions: Stochastic model (continuous lines), interaction time model (dashed lines) and experimental data (squares)

3.3.3.3. Dispersed phase

The particle mass fluxes through the different downstream registration planes (see Fig. 3.21) show only minor differences between the models. Due to the excellent agreement in all other registration planes, the deviation in Fig. 3.21c is attributed to measurement inaccuracies. The distributions of the axial, radial and tangential mean particle velocity over the radius are illustrated in Fig. 3.22, 3.23 and 3.24, respectively. The fluctuations of the velocity components in axial, radial and tangential direction are depicted in Fig. 3.25, 3.26 and 3.27, respectively. Again, continuous lines reflect the results obtained with the stochastic dispersion model while the ones calculated with the interaction time model are given by the dashed lines. The experimental data is represented by squares. Furthermore, three different diameter classes are distinguished, i.e. 30 μm (red), 45 μm (blue) and 60 μm (black). Firstly, it has to be mentioned that the results of the time interaction model in the registration plane (a) and (h) suffer from insufficient statistics, as no particle passed the registration cells in areas clearly marked by highly negative numbers. Secondly, the measurement data reveal some inconsistency in terms of asymmetric profiles (see Fig. 3.22b and 3.22c) and unrealistic values (see values of zero at low radial positions in Fig. 3.22h, 3.24h,3.25h and 3.27h). Despite an overall excellent agreement and only minor differences between the models, Fig. 3.22e, 3.22f and 3.22g show disparities for small radial positions. In the transition zone from down- to upstream flow in the central recirculation zone, the interaction time model seems to react too fast. The same applies to the stochastic model for larger particles (see black color in Fig. 3.22f). Furthermore, small particles overreacted to the back flow in the computations with the stochastic dispersion model (see undershoot in Fig. 3.22g, red color). The radial particle velocity profiles exhibit slight overshoots (see Fig. 3.23b and 3.23c) and undershoots (see Fig. 3.23d and 3.23e) of both models in the high velocity regions. The mean tangential velocity profiles (Fig. 3.24) were well reproduced showing only minor deviations. Concerning the particle velocity fluctuations, the trends were excellently predicted by both models despite Fig. 3.27f and 3.27g showing an opposite behavior very close to the center. Overall, the stochastic dispersion model leads to higher particle velocity fluctuations compared to the interaction time model. This is consistent with the prior observation concerning the behaviour in the transition region from down- to upstream flow, as the stochastic model is more resistant to the reverse flow. Furthermore, the stochastic model tends to overpredict the fluctuations (e.g. 3.26b, 3.26c, 3.27f and 3.27g), while the interaction time dispersion model shows a better agreement for all three components. Summarizing, it can be concluded that despite minor deviations the dispersion of particles in a turbulent, swirling flow can be accurately simulated with the computational platform presented in this thesis.

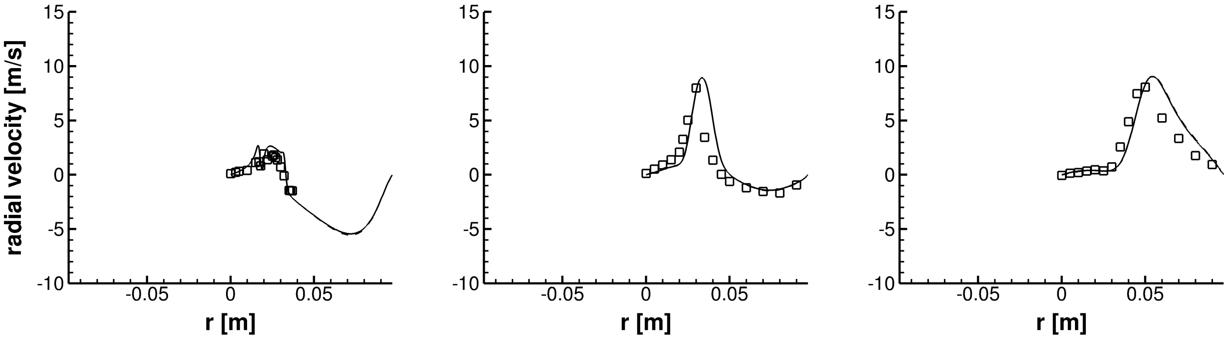

(a) z = 0.003 m (b) z = 0.025 m (c) z = 0.052 m

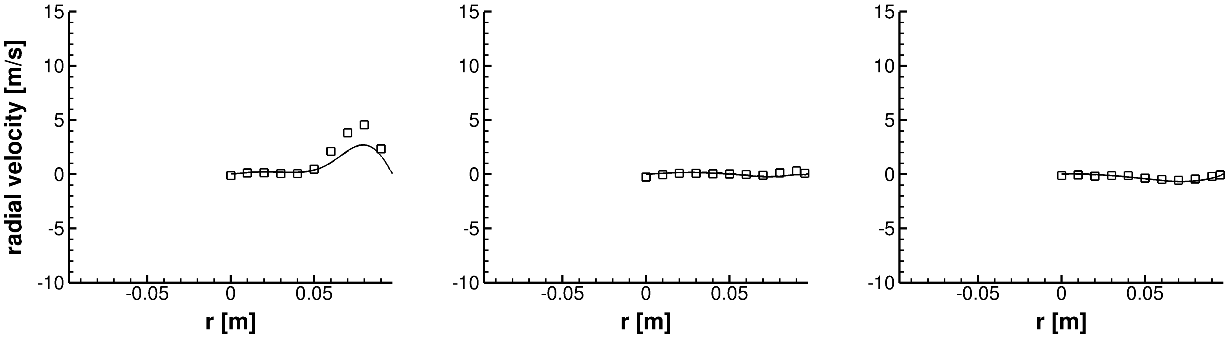

(d) z = 0.085 m (e) z = 0.112 m (f) z = 0.155 m

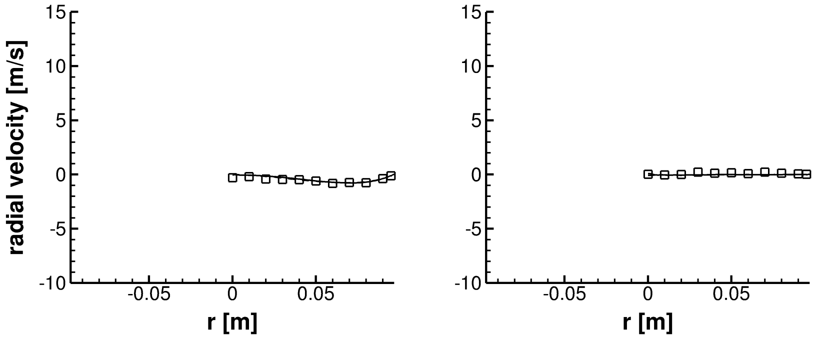

(g) z = 0.195 m (h) z = 0.315 m

Figure 3.16.: Time- and angular-averaged mean radial gas velocity at different downstream positions: Stochastic model (continuous lines), interaction time model (dashed lines) and experimental data (squares)

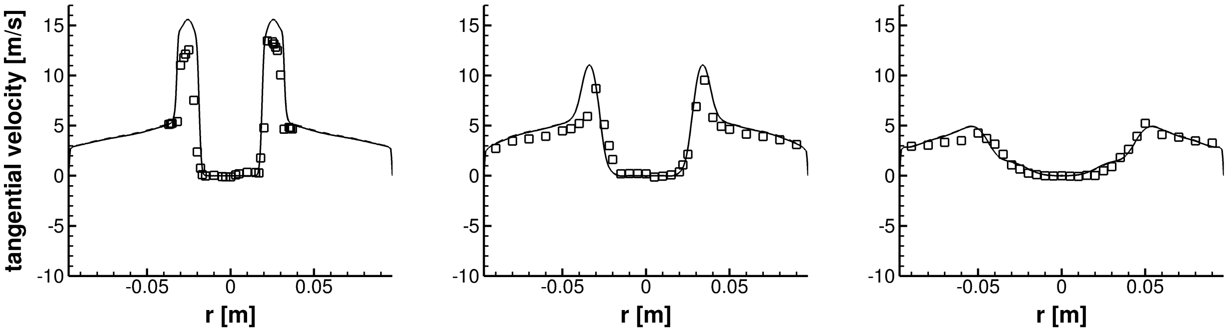

(a) z = 0.003 m (b) z = 0.025 m (c) z = 0.052 m

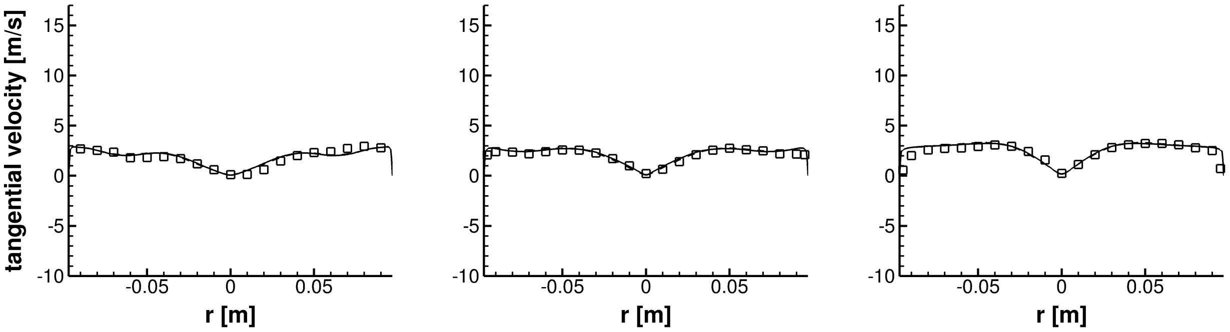

(d) z = 0.085 m (e) z = 0.112 m (f) z = 0.155 m

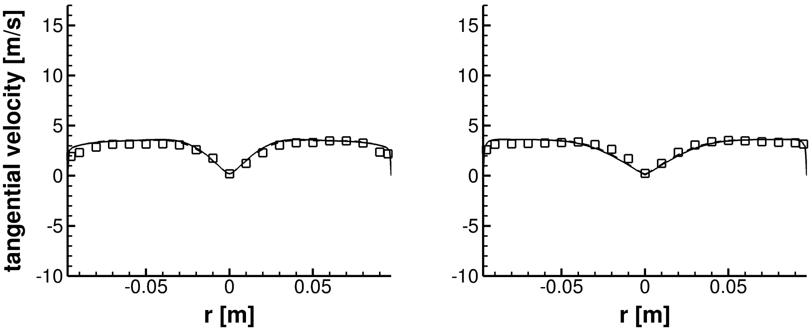

(g) z = 0.195 m (h) z = 0.315 m

Figure 3.17.: Time- and angular-averaged mean tangential gas velocity at different downstream positions: Stochastic model (continuous lines), interaction time model (dashed lines) and experimental data (squares)

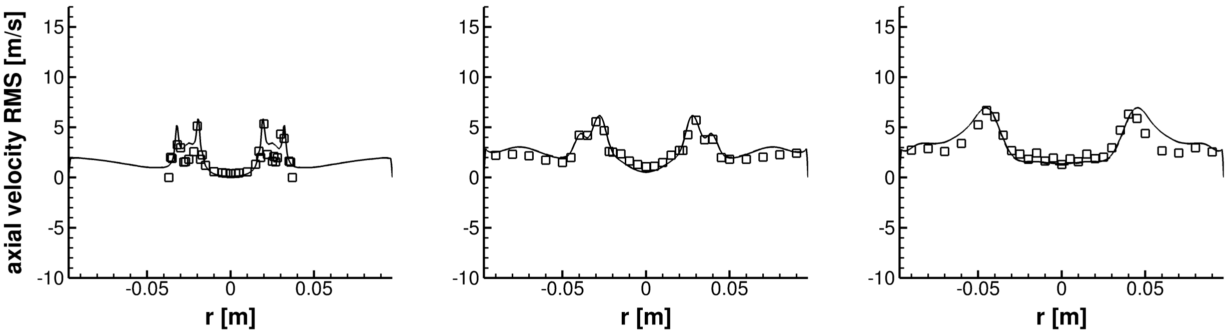

(a) z = 0.003 m

(b) z = 0.025 m

(c) z = 0.052 m

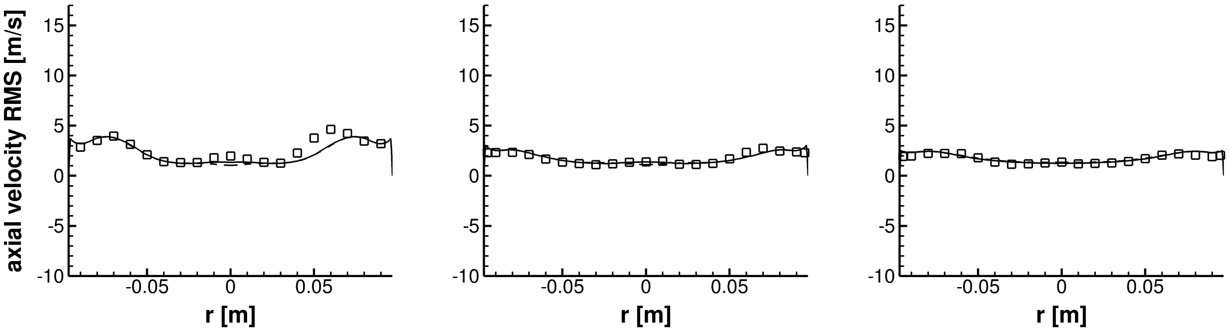

(d) z = 0.085 m

(e) z = 0.112 m

(f) z = 0.155 m

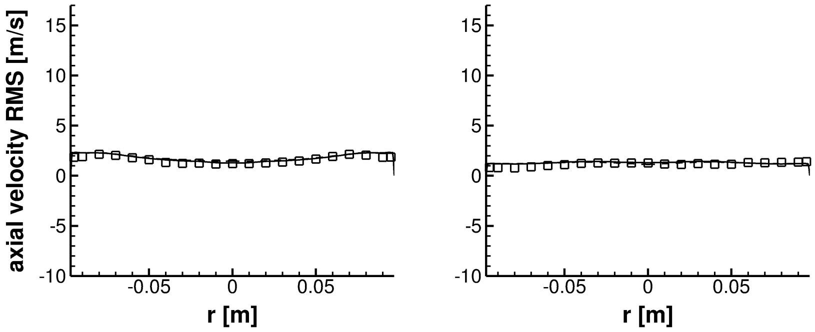

(g) z = 0.195 m

(h) z = 0.315 m

Figure 3.18.: Time- and angular-averaged axial gas velocity fluctuations at different downstream positions: Stochastic model (continuous lines), interaction time model (dashed lines) and experimental data (squares)

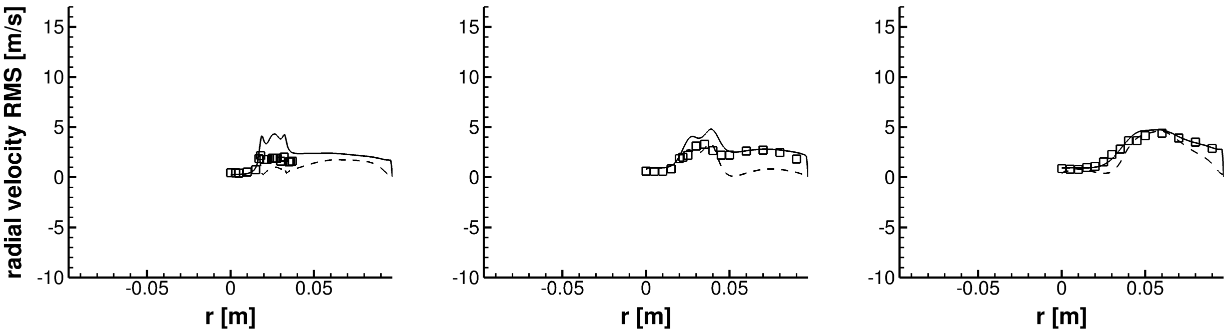

(a) z = 0.003 m (b) z = 0.025 m (c) z = 0.052 m

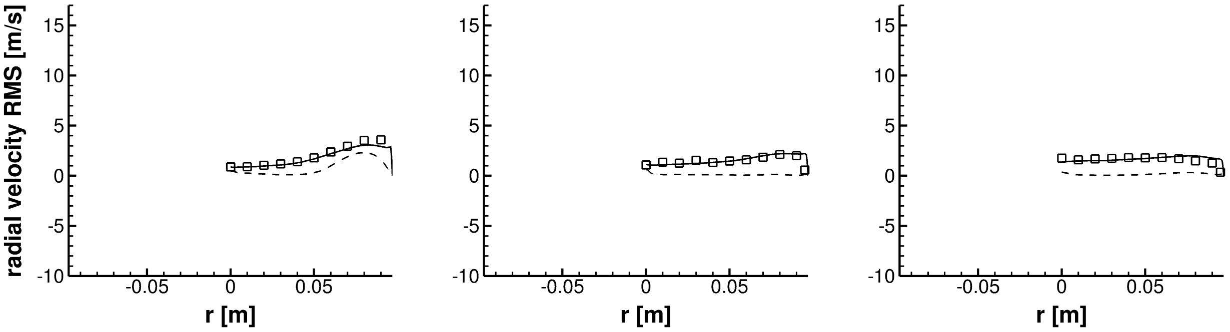

(d) z = 0.085 m (e) z = 0.112 m (f) z = 0.155 m

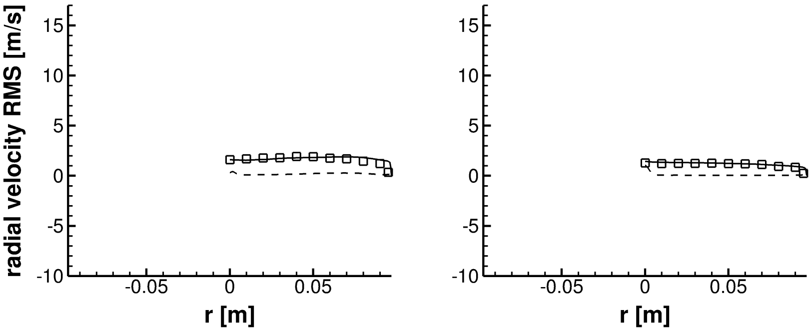

(g) z = 0.195 m (h) z = 0.315 m

Figure 3.19.: Time- and angular-averaged radial gas velocity fluctuations at different downstream positions: Stochastic model (continuous lines), interaction time model (dashed lines) and experimental data (squares)

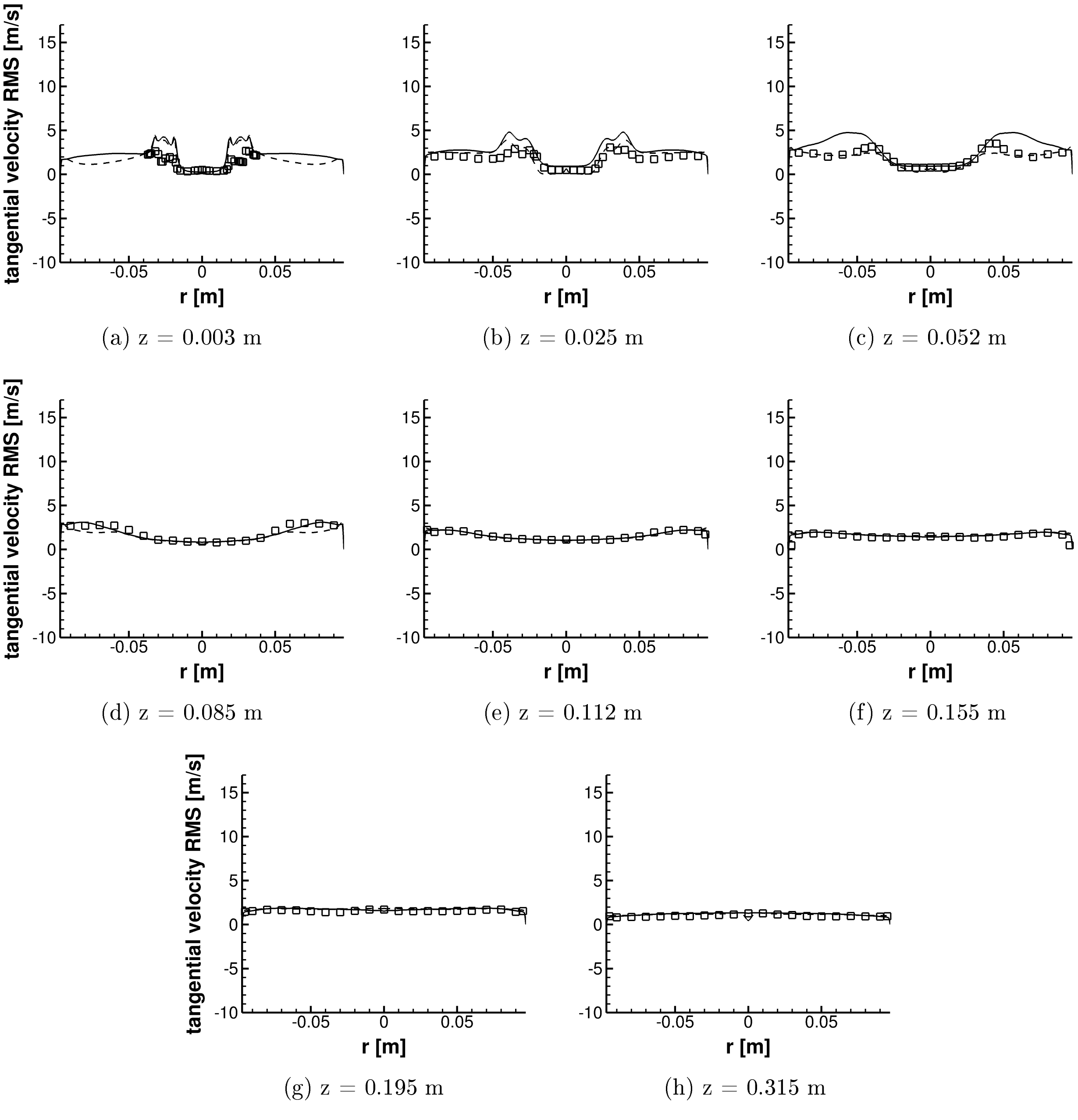

(a) z = 0.003 m (b) z = 0.025 m (c) z = 0.052 m

(d) z = 0.085 m (e) z = 0.112 m (f) z = 0.155 m

(g) z = 0.195 m (h) z = 0.315 m

Figure 3.20.: Time- and angular-averaged tangential gas velocity fluctuations at different downstream positions: Stochastic model (continuous lines), interaction time model (dashed lines) and experimental data (squares)

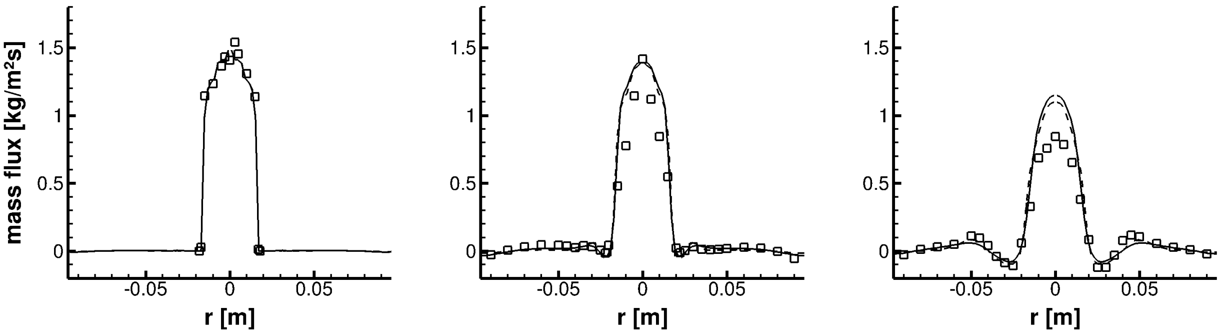

(a) z = 0.003 m (b) z = 0.025 m (c) z = 0.052 m

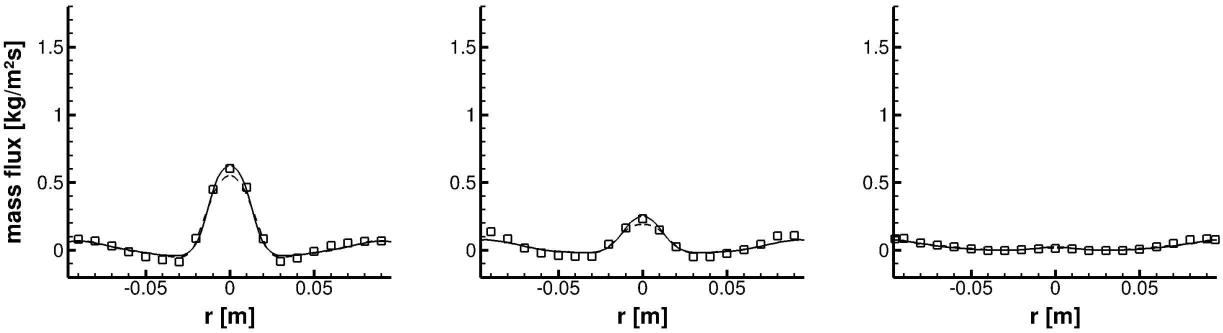

(d) z = 0.085 m (e) z = 0.112 m (f) z = 0.155 m

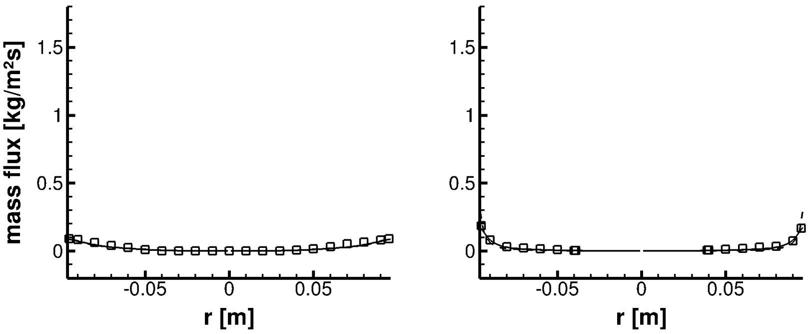

(g) z = 0.195 m (h) z = 0.315 m

Figure 3.21.: Time- and angular-averaged particle mass flux distribution at different downstream positions: Stochastic model (continuous lines), interaction time model (dashed lines) and experimental data (squares)

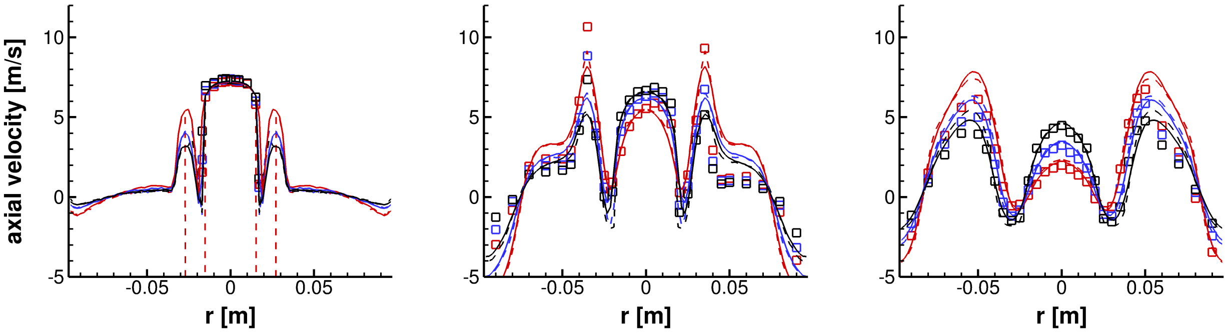

(a) z = 0.003 m (b) z = 0.025 m (c) z = 0.052 m

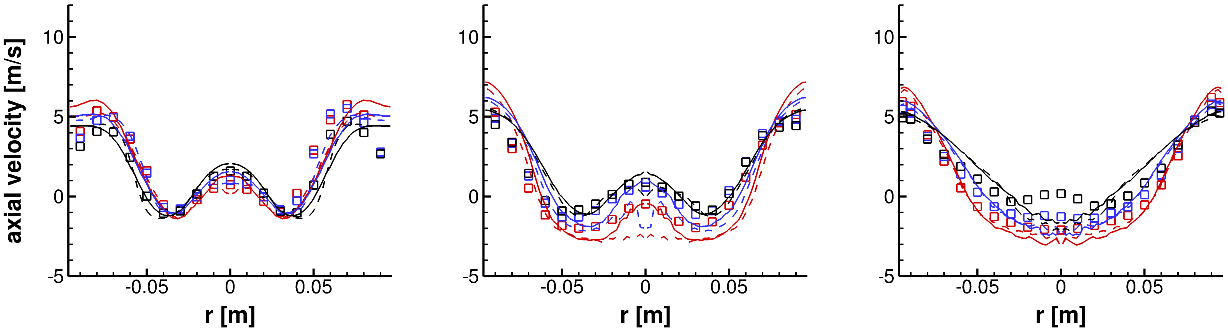

(d) z = 0.085 m (e) z = 0.112 m (f) z = 0.155 m

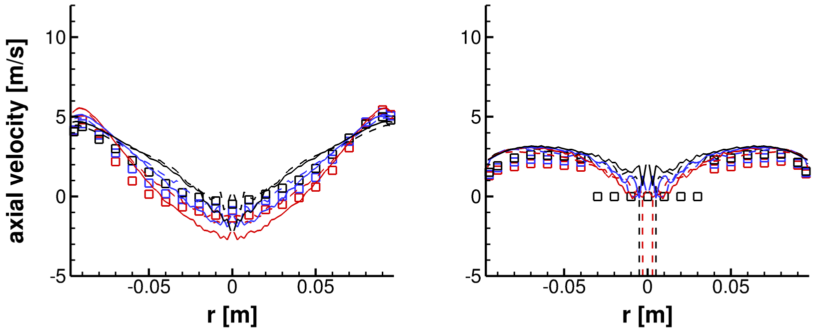

(g) z = 0.195 m (h) z = 0.315 m

Figure 3.22.: Time- and angular-averaged mean axial particle velocity distribution at different downstream positions: Stochastic model (continuous lines), interaction time model (dashed lines) and experimental data (squares). Colors refer to different particle sizes: 30 μm (red), 45 μm (blue) and 60 μm (black)

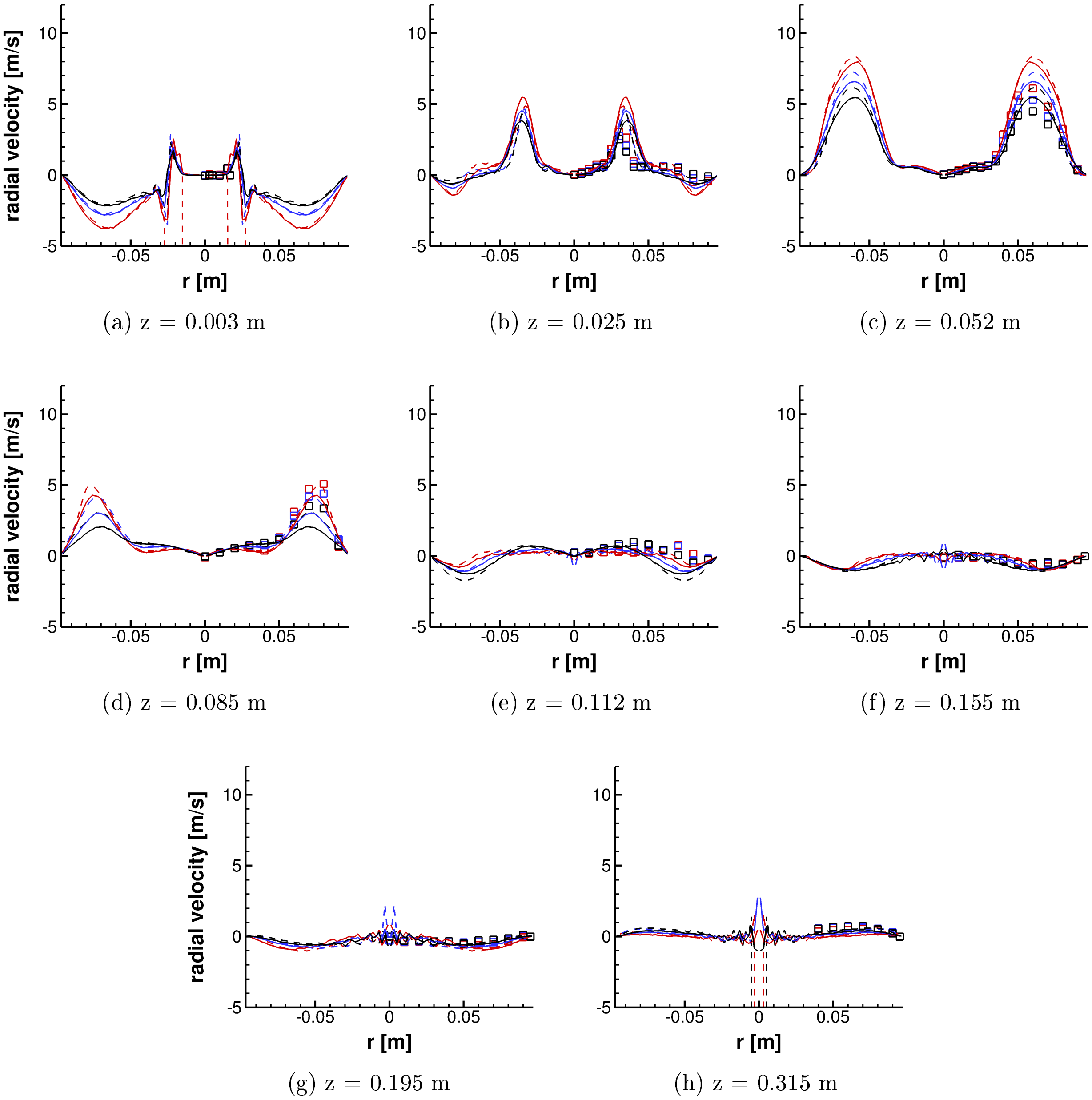

(a) z = 0.003 m (b) z = 0.025 m (c) z = 0.052 m

(d) z = 0.085 m (e) z = 0.112 m (f) z = 0.155 m

(g) z = 0.195 m (h) z = 0.315 m

Figure 3.23.: Time- and angular-averaged mean radial particle velocity distribution at different downstream positions: Stochastic model (continuous lines), interaction time model (dashed lines) and experimental data (squares). Colors refer to different particle sizes: 30 μm (red), 45 μm (blue) and 60 μm (black)

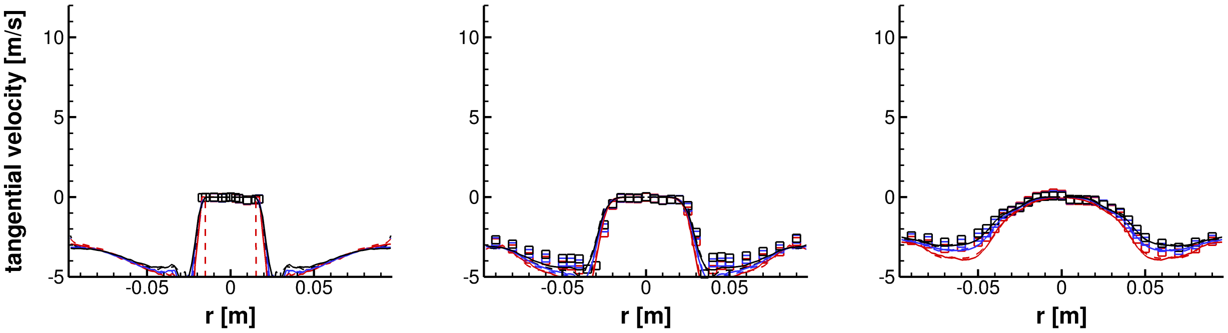

(a) z = 0.003 m (b) z = 0.025 m (c) z = 0.052 m

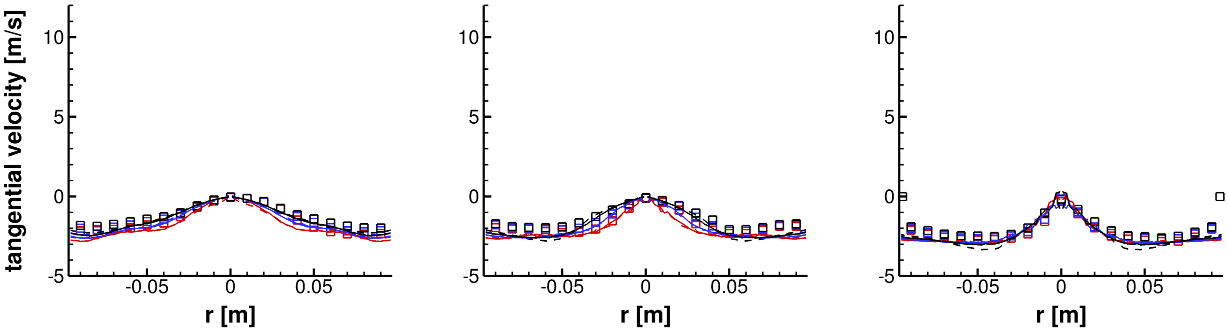

(d) z = 0.085 m (e) z = 0.112 m (f) z = 0.155 m

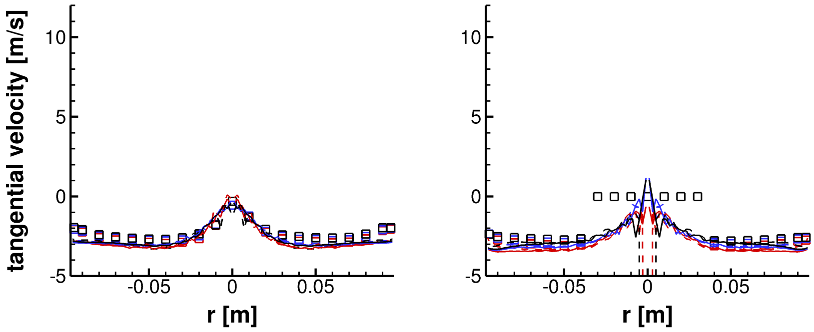

(g) z = 0.195 m (h) z = 0.315 m

Figure 3.24.: Time- and angular-averaged mean tangential particle velocity distribution at different downstream positions: Stochastic model (continuous lines), interaction time model (dashed lines) and experimental data (squares). Colors refer to different particle sizes: 30 μm (red), 45 μm (blue) and 60 μm (black)

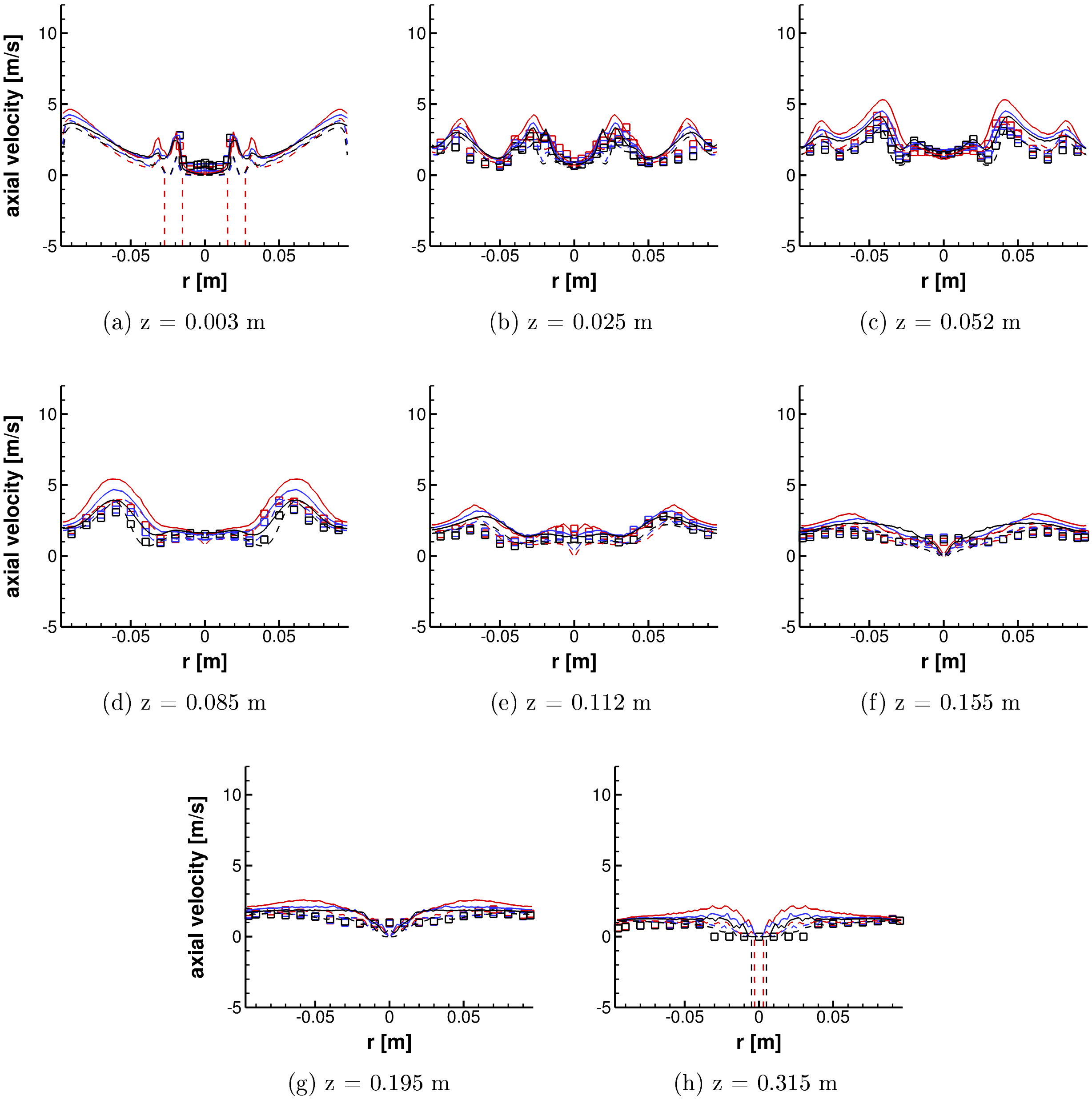

(a) z = 0.003 m

(b) z = 0.025 m

(c) z = 0.052 m

(d) z = 0.085 m

(e) z = 0.112 m

(f) z = 0.155 m

(g) z = 0.195 m

(h) z = 0.315 m

Figure 3.25.: Time- and angular-averaged axial particle velocity fluctuations distribution at different downstream positions: Stochastic model (continuous lines), interaction time model (dashed lines) and experimental data (squares). Colors refer to different particle sizes: 30 μm (red), 45 μm (blue) and 60 μm (black)

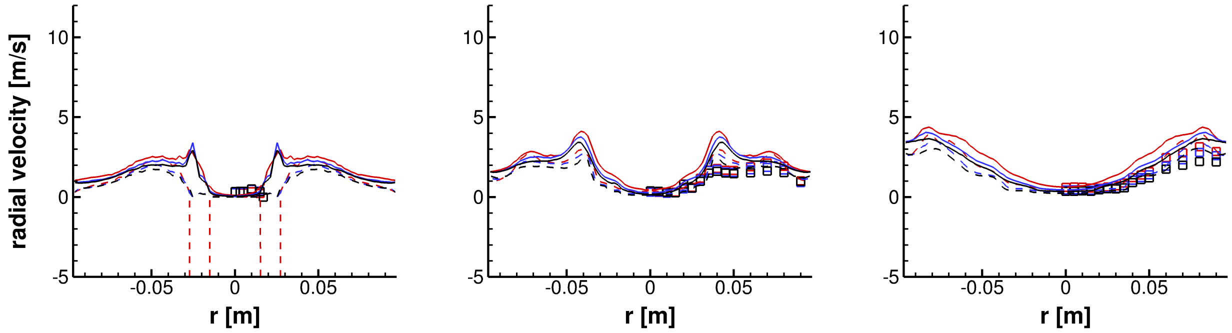

(a) z = 0.003 m (b) z = 0.025 m (c) z = 0.052 m

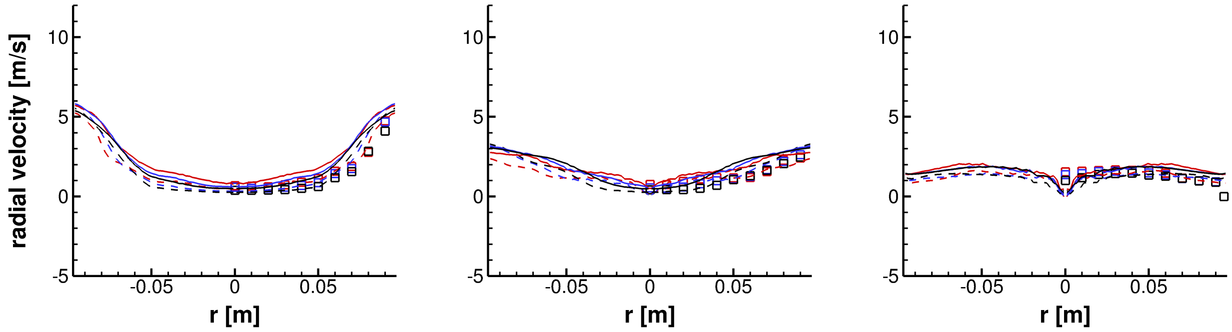

(d) z = 0.085 m (e) z = 0.112 m (f) z = 0.155 m

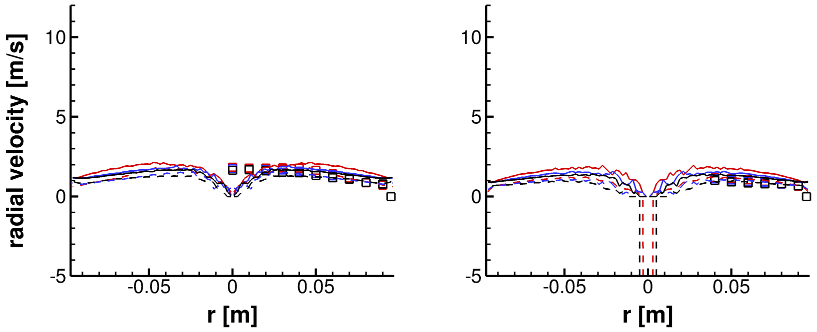

(g) z = 0.195 m (h) z = 0.315 m

Figure 3.26.: Time- and angular-averaged radial particle velocity fluctuations distribution at different downstream positions: Stochastic model (continuous lines), interaction time model (dashed lines) and experimental data (squares). Colors refer to different particle sizes: 30 μm (red), 45 μm (blue) and 60 μm (black)

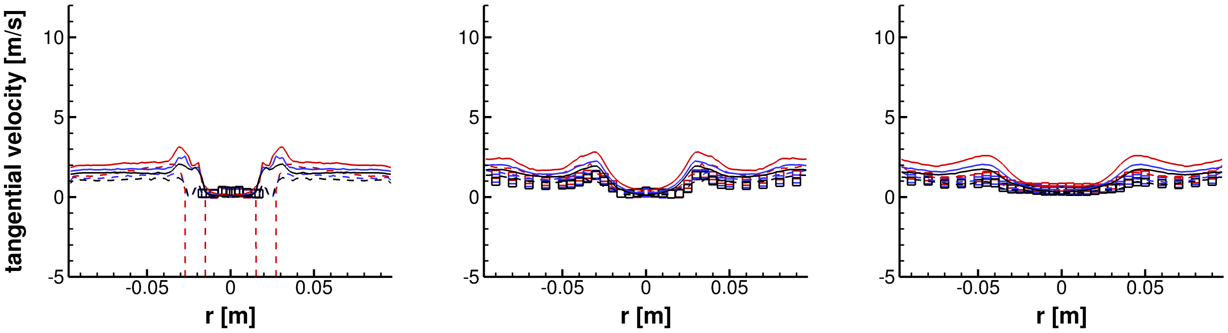

(a) z = 0.003 m (b) z = 0.025 m (c) z = 0.052 m

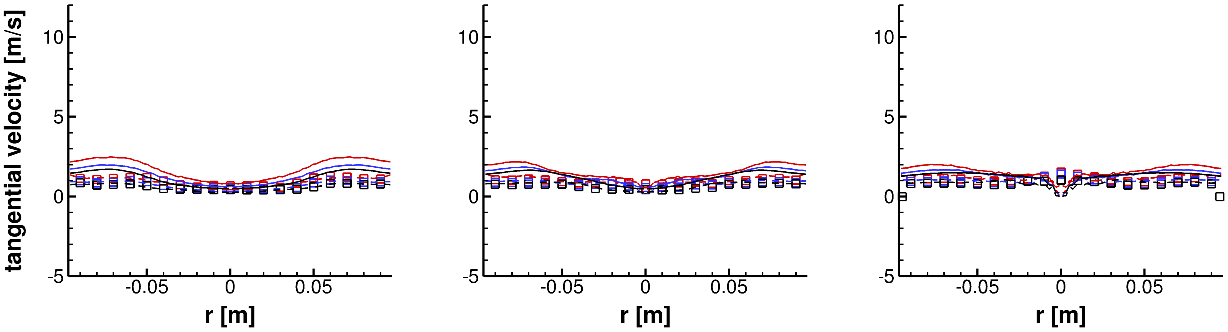

(d) z = 0.085 m (e) z = 0.112 m (f) z = 0.155 m

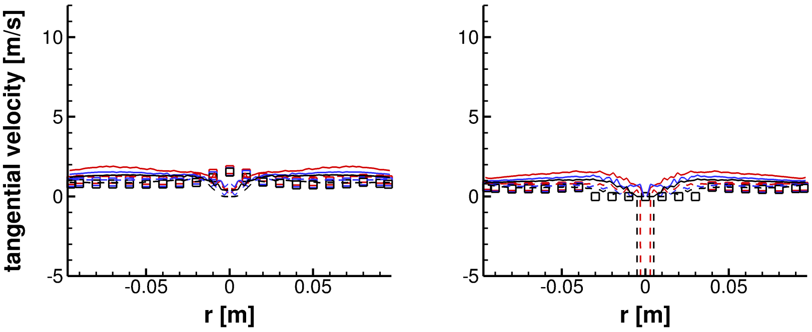

(g) z = 0.195 m (h) z = 0.315 m

Figure 3.27.: Time- and angular-averaged tangential particle velocity fluctuations distribution at different downstream positions: Stochastic model (continuous lines), interaction time model (dashed lines) and experimental data (squares). Colors refer to different particle sizes: 30 μm (red), 45 μm (blue) and 60 μm (black)

4. Reactive test cases

After the sub-model tests in the previous chapter, this chapter deals with the application of the entire spray simulation platform to reactive test cases. The reactive test cases comprise the combustion around mono-disperse droplet chains (section 4.1), an entrained-flow gasifier linked to fuel processing technology (section 4.2) and a swirl-stabilized spray burner related to aero-engine combustors (section 4.3).

4.1. Combustion around mono-disperse droplet chains

Before applying the simulation platform to the complex and expensive test cases, which will be introduced in the following sections 4.2 and 4.3, this test case served as verification for the coupling between the multi-component vaporization model and the detailed chemistry solver. In order to keep the operating expenses for the experiments low, the focus is on a qualitative comparison between the simulations and the experimentally observed flame luminescence (Mosbach and Yin, 2015).

4.1.1. Test case description

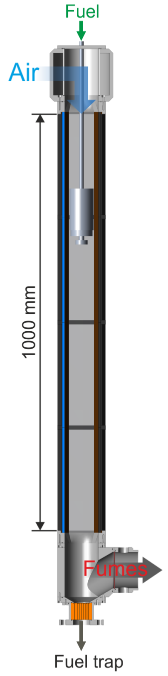

Figure 4.1.: Setup of the mono-disperse droplet chains experiment (adapted from Gebel *et al.* (2015b))

Five mono-disperse droplet chains were injected into a nearly rectangular channel with a cross-sectional area of 62 cm^2 and a length of 1 m (see Fig. 4.1). The mono-disperse droplet chains were generated by a piezoelectric driven "Vibrating Orifice Aerosol Generator" (TSI Corporation, MN, USA) combined with a laser perforated disc having five micro-holes. Each of the five orifices in the injector plane had a diameter of $50\,\mu m$ resulting in a droplet diameter of $\sim 100\,\mu m$ and a droplet spacing of the order of $\sim 250\,\mu m$. Good optical accessibility of the ignition and combustion region with a maximum field of view of 24 cm x 6 cm allowed for optical measurement techniques. The partially vaporized chains of fuel-droplets were ignited by a focused laser pulse created by a flash lamp-pumped, Q-switched and frequency-doubled Nd:YAG laser. For a detailed description of the experimental device and the ignition procedure, the reader is referred to Gebel *et al.*

(2015a,b). Air with a temperature of 295.15 K and a volume flow rate of $40\,m^3/h$ at ambient pressure was used as oxidizer. The low air volume flow rate resulted in a laminar flow around the central body, where the injector was mounted. The fuels, which were examined in this study, involved a conventional kerosene (Jet A-1), a fully synthetic Jet Fuel from Sasol (FSJF) and a dearomatized hydrocarbon blend (Exxsol D80). All fuels were studied keeping the temperature and the mass flow rates of both air and fuel constant. Keeping the mass flow rates constant, however, leads to two drawbacks. Firstly, the global equivalence ratio varied between the fuels and secondly the droplet inlet velocity changed with the different liquid densities of the fuels. A summary of the fuel specific boundary conditions can be found in Table 4.1. The flame luminescence was recorded 0.05 s after the igniting laser pulse by a LaVision Imager Intense CCD camera with an UV lens (25 mm, F/2.8, UKA UV2528B) and two UG 11 filters. The gate exposure time was 0.9 s. Several runs were averaged to obtain the average flame luminescence of the individual fuels.

Fuel			Jet A-1	FSJF	Exxsol D80
Temperature	T_{liq}	$[K]$	303.15	303.15	303.15
Density	ρ_{liq}	$[kg/m^3]$	810.75	818.68	793.84
Mean molar weight	M_{liq}	$[kg/mol]$	148.84	153.04	173.18
Mass flow rate	$\dot{m}_{liq}$	$[g/min]$	2.0	2.0	2.0
Inlet velocity	v_{liq}	$[m/s]$	4.19	4.15	4.28

Table 4.1.: Fuel specific boundary conditions

4.1.2. Numerical setup

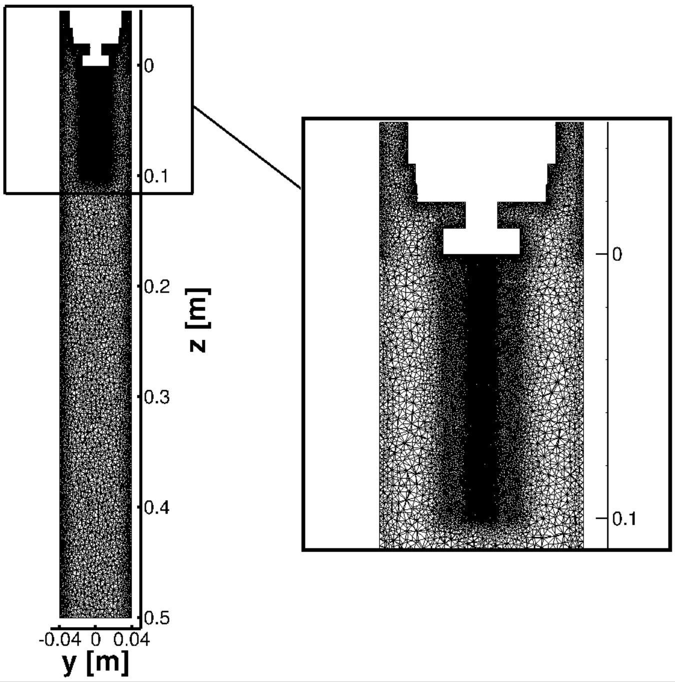

Figure 4.2.: Cut through the center plane of the computational grid

Discretization The computational domain shown in Fig. 4.2 comprises the combustion chamber and the central body with the mounted injector. The geometry is discretized by a fully unstructured tetrahedral mesh. The grid is refined in the area of the droplet chains and in near-wall regions. This leads to a grid size of 600 000 points corresponding to 3.2 million volume elements.

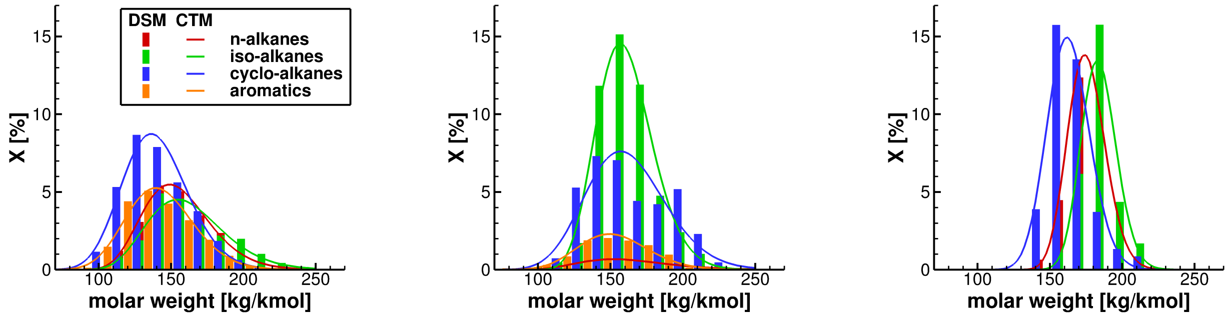

(a) Jet A-1 (b) FSJF (c) Exxsol D80

Figure 4.3.: Discrete species distribution from GCxGC measurement (bars) and the approximation by the continuous thermodynamics model (lines)

Description of the liquid mixture Fig. 4.3 illustrates the discrete species distributions (bars), which were determined by means of a GCxGC gas chromatography system. The approximation with the CTM model described in section 2.3.3.3 is represented by the solid lines. The colors refer to the different chemical classes (see section 2.3.3.1), i.e. n-alkanes (red), iso-alkanes (green), cyclo-alkanes (blue) and aromatics (orange).

Reaction mechanism The chemical surrogate in the gas phase reaction mechanism consists of one representative species for each chemical class, i.e. n-dodecane ($C_{12}H_{26}$), iso-octane (C_8H_{18}), cyclo-hexane (C_6H_{12}) and toluene (C_7H_8). In total, the chemical kinetics mechanism involves 76 species and 438 reactions (Slavinskaya *et al.*, 2015). The coupling is established by assigning the vapor species of each fuel family to the representative gaseous species listed in Table 4.2. These gaseous species are chosen matching the chemical class of the vapor species with one exception. The GCxGC measurements of Exxsol D80 revealed a narrow distribution of rather long-chained iso-alkanes. Unfortunately, the heaviest molecule of the iso-alkane family in the chemical kinetics mechanism is iso-octane. As a consequence, the vapor species of the iso-alkane family for Exxsol D80 is assigned to n-dodecane.

Fuel vapor species	Assigned gaseous species for		
family	Jet A-1	FSJF	Exxsol D80
n-alkanes	n-dodecane	n-dodecane	n-dodecane
iso-alkanes	iso-octane	iso-octane	n-dodecane
cyclo-alkanes	cyclo-hexane	cyclo-hexane	cyclo-hexane
mono-aromatics	toluene	toluene	-

Table 4.2.: Coupling between fuel vapor species and species in the gas phase reaction mechanism

4.1.3. Results

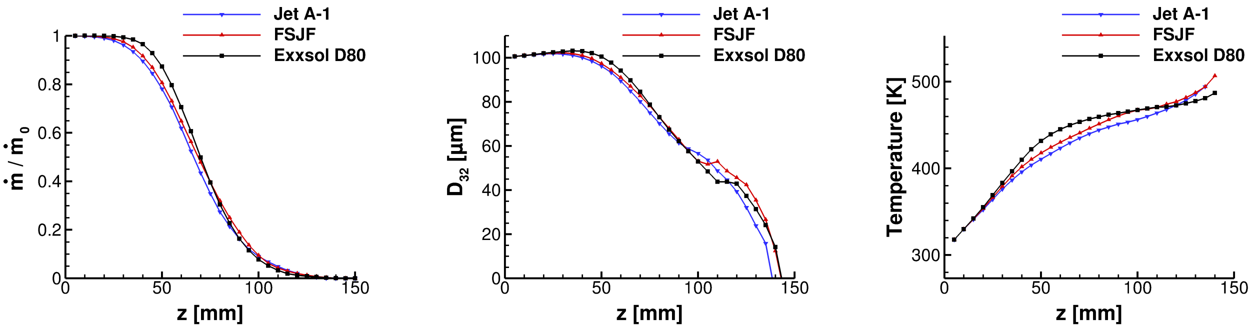

(a) Normalized mass flow rate (b) Droplet diameter (c) Droplet temperature

Figure 4.4.: Preliminary assessment concerning the vaporization of the droplet chains in preheated air (800 K). Each point reflects a registration plane orthogonal to the main flow direction.

4.1.3.1. Preliminary assessment of vaporization rates

Prior to the investigation of the reactive cases, the vaporization of the droplet chains is assessed by means of steady computations in pre-heated air (800 K). Fig. 4.4a, 4.4b and 4.4c display the change in mass flow rate, in the Sauter mean diameter, and in the droplet temperature, respectively. The droplets were detected in registration planes orthogonal to the main flow direction with a downstream spacing of 5 mm. While Jet A-1 and FSJF show similar vaporization rates, the vaporization of Exxsol D80 is slower. Besides, Fig. 4.4b nicely illustrates the volume expansion while the droplet temperature rises (see Fig. 4.4c). Once the evaporation begins (see Fig. 4.4a and 4.4b), the droplet diameter starts to decrease. Between 95 mm and 125 mm an unexpected behavior in the Sauter Mean Diameter curves can be observed. This is due to the fact that the droplets from the five droplet chains disperse in the flow experiencing slightly different surrounding conditions. As a consequence, between 95 mm and 125 mm some of the droplet chains have already fully evaporated. Collecting data in the registration planes introduces an implicit averaging. Therefore, the complete evaporation of some of the droplet chains can lead to constant or even rising Sauter mean diameters.

4.1.3.2. Combustion

The average flame luminescence, which was experimentally determined by the line-of-sight imaging, is depicted in Fig. 4.5. The numerical results of the time-averaged temperature distribution in the center plane are shown in Fig. 4.6. Although a one to one comparison is not possible, the qualitative features of the flames and the relative information can be evaluated. The central cold (dark) area in Fig. 4.6 corresponds to the location of the droplet chains. Obviously, these areas are not visible in Fig. 4.5 due to the line-of-sight technique. The change in flame length switching from Jet A-1 to FSJF (4.5a and Fig. 4.5b) is well captured by the simulation (see Fig. 4.6a and 4.6b). It is also noteworthy that it was difficult to stabilize the flame, which tended to blow-off, in the simulation of Exxsol D80. Interestingly, this behavior was also observed in the experiment. Only in roughly 5 % of the cases the flame stabilized after the laser ignition. In the rare cases of a stable flame, it can be seen from Fig. 4.5c that the region with high luminosity (yellow) does not extend to the injector like in the Jet A-1 and FSJF cases. In the simulation of Exxsol D80, this is much more pronounced resulting in a lifted flame close to blow-off (Fig. 4.6c). The stabilization mechanism of the three flames can be seen in Fig. 4.7 illustrating a close-up of the injector-near region. The instantaneous gas temperature is plotted together with the blue-colored droplets. The interaction between the droplet chain, the flame front and large scale coherent vortical structures can be clearly observed. A hot streak even interrupted the droplet chain in the Jet A-1 case (Fig. 4.7a). Furthermore, the lower grid resolution, which starts from a downstream distance of roughly 0.11 m, leads to a clearly visible numerical diffusion of the flame fronts. The Jet A-1 and FSJF (Fig. 4.6b) flames stabilize by anchoring to the low velocity regions around the injector mounting. In contrast, the Exxsol D80 flame (Fig. 4.6c) is almost lifted exhibiting only delicate flamelets close to the injector. This can be explained by the lower vaporization rates for Exxsol D80 compared to the other fuels, which were found in the preliminary assessment of the vaporization in the previous section (section 4.1.3.1).

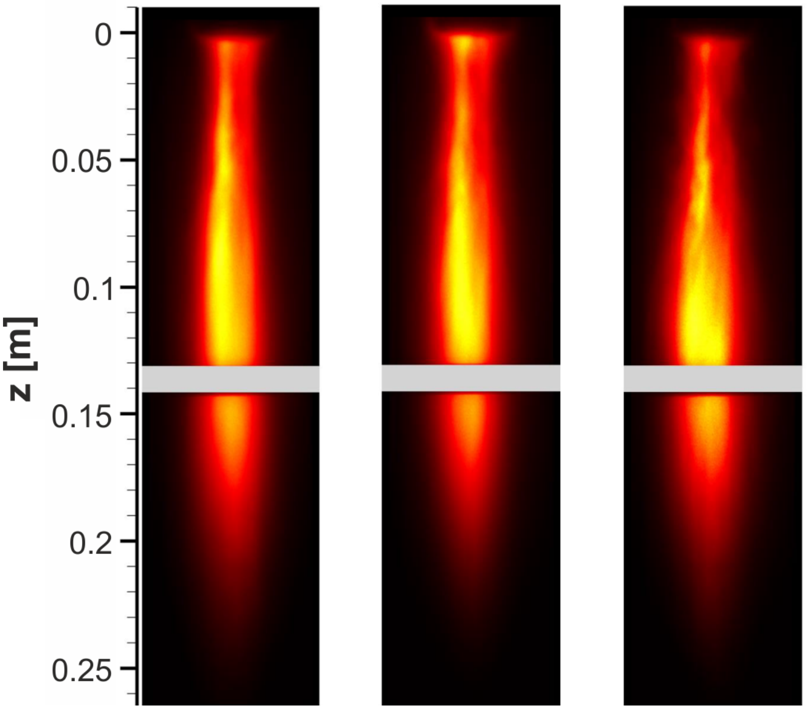

(a) Jet A-1 (b) FSJF (c) Exxsol D80

Figure 4.5.: Flame luminescence for different fuels in the experiment

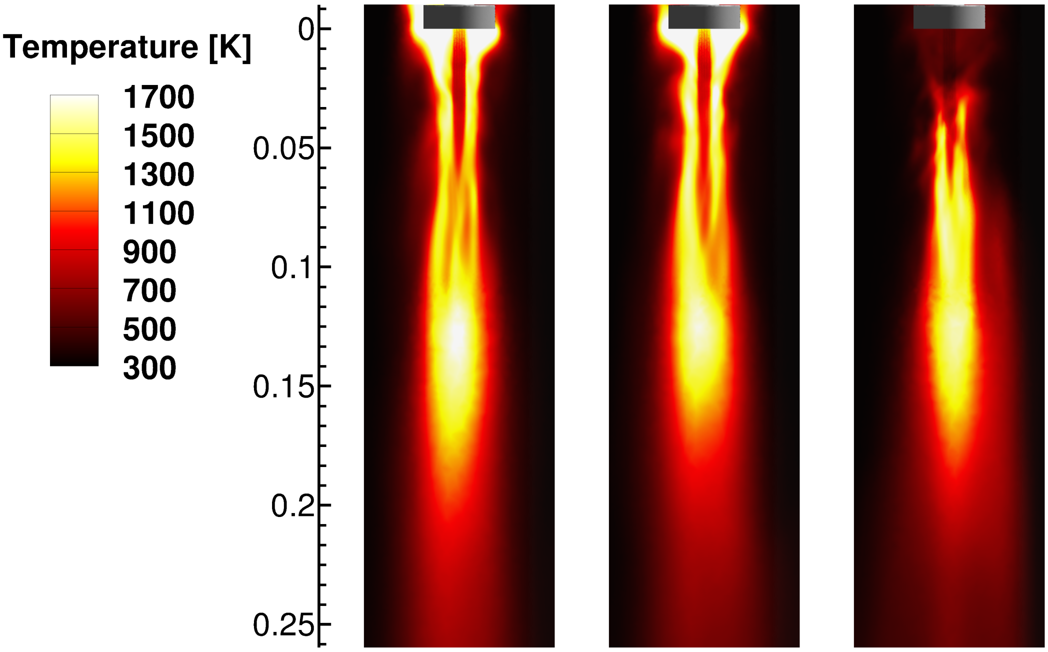

(a) Jet A-1 (b) FSJF (c) Exxsol D80

Figure 4.6.: Time-averaged temperature distribution in the center plane of the simulation

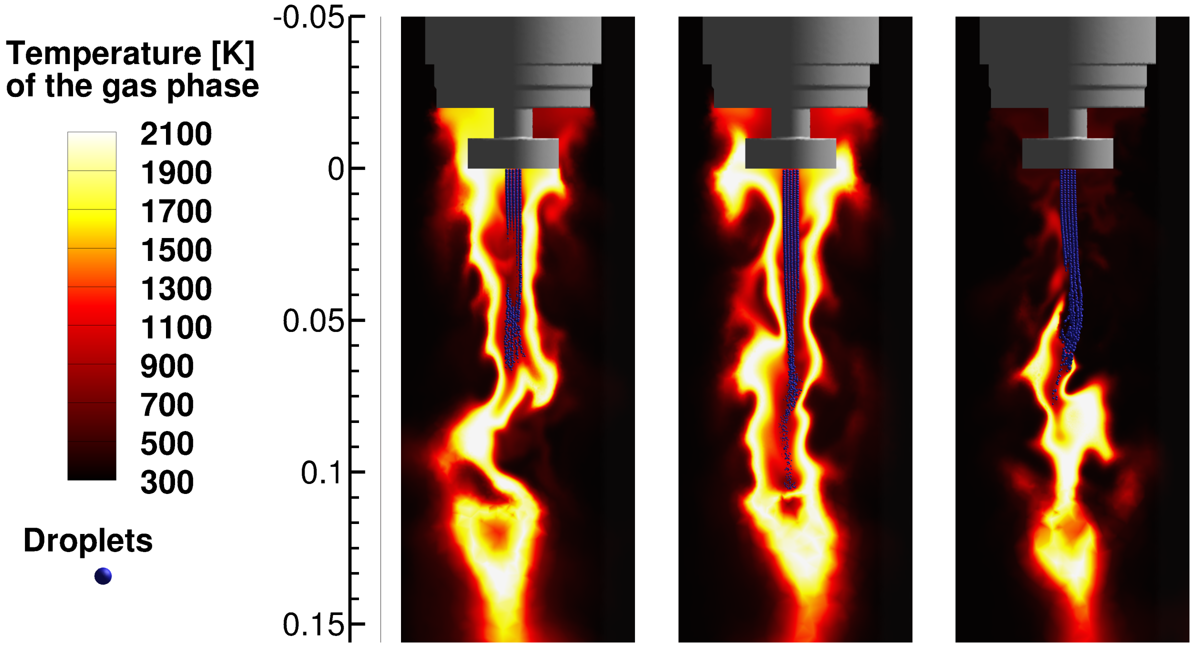

(a) Jet A-1 (b) FSJF (c) Exxsol D80

Figure 4.7.: Close-up with the instantaneous temperature and droplet distribution in the center plane of the simulation

4.2. Entrained-flow gasifier

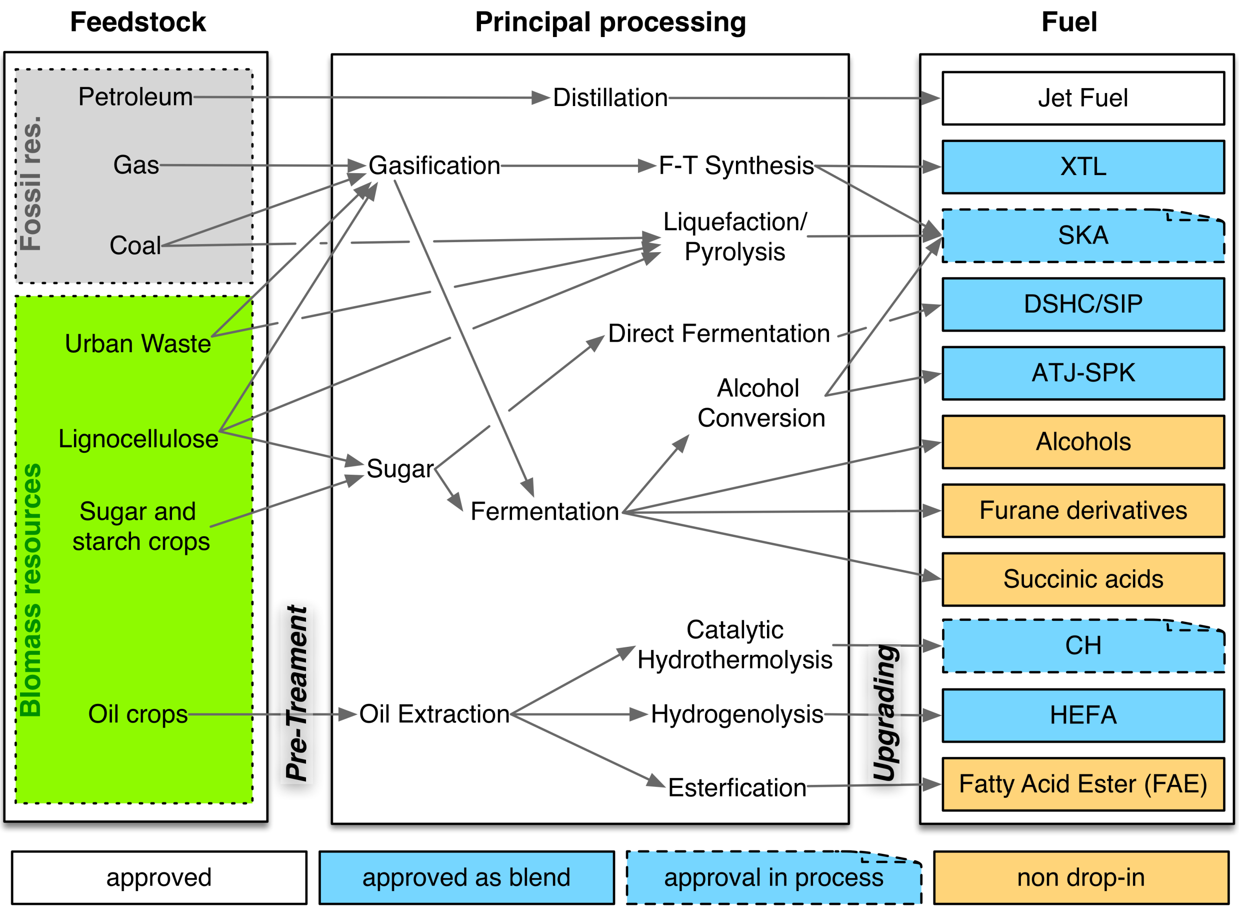

Figure 4.8.: Pathways in the production of alternative fuels (from Rauch (2017))

As mentioned in the introductory section 1.1.2, new challenges arise due to the introduction of alternative fuels. The change towards sustainable aviation fuels comes along with a variety of new fuel production pathways (Fig. 4.8). Resources comprise conventional fossil energy carriers as well as waste and biomass. The diverse feedstocks are processed to high-quality fuels, which can be finally used to store the energy on the aircraft. For a detailed explanation of the entire graph, the reader is referred to Rauch (2017). The focus will be on the gasification process, in particular entrained flow gasification, in the following. While combustion systems aim at converting fuel completely into usable heat, not all feedstock types are easily, and most importantly efficiently directly usable as combustible fuel. Gasification is another thermo-chemical conversion process, which consists in “the conversion of any carbonaceous feedstock to a gaseous product with usable heating value ”(Luque and Speight, 2015), which *stricto sensu*, avoids complete combustion. In practice and in order to be energetically efficient, there is often a portion of the feedstock which is burned. Actually, autothermal gasifiers rely on the partial oxidation of the feedstock to generate the heat for the endothermic thermochemical sub-processes that do also occur in a gasifier. Entrained flow gasification is a promising process for the conversion of low-grade feedstock, e.g. highly viscous slurries and suspensions with a significant content of solid particles, to synthetic gas (syngas). Syngas, a mixture mainly of hydrogen and carbon monoxide, can be used directly as a fuel in gas engines or gas turbines. However, as its energy density is about half the one of natural gas, it is mostly suited for the production of transportation fuels and other chemicals. Actually, syngas is a building block for the production (synthesis) of various fuels in particular synthetic natural gas, methanol, or synthetic liquid fuels: dimethyl ether (DME), gasoline, jet fuel (e.g. Synthetic Kerosene with Aromatics (SKA)) or diesel (Luque and Speight, 2015). The latter liquid fuels are often produced by means of a heterogeneous catalytic process like Fischer-Tropsch (F-T). The prediction of physical and chemical phenomena occurring in high temperature and high pressure multi-phase flow systems such as industrial entrained flow gasifiers remains a major scientific challenge even with modern CFD tools. Numericists face challenges due to the multi-scale nature of the problem, complex fuel compositions and particle topologies as well as the many sub-processes involved. Concerning the multi-scale nature, length scales for example vary from particle sizes of the order of $\mathcal{O}(1-100\mu m)$ to geometrical dimensions of the reaction chamber of the order of $\mathcal{O}(1-10m)$. Time scales differ several orders of magnitude between fast homogeneous reactions ($\mathcal{O}(10^{-3}-10^{-10}s)$) (Warnatz *et al.*, 2006) and residence times of residual fly ash ($\mathcal{O}(10s)$). Velocities range from $\mathcal{O}(100-150m/s)$ in the injector near-field to $\mathcal{O}(0-1m/s)$ in far-field regions. The complex fuel compositions and topologies result from the fact that waste and biomass based slurries are heterogeneous mixtures composed of immiscible liquids (emulsions) and solid non-uniform particles (suspensions).

4.2.1. Test case description

The Research Entrained flow Gasifier (REGA) of the Karlsruhe Institute of Technology, Institute for Technical Chemistry was experimentally investigated by Fleck *et al.* (2018). The atmospheric gasifier consists of a tubular reactor with a length of 3.0 m and an inner diameter of 0.28 m. The liquid fuel (mono-ethylene glycol) is injected at the top of the reactor via a twin-fluid atomizer (Jakobs *et al.*, 2012). The oxidizer consists of oxygen-enriched air and serves as atomizing agent. Flanges and an axially movable burner allow for either intrusive or optical measurements at different downstream distances from the nozzle exit. The side walls of the reactor are maintained at a constant temperature by an electric heater. The temperature measurements were performed with a double bead thermocouple type B. Using correlations, the error due to radiation was corrected. The concentration measurements were carried out by introducing an oil-cooled suction probe with a ceramic tip into the reactor. The coolant had a temperature of 80°C to quench the chemical reactions. Before the gas analysis, the gas sample was filtered and cooled to 3°C in order to remove particles and water. The gas analytics consisted of a standard ABB gas analytics. The concentrations of CO, CO_2, CH_4 were determined by infrared absorption (ABB-Uras14). A magnetomechanical oxygen analyzer (ABB-Magnos106) and a thermal conductivity analyzer (ABB-Caldos17) detected O_2 and H_2, respectively. For details of the measurements the reader is referred to Fleck *et al.* (2018).

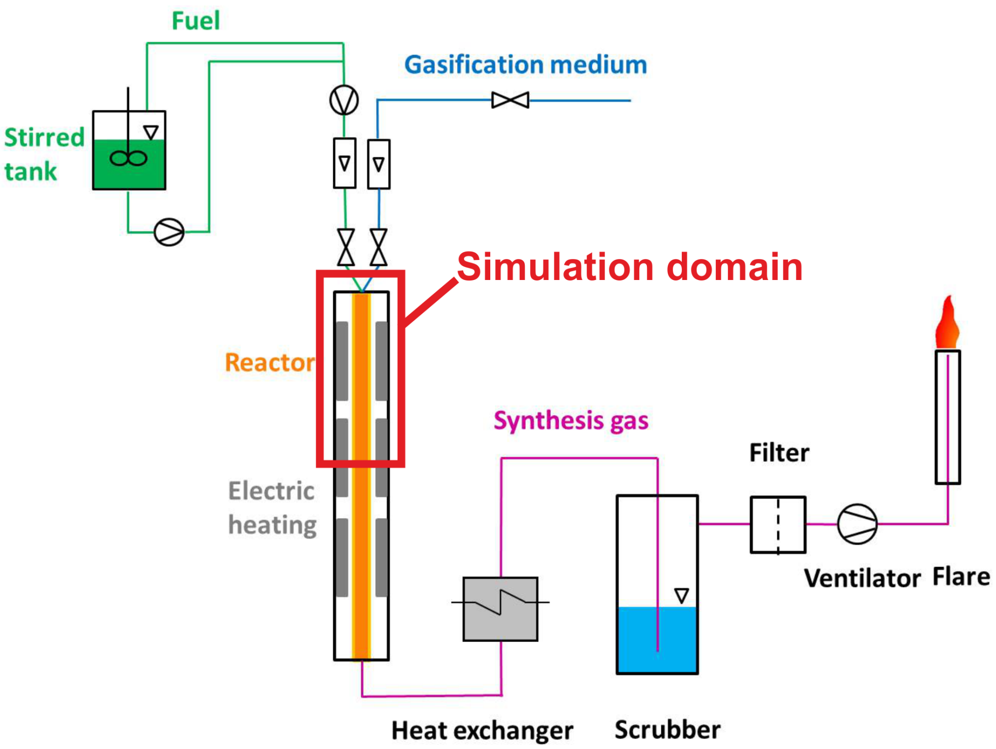

Figure 4.9.: Simulation domain (Schematic of the experimental setup from Fleck *et al.* (2018))

In order to reduce the complexity, experiments and numerical simulations within this study were conducted on a well-defined gas-liquid flow system with a model fuel (mono-ethylene glycol) under atmospheric but realistic flow and temperature conditions. This configuration serves as a reference avoiding the high uncertainties regarding initial slurry composition, heterogeneous reactions and related phenomena. In particular, processes inside the porous particles during gasification are not well understood, up to now (Gräbner, 2014). The model fuel was chosen to be mono-ethylene glycol due to the fact that its chemical structure (C/H-ratio, C/O-ratio), lower heating value and physical properties are comparable to those of pyrolysis oil (details see Fleck *et al.* (2018)).

4.2.2. Numerical setup

Discretization The simulation domain, highlighted in Fig. 4.9, is discretized by a fully unstructured tetrahedral mesh. The grid (Fig. 4.10) is refined within the injector vanes, in the vicinity of the flame, and in near wall regions. This leads to a grid size of 2.7 million points corresponding to 15.9 million volume elements.

Boundary conditions Table 4.3 lists the boundary conditions used in the LES of the REGA-glycol-T1 experiment. The input streams are defined according to the set point defined in Table 4 of Fleck *et al.* (2018). The purge nitrogen is neglected. Furthermore, the leakage air, which was determined by balancing (see Fleck *et al.* (2018)) after the LES was almost completed, is not considered in this computation. The starting conditions for the droplets are derived from Phase Doppler Anemometry (PDA). The twin-fluid atomizer produces a full cone

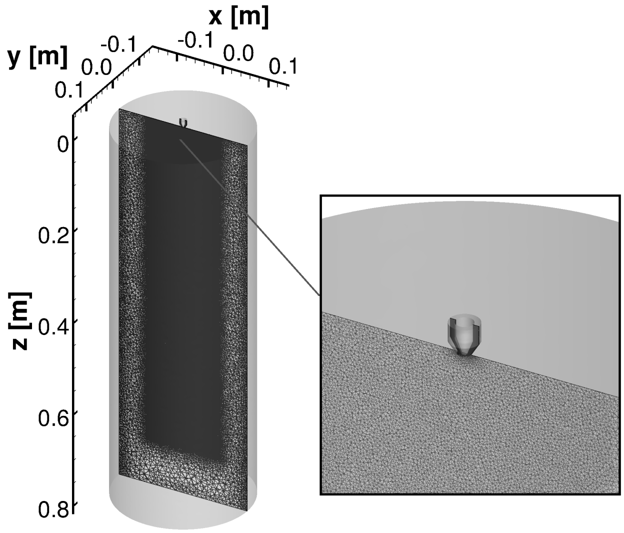

Figure 4.10.: Computational grid of the entrained-flow gasifier test case

Fuel		Mono-ethylene glycol
Gasification medium		O_2-enriched air
Fuel mass flow rate	$\dot{m}_{fuel}$	12.56 kg/h
Mass flow rate of air	$\dot{m}_{air}$	9.05 kg/h
Oxygen mass flow rate	$\dot{m}_{O_2}$	7.11 kg/h
Stoichiometric ratio	$\lambda_{tech}/\lambda_{abs}$	0.57/0.69
Pressure	p_{atm}	1.0 bar
Wall temperature	T_{wall}	1468.15 K

Table 4.3.: Boundary conditions used in the LES of the REGA-glycol-T1 experiment (set point defined in Table 4 of Fleck *et al.* (2018))

spray. The droplet velocity and the liquid mass flow rate peak at the center and decrease towards larger radii. Details concerning the spray characterization can be found in Fleck *et al.* (2018). The graphs indicate a slight w-shape and a Sauter mean diameter ranging from 60 to 80 μm. As measurements close to the atomizer are difficult because of the dense spray as well as non-spherical droplets and ligaments (Tropea, 2011), the PDA was performed 50 mm downstream of the nozzle. However, the simulations require droplet starting conditions close to the nozzle exit as the heat-up of the spray strongly influences the position of the reaction zone. Hence, the measured profiles (50 mm downstream) are projected to a starting plane 3 mm away from the nozzle exit plane, using the intercept theorem. In this starting plane, the starting positions of the droplets are randomly generated during run-time. The characteristic droplet diameters, velocities and mass flow rates at the starting positions are obtained by linear interpolations between the experimental values at the projected points. As PDA measurements of the absolute mass flow rate have high uncertainties (Tropea, 2011), the local mass flow rate is determined by using the relative information obtained by the PDA in conjunction with the total mass flow rate supplied by the mass flow controller. An automated fitting routine is used to determine the optimum size distribution based on the characteristic diameters for each starting location. This results in a log-normal distribution close to the centerline and a log-Rosin-Rammler distribution towards larger radii. The quality of this procedure is verified by a comparison of the droplet size distribution for the entire spray illustrated in Fig. 4.11. Red bars represent the measured droplet size distribution. The blue line shows the droplet size distribution resulting from the summation of the fitted droplet size distributions of the individual starting positions. Despite the excellent agreement, it should be noted that this procedure of setting spray boundary conditions is based on approximation and introduces errors as detailed information at the location of interest is not available.

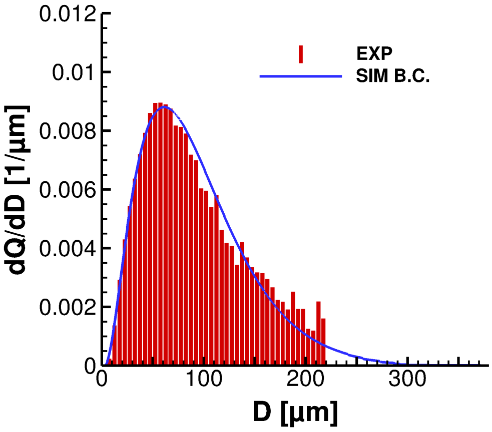

Figure 4.11.: Comparison of the measured (red bars) and fitted (blue line) volumetric droplet size distributions for the entire spray

Reaction mechanism The reduced reaction mechanism of mono-ethylene glycol used within this study originates from the detailed reaction mechanism of Hafner (2010); Hafner *et al.* (2011) containing 81 species and 666 elementary reactions. It includes reactions of mono-ethylene glycol with base C1-C4 chemistry. Being unimportant to the mono-ethylene glycol system, mainly reactions of the C3-C4 chemistry were removed resulting in a reduced reaction mechanism of 44 species and 329 reactions. The fuel mono-ethylene glycol is consumed mainly via decomposition reactions or by removal of H-atoms via abstraction reactions. The H-abstraction leads to fuel radicals $HOCH_2CHOH$ and $HOCH_2CH_2O$, the latter being less likely to form than the secondary fuel radical $HOCH_2CHOH$. In the fuel decomposition channel, the main reactions are the C-C bond breaking of mono-ethylene glycol resulting in two hydroxy-methyl radicals as well as the C-O and O-H bond dissociation finally reforming to acetaldehyde. Further decomposition and intermediate formation chemistry is governed by the kinetics of these species.

4.2.3. Results

4.2.3.1. Overall flow features

The fuel is injected at the top of the gasifier. Disrupted and accelerated by the surrounding high-velocity oxidizer jet, the spray disperses in the reaction chamber interacting with turbulent structures (Fig. 4.12). While dispersing, the spray is heated up by the high gas temperature in the combustion region and starts to vaporize. The droplets reduce in size until they are completely evaporated. Under the present conditions, the bigger mono-ethylene glycol droplets finish evaporating in the range 600-800 mm.

4.2.3.2. Axial velocity and temperature fields

As the high-velocity oxidizer stream passes the nozzle exit, vortices are shed from the sharp corner of the injector. This can be seen in Fig. 4.13a, where the contour plot of the instantaneous axial velocity in the center plane is displayed, with streamlines also plotted in the right-hand half. The time-averaged axial velocity (Fig. 4.13b) shows the vortex street forming a large recirculation zone. It reaches 0.8 m downstream of the nozzle and covers the entire radial direction from the jet center to the confinement of the reactor. Fig. 4.13 shows how the simulation takes full advantage of the LES features in the near injector region. At the length and time scales defined by the injector geometry and the incoming mass flow rate, the LES turbulence model captures the development of coherent structures. These coherent structures result very rapidly in a highly unsteady turbulent mixing-layer and contribute substantially to the local mixing between the incoming enriched air, the recirculating syngas, and the liquid fuel droplets. The time-averaged axial velocity (Fig. 4.13b) is characterized by length and time scales closer to the integral scales of the reactor, thus closer to what one could expect from a RANS turbulence model. At integral scales, the confined turbulent jet-flow is the main driver of the recirculation, which brings the gaseous components stemming from the chemical reactions along the jet axis back into the near injector region. Although the details of the twin-fluid atomizer (injection of liquid in the middle and surrounding enriched-air impinging upon it (Jakobs *et al.*, 2012)) depart from a classical confined jet, from a fluid dynamics perspective the flow generated downstream the injector is qualitatively similar to it. The Reynolds number based on the hydraulic diameter of the nozzle and the average velocity through the nozzle annulus is equal to 28800 (turbulent). Fig. 4.14 depicts the instantaneous (Fig. 4.14a) and time-averaged (Fig. 4.14b) temperature field in the center plane of the reaction chamber. From the flow patterns and the temperature field, five zones characterizing the near field of the injector can be defined:

1. Jet-flow along the axis close to the injector ($0 < z < 0.1$ m): This region is the potential core of the jet, which expands radially and entrains the surrounding fluid. It is characterized by a high velocity of 110 m/s and by relatively low temperatures of $300 < T < 1500$ K.

2. Jet-flow along the axis further downstream from the injector ($0.1 < z < 0.4$ m): This region is characterized by a reduced axial velocity of $40 <$ z-velocity < 100 m/s, with respect to the near injector jet region and high temperatures of $T > 2100$ K.

3. Transition region where the jet goes from occupying nearly half to almost the entire reactor cross-section ($0.4 < z < 0.8$ m). This region is characterized by moderate axial

velocities of $10 <$ z-velocity < 40 m/s and relatively high temperatures of $1500 < T < 2100$ K.

4. Mixing-layer, which is the thin layer surrounding the incoming jet close to the injector. This region is characterized by high velocity gradients and high temperatures ($T > 2100$ K).
5. Recirculation zone (see streamlines in Fig. 4.13b). This region is characterized by low velocities (i.e. a long residence time) and by an average temperature of around 1500 K.

This definition will assist the analysis of the different reaction zones as well as the flame stabilization mechanism later on.

4.2.3.3. Vapor concentration

Ethylene glycol is injected at ambient temperature (300 K). It evaporates slowly along the expanding jet (Zone 1, 2, and 3). The evaporation of the droplets results in the mono-ethylene glycol vapor concentration field shown in Fig. 4.15a for an instantaneous snapshot and Fig. 4.15b for the time-averaged field; both in the center plane. The exponential scale allows displaying several orders of magnitude in the concentration values. The mono-ethylene glycol instantaneous vapor concentration (Fig. 4.15a) and consumption rates (Fig. 4.15c) demonstrate that predominant length scales differ among the zones defined above. While Zone 1 is densely populated, these fields have a discrete character in Zone 2. This is related to the fact that they stem from the discrete numerical parcels representing the evaporating liquid droplets. It should be noted that the color scale of all figures displaying the production rate (in red) and the consumption rate (in blue) (Fig. 4.15c to Fig 4.20c) is adjusted to emphasize details. Consequently, the intensity of the blue or red cannot be directly correlated to the instantaneous concentrations displayed on the far left of each series.

4.2.3.4. Main reaction paths and species concentrations

Ethylene glycol has to decompose before reacting. The decomposition reactions consuming the mono-ethylene glycol (Fig. 4.15c) lead to the formation of hydrogen (Fig. 4.16c) and carbon monoxide (Fig. 4.17c). Carbon monoxide (CO) is formed as mono-ethylene glycol ($HOCH_2CH_2OH$) decomposes to acetaldehyde (CH_3CHO) in a thermal major decomposition reaction $HOCH_2CH_2OH \rightarrow CH_3CHO + H_2O$. The acetaldehyde is then converted to CH_3CO by H-abstraction reactions which further decomposes to CO (and CH_3). Similarly, CH_2OH is formed in a second major mono-ethylene glycol decomposition reaction ($HOCH_2CH_2OH \rightarrow 2\ CH_2OH$). This species is another source of CO through reactions with oxygen O_2 or H-abstraction reactions following the pathway $CH2OH \rightarrow CH2O \rightarrow CHO \rightarrow CO$. The main sources of hydrogen (H_2) are the decomposition reaction of mono-ethylene glycol to glycolaldehyde $HOCH_2CH_2OH \rightarrow HOCH_2CHO + H_2$ and the H-abstraction reactions of acetaldehyde $CH_3CHO + H \rightarrow CH3CO + H_2$. In regions of high temperatures, hydrogen can be additionally produced by $CH_2O + H \rightarrow HCO + H_2$. As can be seen in Fig. 4.16c and Fig. 4.17c, carbon monoxide and hydrogen, i.e. the syngas, are mainly produced on the jet axis (Zone 1 and Zone 2) of the reactor. Precisely, the syngas is produced at the edge of the jet core in Zone 1 and also within Zone 2, at the scale of the liquid spray (see red dots characterizing the production along the axis in Fig. 4.16c and 4.17c). This demonstrates that the syngas stems directly from the decomposition of the mono-ethylene glycol droplets. Thereafter, CO and H_2 are transported back upstream by the recirculating flow in Zone 5. This results in the concentration fields of H_2 and CO illustrated in Fig. 4.16a, 4.16b and Fig. 4.17a, 4.17b, respectively. As the recirculated syngas encounters and mixes with the oxygen-rich region close to the injector, Zone 1 (Fig. 4.18), hydrogen and oxygen immediately react (see consumption of O_2 in Fig. 4.18c, especially in the mixing-layer region) to water in a thin layer wrapping the area of high oxygen concentration (Fig. 4.19). The recirculated carbon monoxide reacts with the oxygen forming CO_2 (Fig. 4.20). The water production on the centerline within the first 0.1 m (Fig. 4.19c) originates directly from the fuel and is a result of the decomposition reaction of mono-ethylene glycol to acetaldehyde described above. Comparing Fig. 4.16c, 4.17c, 4.19c and 4.20c, inverted regions of production and consumption can be observed. This is a consequence of the elementary reactions summing up to the homogeneous water-gas shift reaction $CO + H_2O \rightleftharpoons CO_2 + H_2$. The equilibrium of this chain of elementary reactions is highly temperature dependent, i.e. the equilibrium constant decreases with an increase in temperature (Bustamante *et al.*, 2004). Hence, with rising temperature the equilibrium is shifted towards the water gas (CO and H_2O) and vice versa. More specifically in the mixing-layer, the inverted regions correspond to a competition between oxidation reactions and water-gas shift reactions. When locally and temporarily there is no O_2 to mix with H_2, then the abundant H_2 delivered by the recirculating flow reacts with the CO_2 stemming from the CO oxidation. This can be seen in the thin outer sub-layer of the mixing-layer, which is colored red in Fig. 4.17c (CO production) and colored blue in Fig. 4.20c (CO_2 consumption). Then, further inside the mixing-layer, CO is being consumed through the oxidation reaction thus colored blue in Fig. 4.17c and CO_2 is being produced thus colored red in Fig. 4.20c. In summary, due to the competing effect of the CO oxidation reaction and the water-gas shift reaction, there is a non-uniform and temporally alternating production and consumption of CO and H_2O in the radial as well as axial directions. These are slightly discernible in the instantaneous concentration contour plots (Fig. 4.17a and Fig. 4.19a) but are smoothed out in the averaged field (Fig. 4.17b and Fig. 4.19b). The temperatures and fluid dynamic time scales in each separate sub-region determine which reaction prevails showing the importance of such detailed computations.

4.2.3.5. Flame stabilization mechanism

The high temperature region (Fig. 4.14), which builds up from the early stages of the developing mixing-layer, close to the injector (Zone 4), cannot be explained by a direct reaction of the fuel with the oxidizer. The syngas recirculation and the subsequent syngas oxidation reactions occurring in the mixing-layer, as described above, stabilize the flame. Flames anchored very close to the injector tip can be detrimental to the integrity and durability of the burner. This should be investigated when up-scaling the reactor and defining the fuel composition/morphology.

4.2.3.6. Temperature and species profiles

Fig. 4.21 and Fig. 4.22 show the time- and angular-averaged radial temperature and species distributions, respectively. The downstream positions, where the profiles were extracted, are depicted in Fig. 4.21a and Fig. 4.22a. The scenario described above by means of the contour plots is also reflected in the temperature and species line plots. Close to the injector the local excess of oxidizer leads to an immediate reaction of the recirculated gas with the oxygen (Fig. 4.21b) resulting in high temperatures at the flanks of the oxidizer jet while the jet center remains at the inflow temperature (Fig. 4.22b). As the oxygen is more and more consumed further downstream, the elementary reactions summing up to the homogeneous water-gas shift reaction gain in importance (see H_2 and CO_2 concentrations). At a downstream distance of about 0.2 m, the unsteadiness of the system and the resultant enhanced mixing as well as diffusion processes cause both temperature and species to smooth out until the distributions in Fig. 4.21h and 4.22h are reached being close to equilibrium. While a good agreement between experiment and simulation can be observed in terms of temperature trends, the absolute temperature was slightly overestimated in the simulation (Fig. 4.21g and 4.21h). Small discrepancies can also be observed with respect to the species distributions (Fig. 4.22g and 4.22h). The differences may be due to two effects. Firstly, the inspection windows at the flanges were equipped with a purging system. Secondly, the balancing, presented in Fleck *et al.* (2018), revealed that infiltration air entered the gasifier at an unknown entry point. Both the purging medium, i.e. nitrogen (0.64 kg/h), and the infiltration air (1.93 kg/h) were not considered in the computations presented in this thesis. Equilibrium calculations accounting for the purge nitrogen and the infiltration air showed a negligible effect on temperature ($\varDelta T = 15K$) but an impact on the concentrations showing a decrease in CO ($\varDelta X_{CO,N_2-free} = -2.8\%$) and H_2 ($\varDelta X_{H_2,N_2-free} = -5.2\%$) concentrations as well as an increase in CO_2 concentration ($\varDelta X_{CO_2,N_2-free} = 8.2\%$). As a consequence, the deviations in the species concentrations shown in Fig. 4.22h could be attributed to differences in the boundary conditions due to the neglected purging agent and the leakage of the experimental setup. Nevertheless, uncertainties related to the chemical kinetics mechanism used within this study cannot be excluded.

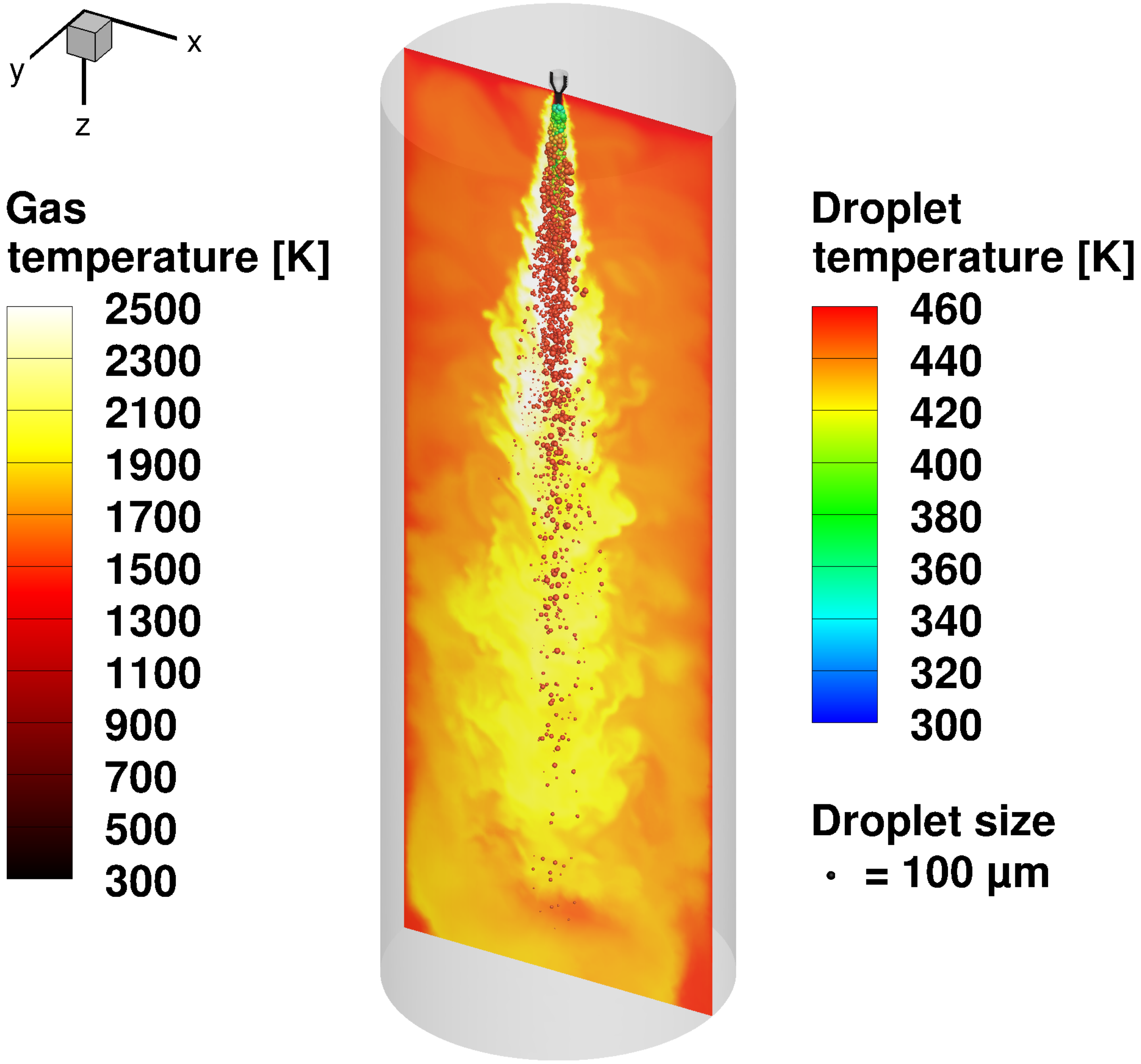

Figure 4.12.: Droplet dispersion and heat up in the entrained-flow gasifier

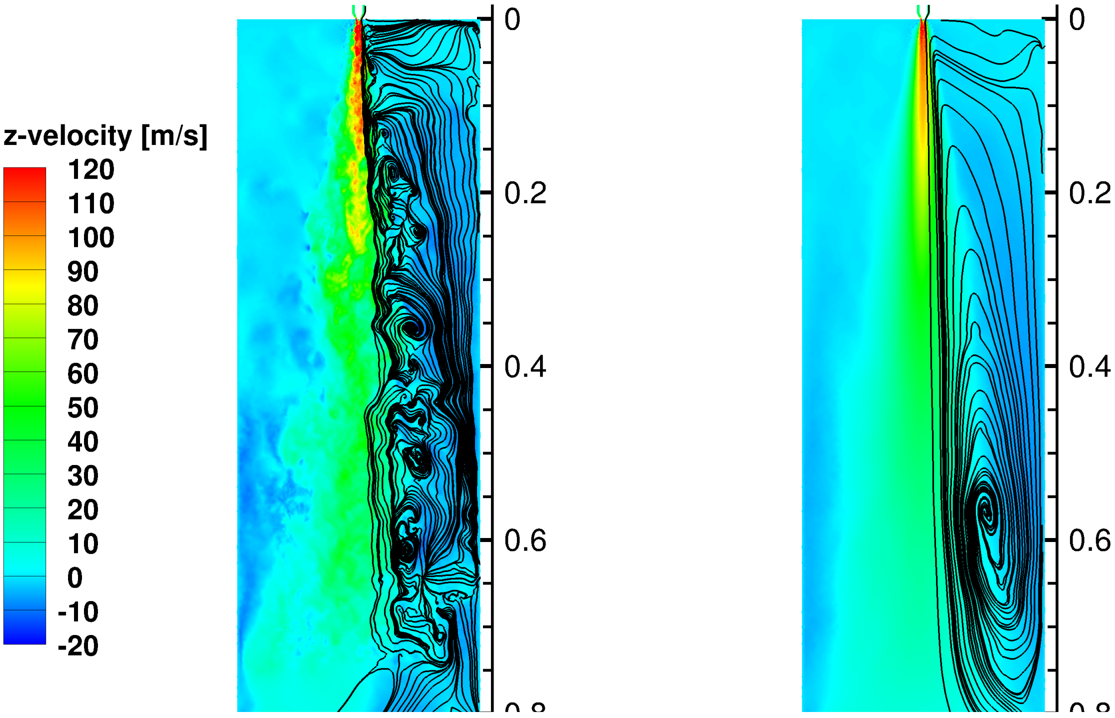

(a) instantaneous (b) time-averaged

Figure 4.13.: Flow field

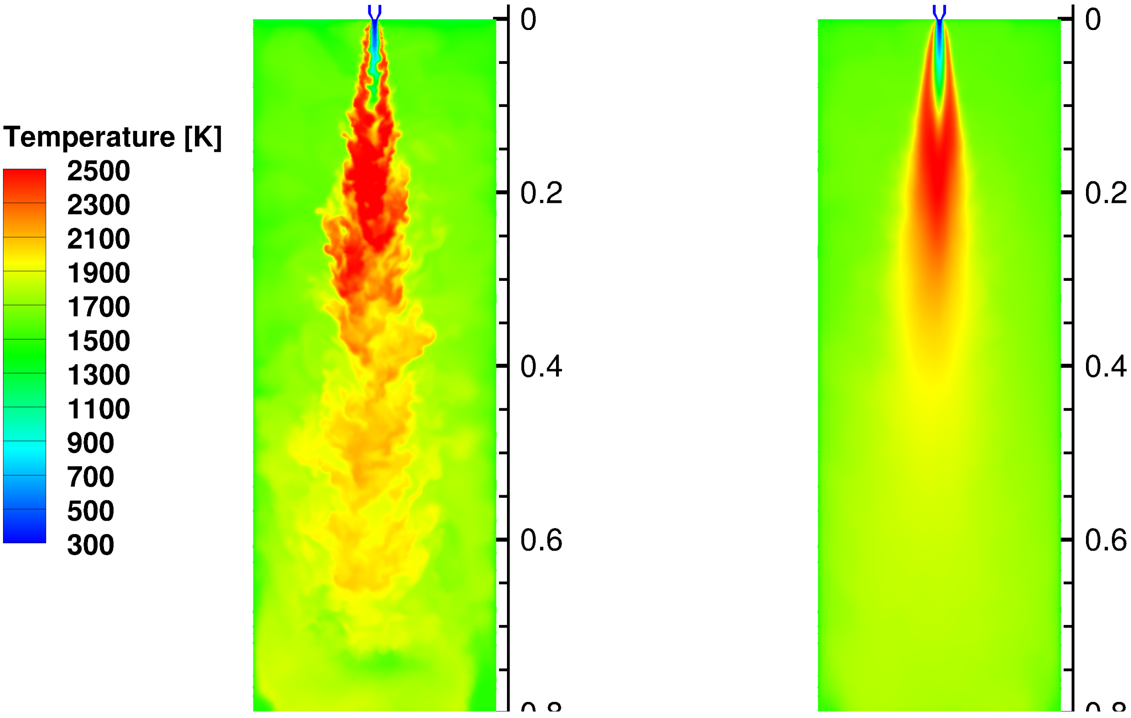

(a) instantaneous (b) time-averaged

Figure 4.14.: Temperature field

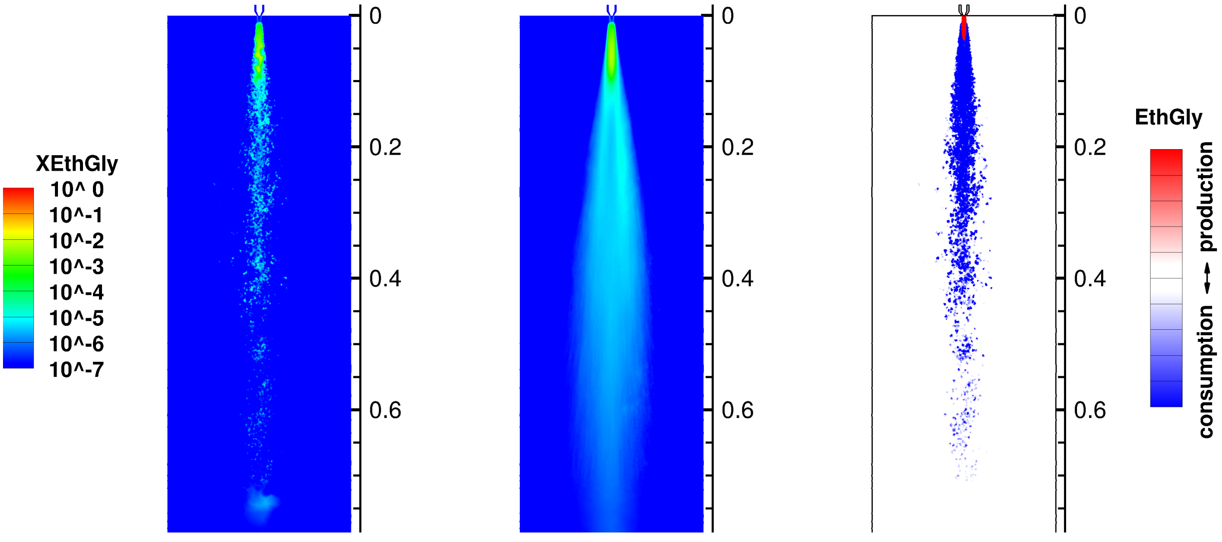

(a) (b) (c)

Figure 4.15.: Instantaneous (a) and time-averaged (b) gas concentration field (exp. scale) as well as instantaneous net production / consumption rate (c) of mono-ethylene glycol

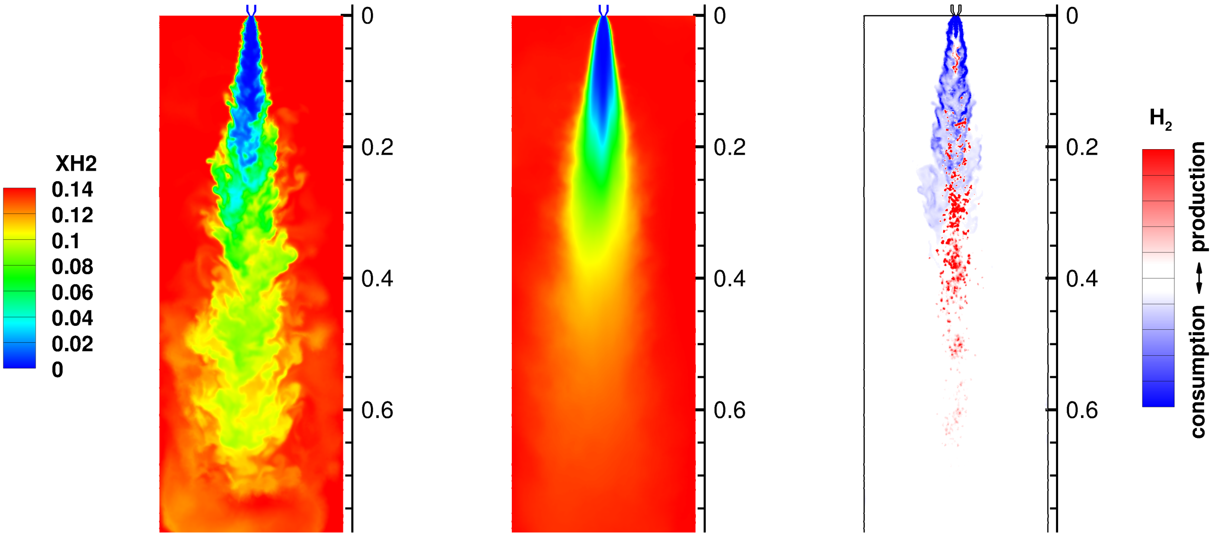

(a) (b) (c)

Figure 4.16.: Instantaneous (a) and time-averaged (b) gas concentration field as well as instantaneous net production / consumption rate (c) of H_2

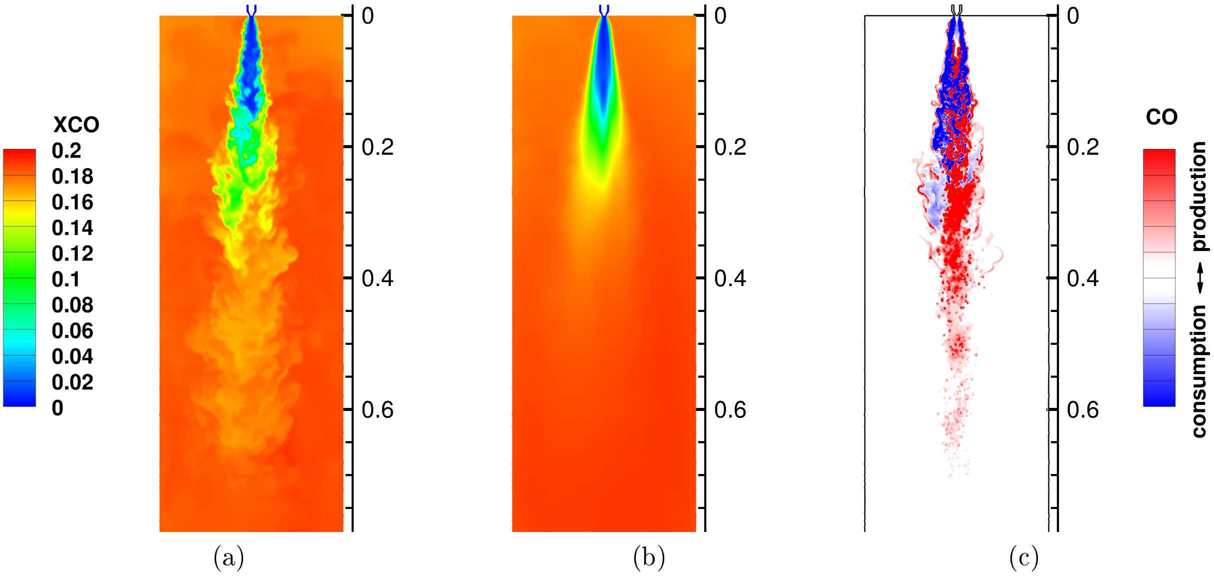

Figure 4.17.: Instantaneous (a) and time-averaged (b) gas concentration field as well as instantaneous net production / consumption rate (c) of CO

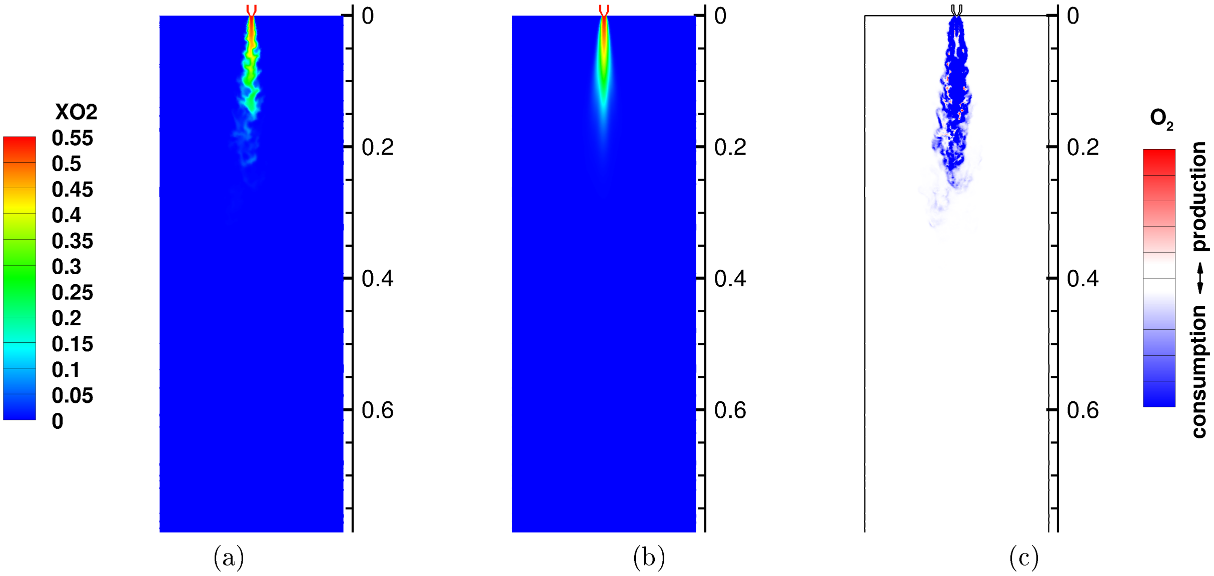

Figure 4.18.: Instantaneous (a) and time-averaged (b) gas concentration field as well as instantaneous net production / consumption rate (c) of O_2

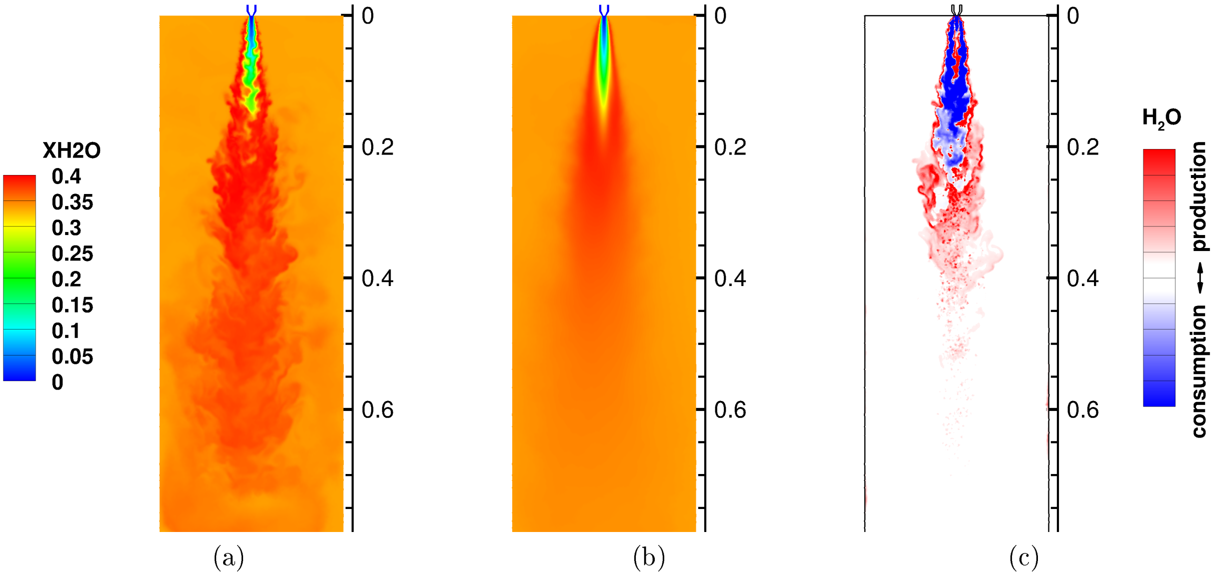

(a) (b) (c)

Figure 4.19.: Instantaneous (a) and time-averaged (b) gas concentration field as well as instantaneous net production / consumption rate (c) of H_2O

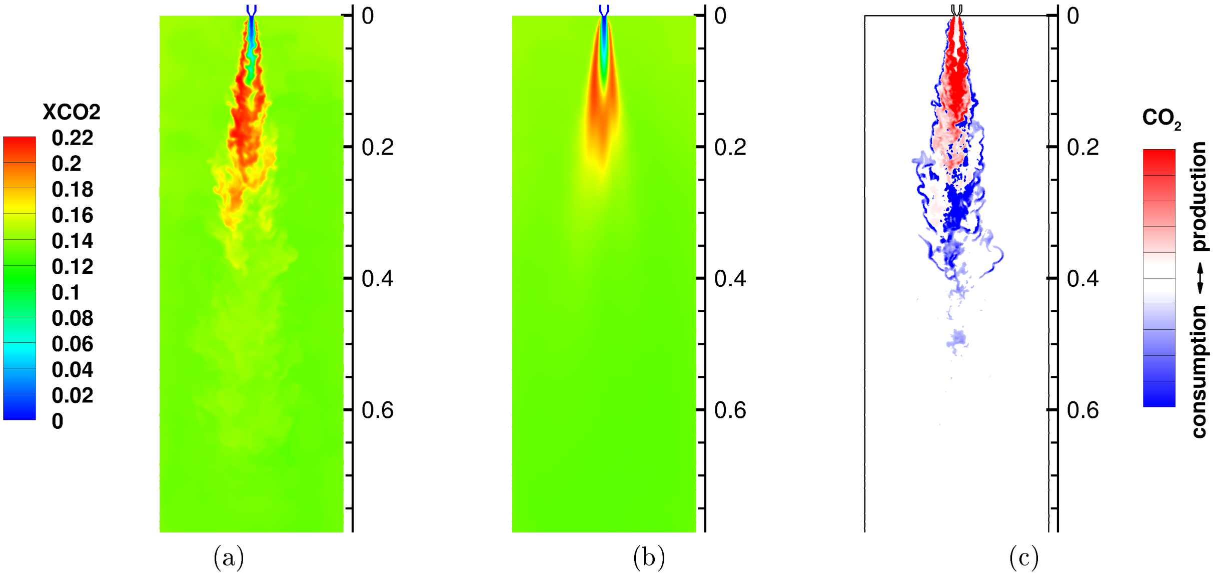

(a) (b) (c)

Figure 4.20.: Instantaneous (a) and time-averaged (b) gas concentration field as well as instantaneous net production / consumption rate (c) of CO_2

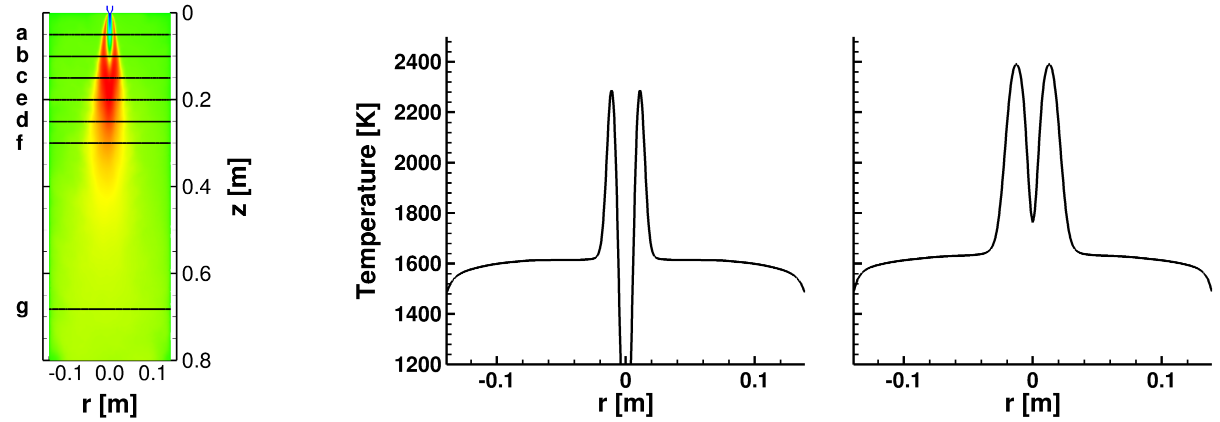

(a) Positions (b) z = 0.050 m (c) z = 0.100 m

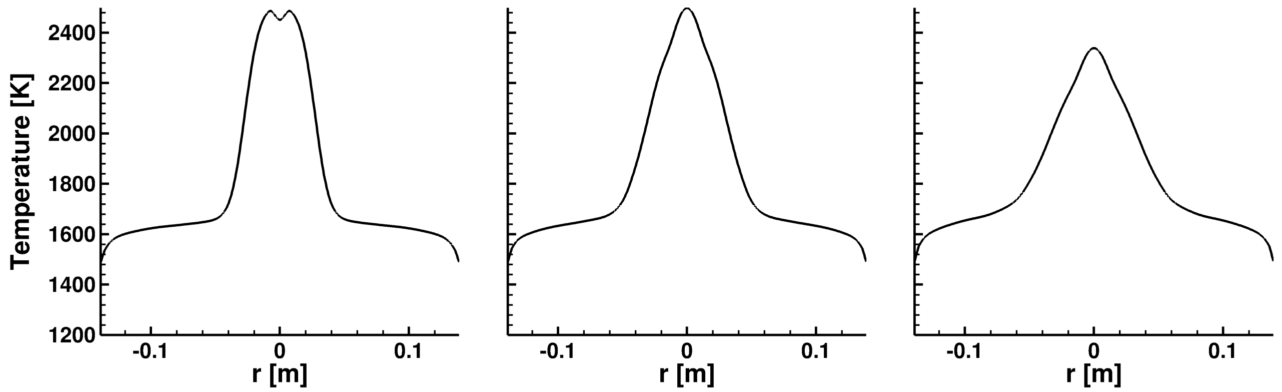

(d) z = 0.150 m (e) z = 0.200 m (f) z = 0.250 m

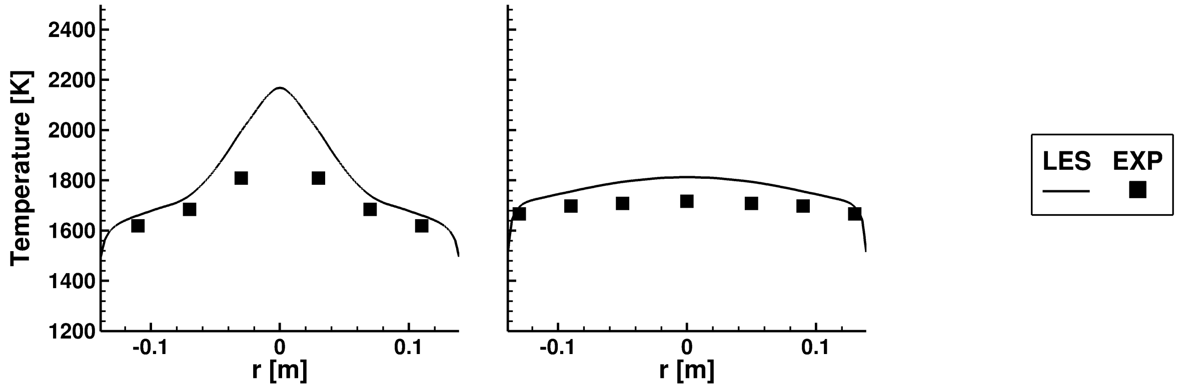

(g) z = 0.300 m (h) z = 0.682 m

Figure 4.21.: Time- and angular-averaged radial temperature distribution (b)-(h) at the downstream positions depicted in (a): LES (lines) and experimental data (squares)

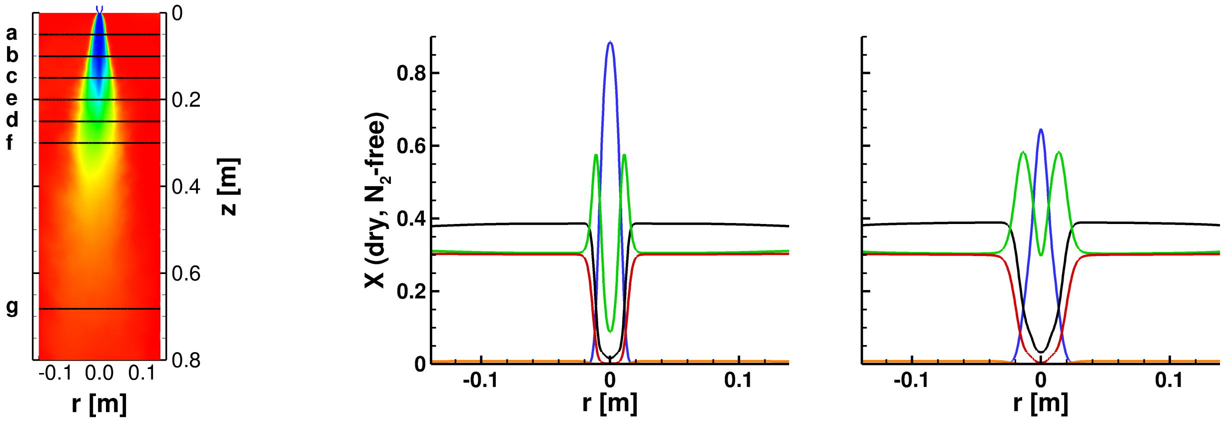

(a) Positions (b) z = 0.050 m (c) z = 0.100 m

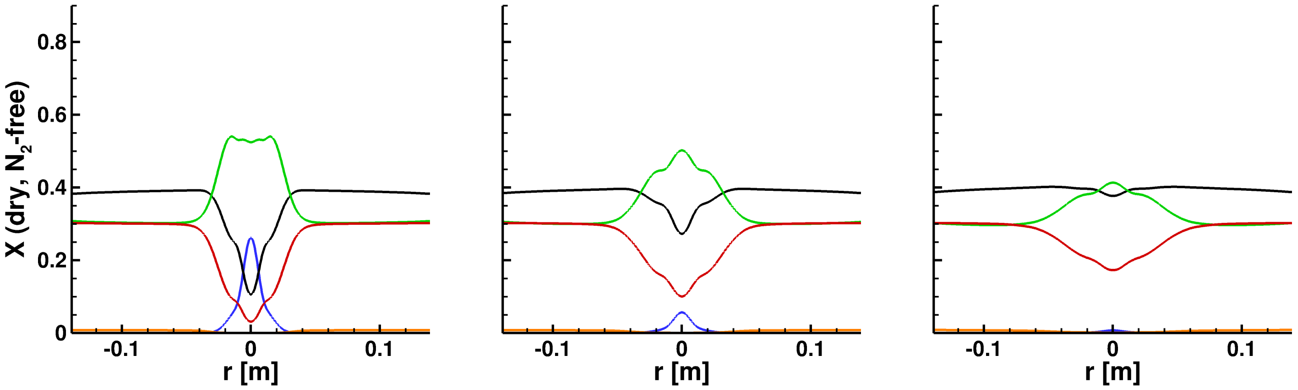

(d) z = 0.150 m (e) z = 0.200 m (f) z = 0.250 m

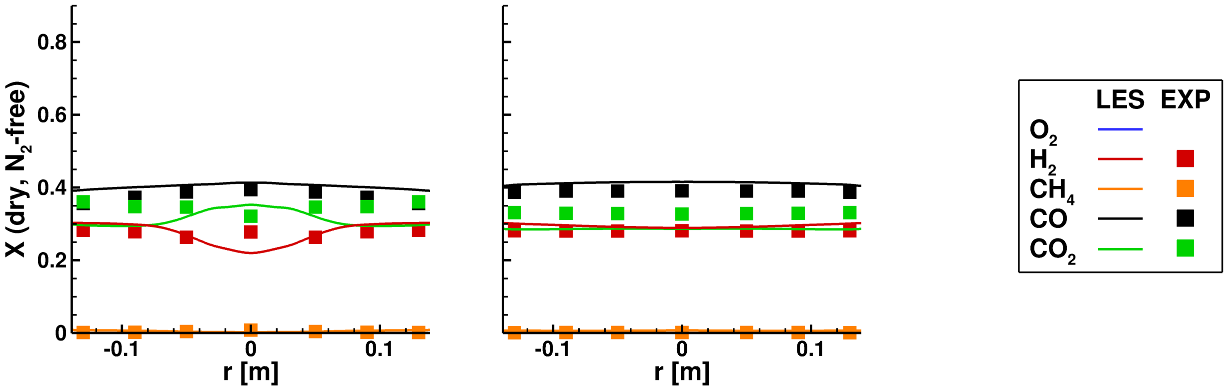

(g) z = 0.300 m (h) z = 0.682 m

Figure 4.22.: Time- and angular-averaged radial species concentration distributions (b)-(h) at the downstream positions depicted in (a): LES (lines) and experimental data (squares)

4.3. Swirl-stabilized spray burner

4.3.1. Test case description

The generic swirl-stabilized spray burner with a pre-filming airblast atomizer was experimentally investigated by Grohmann *et al.* (2016a,b). It provides good optical accessibility by means of a 90 x 90 x 170 mm vitreous combustion chamber. Air pre-heated up to 423 K can be supplied with a volume flow rate of 200 to 600 l/min. The maximum fuel mass flow rate amounts to 5 kg/h. For the thesis at hand the baseline condition listed in Table 4.4 is chosen for the simulation. The cold gas flow field was measured by Particle Image Velocimetry (PIV). Phase Doppler Anemometry (PDA) and a Mie-scattering technique were applied to determine the spray distribution. The reactive case was qualitatively characterized by CH^*-Chemiluminescence. Furthermore, temperature measurements were performed applying Coherent Anti-Stokes Raman Scattering (CARS) spectroscopy.

Fuel	Jet A-1		
Liquid temperature	T_{liq}	$[K]$	303
Fuel mass flow rate	$\dot{m}_{fuel}$	$[g/h]$	850
Oxidizer	Air		
Air pressure	p_{air}	$[bar]$	1.0
Air temperature	T_{air}	$[K]$	323
Air volume flow rate	$\dot{V}_{air}$	$[l/min]$	200
Global equivalence ratio	ϕ	[-]	0.8
Thermal power	$P_{thermal}$	[kW]	10.2

Table 4.4.: Boundary conditions of the experiment at baseline conditions

4.3.2. Numerical setup

Discretization The computational domain shown in Fig. 4.23 comprises the combustion chamber and the air supply system including both swirlers. Due to its complexity, the geometry is discretized by a fully unstructured tetrahedral mesh. The grid is refined within the swirler vanes, the mixing zone and in the vicinity of the flame as well as in near wall regions. This leads to a grid size of 14.7 million points corresponding to 80.7 million volume elements.

Chemical kinetics mechanism The detailed chemical reaction mechanism for Jet A-1 consists of $N_{sp} = 80$ species and a set of $N_r = 464$ elementary reactions. The basis of this mechanism was the 76 species kerosene mechanism from Slavinskaya *et al.* (2015). Sub-mechanisms for the formation of thermal NO and OH^* were added from Smith *et al.* (2000) and Kathrotia (2011), respectively.

Description of the liquid mixture The composition of the Jet A-1, which was burned in the experiment, was equivalent to Fig. 4.3a. In the simulation, the kerosene is represented by a multi-component mixture based on the chemical analysis. Vaporization is modeled by the multi-component vaporization model (section 2.3.3.3) approximating the discrete species

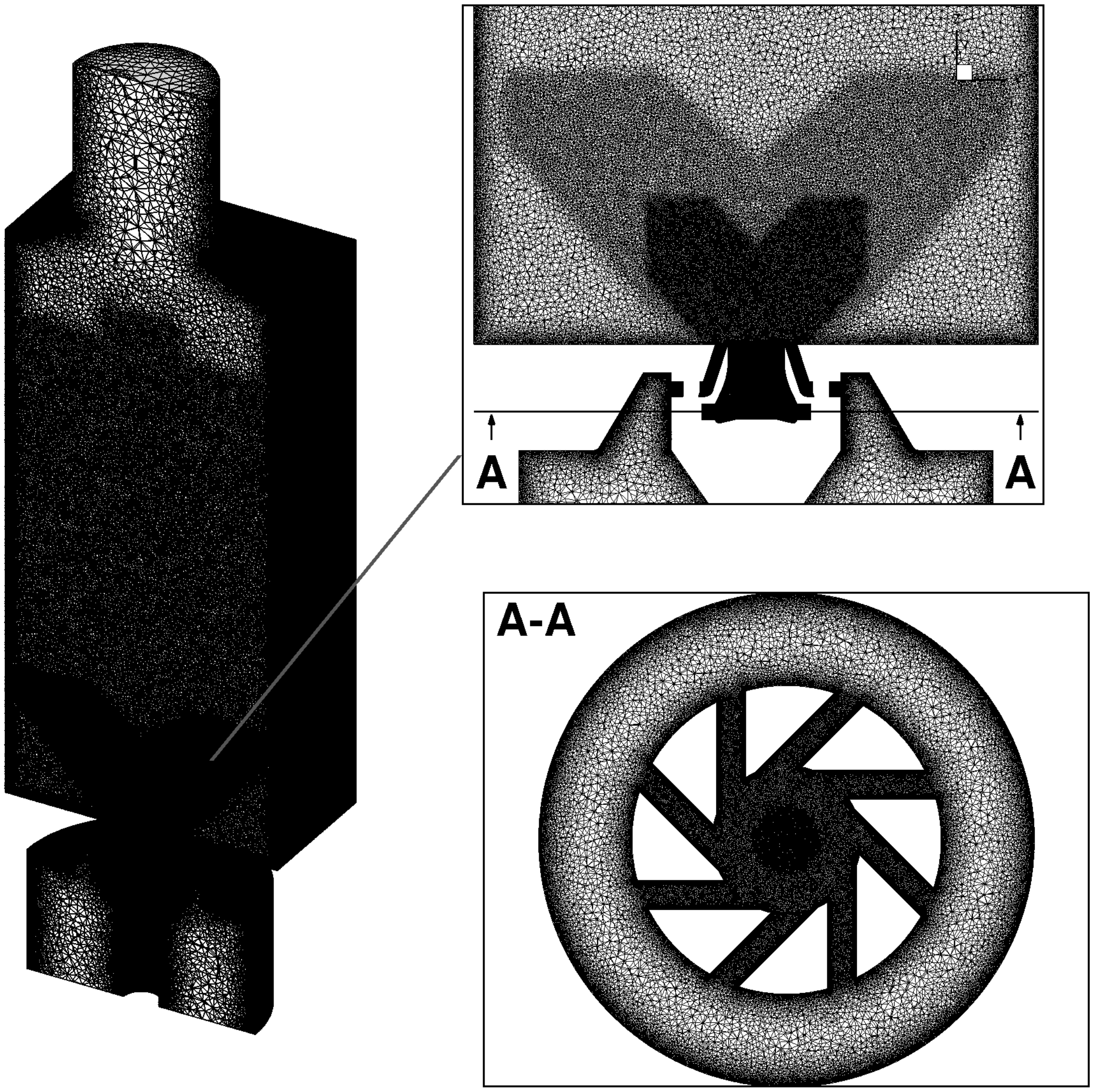

Figure 4.23.: Computational grid for the swirl-stabilized burner test case

distributions by a continuous description via gamma PDFs. The components are grouped into a PDF for each of the four main fuel families (n-alkanes, iso-alkanes, cyclo-alkanes, and aromatics). The coupling of fuel vapor species to the chemical surrogate in the gas field CFD code is established by assigning one equivalent gaseous species for each family according to Table 4.2.

Wall boundary conditions The wall temperatures were experimentally determined by phosphor thermometry. On the bottom plate of the combustion chamber, three zones can be identified (see Fig.4.24). According to the measured temperatures in these zones, the temperatures are set to a constant value of 717 K, 901 K and 831 K in the central part, the glowing ring and the corners of the bottom plate, respectively. The side windows are set to a constant temperature of 1205 K being the average temperature of 36 measurement positions (10-120 mm above the burner). All other walls, e.g. within the swirler vanes, the plenum and the outlet, are assumed to be adiabatic.

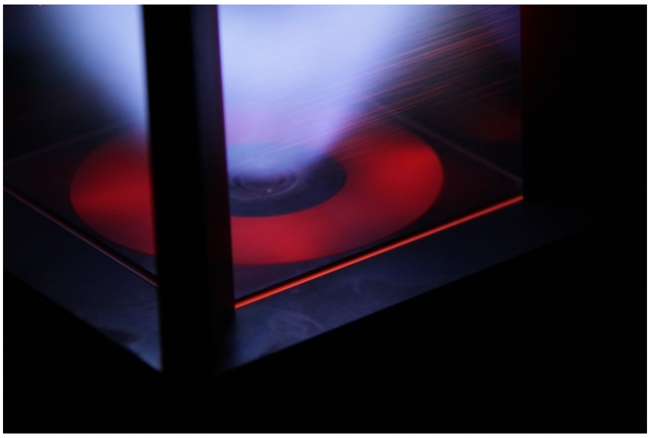

Figure 4.24.: Glowing base plate in the ignited swirl-stabilized spray burner (Grohmann and Nau, 2015)

Droplet starting conditions The starting conditions for the droplets are derived from PDA measurements. As already mentioned in section 4.2, measurements close to atomizers are difficult because of the dense spray as well as non-spherical droplets and ligaments (Tropea, 2011). Hence, the PDA sampling volumes were located 15 mm downstream of the nozzle. However, the simulation requires droplet starting conditions close to the nozzle exit as the heat-up of the spray strongly influences the position of the reaction zone. The same procedure as described in 4.2 is followed. Using the intercept theorem, the measured profiles are projected to an annular area 1.5 mm above the pre-filmer lip with an inner and outer diameter of 7 mm and 9 mm, respectively. Within this area, the starting positions of the droplets are randomly generated during run-time. An automated fitting routine determines the optimum size distribution based on the characteristic diameters for each starting location. This results in a combination of modified log-Rosin-Rammler and root-normal distributions at smaller radii and log-Rosin-Rammler distributions towards larger radii of the annular area. As PDA measurements of the absolute mass flow rate have high uncertainties (Tropea, 2011), the local mass flow rate is determined by using the relative information obtained by PDA in conjunction with the total mass flow rate supplied by the mass flow controller.

4.3.3. Results

4.3.3.1. Flow features of the cold single-phase flow

Fig. 4.25 shows the instantaneous and time-averaged (162.5 ms) flow field of the cold single-phase flow. It can be seen from Fig. 4.25a that a highly unsteady turbulent flow is present in the combustion chamber. The air exits the nozzle with a high velocity which induces the generation and shedding of small vortices from the sharp edges. A time-average of the velocity data reveals large (integral scale) flow recirculations (Fig. 4.25b). A small central recirculation zone forms close to the nozzle exit (-10 mm $< y <$ 10 mm, 0 mm $< z <$ 20 mm). The swirling flow leads to a radial pressure gradient with a low pressure region towards the axis (Syred, 2006). The expansion after the nozzle causes a decay of the tangential velocity equalizing the radial pressure profile. As a consequence, a negative axial pressure gradient builds up close to the z-axis resulting in a flow reversal. Due to the confinement and driven by the high momentum air, two pairs of counter-rotating external recirculations establish close to the walls. The low pressure zone close to the central z-axis described before supports the backflow towards the nozzle. Fig. 4.25c depicts experimental data taken by PIV. The agreement of the qualitative flow features between the PIV measurements and the LES prediction in Fig. 4.25b is excellent.

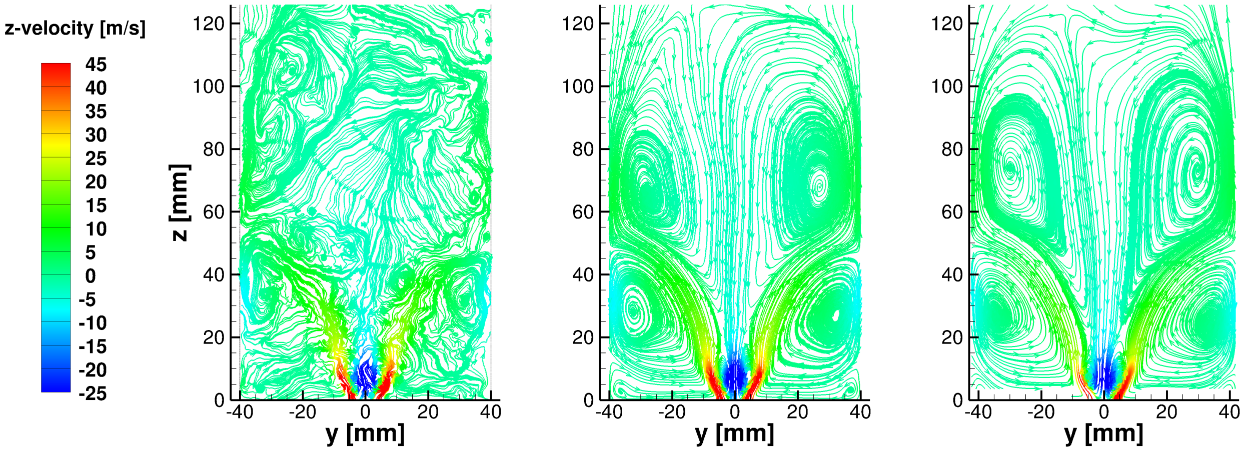

(a) LES (instantaneous) (b) LES (time-averaged) (c) PIV (time-averaged)

Figure 4.25.: Instantaneous (a) and time-averaged (b) mean velocity field of the LES as well as time-averaged PIV data (c) of the cold single phase flow

4.3.3.2. Velocity profiles of the cold single-phase flow

To assess the accuracy of the LES computations with respect to the cold single-phase flow, the numerical results are quantitatively compared with the PIV measurements at different downstream positions from the swirler exit plane. The time-averaged mean velocity distributions (x,y, and z-direction) in planes 5 to 100 mm downstream of the nozzle exit plane are depicted in Fig. 4.26-4.28. The time-averaged velocity fluctuations in the same planes are given in Fig. 4.29-4.31. The blue lines refer to the LES predictions while the black squares represent the experimental PIV data. An overall excellent agreement can be observed. The negligible deviations are well within the temporal and spatial accuracy of the measurement system. It is noteworthy that not only the mean quantities but also the fluctuations are remarkably well reproduced.

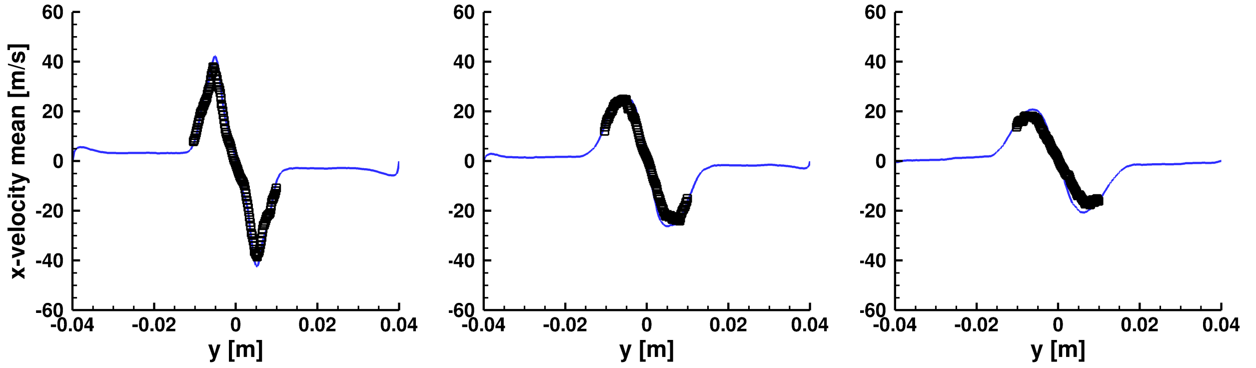

(a) z = 0.005 m (b) z = 0.010 m (c) z = 0.015 m

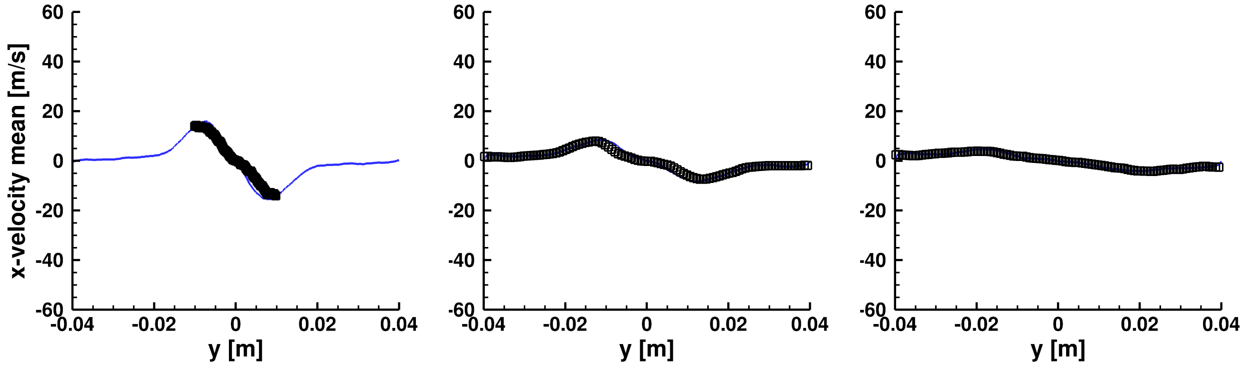

(d) z = 0.020 m (e) z = 0.030 m (f) z = 0.040 m

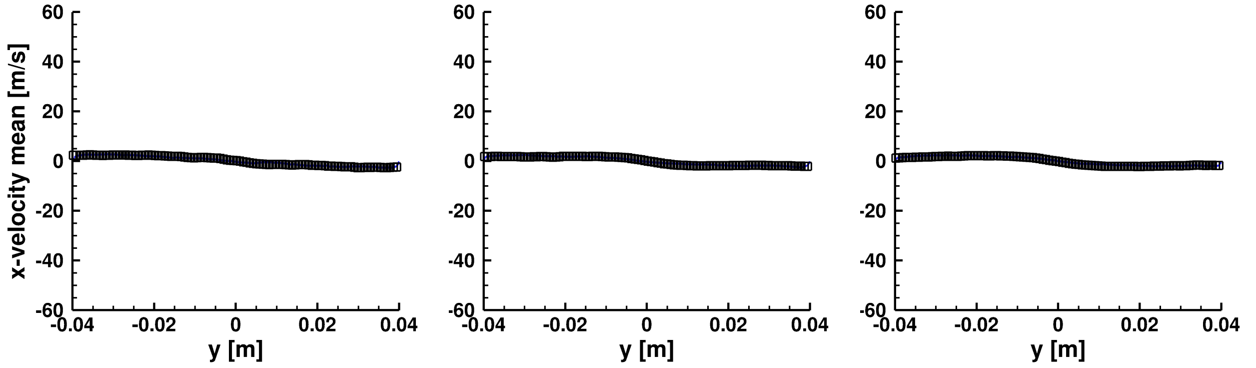

(g) z = 0.050 m (h) z = 0.060 m (i) z = 0.070 m

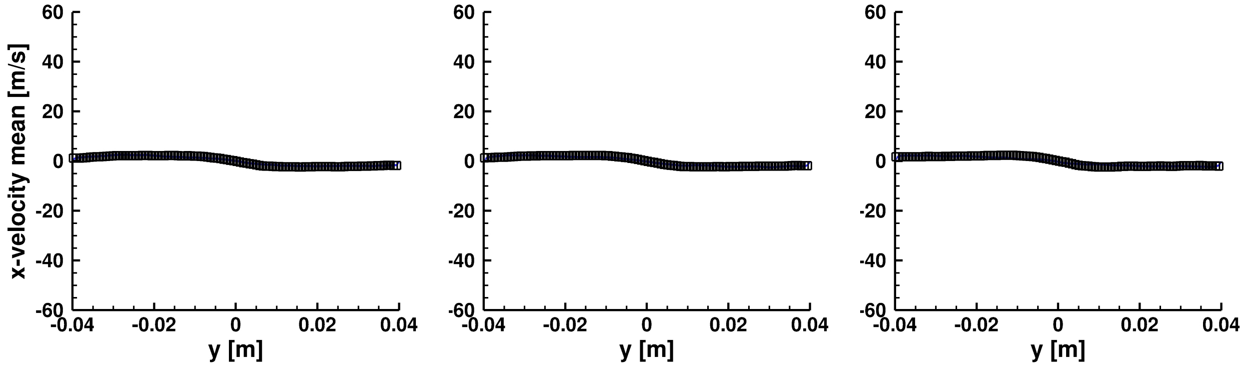

(j) z = 0.080 m (k) z = 0.090 m (l) z = 0.100 m

Figure 4.26.: Time-averaged mean x-velocity distribution at different downstream positions: LES (blue lines) and experimental data (black squares)

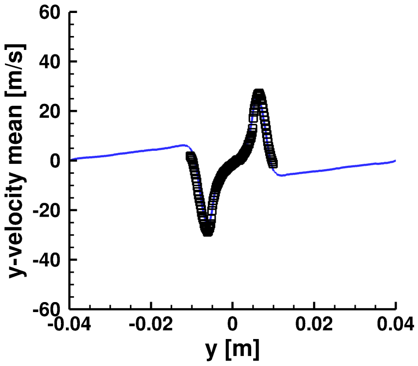

(a) z = 0.005 m (b) z = 0.010 m (c) z = 0.015 m

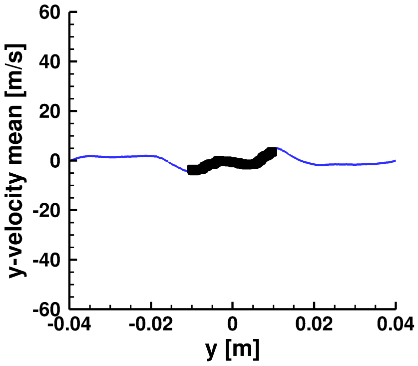

(d) z = 0.020 m (e) z = 0.030 m (f) z = 0.040 m

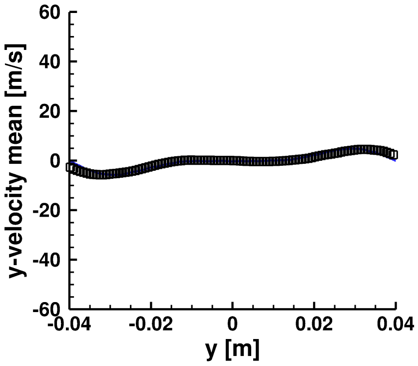

(g) z = 0.050 m (h) z = 0.060 m (i) z = 0.070 m

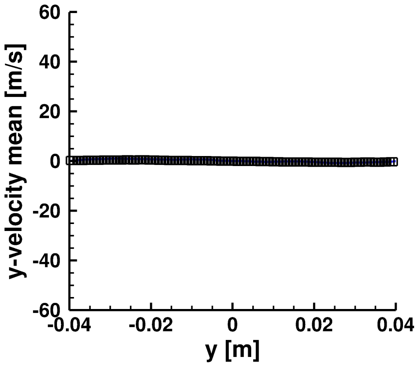

(j) z = 0.080 m (k) z = 0.090 m (l) z = 0.100 m

Figure 4.27.: Time-averaged mean y-velocity distribution at different downstream positions: LES (blue lines) and experimental data (black squares)

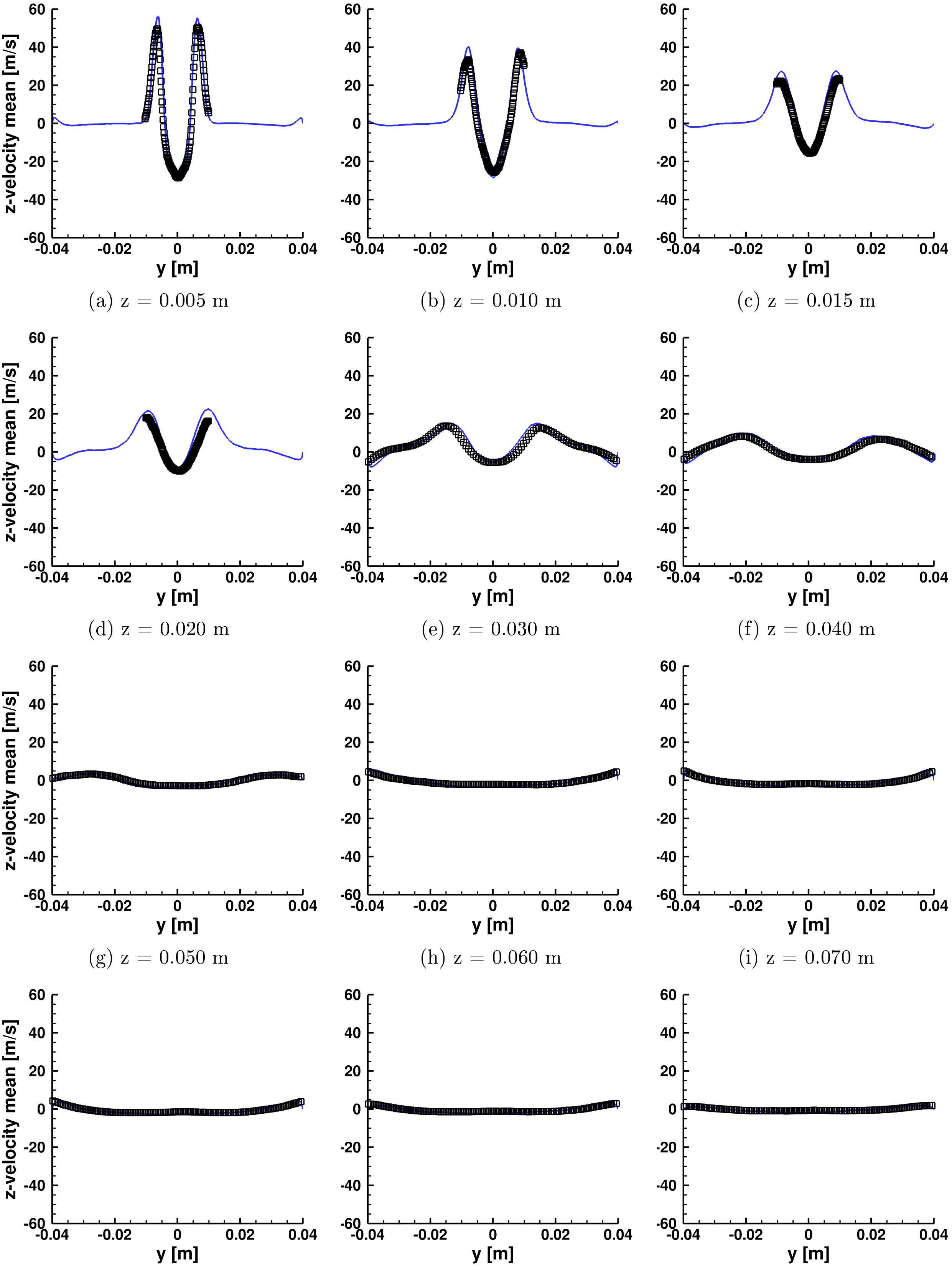

(a) z = 0.005 m
(b) z = 0.010 m
(c) z = 0.015 m
(d) z = 0.020 m
(e) z = 0.030 m
(f) z = 0.040 m
(g) z = 0.050 m
(h) z = 0.060 m
(i) z = 0.070 m
(j) z = 0.080 m
(k) z = 0.090 m
(l) z = 0.100 m

Figure 4.28.: Time-averaged mean z-velocity distribution at different downstream positions: LES (blue lines) and experimental data (black squares)

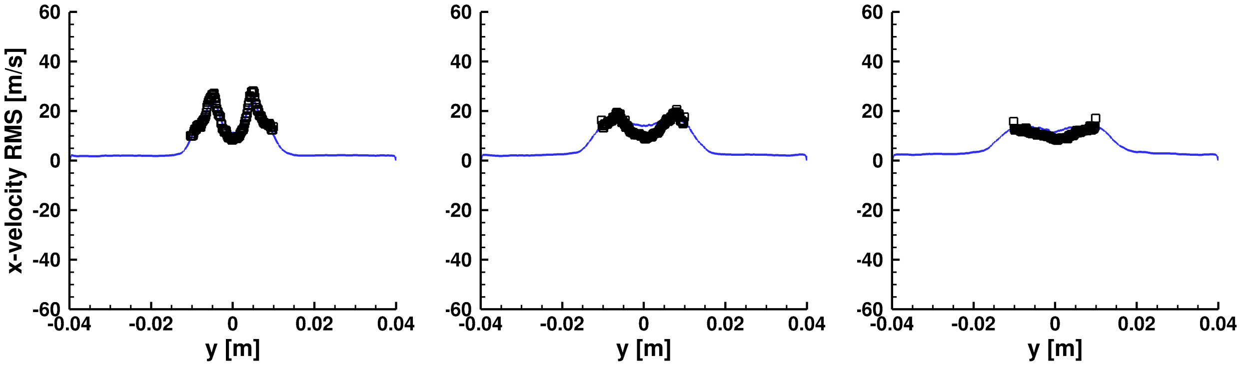

(a) z = 0.005 m (b) z = 0.010 m (c) z = 0.015 m

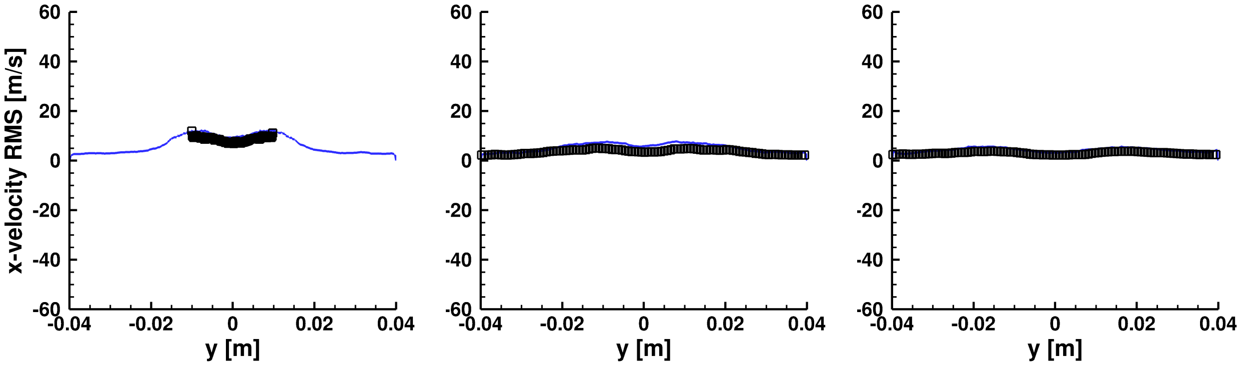

(d) z = 0.020 m (e) z = 0.030 m (f) z = 0.040 m

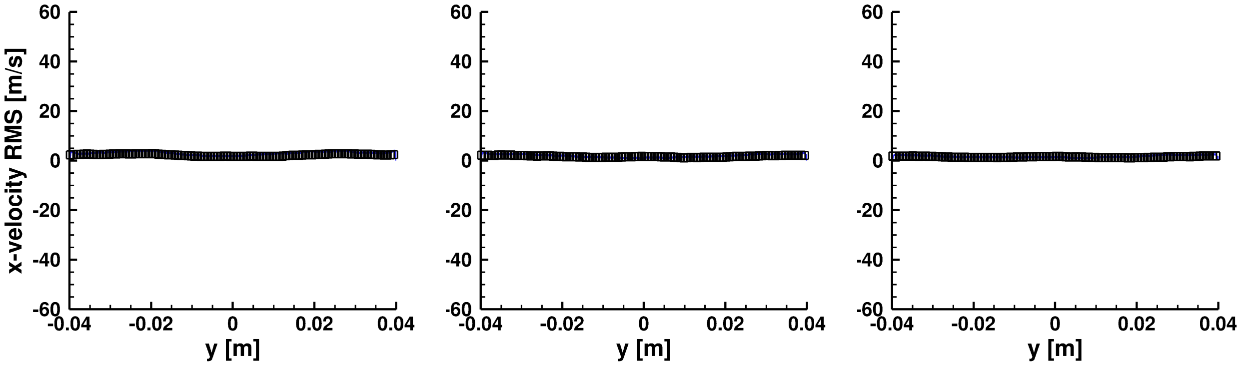

(g) z = 0.050 m (h) z = 0.060 m (i) z = 0.070 m

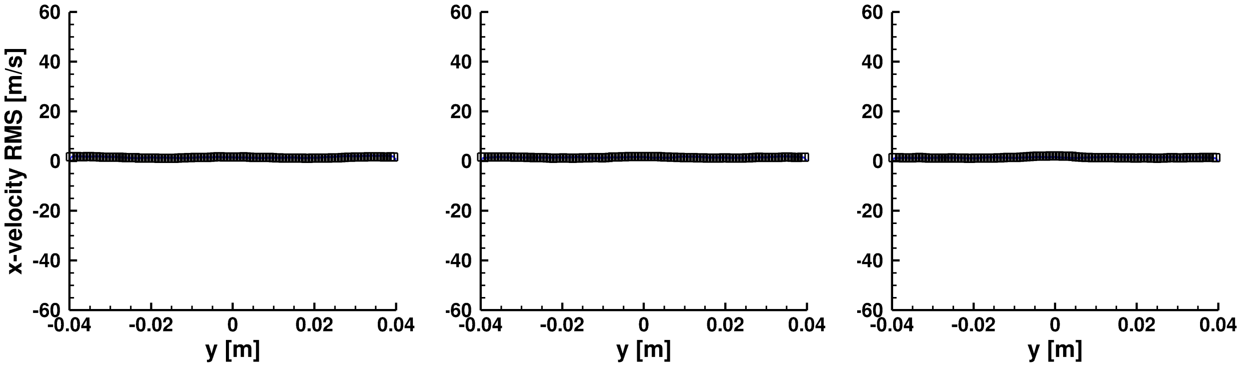

(j) z = 0.080 m (k) z = 0.090 m (l) z = 0.100 m

Figure 4.29.: Time-averaged x-velocity fluctuations (RMS) distribution at different downstream positions: LES (blue lines) and experimental data (black squares)

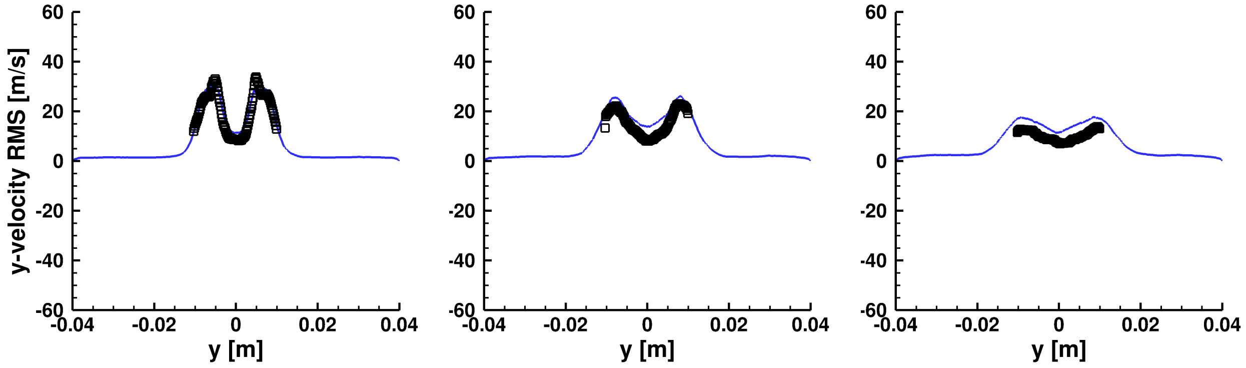

(a) z = 0.005 m (b) z = 0.010 m (c) z = 0.015 m

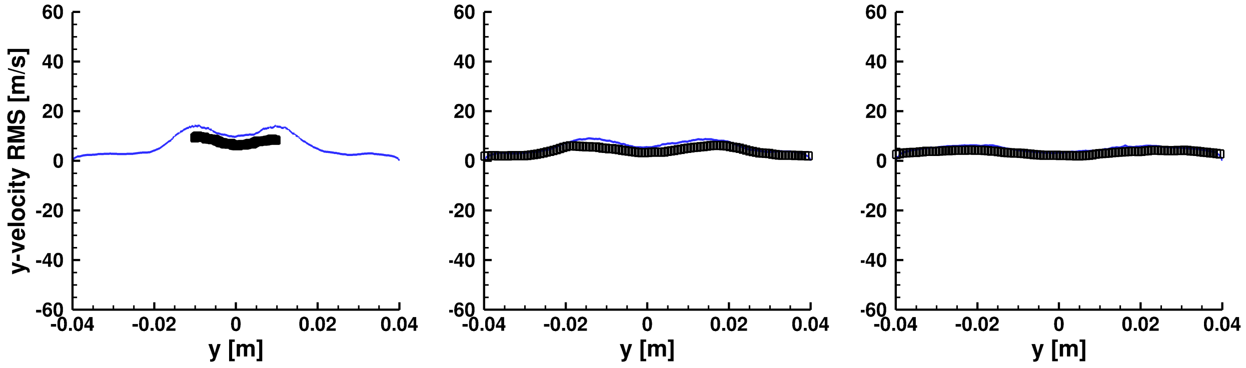

(d) z = 0.020 m (e) z = 0.030 m (f) z = 0.040 m

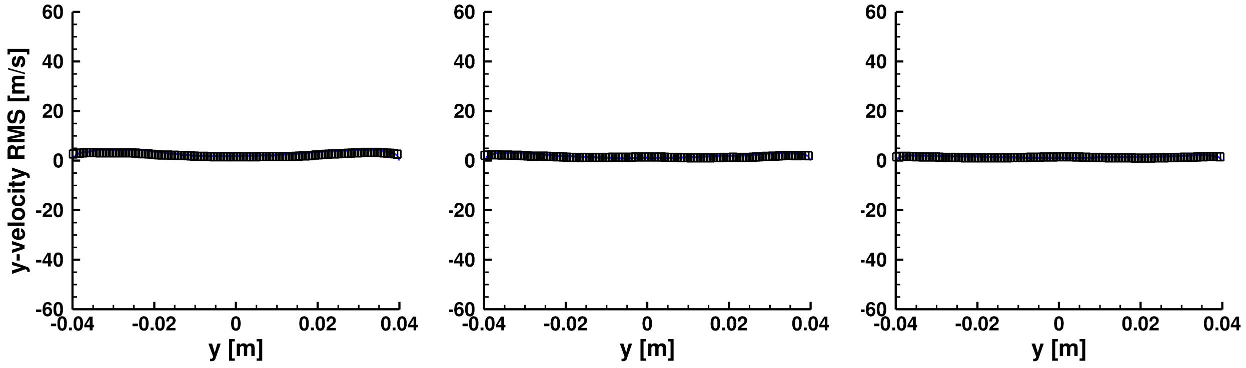

(g) z = 0.050 m (h) z = 0.060 m (i) z = 0.070 m

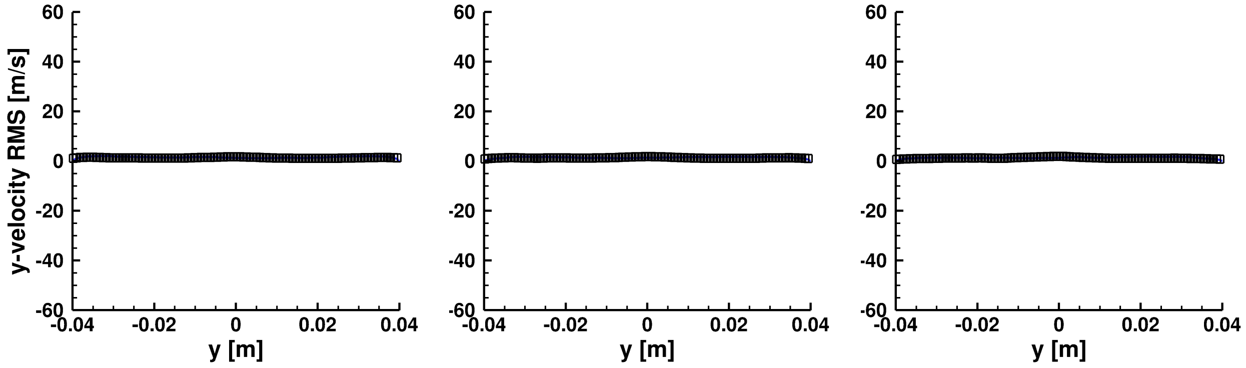

(j) z = 0.080 m (k) z = 0.090 m (l) z = 0.100 m

Figure 4.30.: Time-averaged y-velocity fluctuations (RMS) distribution at different downstream positions: LES (blue lines) and experimental data (black squares)

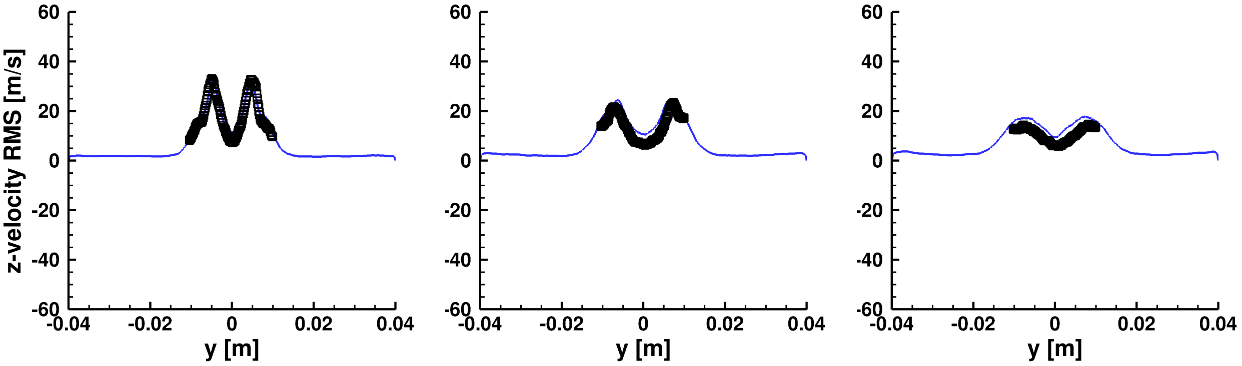

(a) z = 0.005 m (b) z = 0.010 m (c) z = 0.015 m

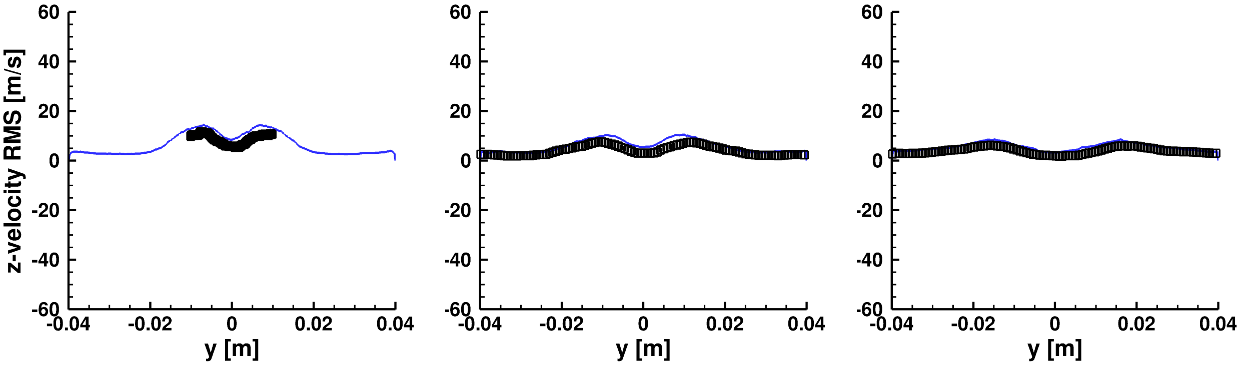

(d) z = 0.020 m (e) z = 0.030 m (f) z = 0.040 m

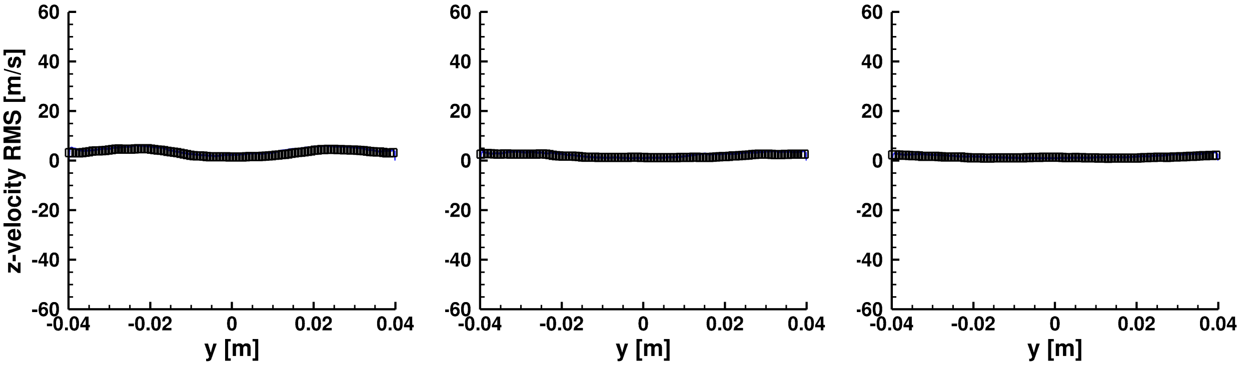

(g) z = 0.050 m (h) z = 0.060 m (i) z = 0.070 m

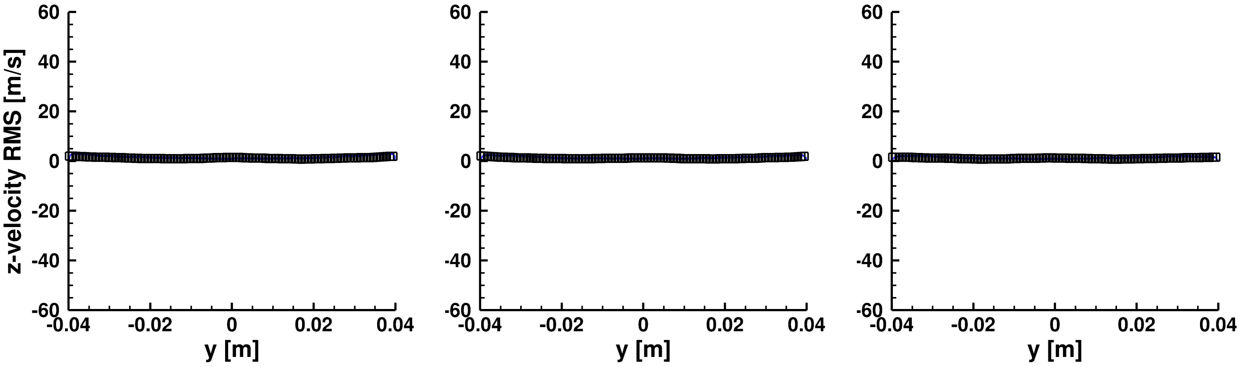

(j) z = 0.080 m (k) z = 0.090 m (l) z = 0.100 m

Figure 4.31.: Time-averaged z-velocity fluctuations (RMS) distribution at different downstream positions: LES (blue lines) and experimental data (black squares)

4.3.3.3. Phenomena and overall characteristics of the ignited multi-phase flow

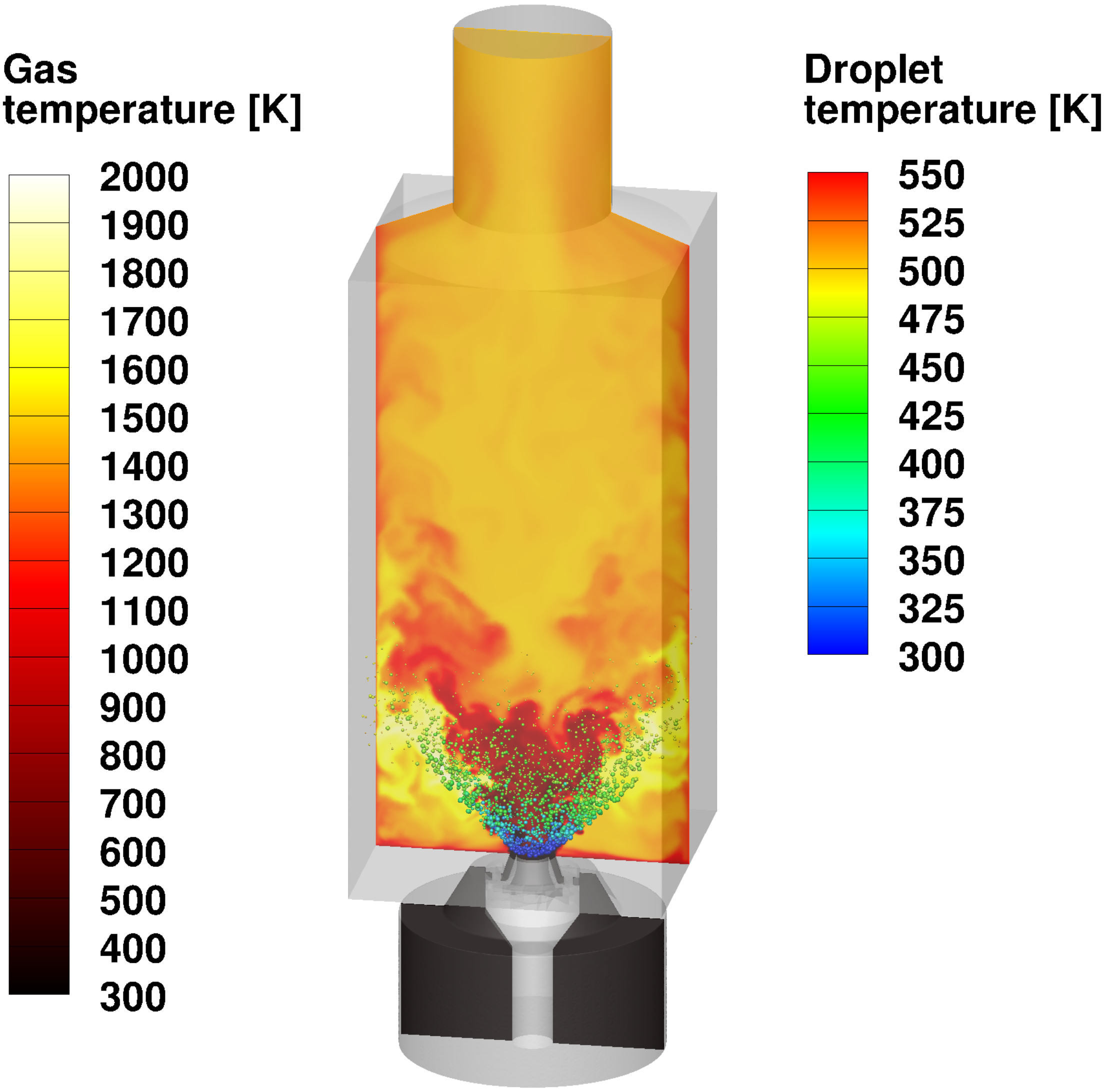

Figure 4.32.: Spray combustion in the swirl-stabilized spray burner

Fig. 4.32 illustrates the combustion of Jet A-1 in the swirl-stabilized spray burner. The fuel droplets, launched above the pre-filmer lip, disperse in the combustion chamber while interacting with the turbulent eddies. During the dispersion, the surrounding hot gases heat the droplets up until they start to evaporate. As soon as the fuel is evaporated, it mixes and reacts with the oxygen in the air. A highly wrinkled flame forms touching the side windows of the combustion chamber.

4.3.3.4. Flow and temperature fields of the ignited multi-phase flow

As the air mass flow rate is equivalent to the one in section 4.3.3.1, the ignited multi-phase flow shows strong similarities to the cold single-phase flow. The flow is highly turbulent (see Fig. 4.33a) and the time average (32.5 ms, Fig. 4.33b) reveals large (integral scale) flow recirculations, which are induced by the swirling high-velocity stream coming from the nozzle.

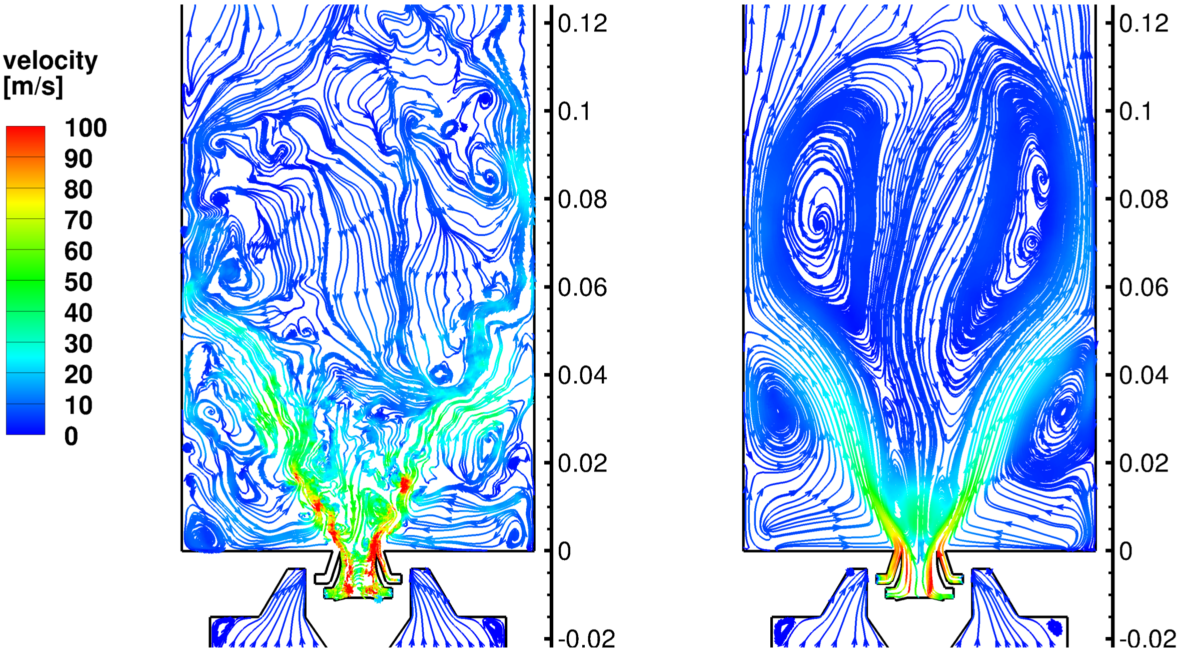

(a) instantaneous (b) time-averaged

Figure 4.33.: Streamlines and velocity magnitude in the center plane of the ignited swirl-stabilized spray burner

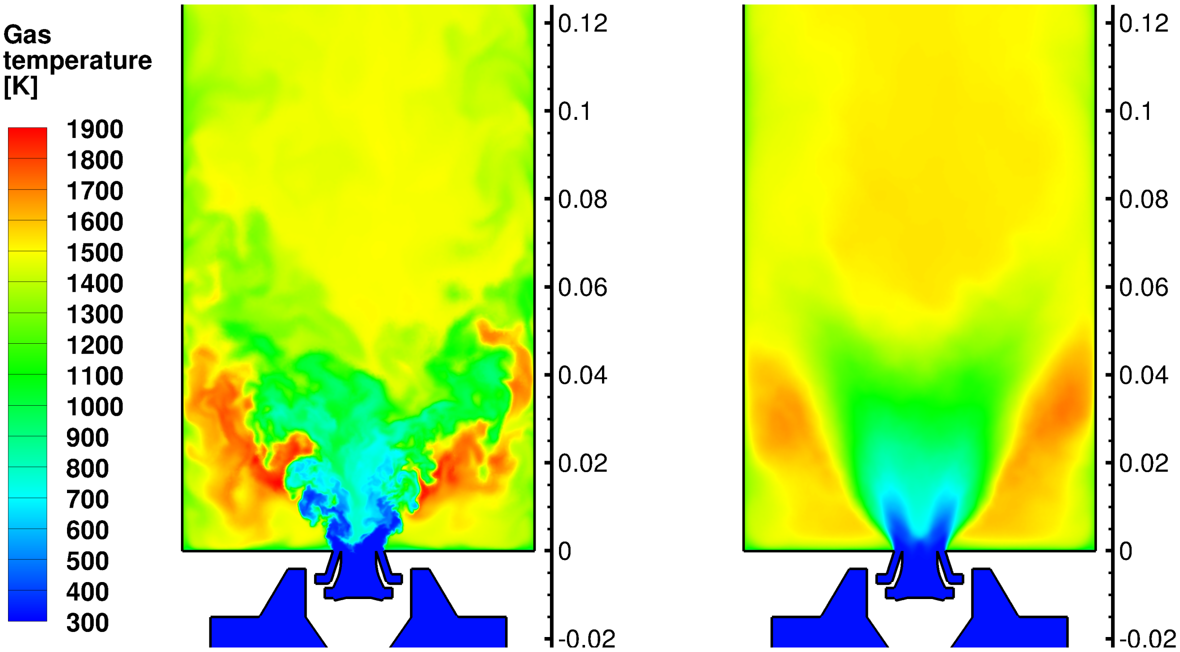

(a) instantaneous (b) time-averaged

Figure 4.34.: Temperature field in the center plane of the ignited swirl-stabilized spray burner

The temperature field (Fig. 4.34) exhibits a high temperature region ($T > 1600$ K) within the lower external recirculation zones and a low temperature region ($T < 800$ K) in the swirling air stream coming from the nozzle. In the large downstream recirculation zones, the temperature reaches 1400 - 1500 K. In the central mixing zone, temperatures range from 800 K to 1400 K. Furthermore, the cooling (due to the isothermal boundary conditions) in the vicinity of the confinements is visible, i.e. $T \approx 1200$ K close to side windows and $900 \text{ K} < T < 1000$ K close to the bottom plate.

A closer look at Fig. 4.33a reveals a regular flow pattern in the region close to the nozzle. As explained in section 4.3.3.1, the swirl (see red spots with high velocities close to the nozzle) leads to a static pressure drop close to the central z-axis resulting in a toroidal flow reversal (see vortices in the central recirculation close to the nozzle) sucking hot gases back. This so-called precessing vortex core (PVC) is visualized in Fig. 4.35a . The PVC extends to roughly 2 burner exit diameters from the nozzle exit plane where the vortex starts to break down. The Fourier transformation of the relative pressure signal at a monitor point located within the PVC indicates that the PVC rotates with a frequency of 4180 Hz (see Fig. 4.35b). Besides the distinct peak at 4180 Hz, a first higher harmonic at 8360 Hz is also visible.

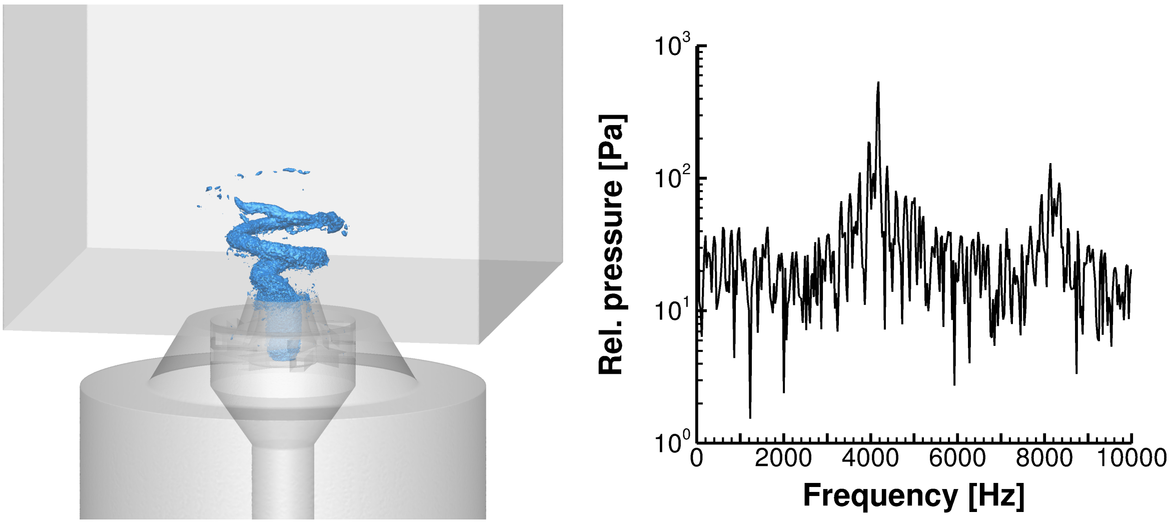

(a) Visualization by an iso-contour of pressure

(b) Fourier transformation of the pressure signal at a monitor point

Figure 4.35.: Precessing vortex core computed by the simulation

4.3.3.5. Droplet distribution and vaporization

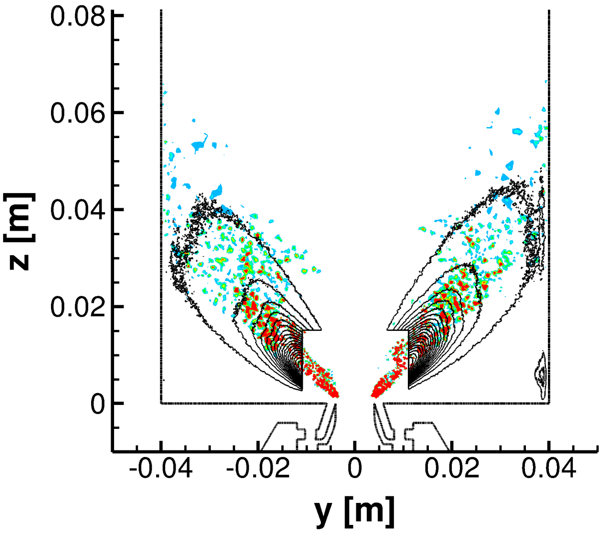

Figure 4.36.: Instantaneous liquid volume fraction predicted by the LES (colored) superimposed by Mie signal (black lines)

Fig. 4.36 shows an instantaneous snapshot of the liquid volume faction in the center plane of the LES together with time-averaged experimental data obtained by evaluating the Mie scattering on the droplets. Although a one to one comparison of instantaneous and time-averaged data is not advisable, Fig. 4.36 gives an impression of the qualitatively good agreement between simulation and experiment. However, the droplet trajectories in the LES seem to have a slightly steeper angle than the ones observed in the experiment. Besides, it can be seen that some of the droplets impinge the side windows of the combustion chamber (see e.g. Mie signal at $y = 0.037$ m, $0.025 \text{ m} < z < 0.045$). In the simulation, these droplets undergo a perfectly elastic reflection without any proper droplet-wall interaction model. As only 3.9 % of the injected liquid mass hits the side windows in the simulation, an influence is expected to be minor but cannot be excluded. Fig. 4.37 illustrates evaporation related profiles over the axial distance from the nozzle. Each point reflects a registration plane orthogonal to the main flow direction (z-axis). Within the first 0.05 m, the droplets experience the hot combustion zone. The droplet temperature (mass-averaged over each registration plane) rapidly rises from 300 to 450 K (Fig. 4.37a). In this region, 95 mass-% of the fuel evaporates (Fig. 4.37b). The mean molar masses of the fuel family pdfs rise as the components with shorter chain lengths more and more evaporate (Fig. 4.37c). At the same time, the distributions become narrower (Fig. 4.37d). The mass fluxes through the registration planes of the four fuel families (Fig. 4.37e) indicate that the cyclo-alkanes evaporate first, followed by the iso-alkanes, the n-alkanes and the aromatics. It is explained by looking at the vapor pressure of the four fuel families as a function of temperature (Fig. 4.37f). The cyclo-alkane family exhibits the highest vapor pressure, followed by the iso-alkane family, the n-alkanes and the aromatics. Here, it should be remarked that the vapor pressure for an entire family is depicted. It depends not only on

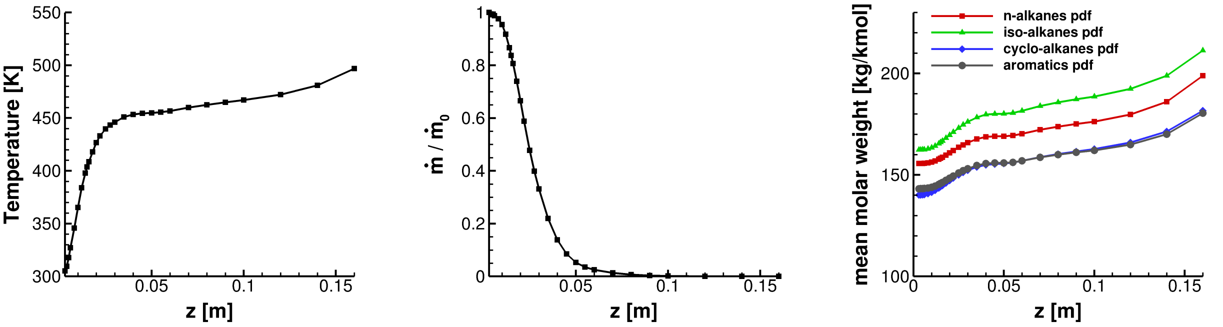

(a) Average droplet temperature

(b) Total mass flux normalized by the total injected mass flux

(c) Mean molar weight of the Jet A-1 fuel families

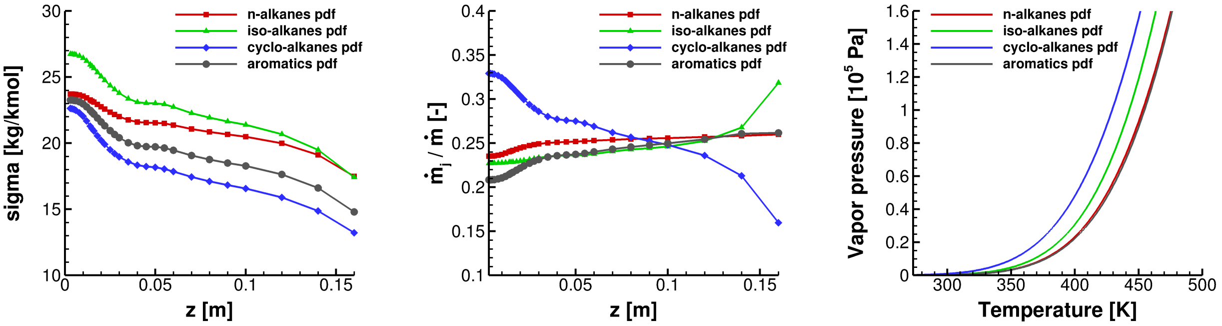

(d) Standard deviation of the molar weight of the Jet A-1 fuel families

(e) Mass flux of the Jet A-1 fuel families normalized by the local mass flux

(f) Vapor pressure of the Jet A-1 fuel families over temperature

Figure 4.37.: Evaporation related profiles over the axial distance from the nozzle in the ignited swirl-stabilized spray burner (a-e). Vapor pressure of the individual fuel families for the Jet A-1 composition shown in Fig. 4.3a as a function of temperature (f).

the physical properties for a specific molecular structure but also on the chain length. For the specific composition of Fig. 4.3a for example, the cyclo-alkanes hold the molecules with the shortest chain length, i.e. lowest molar mass. This leads to the highest vapor pressure. On the contrary, the lowest vapor pressure is observed for the mono-aromatics, despite the fact that they exhibit similar chain lengths. In this case, the different molecular structures lead to differences in volatility.

4.3.3.6. Mixing and flame stabilization

As mentioned in section 1.1.1, flame stabilization is a central design criterion for combustion chambers in aero-engines as a stable and safe operation has to be guaranteed at any operating point. To understand the flame stabilization in the lab-scale swirl-stabilized spray burner, it is important to analyze, in addition to the vaporization of the fuel components, also the mixing of these components with the oxygen in the air. Therefore, the mixture fraction definition by Bilger *et al.* (1990) is introduced:

$$Z = \frac{2\frac{Y_C}{M_C} + \frac{1}{2}\frac{Y_H}{M_H} + \frac{Y_{O,ox}-Y_O}{M_O}}{2\frac{Y_{C,fuel}}{M_C} + \frac{1}{2}\frac{Y_{H,fuel}}{M_H} + \frac{Y_{O,ox}}{M_O}} \tag{4.3.1}$$

It is based on the elemental mass fractions Y_C, Y_H and Y_O of the elements C, H and O, respectively. Z amounts to $Z = 1$ in the fuel stream (subscript fuel) and $Z = 0$ in the oxidizer stream (subscript ox). The stoichiometric value is given by:

$$Z_{st} = \frac{\frac{Y_{O,ox}}{M_O}}{2\frac{Y_{C,fuel}}{M_C} + \frac{1}{2}\frac{Y_{H,fuel}}{M_H} + \frac{Y_{O,ox}}{M_O}} \tag{4.3.2}$$

At the investigated condition, the stoichiometric mixture fraction in the swirl-stabilized spray burner yields $Z_{st} = 0.0635$. The mixture fraction Z is a passive scalar changing because of diffusion and convection, but not because of reaction or heat extraction (Poinsot and Veynante, 2011). In other words, it allows to decompose a combustion problem into a mixing problem and a reaction problem. Fig. 4.38 displays the instantaneous temperature field (gray scale contours) in combination with the instantaneous mixture fraction field (lines) as defined by Eq. 4.3.1. At a glance, a direct correlation between the both can be noted and different characteristic zones can be identified:

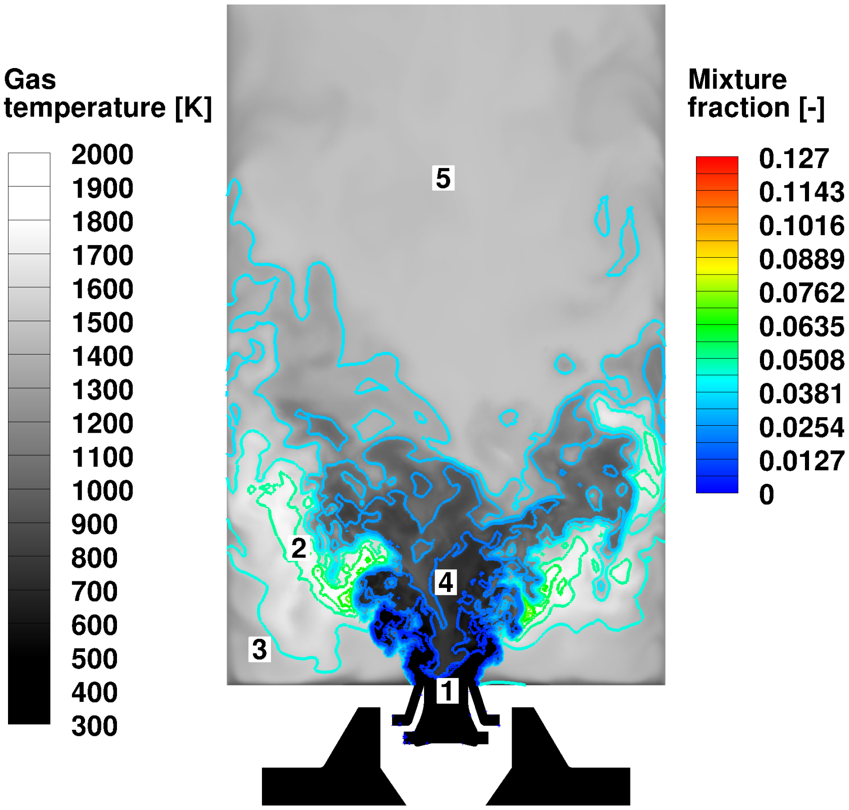

Figure 4.38.: Instantaneous temperature (gray scale contours) and mixture fraction (colored lines) fields; characteristic zones marked by numbers

1. Unmixed air stream: The lowest temperatures correspond to a zone close to the nozzle (T < 400 K), which is only covered by the oxidizer from the high-velocity swirling air stream (see dark blue lines). In this zone, the droplets have not yet evaporated and no combustion products have yet mixed with the incoming fresh air.

2. Flame zone: The highest temperatures (T > 1600 K) are encountered in this region with mixture fractions close to the stoichiometric value of $Z_{st} = 0.0635$ (see greenish line colors). The majority of the fuel vaporization takes place here and insular spots around droplet clusters with rich mixtures can be found.

3. Lower external mixing zone: This zone is confined by the side windows and the bottom plate of the combustion chamber as well as the flame zone (zone 2) and the unmixed air stream (zone 1). The mixing in this zone is driven by the lower external recirculations. These recirculations transport hot combustion products back towards the burner, where they mix with the incoming fresh air. During this transport, the hot gases are cooled by the side windows and the bottom plate.

4. Lower central mixing zone: This zone is confined by the unmixed air stream (zone 1). The mixing in this zone is driven by the small central recirculations and the precessing vortex core, which transport hot gases to the nozzle exit plane.

5. Upper mixing zone: The mixing in this zone is driven by the upper external recirculations. In the upper external region close to the side windows (especially in the corners of the combustion chamber), hot gases together with unburned droplets from the flame zone (zone 2) are entrained into the upper recirculation zone. These hot gases are slightly cooled by the colder side windows and then transported back towards the nozzle in the central region. On their way towards the nozzle, these hot gases mix with the cold flow of the air stream (zone 1).

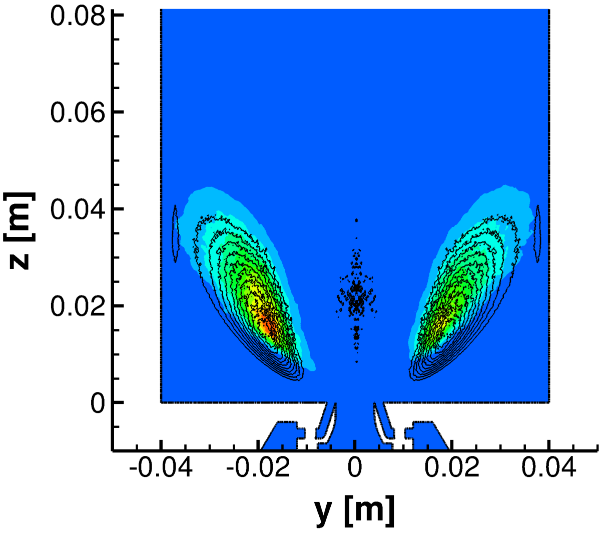

Figure 4.39.: Time-averaged OH*-distribution predicted by the LES (colored) superimposed by CH*-Chemiluminescence, Abel deconvoluted (black lines)

The recirculation of hot products in the lower external mixing zone (zone 3), the lower central mixing zone (zone 4) and upper mixing zone (zone 5) provides the necessary energy to continuously ignite the incoming reactants after being sufficiently mixed. By the transport of hot combustion products back to the flame root, the flame stabilizes in the lower external recirculation zones along the mean spray trajectory. On a time average basis, a v-shaped reaction zone can be observed. Fig. 4.39 illustrates a center plane cut through this reaction zone. The LES prediction of the OH*-field (represented by the colored contours) is depicted together with the Abel-deconvoluted CH*-Chemiluminescence measured in the experiment (black lines). Besides a small offset, the position of the main reaction zone is well reproduced by the computation. This offset might be due to the slightly steeper spray angle in comparison to the experimental findings mentioned in section 4.3.3.5. The discontinuous CH*-Chemiluminescence signal close to the z-axis is not matched by the simulation. Necessitating a further analysis, it could not be clarified during the course of this thesis whether it is an artifact of the deconvolution operation or an actual chemical reaction taking place.

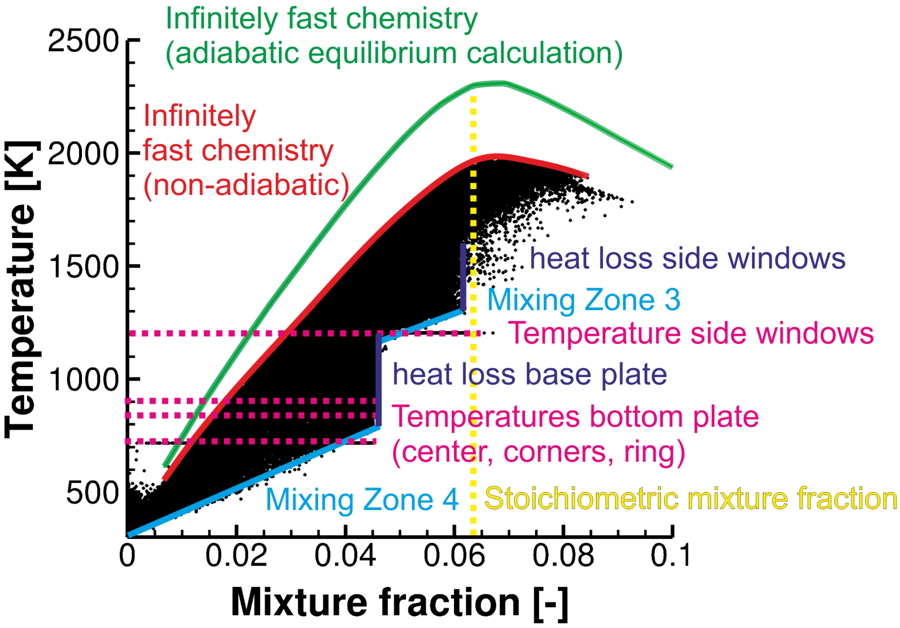

Figure 4.40.: Scatter plot of the states of the reacting multi-phase flow

Fig. 4.40 shows the states of the reacting multi-phase flow within the entire domain (black points) in a Z-T diagram. The "frozen chemistry" or "pure mixing" limit is reached if the diffusion and flow time scales are considerably shorter than chemical time scales. In Z-T space, this limit is represented by straight lines. In Fig. 4.40, two mixing zones are clearly visible, i.e. the lower central mixing zone (zone 4) and the lower external mixing zone (zone 3), which are highlighted by light blue and yellow, respectively. On the contrary, equilibrium or infinitely fast chemistry is reached if the chemical time scales are considerably shorter than diffusion and flow time scales. The maximum temperature is found around the stoichiometric value of the mixture fraction ($Z_{st} = 0.0635$). The green line represents the limit of infinitely fast chemistry under adiabatic conditions determined by an adiabatic equilibrium calculation with CANTERA (Goodwin *et al.*, 2017). This limit cannot be reached as the system suffers from heat losses at the side windows and the bottom plate. Therefore, the upper boundary (red line) of the scatter points is given by the limit of infinitely fast chemistry (equilibrium) under non-adiabatic conditions. A substantial share of the points is situated close to the red line suggesting that these states are controlled by evaporation and mixing and not by the reaction kinetics. Nevertheless, many states are apparent which follow a finite rate chemistry. In these states, fuel and oxidizer can coexist. Additionally, they can be diluted by recirculating reaction products or be influenced by heat transfer in the vicinity of the confinements. Hence, depending on the flow time scales, evaporation time scales and the chemical time scales, the structures in the reacting multi-phase flow become more complex, e.g. around droplets and droplet clusters insular spots of rich mixtures can be found (see points with $Z > 0.0635$).

4.3.3.7. Spray and temperature profiles

Fig. 4.41 displays time-averaged profiles of spray characteristics in a plane 15 mm downstream of the nozzle exit. These spray characteristics comprise the Sauter mean diameter (Fig. 4.41a), the normalized volume flux (Fig. 4.41b) as well as the axial, radial and tangential droplet velocities (Fig. 4.41c-4.41e). The LES data is represented by the colored symbols. The experimental data measured by a PDA system is illustrated by black squares. As can be seen from Fig. 4.41a, the Sauter mean diameter in the LES is in the range $5 - 40\mu m$ and shows a distinct peak of $\sim 40\mu m$ at $y \approx \pm 0.02m$. In contrast, the measured SMD almost monotonically increases with the distance from the central axis from $18\mu m$ to $35\mu m$. The discrepancy amounts to $0 - 8\mu m$ in the area of the maximum volume flux (see 4.41b) but up to $12\mu m$ for the highest SMD measured. The normalized volume flux (Fig. 4.41b) predicted by the LES agrees well with the one measured by Mie scattering on the droplets. The origin of the non-uniformity in the measured profile could not be clarified during the course of this thesis. In Fig. 4.41c-4.41e, the droplet velocities for three diameter classes, i.e. $10\mu m$ (red symbols), $30\mu m$ (green symbols), and $50\mu m$ (blue symbols), are plotted for the LES computation. In order to improve the statistics, a ±10% margin was introduced resulting in the following diameter ranges: $9\mu m < d < 11\mu m$, $27\mu m < d < 33\mu m$ and $45\mu m < d < 55\mu m$. From the PDA measurement, only the average velocity for all droplets is available. A one to one comparison is not possible, but from Fig. 4.41a it can be inferred that the measured profile reflects droplets in the size range $18\mu m < d < 25\mu m$ and $25\mu m < d < 35\mu m$ in the inner and outer region, respectively. Hence, in the outer range the measured velocities are comparable to the ones of the $30\mu m$ diameter class (green symbols). The axial and tangential velocity match well, while the radial velocity predicted by the LES is slightly lower. In the inner region, there is no corresponding diameter class but the values are expected to be between the ones for the $10\mu m$ and $30\mu m$ diameter class. This suggests that the radial and tangential velocities are well predicted by the LES while the axial velocity is slightly overpredicted.

Fig. 4.42 shows a comparison of the time-averaged temperature profiles between the LES (lines) and experimental data (squares) from a CARS measurement system. Three horizontal profiles at z = 0.015 m, z = 0.025 m and z = 0.035 m (Fig. 4.42a-4.42c) together with two vertical profiles at x = -0.02 m (Fig. 4.42d) and x = 0.0 m (Fig. 4.42e) are presented. The temperature rise at the beginning of the flame zone (zone 2) in the lower external recirculation zones is well reflected by the LES computation. In this region, the profiles match for all horizontal profiles (Fig. 4.42a-4.42c). This is also confirmed by the vertical profile at y = -0.02 m (Fig. 4.42d). Although the temperatures at the confinements were measured, the cooling effect due to the isothermal walls seems to be overestimated in the computation resulting in a rapid temperature decay close to the confinements (see $|y| \geq 0.03$ in Fig. 4.42a-4.42c and $z \leq 0.005$ in Fig. 4.42d). The experimentally observed maximum (time-averaged) temperature of 1820 K is therefore never reached in the entire simulation domain with a maximum (time-averaged) temperature in the LES of 1730 K. Furthermore, a clear discrepancy is observable in the central region, where the measurement shows another distinct temperature peak. A small peak is also visible in the simulation data but far less pronounced. This is also confirmed by the vertical profile along the z-axis (Fig. 4.42e). Although a similar temperature rise is visible in the LES data compared to the CARS data, a significant vertical offset of about 15 to 20 mm is evident. Furthermore, the final temperature level ($\sim$ 1660 K), which is reached for $z > 0.05m$, is 100 K hotter than the one predicted by the LES. The discrepancies between measurement and computation might be due to differences in the temperature boundary conditions for the confinements mentioned above or the droplet starting conditions. For the latter, it was assumed that the entire spray issuing from the central pressure nozzle impinges on the pre-filmer surface and forms a film, which is finally atomized. However, it cannot be excluded that small droplets evaporate before hitting the surface. Furthermore, uncertainties concerning the reaction mechanism cannot be excluded. In order to clarify if the observed temperature differences are related to wrong boundary conditions or still existing deficiencies in the sub-models, further simulations will be necessary to analyze the sensitivity of the results on these aspects.

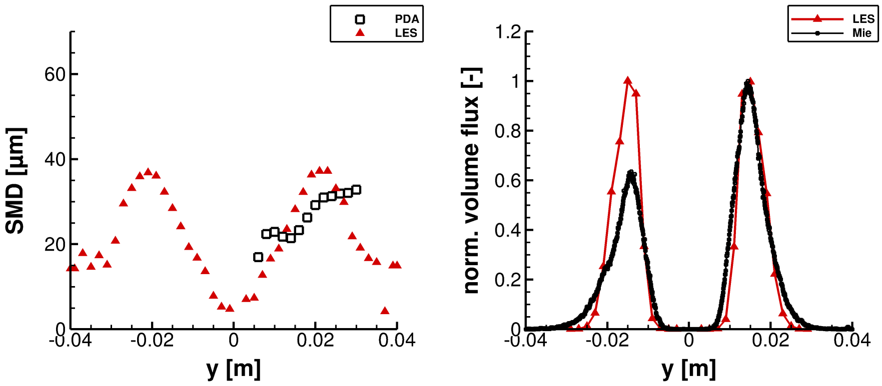

(a) SMD (b) normalized volume flux

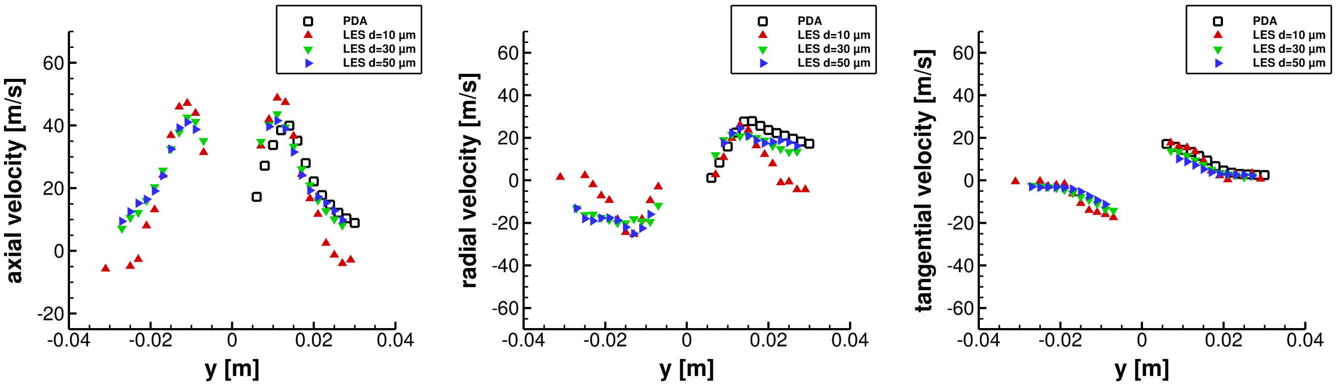

(c) Axial droplet velocity (d) Radial droplet velocity (e) Tangential droplet velocity

Figure 4.41.: Time-averaged profiles of spray characteristics 15 mm downstream of the nozzle: LES (colored symbols) and experimental data (black symbols)

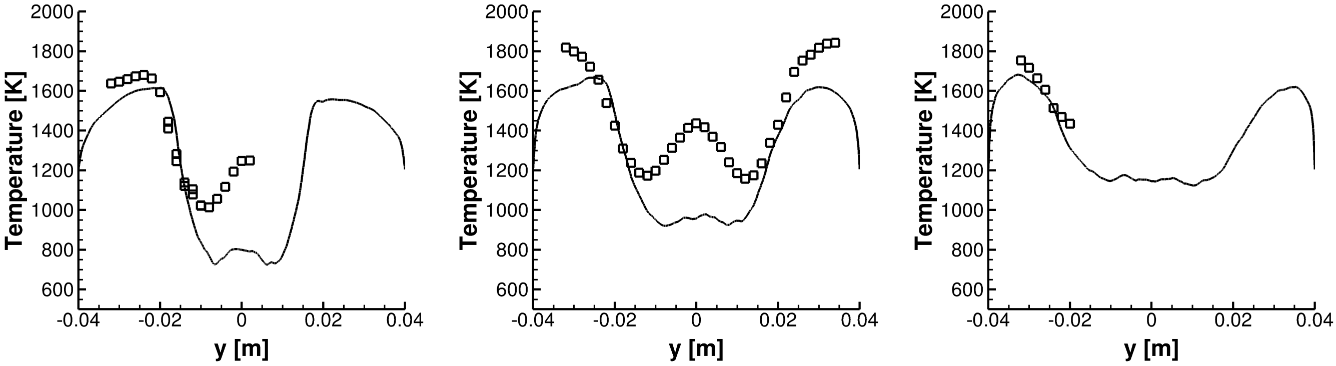

(a) z = 0.015 m (b) z = 0.025 m (c) z = 0.035 m

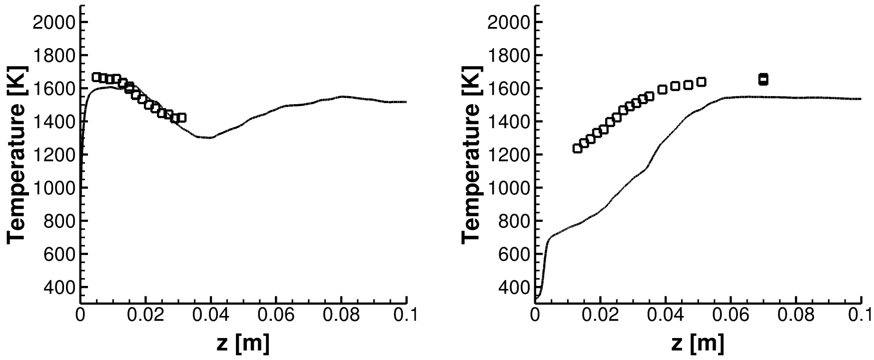

(d) y = - 0.020 m (e) y = 0.000 m

Figure 4.42.: Time-averaged temperature distribution at different downstream positions: LES (black lines) and experimental data (black symbols)

	Experiment	Simulation
CO	19.0 ppm	18.6 ppm
NO	21.0 ppm	1.3 ppm

Table 4.5.: Comparison of exhaust gas emissions

4.3.3.8. Vapor species fields, pollutant formation and emissions

Fig. 4.43-4.46 show the instantaneous (a) and time-averaged gas concentrations of the fuel species as well as the instantaneous net production and consumption rate (c). The instantaneous snapshots (a and c) are overlaid with black lines representing the locations of the fuel component's evaporation. Fig. 4.43c-4.46c suggest that the evaporated fuel species immediately react in the flame zone (zone 2). In the flame zone, evaporation appears to be the rate controlling step, i.e. evaporation and mixing times introduce an inherent damping to combustion. This explains why systems with a high degree of prevaporization and premixing are more susceptible to instabilities. In case the evaporated fuel species encounter a cold region in the incoming swirling air stream (zone 1) or the lower part of the upper mixing zone (zone 5), pockets of unburned gaseous fuel species can form (see Fig. 4.43a-4.46a). On average (Fig. 4.43b-4.46b), the maxima of the fuel species mass fractions are found in the shear layer between unmixed air stream (zone 1) and the flame zone (zone 2). The amount of species entrained into the lower central mixing zone (zone 4) is attributed to the evaporation and the conversion rates of the individual species. The effect of different volatility can be seen for n-dodecane, iso-octane and cyclo-hexane (Fig. 4.43-4.45), i.e. the faster the evaporation, the higher the mass fractions in the lower central recirculation zone. In section 4.3.3.5, it is shown that the cyclo-alkanes evaporate before the iso-alkanes and the n-alkanes. The absolute values are also strongly related to the initial fuel composition of 22.49 % n-alkanes, 20.82 % iso-alkanes, 35.05 % cyclo-alkanes and 21.64 % aromatics. However, the toluene concentrations show that besides evaporation the conversion rates of the individual fuel surrogate species effect the entrainment into the lower central mixing zone. Toluene exhibits a slow evaporation, but also the slowest conversion rates of the four fuel surrogate species, which was observed in 1-d flames calculated with the same reaction mechanism. As a consequence, toluene is present in the lower central recirculation zone, which has not yet reacted.

Pollutant formation and emissions are not in the primary focus of this thesis, i.e. the detailed formation mechanisms for soot and NO_x were not considered. Nevertheless, the Zeldovich submechanism for thermal NO formation from the GRI 3.0 reaction mechanism (Smith *et al.*, 2000) and soot precursors such as benzene are included in the reaction mechanism (see section 4.3.2). Fig. 4.47, 4.48 and 4.50 illustrate the instantaneous (a) and time-averaged gas concentrations of NO, CO and benzene as well as the instantaneous net production and consumption rate (c). As expected, NO forms in the high temperature region (T $>$ 1600 K) (see Fig. 4.47) leading to the highest concentrations in the flame zone (zone 2). Nevertheless, the NO emissions in the exhaust gas are not correctly predicted in the simulation being an order of magnitude lower than the measured values (see Table 4.5). One reason for the discrepancy can be the underestimation of temperatures in the LES shown in section 4.3.3.7. Besides, a closer look at the thermal NO sub-mechanism in the GRI 3.0 mechanism reveals that the constants differ from the ones given in the literature, e.g. in Warnatz *et al.* (2006). It is quite possible that the constants are only valid in conjunction with the other NO_x formation paths and the sub-mechanism should not be used isolated from these formation paths. According to Fig. 4.48 and 4.49, CO is mainly produced at the early stages of the fuel oxidation and then further oxidized in the presence of OH to CO_2. In this manner, the major portion of CO is consumed but a small rest in the ppm-range is emitted. Table 4.5 shows that the CO emissions predicted by the LES are close to the ones experimentally determined in the exhaust gas. The soot precursor benzene (Fig. 4.50) is mainly formed from toluene (C_7H_8) in regions where toluene is not directly oxidized, i.e. in locally toluene-rich discrete spots around the droplets and in regions occupied by toluene and temperatures $T < 1200K$. It is consumed encountering regions with high temperatures. The example of benzene formation from one specific fuel family shows that a multi-component description of the liquid phase and the evaporation process is a necessary requirement for the prediction of soot emissions.

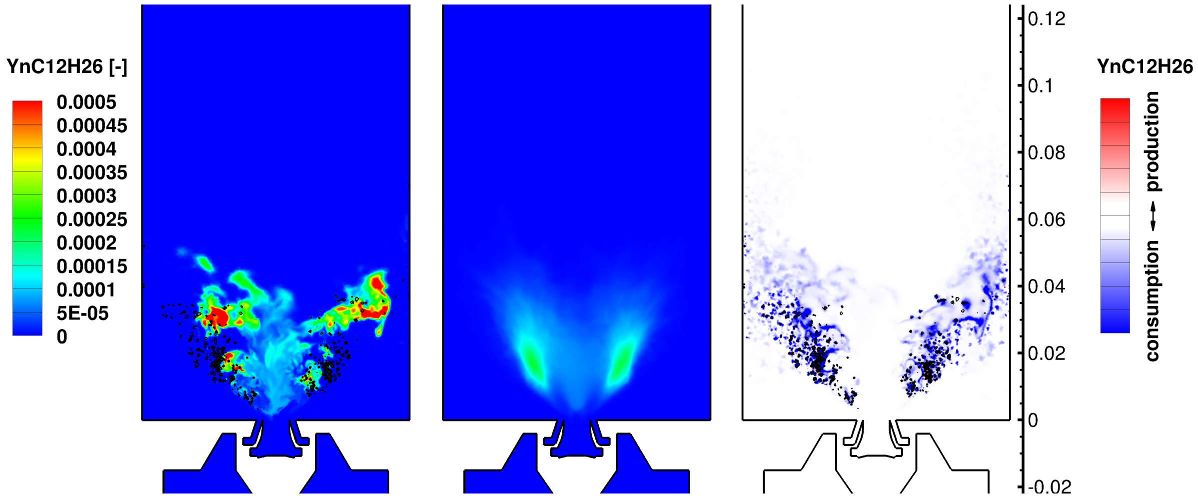

(a) (b) (c)

Figure 4.43.: Instantaneous (a) and time-averaged (b) gas concentration field as well as instantaneous net production / consumption rate (c) of n-dodecane. Black lines show the instantaneous locations of n-dodecane evaporation

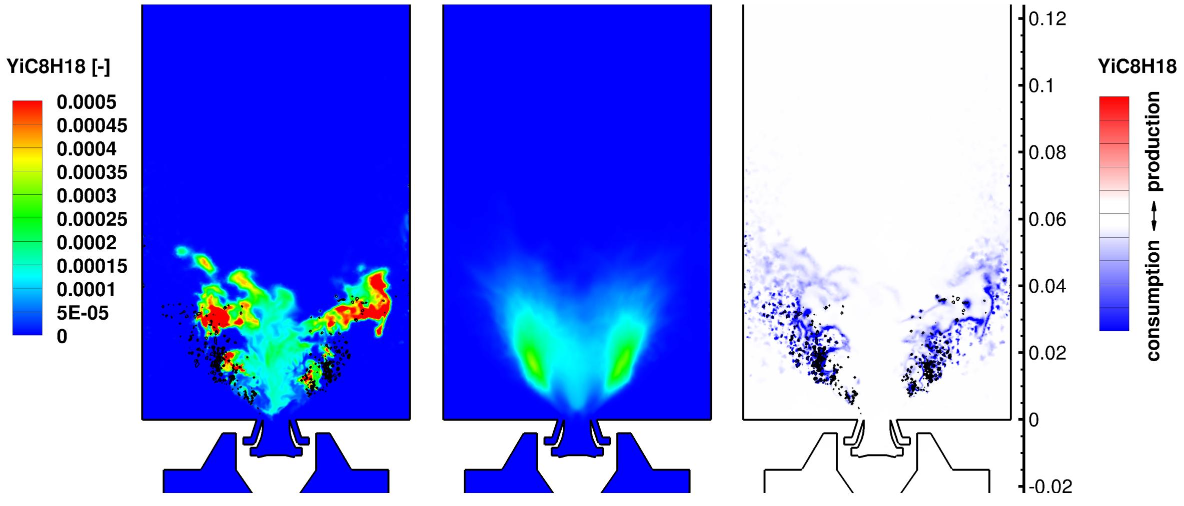

(a) (b) (c)

Figure 4.44.: Instantaneous (a) and time-averaged (b) gas concentration field as well as instantaneous net production / consumption rate (c) of iso-octane. Black lines show the instantaneous locations of iso-octane evaporation

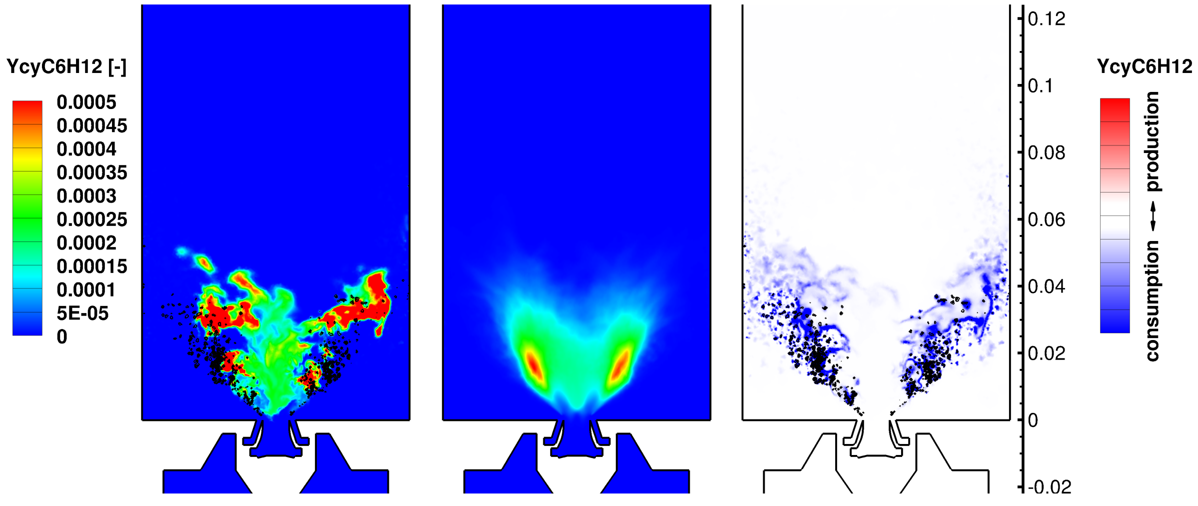

(a) (b) (c)

Figure 4.45.: Instantaneous (a) and time-averaged (b) gas concentration field as well as instantaneous net production / consumption rate (c) of cyclo-hexane. Black lines show the instantaneous locations of cyclo-hexane evaporation

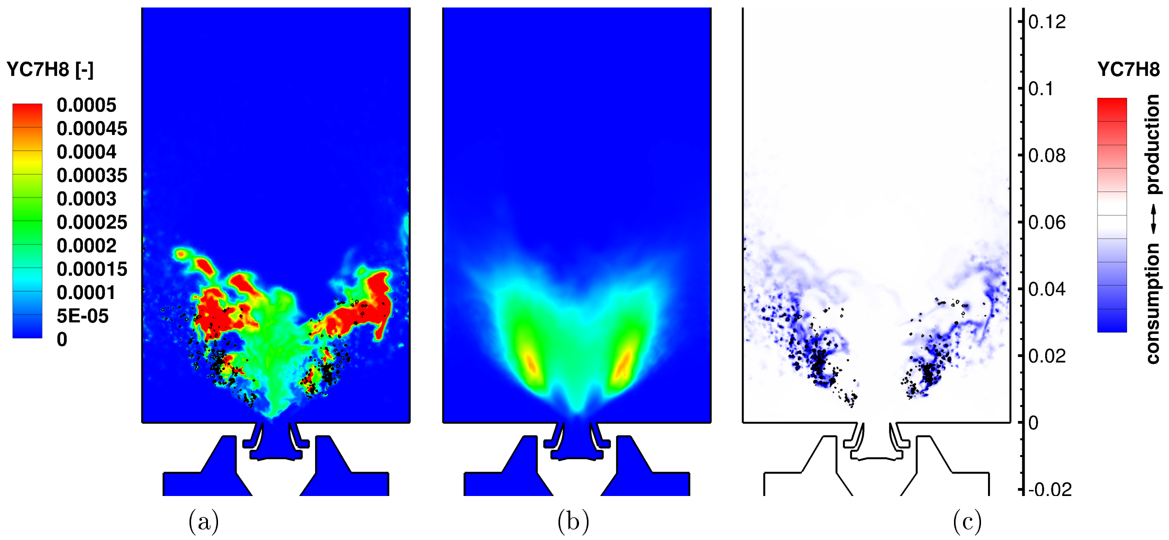

Figure 4.46.: Instantaneous (a) and time-averaged (b) gas concentration field as well as instantaneous net production / consumption rate (c) of toluene. Black lines show the instantaneous locations of toluene evaporation

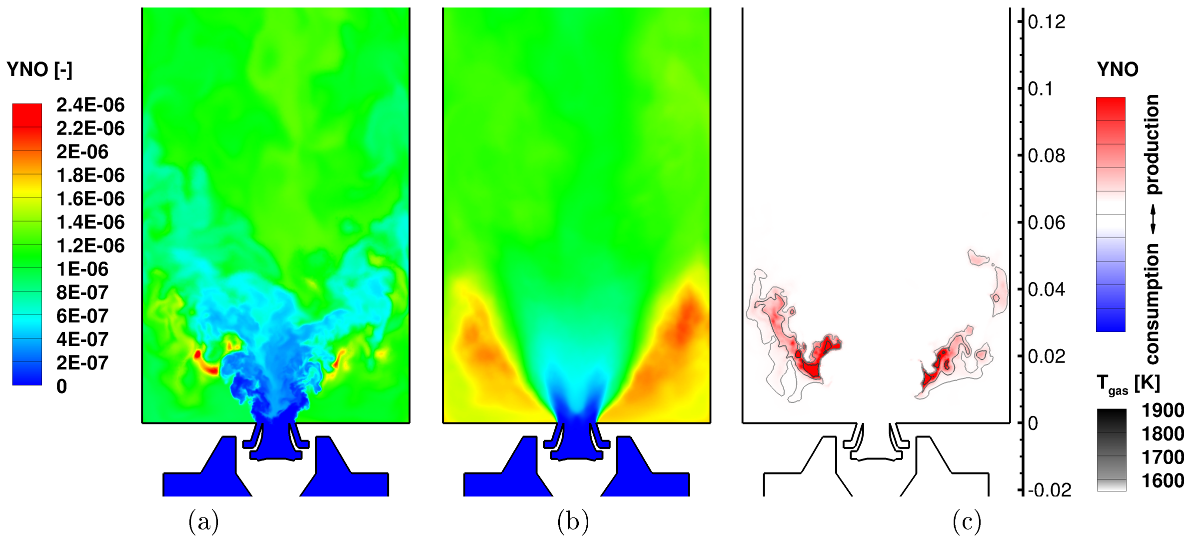

Figure 4.47.: Instantaneous (a) and time-averaged (b) gas concentration field as well as instantaneous net production / consumption rate (c) of nitrogen monoxide.

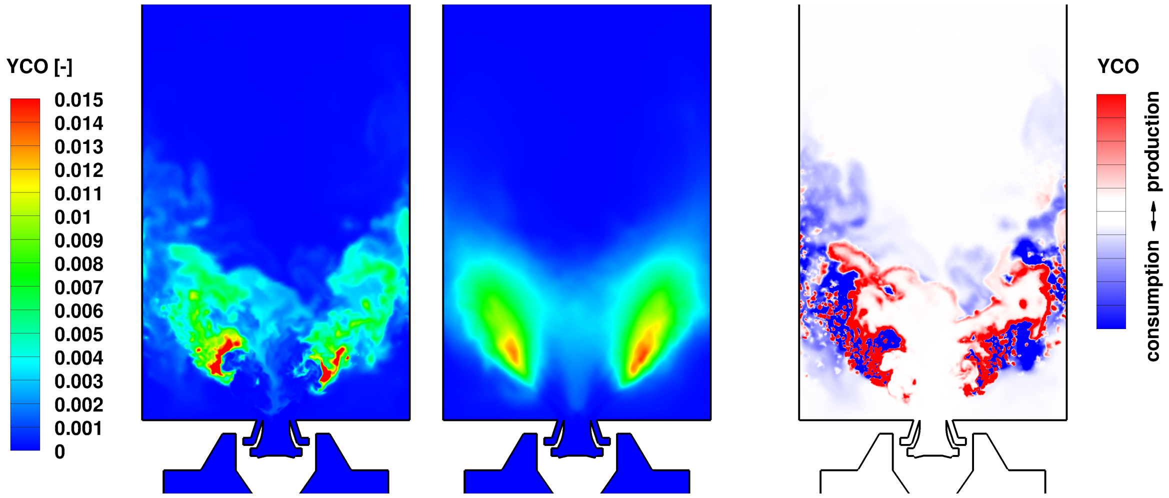

(a) (b) (c)

Figure 4.48.: Instantaneous (a) and time-averaged (b) gas concentration field as well as instantaneous net production / consumption rate (c) of carbon monoxide.

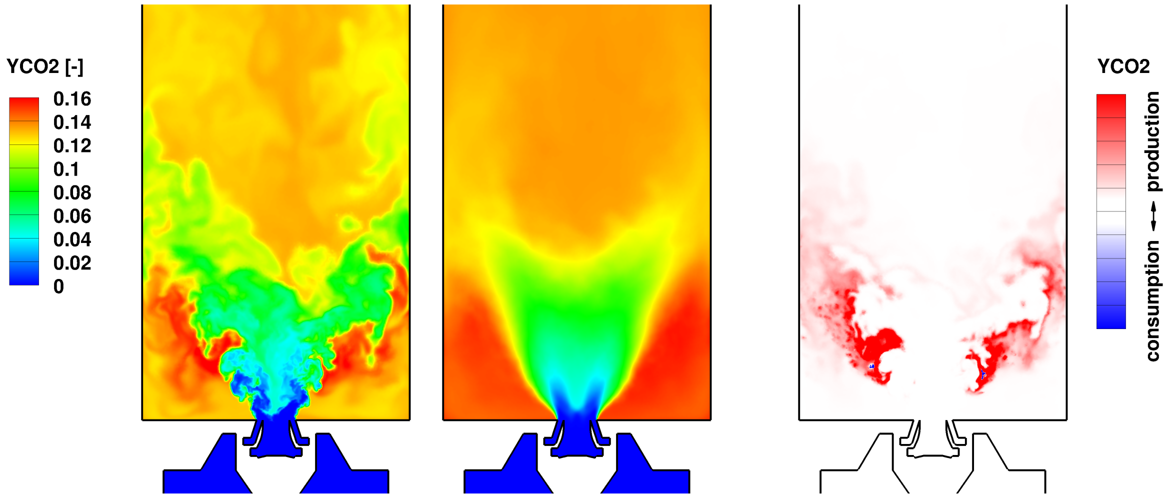

(a) (b) (c)

Figure 4.49.: Instantaneous (a) and time-averaged (b) gas concentration field as well as instantaneous net production / consumption rate (c) of carbon dioxide.

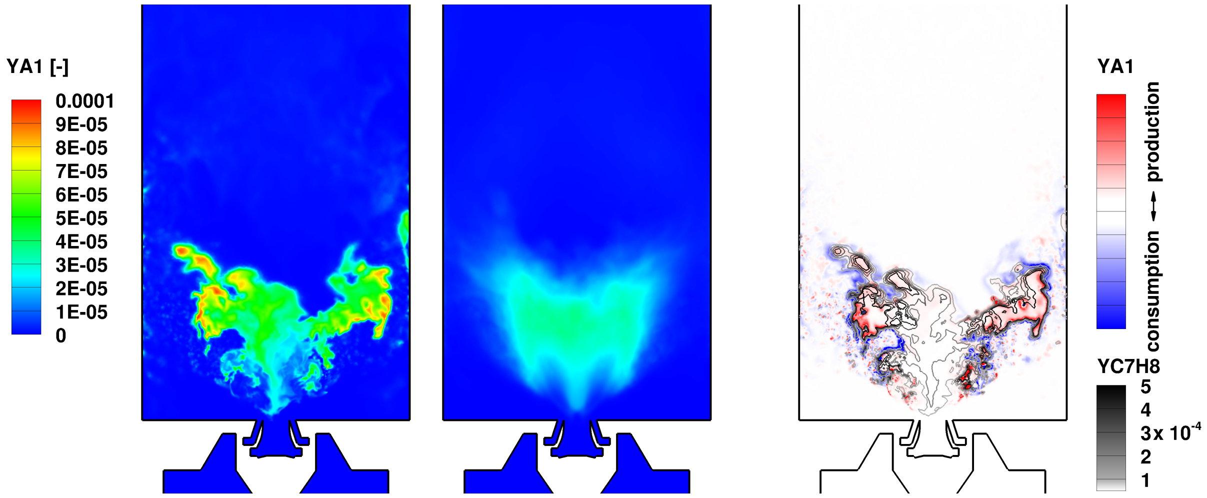

(a) (b) (c)

Figure 4.50.: Instantaneous (a) and time-averaged (b) gas concentration field as well as instantaneous net production / consumption rate (c) of benzene.

5. Conclusions

The thesis at hand aimed at combining state-of-the-art sub-models, which were previously used for isolated individual sub-processes, to obtain a computational platform for the simulation of turbulent reacting multi-phase flows. Due to the new challenges related to fuel flexibility, a special focus was on fuel dependencies in the modeling. The simulation platform for turbulent reactive, multi-phase flows (THETA-SPRAYSIM) of the DLR Institute of Combustion Technology was upgraded to Eulerian-Lagrangian Large Eddy Simulations. This included the coupling of LES sub-grid scale quantities in THETA with the droplet equations in SPRAYSIM. In this context, LES sub-grid scale models for (turbulent) dispersion and vaporization were implemented and a coupling of the multi-component vaporization model in SPRAYSIM with the detailed chemistry solver in THETA was established. Additionally, the steady versions of the jet in cross-flow breakup model and the secondary breakup models were upgraded to unsteady flows. An empirical approach for the derivation of spray initial/boundary conditions resulting from the breakup of liquid films was deduced. The complete platform was subsequently tested on non-reactive and reactive test cases. The non-reactive test cases comprised sub-model tests for the atomization and dispersion models. The reactive test cases included the combustion around droplet chains, a swirl-stabilized lab-scale spray burner and a reactor related to fuel processing technology. The following conclusions are based on the experiences gained during the development, implementation and application of the models for the individual sub-processes including the outcomes of the simulation.

Atomization As already mentioned in section 2.3.1.4, the atomization models presented in this thesis do not aim at resolving the gas-liquid interface in detail. Therefore, they partly (jet in cross-flow model) or entirely (pre-filming airblast model) depend on empiricism and can only represent key features of the atomization process at specific conditions. As a consequence, the models cannot be universally valid and are restricted to a limited range of applicability. Within their range of applicability, the comparison with experimental findings generally shows a good agreement. Not only providing integral values but also delivering droplet size distributions and starting positions (by a prediction of the location of droplet detachment from the liquid body), the models can deliver initial and boundary conditions for Lagrangian particle tracking without the necessity of experimental data. However, a proper representation of the atomization process in combustion simulations is still a major scientific challenge and involves high uncertainties. Universally valid, accurate and efficient models, which can be embedded into simulation tools, are yet not available and need to be in the focus of future research programs.

Turbulence and turbulent dispersion The iso-thermal flow simulation of the swirl-stabilized spray burner (section 4.3.3.1) shows that iso-thermal, turbulent, confined flows can be predicted with a high level of accuracy given that the mesh resolution is sufficiently high. Large Eddy Simulations with the WALE sub-grid scale closure for the unresolved sub-grid Reynolds stresses provide accurate predictions of not only the average velocities but also the velocity fluctuations. However, with the transition from RANS to LES, the accuracy and fidelity of boundary conditions becomes critical. In the simulations presented here, this refers to inlet conditions and boundary conditions at the confinements. In the case of compressible flows, which were not part of this thesis, the outlet condition additionally requires special attention. At the inlets not only the mean flow properties are necessary but also the turbulent fluctuations of these quantities (ideally resolved in time). In most configurations, these boundary conditions are unknown but they probably control the flow more than the details of the individual sub-models (Gicquel *et al.*, 2012). Of course, this also applies to scalar quantities in reacting conditions discussed later on. Concerning the turbulent dispersion of solid particles in iso-thermal, turbulent, confined flows, the investigation presented in section 3.3 showed that the turbulent dispersion of solid spherical particles in swirling flows can be well predicted. Both sub-grid scale models for turbulent dispersion, i.e. the interaction time dispersion model (section 2.3.2.2) and the stochastic dispersion model (section 2.3.2.3), are capable to reproduce the experimental data concerning the mass fluxes as well as the gas and particle velocities (including fluctuations). However, different flow configurations, e.g. shear layers and backward-facing steps, as well as the influence of non-sphericity, i.e. deformation of droplets, need to be tested in further investigations. Furthermore, the point-droplet assumption has to be reviewed for future high resolution computations, which become more and more feasible with increasing computing power. As the cell sizes of the computational grid decreases, the assumption that only a small portion of the volume is occupied by the liquid droplet does not hold anymore and the displacement due to the liquid has to be accounted for.

Vaporization and coupling to the gas phase kinetics The simulations of the combustion around the five mono-disperse droplet chains in section 4.1 show that the evaporation models presented in section 2.3.3 are capable to reproduce the influence of different fuel compositions on evaporation and combustion. Besides the fact that the evaporation models were extensively tested and validated in the context of RANS simulations by Rauch (2017), a quantitative study in the context of LES, especially investigating the influence of the unresolved sub-grid scale fluctuations on evaporation, was not part of this thesis and would be advisable for the future. Furthermore, additional fuel families might be necessary to describe small differences in fuel properties related to future fuels. In this context, the correlations for the physical properties within the CTM model need to be reviewed. In addition, the coupling of one fuel family to one single surrogate species in the reaction mechanism of the gas phase may not be sufficient to predict phenomena significantly influenced by the chain length of the molecule, e.g. auto-ignition.

Chemical reaction and gas phase kinetics Within this thesis, the modeling of chemical reactions is based on a finite rate chemistry approach. In this approach, each species is individually transported. The elementary reactions for these species are directly computed from the Arrhenius equations. The benefits of this approach can be seen in the simulation of the swirl-stabilized burner, which reveals several states in the combustion chamber depending on a finite rate chemistry (Fig. 4.40). Nevertheless, the sub-grid scale model for turbulence-chemistry interaction based on presumed probability density functions needs to be reviewed, especially with respect to limitations for spray simulations. Furthermore, reduced reaction mechanisms for complex fuels still involve high uncertainties. Aside from the loss of generality during the reduction step, the reaction mechanisms tend to suffer from unphysical behavior towards the extreme ends of their applicability range, e.g. in low temperature regions like inflows or extremely fuel-rich zones. This can induce numerical instabilities. Furthermore, most reaction mechanisms are only valid for a specific and previously fixed mixture. However, during the evaporation of multi-component fuels in reacting sprays, the local composition in the gas phase can vary significantly depending on the volatility of the components. As a consequence, the reaction mechanism should reproduce laminar flame speeds and ignition delay times not only for the fixed composition of the entire mixture but also for a specific single component in the mixture. In the future, the prediction of fuel dependent phenomena will be impossible if the reaction mechanism relies on a fixed composition. Besides, the designers of new reaction mechanisms need to shift the focus from the reproduction of global target variables (e.g. laminar flame speed, adiabatic flame temperature and ignition delay times) to a detailed validation of intermediate species profiles in order to correctly predict pollutant formation and emissions. For instance, soot formation is known to strongly depend on a correct prediction of intermediate species like acetylene and benzene.

Speed-up of computations and data management LES of turbulent reacting multi-phase flows depend on massively parallel supercomputers. As the data is subdivided and processed in parallel, efficient and minimum exchange of information between the individual processes is necessary to achieve a good scalability. This includes that distributed and shared memory on modern supercomputers have to be efficiently used. In this context, the thesis at hand contributed to the parallelization of the dispersed phase solver (SPRAYSIM). The particle-based parallelization uses the MPI-3 standard. The Message Passing Interface (MPI) is a standardized and efficient message-passing system which allows to access both the shared (since MPI-3) and distributed memory on modern supercomputers. The already existing parallelization of the gas phase solver (THETA) depends on an older version of the MPI standard. Running the codes and computing large reactive cases, e.g. the swirl-stabilized spray burner, a good scale-up performance could be achieved up to ~ 3000 cores. Then, the exchange of data between the two solvers becomes a bottleneck. Furthermore, the generation of large meshes and their partitioning for future high-resolution LES tend to become more and more challenging. Besides, these computations require massive storage capacities and post-processing routines which are adapted to efficiently access the large data sets.

Simulation of entrained-flow gasification The change towards sustainable aviation fuels comes along with a variety of new fuel production pathways. Entrained flow gasification is a promising process for the conversion of biomass and other low-grade feedstock, e.g. highly viscous slurries and suspensions with a significant content of solid particles, to high quality fuels. A major scientific challenge is the prediction of the physical and chemical phenomena occurring in such high-temperature and high-pressure multi-phase flow systems. In order to reduce complexity, the study within this thesis focused on a two-phase (gas and liquid) flow system with a model fuel (mono-ethylene glycol) under atmospheric conditions. Downstream comparisons with experimental data showed a reasonable agreement concerning temperature and species profiles. The analysis of the injector near-field revealed that the high temperature reaction zone close to the injector could not be explained by a direct reaction of the fuel with the oxidizer. Instead, carbon monoxide and hydrogen mainly formed on the axis were transported upstream by the recirculation zone. The reactions of CO and H_2 with the oxygen stabilized the flame. The heat release from these reactions supported the vaporization and decomposition of fuel as well as the downstream gasification reactions. The investigations presented in this thesis helped to gain insight into rich-burn and gasification. Furthermore, they showed the wide applicability of the numerical tools developed in the framework of this thesis. In the future, the focus needs to be shifted from a single-component model fuel towards real fuels. This implies an increase in complexity to the point of waste and biomass based slurries. More research is needed to incorporate the complex fuel compositions and topologies into numerical tools in order to improve the predictive capabilities of the simulation. Moreover, further examinations regarding chemical kinetics under fuel-rich conditions are advisable as most of the mechanisms were derived and optimized for combustion.

Simulation of swirl-stabilized spray combustion The final test case consisted in a lab-scale, swirl-stabilized spray burner, which exhibits some of the key features of current aero-engines combustors. In the framework of this thesis, the simulation of this burner involved the highest complexity. This is due to the fact that a multi-component fuel is introduced via a hybrid fuel injector with a complex atomization pattern into a complex geometry with significant heat loss at the confinements. Accurate predictions of such complex systems are very challenging, especially as uncertainties concerning the boundary conditions for the confinements and the spray cannot be excluded. Despite these complications, global features like the measured spray distribution and the measured position of the reaction zone are well reproduced by the LES. The quantitative comparison of droplet size, droplet velocity and liquid volume flux profiles show a good agreement. However, the temperature profiles reveal a significant discrepancy in the central mixing zone. In the LES, the temperature rise on the central axis is observed further towards the outlet. It could not be finally clarified if the discrepancies are related to differences in boundary conditions or still existing deficiencies in the sub-models. Further simulations will be necessary to analyze the sensitivity of the results on these aspects. Nevertheless, the analysis presented in section 4.3.3 show the great potential of spray combustion LES. In comparison to measurements, a large set of simultaneously taken three-dimensional data with a high temporal and spatial resolution is available. Therefore, LES can help in the understanding and interpretation of complex phenomena. In this context, the simulations showed that evaporation and mixing are the rate-controlling steps in the flame zone. In this zone, chemistry can be assumed to be infinitely fast. That means that evaporation and mixing times introduce an inherent damping to combustion. These findings directly relate to modern combustion concepts as described in section 1.1.2 explaining why the trend towards a higher degree of prevaporization and premixing makes these combustion systems more susceptible to instabilities. In contrast to the infinitely fast chemistry in the flame zone, other zones exist where finite rate chemistry effects prevail. Future developments concerning the simulation of swirl-stabilized spray combustion should focus on incorporating high pressure effects in the individual sub-models as current aero-engines already have combustor inlet pressures and temperatures of about 50 bar and 900 K with rising trends (Epstein, 2012). Furthermore, fuel-dependencies need to be revised in all sub-processes to enable predictions about the impact of future fuels on the combustion process.

A. Species profile in a steady 1-D diffusion-governed vapor film

Neglecting time derivatives and convective terms Eq. 2.2.2 reduces to:

$$\frac{\partial j_\alpha}{\partial x} = 0 \tag{A.0.1}$$

Introducing Fick's law (Eq. 2.2.23) yields:

$$\frac{\partial}{\partial x}\left(-\rho_g D_\alpha \frac{\partial Y_\alpha}{\partial x}\right) = 0 \tag{A.0.2}$$

Integrating twice results in a linear profile:

$$\rho_g D_\alpha \frac{\partial Y_\alpha}{\partial x} = C_1 \tag{A.0.3}$$

$$Y_\alpha = \frac{C_1}{\rho_g D_\alpha} x + C_2 \tag{A.0.4}$$

The boundary conditions at the position of the surface x^S and in the farfield x^∞ are:

$$\begin{aligned} Y_\alpha(x = x^S) &= Y_\alpha^S \\ Y_\alpha(x = x^\infty) &= Y_\alpha^\infty \end{aligned} \tag{A.0.5}$$

Inserting the boundary conditions the constants C_1 and C_2 can be determined. This results in the species mass fraction distribution:

$$Y_\alpha = \frac{x - x^S}{x^S - x^\infty}\left(Y_\alpha^S - Y_\alpha^\infty\right) + Y_\alpha^S \tag{A.0.6}$$

The gradient in x-direction is obtained by differentiation:

$$\frac{\partial Y_\alpha}{\partial x} = \frac{Y_\alpha^S - Y_\alpha^\infty}{x^S - x^\infty} \tag{A.0.7}$$

Inserting this and a characteristic length $L = 2x^\infty$ into the definition of the Sherwood number (Eq. 2.3.162) yields:

$$Sh_\alpha = \frac{\left(\frac{\partial Y_\alpha}{\partial r}\right)^S}{\frac{Y_\alpha^S - Y_\alpha^\infty}{2x^\infty}} = \frac{2x^\infty}{x^S - x^\infty} \tag{A.0.8}$$

B. Physical properties in CTM formulation

In the equations derived in section 2.3.3.3, several physical properties are needed in a continuous form. All physical properties were calculated according to Rachner and Doué (2009). The coefficients were determined by matching properties of discrete components. The molar weight is given by:

$$M_i = M_j(I) = C_{M_j,0} + C_{M_j,1} I + C_{M_j,2} I^2 \tag{B.0.1}$$

Hence, the mean molar weight can be directly calculated by the first θ_j (Eq. 2.3.209) and second moment ψ_j (2.3.210):

$$\bar{M}_j = \frac{1}{X_i} \int_{\gamma}^{\infty} X_i f_j(I) M_i dI = C_{M_j,0} + C_{M_j,1} \theta_j + C_{M_j,2} \psi_j \tag{B.0.2}$$

The vapor pressure is calculated according to:

$$p_{vap,j}(I) = p_g \; exp \left(\frac{C_{p_{vap,j},a0} + C_{p_{vap,j},b0} T + C_{p_{vap,j},c0} T^2 + (C_{p_{vap,j},a1} + C_{p_{vap,j},b1} T + C_{p_{vap,j},c1} T^2) I}{T_g^S} \right) \tag{B.0.3}$$

The enthalpy of vaporization yields:

$$\varDelta H_{vap} = \left(C_{\varDelta H_{vap},0} + C_{\varDelta H_{vap},1} I + C_{\varDelta H_{vap},2} I^2 \right) \left(\frac{T_c - T}{T_c - T_{nb}} \right)^{0.38} \tag{B.0.4}$$

with the critical temperature T_c and the normal boiling point T_{nb} given by:

$$T_c = C_{T_c,0} + C_{T_c,1} I + C_{T_c,2} I^2 \tag{B.0.5}$$

$$T_{nb} = C_{T_{nb},0} + C_{T_{nb},1} I + C_{T_{nb},2} I^2 \tag{B.0.6}$$

The heat capacity $c_{p,g}$, dynamic viscosity μ_g and the thermal conductivity λ_g of the gas were determined according to:

$$C_{p,g} = \left(C_{C_{p,g},a0} + C_{C_{p,g},b0} T + C_{C_{p,g},c0} T^2 \right) + \left(C_{C_{p,g},a1} + C_{C_{p,g},b1} T + C_{C_{p,g},c1} T^2 \right) I \tag{B.0.7}$$

$$\mu_g = \left(C_{\mu_g,a0} + C_{\mu_g,b0} T + C_{\mu_g,c0} T^2 \right) + \left(C_{\mu_g,a1} + C_{\mu_g,b1} T + C_{\mu_g,c1} T^2 \right) I \tag{B.0.8}$$

$$\lambda_g = \left(C_{\lambda_g,a0} + C_{\lambda_g,b0} T + C_{\lambda_g,c0} T^2 \right) + \left(C_{\lambda_g,a1} + C_{\lambda_g,b1} T + C_{\lambda_g,c1} T^2 \right) I \tag{B.0.9}$$

The heat of formation is given by:

$$h_f^0 = C_{h_f^0,0} + C_{h_f^0,1} I + C_{h_f^0,2} I^2 \tag{B.0.10}$$

The mole density c_l and the heat capacity $C_{p,l}$ of the liquid result from:

$$c_l = \left(C_{c_l,a0} + C_{c_l,b0} T\right) + \left(C_{c_l,a1} + C_{c_l,b1} T\right) I + \left(C_{c_l,a2} + C_{c_l,b2} T\right) I^2 \tag{B.0.11}$$

$$C_{p,l} = \left(C_{C_{p,l},a0} + C_{C_{p,l},b0} T\right) + \left(C_{C_{p,l},a1} + C_{C_{p,l},b1} T\right) I + \left(C_{C_{p,l},a2} + C_{C_{p,l},b2} T\right) I^2 \tag{B.0.12}$$

The surface tension is determined by:

$$\sigma_l = C_{\sigma_l,0} + C_{\sigma_l,1} I + C_{\sigma_l,2} I^2 \tag{B.0.13}$$

The liquid viscosity is given by:

$$log\left(\mu_l\right) = \left(C_{\mu_l,a0} + C_{\mu_l,a1} I + C_{\mu_l,a2} I^2\right) \left(\frac{1}{T} \frac{1}{C_{\mu_l,b0} + C_{\mu_l,b1} I + C_{\mu_l,b2} I^2}\right) \tag{B.0.14}$$

The liquid thermal conductivity yields:

$$\lambda_l = \left(C_{\lambda_l,a0} + C_{\lambda_l,b0} T + C_{\lambda_l,c0} T^2\right) + \left(C_{\lambda_l,a1} + C_{\lambda_l,b1} T + C_{\lambda_l,c1} T^2\right) I \tag{B.0.15}$$

Bibliography

B. Abramzon and W. Sirignano. Droplet vaporization model for spray combustion calculations. *International Journal of Heat and Mass Transfer*, 32(9):1605–1618, 1989. URL `http://linkinghub.elsevier.com/retrieve/pii/0017931089900434`.

Manfred Martin Aigner. *Charakterisierung der bestimmenden Einflußgrößen bei der luftgestützten Zerstäubung.* PhD thesis, Universität Karlsruhe, 1986.

A. A. Amsden, P. J. O'Rourke, and T. D. Butler. Kiva-ii: A computer program for chemically reactive flows with sprays. Technical Report LA-11560-MS, Los Alamos National Lab., May 1989.

S.V. Apte, K. Mahesh, P. Moin, and J.C. Oefelein. Large-eddy simulation of swirling particle-laden flows in a coaxial-jet combustor. *International Journal of Multiphase Flow*, 29(8): 1311 – 1331, 2003. ISSN 0301-9322. doi: 10.1016/S0301-9322(03)00104-6. URL `http://www.sciencedirect.com/science/article/pii/S0301932203001046`.

Marco Arienti and Marios C. Soteriou. Time-resolved proper orthogonal decomposition of liquid jet dynamics. *Physics of Fluids*, 21(11):112104, 2009. doi: 10.1063/1.3263165. URL `http://dx.doi.org/10.1063/1.3263165`.

Vincenzo Armenio, Ugo Piomelli, and Virgilio Fiorotto. Effect of the subgrid scales on particle motion. *Physics of Fluids*, 11(10):3030–3042, 1999. doi: http://dx.doi.org/10.1063/1.870162. URL `http://scitation.aip.org/content/aip/journal/pof2/11/10/10.1063/1.870162`.

N. Ashgriz. *Numerical Techniques for Simulating the Atomization Process*, chapter 17, pages 339–357. Springer US, Boston, MA, 2011. ISBN 978-1-4419-7264-4. doi: 10.1007/978-1-4419-7264-4_17. URL `http://dx.doi.org/10.1007/978-1-4419-7264-4_17`.

ASTM D1655. Standard specification for aviation turbine fuels. Standard, American Society for Testing and Materials (ASTM), 2016.

ASTM D7566. Standard specification for aviation turbine fuel containing synthesized hydrocarbons. Standard, American Society for Testing and Materials (ASTM), 2016.

H.D. Baehr and K. Stephan. *Wärme- und Stoffübertragung.* Springer, Berlin, 2006.

S. Balachandar and John K. Eaton. Turbulent dispersed multiphase flow. *Annual Review of Fluid Mechanics*, 42(1):111–133, 2010. doi: 10.1146/annurev.fluid.010908.165243. URL `http://www.annualreviews.org/doi/abs/10.1146/annurev.fluid.010908.165243`.

Steven R. H. Barrett, Rex E. Britter, and Ian A. Waitz. Global mortality attributable to aircraft cruise emissions. *Environmental Science & Technology*, 44(19):7736–7742, 2010. doi: 10.1021/es101325r. URL `http://dx.doi.org/10.1021/es101325r`. PMID: 20809615.

F.-O. Bartz, R. Schmehl, R. Koch, and H.-J. Bauer. An extension of dynamic droplet deformation models to secondary atomization. In *ILASS Europe 2010 - 23rd European Conference on Liquid Atomization and Spray Systems*, Brno, Czech Republic, September 2010.

F.-O. Bartz, D. R. Guildenbecher, R. Schmehl, R. Koch, H.-J. Bauer, and P. E. Sojka. Model comparison for single droplet fragmentation under varying accelerations. In *ILASS Europe 2011, 24th European Conference on Liquid Atomization and Spray Systems*, Estoril, Portugal, September 2011.

Feras Z. Batarseh, Ilia V. Roisman, and Cameron Tropea. Characterization of a spray generated by an airblast atomizer with prefilmer. *Atomization and Sprays*, 20(10):887–903, 2010. ISSN 1044-5110.

J. Becker and C. Hassa. Breakup and atomization of a kerosene jet in crossflow at elevated pressure. *Atomization and Sprays*, 12(1-3):49–67, 2002. URL `http://elib.dlr.de/1169/`.

A. S. Berrouk, D. Laurence, J.J. Riley, and D.E. Stock. Stochastic modelling of inertial particle dispersion by subgrid motion for les of high reynolds number pipe flow. *Journal of Turbulence*, 8:N50, 2007. doi: 10.1080/14685240701615952. URL `http://dx.doi.org/10.1080/14685240701615952`.

U. Bhayaraju and C. Hassa. Planar liquid sheet breakup of prefilming and nonprefilming atomizers at elevated pressure. *Atomization And Sprays*, 19(12):1147–1169, Dezember 2009. URL `http://elib.dlr.de/63171/`.

R.W. Bilger, S.H. Stårner, and R.J. Kee. On reduced mechanisms for methane-air combustion in nonpremixed flames. *Combustion and Flame*, 80(2):135 – 149, 1990. ISSN 0010-2180. doi: http://dx.doi.org/10.1016/0010-2180(90)90122-8. URL `http://www.sciencedirect.com/science/article/pii/0010218090901228`.

M. Bini and W. P. Jones. Large-eddy simulation of particle-laden turbulent flows. *Journal of Fluid Mechanics*, 614:207–252, 2008. doi: 10.1017/S0022112008003443. URL `http://dx.doi.org/10.1017/S0022112008003443`.

Robert Byron Bird, Warren E. Stewart, and Edwin N. Lightfoot. *Transport phenomena*. Wiley, New York, 2. ed. edition, 2002. ISBN 0-471-41077-2; 0-471-36474-6.

Thomas Blacha. *Effiziente Rußmodellierung in laminaren und turbulenten Flammen unterschiedlicher Brennstoffe.* PhD thesis, Fakultät für Luft- und Raumfahrttechnik und Geodäsie, Universität Stuttgart, Stuttgart, 2012. URL `http://elib.uni-stuttgart.de/opus/volltexte/2013/7809`.

M. Boileau, S. Pascaud, E. Riber, B. Cuenot, L. Y. M. Gicquel, T. J. Poinsot, and M. Cazalens. Investigation of two-fluid methods for large eddy simulation of spray combustion in gas turbines. *Flow, Turbulence and Combustion*, 80(3):291–321, 2008. ISSN 1573-1987. doi: 10.1007/s10494-007-9123-1. URL `http://dx.doi.org/10.1007/s10494-007-9123-1`.

Joseph Boussinesq. Essai sur la théorie des eaux courantes. Rapport sur un mémoire de M. Boussinesq. *Mémoires présentés par divers savants à l'Académie des sciences de l'Institut de France : sciences mathématiques et physiques*, 1:XXII–680, 1877.

M. Brandt, M. Rachner, and G. Schmitz. An experimental and numerical study of kerosine spray evaporation in a premix duct for gas turbine combustors at high pressure. *Combustion Science and Technology*, 138(4):313 – 348, 1998.

Enrico Bärow, Sebastian Gepperth, Rainer Koch, and Hans-Jörg Bauer. Effect of the precessing vortex core on primary atomization. *Zeitschrift für Physikalische Chemie*, 229(6):909–929, 2015. doi: doi:10.1515/zpch-2014-0619.

M. Burger, R. Schmehl, K. Prommersberger, O. Schäfer, R. Koch, and S. Wittig. Droplet evaporation modeling by the distillation curve model: accounting for kerosene fuel and elevated pressures. *International Journal of Heat and Mass Transfer*, 46(23):4403 – 4412, 2003. ISSN 0017-9310. doi: http://dx.doi.org/10.1016/S0017-9310(03)00286-2. URL `http://www.sciencedirect.com/science/article/pii/S0017931003002862`.

F. Bustamante, R. M. Enick, A.V. Cugini, R. P. Killmeyer, B. H. Howard, K. S. Rothenberger, M. V. Ciocco, B. D. Morreale, S. Chattopadhyay, and S. Shi. High-temperature kinetics of the homogeneous reverse water-gas shift reaction. *AIChE Journal*, 50(5):1028–1041, 2004. ISSN 1547-5905. doi: 10.1002/aic.10099. URL `http://dx.doi.org/10.1002/aic.10099`.

T.D. Butler and P.J. O'Rourke. A numerical method for two dimensional unsteady reacting flows. *Symposium (International) on Combustion*, 16(1):1503 – 1515, 1977. ISSN 0082-0784. doi: http://dx.doi.org/10.1016/S0082-0784(77)80432-3. URL `http://www.sciencedirect.com/science/article/pii/S0082078477804323`.

M.J. Cernick, S.W. Tullis, and M.F. Lightstone. Particle subgrid scale modelling in large-eddy simulations of particle-laden turbulence. *Journal of Turbulence*, 16(2):101–135, 2014. doi: 10.1080/14685248.2014.969888. URL `http://dx.doi.org/10.1080/14685248.2014.969888`.

G. Chaussonnet, O. Vermorel, E. Riber, and B. Cuenot. A new phenomenological model to predict drop size distribution in large-eddy simulations of airblast atomizers. *International Journal of Multiphase Flow*, 80:29 – 42, 2016. ISSN 0301-9322. doi: http://dx.doi.org/10.1016/

j.ijmultiphaseflow.2015.10.014. URL `http://www.sciencedirect.com/science/article/pii/S0301932215002566`.

Sergio Chibbaro and Jean-Pierre Minier. Langevin pdf simulation of particle deposition in a turbulent pipe flow. *Journal of Aerosol Science*, 39(7):555 – 571, 2008. ISSN 0021-8502. doi: 10.1016/j.jaerosci.2008.03.002. URL `http://www.sciencedirect.com/science/article/pii/S0021850208000517`.

W.-H. Chou and G.M. Faeth. Temporal properties of secondary drop breakup in the bag breakup regime. *International Journal of Multiphase Flow*, 24(6):889 – 912, 1998. ISSN 0301-9322. doi: 10.1016/S0301-9322(98)00015-9. URL `http://www.sciencedirect.com/science/article/pii/S0301932298000159`.

W.-H. Chou, L.-P. Hsiang, and G.M. Faeth. Temporal properties of drop breakup in the shear breakup regime. *International Journal of Multiphase Flow*, 23(4):651 – 669, 1997. ISSN 0301-9322. doi: http://dx.doi.org/10.1016/S0301-9322(97)00006-2. URL `http://www.sciencedirect.com/science/article/pii/S0301932297000062`.

Mouldi Chrigui, James Gounder, Amsini Sadiki, Assaad R. Masri, and Johannes Janicka. Partially premixed reacting acetone spray using les and fgm tabulated chemistry. *Combustion and Flame*, 159(8):2718 – 2741, 2012. ISSN 0010-2180. doi: http://dx.doi.org/10.1016/j.combustflame.2012.03.009. URL `http://www.sciencedirect.com/science/article/pii/S0010218012000971`.

Mouldi Chrigui, Fernando Sacomano, Amsini Sadiki, and Assaad R. Masri. *Evaporation Modeling for Polydisperse Spray in Turbulent Flow*, pages 55–77. Springer International Publishing, Cham, 2014. ISBN 978-3-319-04678-5. doi: 10.1007/978-3-319-04678-5_3. URL `http://dx.doi.org/10.1007/978-3-319-04678-5_3`.

R. Clift, John R. Grace, and Martin E. Weber. *Bubbles, drops, and particles*. Academic Press New York, 1978. ISBN 012176950.

O. Colin, F. Ducros, D. Veynante, and T. Poinsot. A thickened flame model for large eddy simulations of turbulent premixed combustion. *Physics of Fluids*, 12(7):1843–1863, 2000. doi: 10.1063/1.870436. URL `http://dx.doi.org/10.1063/1.870436`.

Edwin Corporan, James T. Edwards, Linda Shafer, Matthew J. DeWitt, Christopher Klingshirn, Steven Zabarnick, Zachary West, Richard Striebich, John Graham, and Jim Klein. Chemical, thermal stability, seal swell, and emissions studies of alternative jet fuels. *Energy & Fuels*, 2011.

B. Cuenot, M. Boileau, S. Pascaud, J.-B. Mossa, E. Riber, T. Poinsot, and C. Bérat. Large eddy simulation of two-phase reacting flows. In *ECCOMAS CFD 2006 - European Conference on Computational Fluid Dynamics*, Egmond Aan Zee, The Netherlands, 2006. URL `http://www.cerfacs.fr/~cfdbib/repository/TR_CFD_06_46.pdf`.

Philippe Dagaut and Michel Cathonnet. The ignition, oxidation, and combustion of kerosene: A review of experimental and kinetic modeling. *Progress in Energy and Combustion Science*, 32(1):48 – 92, 2006. ISSN 0360-1285. doi: http://dx.doi.org/10.1016/j.pecs.2005.10.003. URL `http://www.sciencedirect.com/science/article/pii/S0360128505000523`.

Z. Dai and G.M. Faeth. Temporal properties of secondary drop breakup in the multimode breakup regime. *International Journal of Multiphase Flow*, 27(2):217 – 236, 2001. ISSN 0301-9322. doi: 10.1016/S0301-9322(00)00015-X. URL `http://www.sciencedirect.com/science/article/pii/S030193220000015X`.

S. de Chaisemartin, F. Laurent, M. Massot, and J. Reveillon. Evaluation of eulerian multi-fluid versus lagrangian methods for ejection of polydisperse evaporating sprays by vortices. *Journal of Computational Physics*, 2007.

J.-P. Delplanque. *Liquid-oxygen droplet vaporization and combustion: analysis of transcritical behavior and application to liquid rocket combustion instability.* PhD thesis, University of California, Irvine, 1992.

Jean-Pierre Delplanque and William A. Sirignano. Boundary-layer stripping effects on droplet transcritical convective vaporization. *Atomization and Sprays*, 4(3):325–349, 1994. ISSN 1044-5110.

Massimiliano Di Domenico. *Numerical Simulations of Soot Formation in Turbulent Flows.* PhD thesis, Fakultät für Luft- und Raumfahrttechnik und Geodäsie, Universität Stuttgart, 2008. URL `http://elib.dlr.de/57173/`.

T. Doerr. Introduction to aero-engine gas turbine combustion. In R. Denos and G. Paniagua, editors, *Lecture series - Aeroengine design: From state of the art of turbofans towards innovative architectures*, number 4, Rhode Saint Genese, Belgium, April 2013. Von Karman Institute for Fluid Dynamics.

Nicolas Doué, Patrick Le Clercq, and Manfred Aigner. Validation of a multicomponent-fuel droplet evaporation model based on continuous thermodynamics. In *ICLASS 2006 - 10th International Conference on Liquid Atomization and Spray Systems*, 2006. URL `http://elib.dlr.de/47485/`.

F. Ducros, F. Nicoud, and T. Poinsot. A wall-adapting local eddy-viscosity model for simulations in complex geometries. In *Conference on Numerical Methods for Fluid Dynamics*, Oxford, UK, 1998.

C. Eberle, P. Gerlinger, K.P. Geigle, and M. Aigner. Numerical investigation of transient soot evolution processes in an aero-engine model combustor. *Combustion Science and Technology*, 187:1841–1866, 2015. doi: 10.1080/00102202.2015.1065254. URL `http://dx.doi.org/10.1080/00102202.2015.1065254`.

G. Eckel, M. Rachner, P. Le Clercq, M. Di Domenico, and M. Aigner. Unsteady simulation of liquid jet atomization in cross-flow at gas turbine conditions. In *ILASS Europe 2011 - 24th European Conference on Liquid Atomization and Spray Systems*, Estoril, Portugal, September 2011.

G. Eckel, M. Rachner, P. Le Clercq, and M. Aigner. Semi-empirical primary atomization models for transient lagrangian spray simulation. In *ICMF 2013 - 8th International Conference on Multiphase Flow*, Jeju, Korea, May 2013.

Georg Eckel, Michael Rachner, Patrick Le Clercq, and Manfred Aigner. Semi-empirical model for the unsteady shear breakup of liquid jets in cross-flow. *Atomization and Sprays*, 26(7): 687–712, 2016. ISSN 1044-5110. doi: 10.1615/AtomizSpr.2015011185.

Tim Edwards and Lourdes Q. Maurice. Surrogate mixtures to represent complex aviation and rocket fuels. *Journal of Propulsion and Power*, 17(2):461 – 466, 2001. doi: doi:10.2514/2.5765. URL `http://dx.doi.org/10.2514/2.5765`.

Alan H. Epstein. Aircraft engines' needs from combustion science and engineering. *Combustion and Flame*, 159(5):1791 – 1792, 2012. ISSN 0010-2180. doi: http://dx.doi.org/10.1016/j.combustflame.2012.02.022. URL `http://www.sciencedirect.com/science/article/pii/S0010218012000715`.

Moritz Ertl, Grzegorz K. Karch, Filip Sadlo, Thomas Ertl, and Bernhard Weigand. Investigation and visual analysis of direct simulations of quasi-steady primary break-up of shear thinning liquids. In *ICMF 2016 - 9th International Conference on Multiphase Flow*, Florence, Italy, May 2016.

G.M. Faeth. Evaporation and combustion of sprays. *Progress in Energy and Combustion Science*, 9(1):1 – 76, 1983. ISSN 0360-1285. doi: http://dx.doi.org/10.1016/0360-1285(83)90005-9. URL `http://www.sciencedirect.com/science/article/pii/0360128583900059`.

Vital Gutierrez Fernandez, G. Lavergne, and P. Berthoumieu. Dynamic primary atomization characteristics in an airblast atomizer, high pressure conditions. *Atomization and Sprays*, 21 (1):1–16, 2011a. ISSN 1044-5110.

Vital Gutierrez Fernandez, G. Lavergne, and P. Berthoumieu. Geometric primary atomization characteristics in an airblast atomizer, high pressure conditions. *Atomization and Sprays*, 21 (1):17–29, 2011b. ISSN 1044-5110.

J.H. Ferziger and M. Peric. *Numerische Strömungsmechanik*. Springer, Berlin, 2008.

B.D. Fishburn. Boundary layer stripping of liquid drops fragmented by taylor instability. *Acta Astronautica*, 1(9?10):1267 – 1284, 1974. ISSN 0094-5765. doi: http://dx.doi.org/

10.1016/0094-5765(74)90051-4. URL `http://www.sciencedirect.com/science/article/pii/0094576574900514`.

S. Fleck, U. Santo, C. Hotz, T. Jakobs, G. Eckel, M. Mancini, R. Weber, and T. Kolb. Entrained flow gasification. part 1: Gasification of glycol in an atmospheric-pressure experimental rig. *Fuel*, 217:306–319, 2018. ISSN 0016-2361. doi: https://doi.org/10.1016/j.fuel.2017.12.077. URL `https://www.sciencedirect.com/science/article/pii/S0016236117316551`.

Michael Foust, Doug Thomsen, Richard Stickles, Clayton Cooper, and Will Dodds. Development of the ge aviation low emissions taps combustor for next generation aircraft engines. In *50th AIAA Aerospace Sciences Meeting*. American Institute of Aeronautics and Astronautics, 2012. doi: doi:10.2514/6.2012-936. URL `http://dx.doi.org/10.2514/6.2012-936`.

Rodney O. Fox. Large-eddy-simulation tools for multiphase flows. *Annual Review of Fluid Mechanics*, 44(1):47–76, 2012. doi: 10.1146/annurev-fluid-120710-101118. URL `http://www.annualreviews.org/doi/abs/10.1146/annurev-fluid-120710-101118`.

B.M. Franchetti, F. Cavallo Marincola, S. Navarro-Martinez, and A.M. Kempf. Large eddy simulation of a pulverised coal jet flame. *Proceedings of the Combustion Institute*, 34(2):2419 – 2426, 2013. ISSN 1540-7489. doi: http://dx.doi.org/10.1016/j.proci.2012.07.056. URL `http://www.sciencedirect.com/science/article/pii/S1540748912003483`.

Thomas Frank. *Parallele Algorithmen für die numerische Simulation dreidimensionaler, disperser Mehrphasenströmungen und deren Anwendung in der Verfahrenstechnik*. Habilitation, Technische Universität Chemnitz, June 2002. URL `http://monarch.qucosa.de/fileadmin/data/qucosa/documents/4566/data/index.html`.

B. Franzelli, B. Fiorina, and N. Darabiha. A tabulated chemistry method for spray combustion. *Proceedings of the Combustion Institute*, 34(1):1659 – 1666, 2013. ISSN 1540-7489. doi: http://dx.doi.org/10.1016/j.proci.2012.06.013. URL `http://www.sciencedirect.com/science/article/pii/S1540748912001216`.

Jochen Fröhlich. *Large Eddy Simulation turbulenter Strömungen*. B.G. Teubner Verlag / GWV Fachverlage GmbH, 2006. doi: http://dx.doi.org/10.1007/978-3-8351-9051-1. URL `http://ebooks.ub.uni-muenchen.de/7914/`.

K.a Fukagata, S.b Zahrai, and F.H.c Bark. Dynamics of brownian particles in a turbulent channel flow. *Heat and Mass Transfer/Waerme- und Stoffuebertragung*, 40(9):715–726, 2004. URL `https://www.scopus.com/inward/record.uri?eid=2-s2.0-4243156279&partnerID=40&md5=587f2e238c3c71fd5d0a6c2fcc6665fe`.

R. Gaffney, Jr., J. White, S. Girimaji, and J. Drummond. Modeling turbulent/chemistry interactions using assumed pdf methods. In *28th Joint Propulsion Conference and Exhibit*. American Institute of Aeronautics and Astronautics, 1992. doi: doi:10.2514/6.1992-3638. URL `http://dx.doi.org/10.2514/6.1992-3638`.

Crispin W. Gardiner. *Handbook of stochastic methods: for physics, chemistry and the natural sciences*. Springer, Berlin; Heidelberg [u.a.], 3. ed. edition, 2004. ISBN 3-540-20882-8.

G.C. Gebel, T. Mosbach, W. Meier, and M. Aigner. Laser-induced blast waves in air and their effect on monodisperse droplet chains of ethanol and kerosene. *Shock Waves*, 25(4):415–429, 2015a. ISSN 0938-1287. doi: 10.1007/s00193-015-0564-5. URL `http://dx.doi.org/10.1007/s00193-015-0564-5`.

Gregor C. Gebel, Thomas Mosbach, Wolfgang Meier, and Manfred Aigner. Optical and spectroscopic diagnostics of laser-induced air breakdown and kerosene spray ignition. *Combustion and Flame*, 162(4):1599 – 1613, 2015b. ISSN 0010-2180. doi: http://dx.doi.org/10.1016/j.combustflame.2014.11.024. URL `//www.sciencedirect.com/science/article/pii/S0010218014003782`.

S. Gepperth. Pre-filming airblast atomization. private communication, 2013.

S. Gepperth, D. Guildenbecher, R. Koch, and H.J. Bauer. Pre-filming primary atomization: Experiments and modeling. In *ILASS Europe 2010 - 23rd Annual Conference on Liquid Atomization and Spray Systems*, Brno, Czech Republic, September 2010.

S. Gepperth, A. Müller, R. Koch, and H.J. Bauer. Ligament and droplet characteristics in pre-filming air blast atomization. In *ICLASS 2012 - 12th Triennial International Conference on Liquid Atomization and Spray Systems*, Heidelberg, Germany, September 2012.

S. Gepperth, E. Bärow, R. Koch, and H.-J. Bauer. Primary atomization of prefilming airblast nozzles: Experimental studies using advanced image processing techniques. In *ILASS Europe 2014, 26th Annual Conference on Liquid Atomization and Spray Systems*, Bremen, Germany, September 2014.

P. Gerlinger. *Numerische Verbrennungssimulation - Effiziente numerische Simulation turbulenter Verbrennung*. Springer, Berlin, 2005.

P. Gerlinger, H. Möbus, and D. Brüggemann. An implicit multigrid method for turbulent combustion. *Journal of Computational Physics*, 167:247–276, 2001.

Massimo Germano, Ugo Piomelli, Parviz Moin, and William H. Cabot. A dynamic subgrid-scale eddy viscosity model. *Physics of Fluids A: Fluid Dynamics*, 3(7):1760–1765, 1991. doi: 10.1063/1.857955. URL `http://dx.doi.org/10.1063/1.857955`.

Abdulla Ghani, Thierry Poinsot, Laurent Gicquel, and J.-D. Müller. Les study of transverse acoustic instabilities in a swirled kerosene/air combustion chamber. *Flow, Turbulence and Combustion*, 96(1):207–226, 2016. ISSN 1573-1987. doi: 10.1007/s10494-015-9654-9. URL `http://dx.doi.org/10.1007/s10494-015-9654-9`.

S. Ghosal and P. Moin. The basic equations for the large eddy simulation of turbulent flows in complex geometry. *Journal of Computational Physics*, 118(1):24 – 37, 1995. ISSN 0021-9991. doi: http://dx.doi.org/10.1006/jcph.1995.1077. URL `http://www.sciencedirect.com/science/article/pii/S0021999185710777`.

L.Y.M. Gicquel, G. Staffelbach, and T. Poinsot. Large eddy simulations of gaseous flames in gas turbine combustion chambers. *Progress in Energy and Combustion Science*, 38(6):782 – 817, 2012. ISSN 0360-1285. doi: 10.1016/j.pecs.2012.04.004. URL `http://www.sciencedirect.com/science/article/pii/S0360128512000366`.

S. S. Girimaji. Assumed beta-pdf model for turbulent mixing: Validation and extension to multiple scalar mixing. *Combustion Science and Technology*, 78(4-6):177–196, 1991a. doi: 10.1080/00102209108951748. URL `http://dx.doi.org/10.1080/00102209108951748`.

Sharath Girimaji. A simple recipe for modeling reaction-rate in flows with turbulent-combustion. In *22nd Fluid Dynamics, Plasma Dynamics and Lasers Conference*. American Institute of Aeronautics and Astronautics, 1991b. doi: doi:10.2514/6.1991-1792.

Hassan Gomaa. *Modeling of liquid dynamics in spray laden compressor flows.* PhD thesis, Universität Stuttgart, 2014.

David G. Goodwin, Harry K. Moffat, and Raymond L. Speth. Cantera: An object-oriented software toolkit for chemical kinetics, thermodynamics, and transport processes. http://www.cantera.org, 2017. Version 2.3.0.

Mikhael Gorokhovski and Marcus Herrmann. Modeling primary atomization. *Annual Review of Fluid Mechanics*, 40(1):343–366, 2008. doi: 10.1146/annurev.fluid.40.111406.102200. URL `http://www.annualreviews.org/doi/abs/10.1146/annurev.fluid.40.111406.102200`.

A. D. Gosman and E. loannides. Aspects of computer simulation of liquid-fuelled combustors. In *AIAA 19th Aerospace Sciences Meeting*, number 81-0323, St. Louis, Missouri, USA, January 1981.

A.D. Gosman and E. Ioannides. Aspects of computer simulation of liquid-fueled combustors. *Journal of Energy*, 7:482–490, December 1983.

James Dakshina Gounder. *An experimental investigation of non-reacting and reacting spray jets.* PhD thesis, The University Of Sydney, School Of Aerospace, Mechanical And Mechatronic Engineering, Sydney, Australia, 2009.

James Dakshina Gounder, Agisilaos Kourmatzis, and Assaad Rachid Masri. Turbulent piloted dilute spray flames: Flow fields and droplet dynamics. *Combustion and Flame*, 159(11):3372 – 3397, 2012. ISSN 0010-2180. doi: http://dx.doi.org/10.1016/j.combustflame.2012.07.014. URL `http://www.sciencedirect.com/science/article/pii/S0010218012002271`.

Martin Gräbner. *Gasification of Solids: Past, Present, and Future*, chapter 2, pages 29–42. Wiley-VCH Verlag GmbH & Co. KGaA, 2014. ISBN 9783527673186. doi: 10.1002/9783527673186.ch2. URL `http://dx.doi.org/10.1002/9783527673186.ch2`.

Jasper Grohmann and Patrick Nau. Wall temperature measurements in the dlr swirl-stabilized spray burner by phosphor thermometry. private communication, 2015.

Jasper Grohmann, William O'Loughlin, Wolfgang Meier, and Manfred Aigner. Comparison of the combustion characteristics of liquid single-component fuels in a gas turbine model combustor. In *ASME Turbo Expo 2016: Power for Land, Sea, and Air*, number GT2016-56177, 2016a. URL `http://dx.doi.org/10.1115/GT2016-56177`.

Jasper Grohmann, Bastian Rauch, Trupti Kathrotia, Wolfgang Meier, and Manfred Aigner. Investigation of differences in lean blowout of liquid single-component fuels in a gas turbine model combustor. In *52nd AIAA/SAE/ASEE Joint Propulsion Conference*, number AIAA 2016-4647, Salt Lake City, UT, USA, July 2016b. doi: doi:10.2514/6.2016-4647. URL `http://dx.doi.org/10.2514/6.2016-4647`.

D. Guildenbecher, C. López-Rivera, and P. Sojka. Secondary atomization. *Experiments in Fluids*, 46:371–402, 2009. ISSN 0723-4864. URL `http://dx.doi.org/10.1007/s00348-008-0593-2`. 10.1007/s00348-008-0593-2.

Simon Hafner. *Modellentwicklung zur numerischen Simulation eines Flugstromvergasers für Biomasse*. PhD thesis, Ruprechts-Karls-Universität Heidelberg, 2010. URL `http://archiv.ub.uni-heidelberg.de/volltextserver/11309/`.

Simon Hafner, Arash Rashidi, Georgiana Baldea, and Uwe Riedel. A detailed chemical kinetic model of high-temperature ethylene glycol gasification. *Combustion Theory and Modelling*, 15(4):517–535, 2011. doi: 10.1080/13647830.2010.547602. URL `http://dx.doi.org/10.1080/13647830.2010.547602`.

William L.H. Hallett. A simple model for the vaporization of droplets with large numbers of components. *Combustion and Flame*, 121(1-2):334 – 344, 2000. ISSN 0010-2180. doi: http://dx.doi.org/10.1016/S0010-2180(99)00144-3. URL `http://www.sciencedirect.com/science/article/pii/S0010218099001443`.

Frank Haselbach, Alan Newby, and Ric Parker. Next generation of large civil aircraft engines - concepts & technologies. In *ETC11 - 11th European Conference on Turbomachinery Fluid dynamics & Thermodynamics*, Madrid, Spain, March 2015.

M. Herrmann. The influence of density ratio on the primary atomization of a turbulent liquid jet in crossflow. *Proceedings of the Combustion Institute*, 33(2):2079 – 2088, 2011. ISSN 1540-7489. doi: DOI:10.1016/j.proci.2010.07.002. URL `http://www.sciencedirect.com/science/article/pii/S1540748910002312`.

Colin Heye, Venkat Raman, and Assaad R. Masri. Les/probability density function approach for the simulation of an ethanol spray flame. *Proceedings of the Combustion Institute*, 34 (1):1633 – 1641, 2013. ISSN 1540-7489. doi: http://dx.doi.org/10.1016/j.proci.2012.06.107. URL `http://www.sciencedirect.com/science/article/pii/S1540748912002155`.

Colin Heye, Venkat Raman, and Assaad R. Masri. Influence of spray/combustion interactions on auto-ignition of methanol spray flames. *Proceedings of the Combustion Institute*, 35(2): 1639 – 1648, 2015. ISSN 1540-7489. doi: http://dx.doi.org/10.1016/j.proci.2014.06.087. URL `http://www.sciencedirect.com/science/article/pii/S1540748914002454`.

Corina Höfler. *Entwicklung eines Smoothed Particle Hydrodynamics (SPH) Codes zur numerischen Vorhersage des Primärzerfalls an Brennstoffeinspritzdüsen*. PhD thesis, Karlsruher Institut für Technologie (KIT), 2013. Karlsruhe, KIT, Diss., 2013.

James I. Hileman, Pearl E. Donohoo, and Russell W. Stratton. Energy content and alternative jet fuel viability. *Journal of Propulsion and Power*, 26(6):1184 – 1196, 2010. doi: doi: 10.2514/1.46232. URL `http://dx.doi.org/10.2514/1.46232`.

Simon Holz, Geoffroy Chaussonnet, Sebastian Gepperth, Rainer Koch, and Hans-Jörg Bauer. Comparison of the primary atomization model pamela with drop size distributions of an industrial prefilming airblast nozzle. In *ILASS Europe 2016, 27th Annual Conference on Liquid Atomization and Spray Systems*, Brighton, UK, September 2016.

L.-P. Hsiang and G.M. Faeth. Near-limit drop deformation and secondary breakup. *International Journal of Multiphase Flow*, 18(5):635 – 652, 1992. ISSN 0301-9322. doi: 10.1016/0301-9322(92)90036-G. URL `http://www.sciencedirect.com/science/article/pii/030193229290036G`.

L.-P. Hsiang and G.M. Faeth. Drop deformation and breakup due to shock wave and steady disturbances. *International Journal of Multiphase Flow*, 21(4):545 – 560, 1995. ISSN 0301-9322. doi: 10.1016/0301-9322(94)00095-2. URL `http://www.sciencedirect.com/science/article/pii/0301932294000952`.

G.L. Hubbard, V.E. Denny, and A.F. Mills. Droplet evaporation: Effects of transients and variable properties. *International Journal of Heat and Mass Transfer*, 18(9):1003 – 1008, 1975. ISSN 0017-9310. doi: http://dx.doi.org/10.1016/0017-9310(75)90217-3. URL `http://www.sciencedirect.com/science/article/pii/0017931075902173`.

ICAO. Icao annex 16: Environmental protection, volume ii - aircraft engine emissions. Technical report, International Civil Aviation Organization (ICAO), 2008.

ICAO. Environmental technical manual volume ii - procedures for the emissions certification of aircraft engines. Technical report, International Civil Aviation Organization (ICAO), 2016.

Elizaveta Ivanova, Berthold Noll, and Manfred Aigner. Unsteady simulations of turbulent mixing in jet in crossflow. In *40th Fluid Dynamics Conference and Exhibit*, 2010.

F. Jaegle, J.-M. Senoner, M. García, F. Bismes, R. Lecourt, B. Cuenot, and T. Poinsot. Eulerian and lagrangian spray simulations of an aeronautical multipoint injector. *Proceedings of the Combustion Institute*, 33(2):2099 – 2107, 2011. ISSN 1540-7489. doi: DOI:10.1016/j.proci.2010.07.027. URL `http://www.sciencedirect.com/science/article/pii/S1540748910002592`.

T. Jakobs, N. Djordjevic, S. Fleck, M. Mancini, R. Weber, and T. Kolb. Gasification of high viscous slurry r&d on atomization and numerical simulation. *Applied Energy*, 93(0): 449 – 456, 2012. ISSN 0306-2619. doi: 10.1016/j.apenergy.2011.12.026. URL `http://www.sciencedirect.com/science/article/pii/S0306261911008221`.

Patrick Jenny, Dirk Roekaerts, and Nijso Beishuizen. Modeling of turbulent dilute spray combustion. *Progress in Energy and Combustion Science*, 38(6):846 – 887, 2012. ISSN 0360-1285. doi: 10.1016/j.pecs.2012.07.001. URL `http://www.sciencedirect.com/science/article/pii/S0360128512000445`.

Jinhee Jeong and Fazle Hussain. On the identification of a vortex. *Journal of Fluid Mechanics*, 285:69–94, 02 1995. doi: 10.1017/S0022112095000462. URL `https://www.cambridge.org/core/journals/journal-of-fluid-mechanics/article/div-classtitleon-the-identification-of-a-vortexdiv/D26006DDB95FB28DA80E28A581182DF1`.

W.P. Jones, S. Lyra, and A.J. Marquis. Large eddy simulation of a droplet laden turbulent mixing layer. *International Journal of Heat and Fluid Flow*, 31(1):93 – 100, 2010a. ISSN 0142-727X. doi: 10.1016/j.ijheatfluidflow.2009.10.001. URL `http://www.sciencedirect.com/science/article/pii/S0142727X09001416`.

W.P. Jones, S. Lyra, and A.J. Marquis. Large eddy simulation of evaporating kerosene and acetone sprays. *International Journal of Heat and Mass Transfer*, 53(11?12):2491 – 2505, 2010b. ISSN 0017-9310. doi: 10.1016/j.ijheatmasstransfer.2010.01.028. URL `http://www.sciencedirect.com/science/article/pii/S0017931010000384`.

W.P. Jones, S. Lyra, and S. Navarro-Martinez. Large eddy simulation of a swirl stabilized spray flame. *Proceedings of the Combustion Institute*, 33(2):2153 – 2160, 2011. ISSN 1540-7489. doi: 10.1016/j.proci.2010.07.032. URL `http://www.sciencedirect.com/science/article/pii/S1540748910002956`.

W.P. Jones, S. Lyra, and S. Navarro-Martinez. Numerical investigation of swirling kerosene spray flames using large eddy simulation. *Combustion and Flame*, 159(4):1539 – 1561, 2012. ISSN 0010-2180. doi: 10.1016/j.combustflame.2011.10.025. URL `http://www.sciencedirect.com/science/article/pii/S0010218011003300`.

W.P. Jones, A.J. Marquis, and K. Vogiatzaki. Large-eddy simulation of spray combustion in a gas turbine combustor. *Combustion and Flame*, 161(1):222 – 239, 2014. ISSN 0010-2180. doi: http://dx.doi.org/10.1016/j.combustflame.2013.07.016. URL `http://www.sciencedirect.com/science/article/pii/S0010218013002861`.

W.P. Jones, A.J. Marquis, and D. Noh. Les of a methanol spray flame with a stochastic sub-grid model. *Proceedings of the Combustion Institute*, 35(2):1685 – 1691, 2015. ISSN 1540-7489. doi: http://dx.doi.org/10.1016/j.proci.2014.06.086. URL `http://www.sciencedirect.com/science/article/pii/S1540748914002442`.

Trupti Kathrotia. *Reaction Kinetics Modeling of OH*, CH*, and C2* Chemiluminescence*. PhD thesis, Ruprecht-Karls-Universität Heidelberg, 2011.

A.Y. Klimenko and R.W. Bilger. Conditional moment closure for turbulent combustion. *Progress in Energy and Combustion Science*, 25(6):595 – 687, 1999. ISSN 0360-1285. doi: https://doi.org/10.1016/S0360-1285(99)00006-4. URL `http://www.sciencedirect.com/science/article/pii/S0360128599000064`.

R. Koch. Numerische simulation reagierender zweiphasenströmungen. Skriptum zur vorlesung, Institut für Thermische Strömungsmaschinen, Universität Karlsruhe, 2011.

Joel Koplik and Jayanth R. Banavar. Molecular dynamics of interface rupture. *Physics of Fluids A: Fluid Dynamics*, 5(3):521–536, 1993. doi: 10.1063/1.858879. URL `http://link.aip.org/link/?PFA/5/521/1`.

J. G. M. Kuerten. Subgrid modeling in particle-laden channel flow. *Physics of Fluids*, 18 (2):025108, 2006. doi: http://dx.doi.org/10.1063/1.2176589. URL `http://scitation.aip.org/content/aip/journal/pof2/18/2/10.1063/1.2176589`.

Kenneth K. Kuo. *Principles of Combustion*. Wiley, New York, 1986.

Kenneth K. Kuo and Ragini Acharya. *Fundamentals of turbulent and multiphase combustion*. Wiley, Hoboken, NJ, 1st edition, 2012. ISBN 978-0-470-22622-3.

W. R. Lane. Shatter of drops in streams of air. *Industrial & Engineering Chemistry*, 43 (6):1312–1317, 1951. doi: 10.1021/ie50498a022. URL `http://pubs.acs.org/doi/abs/10.1021/ie50498a022`.

C. K. Law and H. K. Law. A d2-law for multicomponent droplet vaporization and combustion. *AIAA Journal*, 20(4):522 – 527, 1982. doi: doi:10.2514/3.51103. URL `http://dx.doi.org/10.2514/3.51103`.

P. C. Le Clercq and J. Bellan. Direct numerical simulation of a transitional temporal mixing layer laden with multicomponent-fuel evaporating drops using continuous thermodynamics. *Physics of Fluids (1994-present)*, 16(6):1884–1907, 2004. doi: http://dx.doi.org/10.1063/1.

1688327. URL `http://scitation.aip.org/content/aip/journal/pof2/16/6/10.1063/1.1688327`.

Patrick Le Clercq, Nicolas Doué, Michael Rachner, and Manfred Aigner. Validation of a multicomponent-fuel model for spray computations. In *47th AIAA Aerospace Sciences Meeting and Exhibit*, 2009. URL `http://elib.dlr.de/57500/`. AIAA 2009-1188.

Patrick C. Le Clercq and Josette Bellan. Direct numerical simulation of gaseous mixing layers laden with multicomponent-liquid drops: liquid-specific effects. *Journal of Fluid Mechanics*, 533:57–94, 6 2005. ISSN 1469-7645. doi: 10.1017/S0022112005003940. URL `http://journals.cambridge.org/article_S0022112005003940`.

Anthony Leboissetier, Nora Okong'o, and Josette Bellan. Consistent large-eddy simulation of a temporal mixing layer laden with evaporating drops. part 2. a posteriori modelling. *Journal of Fluid Mechanics*, 523:37–78, 2005. doi: 10.1017/S0022112004002101. URL `http://dx.doi.org/10.1017/S0022112004002101`.

D.S. Lee, G. Pitari, V. Grewe, K. Gierens, J.E. Penner, A. Petzold, M.J. Prather, U. Schumann, A. Bais, T. Berntsen, D. Iachetti, L.L. Lim, and R. Sausen. Transport impacts on atmosphere and climate: Aviation. *Atmospheric Environment*, 44(37):4678 – 4734, 2010. ISSN 1352-2310. doi: http://dx.doi.org/10.1016/j.atmosenv.2009.06.005. URL `//www.sciencedirect.com/science/article/pii/S1352231009004956`. Transport Impacts on Atmosphere and Climate: The ATTICA Assessment Report.

A.H. Lefebvre. *Atomization and Sprays.* Hemisphere Publishing Corporation, Taylor & Francis Inc, New York, 1989.

Arthur H. Lefebvre and Dilip R. Ballal. *Gas Turbine Combustion: Alternative Fuels and Emissions.* CRC Press, 3rd edition, 2010. URL `http://www.crcnetbase.com/doi/10.1201/9781420086058`.

D. K. Lilly. A proposed modification of the germano subgrid-scale closure method. *Physics of Fluids A: Fluid Dynamics*, 4(3):633–635, 1992. doi: 10.1063/1.858280. URL `http://dx.doi.org/10.1063/1.858280`.

Yue Ling and Stéphane Zaleski. Multi-scale simulation of primary breakup in gas-assisted atomization. In *AIAA SciTech 2015 - 53rd AIAA Aerospace Sciences Meeting.* American Institute of Aeronautics and Astronautics, 2015. doi: doi:10.2514/6.2015-0420.

A. B. Liu and Rolf D. Reitz. Mechanisms of air-assisted liquid atomization. *Atomization and Sprays*, 3(1):55–75, 1993. ISSN 1044-5110.

A. Lozano, E. Calvo, J.A. García, and F. Barreras. Mode transitions in an oscillating liquid sheet. *Phys. Fluids*, 23(4):044103, April 2011.

K. Luo, H. Pitsch, M.G. Pai, and O. Desjardins. Direct numerical simulations and analysis of three-dimensional n-heptane spray flames in a model swirl combustor. *Proceedings of the Combustion Institute*, 33(2):2143 – 2152, 2011. ISSN 1540-7489. doi: http://dx.doi.org/10.1016/j.proci.2010.06.077. URL `http://www.sciencedirect.com/science/article/pii/S1540748910001379`.

Rafael Luque and James Speight. *Gasification for synthetic fuel production : fundamentals, processes, and applications.* Number 69 in Woodhead Publishing series in energy. Elsevier, Woodhead Publ., Amsterdam, 2015. ISBN 978-0-85709-802-3.

Johannes Löwe, Axel Probst, Tobias Knopp, and Roland Kessler. A low-dissipation low-dispersion second-order scheme for unstructured finite-volume flow solvers. In *53rd AIAA Aerospace Sciences Meeting*, Kissimmee, Florida, January 2015.

C. Marchioli, M. V. Salvetti, and A. Soldati. Some issues concerning large-eddy simulation of inertial particle dispersion in turbulent bounded flows. *Physics of Fluids*, 20(4): 040603, 2008. doi: http://dx.doi.org/10.1063/1.2911018. URL `http://scitation.aip.org/content/aip/journal/pof2/20/4/10.1063/1.2911018`.

A. Mashayek and N. Ashgriz. *Dynamics of Liquid Droplets*, chapter 4, pages 97–123. Springer US, Boston, MA, 2011. ISBN 978-1-4419-7264-4. doi: 10.1007/978-1-4419-7264-4_4. URL `http://dx.doi.org/10.1007/978-1-4419-7264-4_4`.

Suresh Menon and Alan R. Kerstein. *The Linear-Eddy Model*, pages 221–247. Springer Netherlands, Dordrecht, 2011. ISBN 978-94-007-0412-1. doi: 10.1007/978-94-007-0412-1_10. URL `http://dx.doi.org/10.1007/978-94-007-0412-1_10`.

W. Michalek, J. G. M. Kuerten, R. Liew, J. C. H. Zeegers, and B. J. Geurts. A hybrid stochastic-deconvolution model for particle-laden les. *AIP Conference Proceedings*, 1558(1): 1075–1078, 2013. doi: http://dx.doi.org/10.1063/1.4825692. URL `http://scitation.aip.org/content/aip/proceeding/aipcp/10.1063/1.4825692`.

R.S. Miller, K. Harstad, and J. Bellan. Evaluation of equilibrium and non-equilibrium evaporation models for many-droplet gas-liquid flow simulations. *International Journal of Multiphase Flow*, 24(6):1025 – 1055, 1998. ISSN 0301-9322. doi: http://dx.doi.org/10.1016/S0301-9322(98)00028-7. URL `http://www.sciencedirect.com/science/article/pii/S0301932298000287`.

Jean-Pierre Minier. On lagrangian stochastic methods for turbulent polydisperse two-phase reactive flows. *Progress in Energy and Combustion Science*, 50:1 – 62, 2015. ISSN 0360-1285. doi: http://dx.doi.org/10.1016/j.pecs.2015.02.003. URL `http://www.sciencedirect.com/science/article/pii/S0360128515000143`.

Jean-Pierre Minier and Eric Peirano. The pdf approach to turbulent polydispersed two-phase flows. *Physics Reports*, 352(1?3):1 – 214, 2001. ISSN 0370-1573. doi: 10.1016/S0370-1573(01)00011-4. URL `http://www.sciencedirect.com/science/article/pii/S0370157301000114`.

Jean-Pierre Minier, Eric Peirano, and Sergio Chibbaro. Pdf model based on langevin equation for polydispersed two-phase flows applied to a bluff-body gas-solid flow. *Physics of Fluids*, 16(7):2419–2431, 2004. doi: 10.1063/1.1718972. URL `http://link.aip.org/link/?PHF/16/2419/1`.

Jean-Pierre Minier, Sergio Chibbaro, and Stephen B. Pope. Guidelines for the formulation of lagrangian stochastic models for particle simulations of single-phase and dispersed two-phase turbulent flows. *Physics of Fluids*, 26(11):113303, 2014. doi: http://dx.doi.org/10.1063/1.4901315. URL `http://scitation.aip.org/content/aip/journal/pof2/26/11/10.1063/1.4901315`.

T. Ménard, S. Tanguy, and A. Berlemont. Coupling level set/vof/ghost fluid methods: Validation and application to 3d simulation of the primary break-up of a liquid jet. *International Journal of Multiphase Flow*, 33(5):510 – 524, 2007. ISSN 0301-9322. doi: DOI: 10.1016/j.ijmultiphaseflow.2006.11.001. URL `http://www.sciencedirect.com/science/article/pii/S0301932206001832`.

Hukam Mongia. Taps: A fourth generation propulsion combustor technology for low emissions. In *AIAA/ICAS International Air and Space Symposium and Exposition: The Next 100 Years*, number AIAA 2003-2657, Dayton, Ohio, USA, July 2003. American Institute of Aeronautics and Astronautics. doi: doi:10.2514/6.2003-2657. URL `http://dx.doi.org/10.2514/6.2003-2657`.

P.S. Monks, C. Granier, S. Fuzzi, A. Stohl, M.L. Williams, H. Akimoto, M. Amann, A. Baklanov, U. Baltensperger, I. Bey, N. Blake, R.S. Blake, K. Carslaw, O.R. Cooper, F. Dentener, D. Fowler, E. Fragkou, G.J. Frost, S. Generoso, P. Ginoux, V. Grewe, A. Guenther, H.C. Hansson, S. Henne, J. Hjorth, A. Hofzumahaus, H. Huntrieser, I.S.A. Isaksen, M.E. Jenkin, J. Kaiser, M. Kanakidou, Z. Klimont, M. Kulmala, P. Laj, M.G. Lawrence, J.D. Lee, C. Liousse, M. Maione, G. McFiggans, A. Metzger, A. Mieville, N. Moussiopoulos, J.J. Orlando, C.D. O'Dowd, P.I. Palmer, D.D. Parrish, A. Petzold, U. Platt, U. Pöschl, A.S.H. Prévôt, C.E. Reeves, S. Reimann, Y. Rudich, K. Sellegri, R. Steinbrecher, D. Simpson, H. ten Brink, J. Theloke, G.R. van der Werf, R. Vautard, V. Vestreng, Ch. Vlachokostas, and R. von Glasow. Atmospheric composition change - global and regional air quality. *Atmospheric Environment*, 43(33):5268 – 5350, 2009. ISSN 1352-2310. doi: http://dx.doi.org/10.1016/j.atmosenv.2009.08.021. URL `//www.sciencedirect.com/science/article/pii/S1352231009007109`.

Mathieu Moreau, Olivier Simonin, and Benoît Bédat. Development of gas-particle euler-euler les approach: A priori analysis of particle sub-grid models in homogeneous isotropic turbulence.

Flow, Turbulence and Combustion, 84:295–324, 2010. ISSN 1386-6184. URL `http://dx.doi.org/10.1007/s10494-009-9233-z`. 10.1007/s10494-009-9233-z.

T. Mosbach and Z. Yin. Measurement of flame luminescence around mono-disperse droplet chains. private communication, 2015.

C.A. Moses and P.N.J. Roets. Properties, characteristics and combustion performance of sasol fully synthetic jet fuel. *Journal of Engineering for Gas Turbines and Power*, 131(4):041502–1 – 041502–17, June 2009. doi: 10.1115/1.3028234. URL `http://dx.doi.org/10.1115/1.3028234`.

F. Nicoud and F. Ducros. Subgrid-scale stress modelling based on the square of the velocity gradient tensor. *Flow, Turbulence and Combustion*, 62(3):183–200, 1999. ISSN 1386-6184. doi: 10.1023/A:1009995426001. URL `http://dx.doi.org/10.1023/A%3A1009995426001`.

Berthold Noll. *Möglichkeiten und Grenzen der numerischen Beschreibung von Strömungen in hochbelasteten Brennräumen*. Universität Karlsruhe, 1992.

Joseph C. Oefelein, Vaidyanathan Sankaran, and Tomasz G. Drozda. Large eddy simulation of swirling particle-laden flow in a model axisymmetric combustor. *Proceedings of the Combustion Institute*, 31(2):2291 – 2299, 2007. ISSN 1540-7489. doi: http://dx.doi.org/10.1016/j.proci.2006.08.017. URL `http://www.sciencedirect.com/science/article/pii/S154074890600280X`.

Hernan Olguin and Eva Gutheil. Influence of evaporation on spray flamelet structures. *Combustion and Flame*, 161(4):987 – 996, 2014. ISSN 0010-2180. doi: http://dx.doi.org/10.1016/j.combustflame.2013.10.010. URL `http://www.sciencedirect.com/science/article/pii/S0010218013003842`.

L. Opfer, I. V. Roisman, and C. Tropea. Aerodynamic fragmentation of drops: Dynamics of the liquid bag. In *ICLASS 2012 - 12th Triennial International Conference on Liquid Atomization and Spray Systems*, Heidelberg, Germany, September 2012.

Peter J. O'Rourke and Anthony A. Amsden. The tab method for numerical calculation of spray droplet breakup. In *SAE Technical Paper*. SAE International, 11 1987. doi: 10.4271/872089. URL `http://dx.doi.org/10.4271/872089`.

J. Park, K.Y. Huh, X. Li, and M. Renksizbulut. Experimental investigation on cellular breakup of a planar liquid sheet from an air-blast nozzle. *Physics of Fluids*, 16(3):625–632, March 2004. ISSN 1070-6631. doi: {10.1063/1.1644575}.

Nayan Patel and Suresh Menon. Simulation of spray-turbulence-flame interactions in a lean direct injection combustor. *Combustion and Flame*, 153(1?2):228 – 257, 2008. ISSN 0010-2180. doi: 10.1016/j.combustflame.2007.09.011. URL `http://www.sciencedirect.com/science/article/pii/S0010218007002647`.

C. Pichard, Y. Michou, C. Chauveau, and L. Gökalp. Average droplet vaporization rates in partially prevaporized turbulent spray flames. *Proceedings of the Combustion Institute*, 29(1): 527 – 533, 2002. ISSN 1540-7489. doi: http://dx.doi.org/10.1016/S1540-7489(02)80068-2. URL `http://www.sciencedirect.com/science/article/pii/S1540748902800682`. Proceedings of the Combustion Institute.

M. Pilch and C.A. Erdman. Use of breakup time data and velocity history data to predict the maximum size of stable fragments for acceleration-induced breakup of a liquid drop. *International Journal of Multiphase Flow*, 13(6):741 – 757, 1987. ISSN 0301-9322. doi: 10.1016/0301-9322(87)90063-2. URL `http://www.sciencedirect.com/science/article/pii/0301932287900632`.

Thierry Poinsot and Denis Veynante. *Theoretical and numerical combustion.* CNRS, Toulouse, 3rd edition, 2011. ISBN 978-2-7466-3990-4.

Bruce E. Poling, John M. Prausnitz, and John P. O'Connell. *The properties of gases and liquids.* McGraw-Hill, New York [i.a.], 5. ed. edition, 2001. ISBN 0-07-011682-2.

S. B. Pope. A monte carlo method for the pdf equations of turbulent reactive flow. *Combustion Science and Technology*, 25(5-6):159–174, 1981. doi: 10.1080/00102208108547500. URL `http://dx.doi.org/10.1080/00102208108547500`.

S.B. Pope. *Turbulent flows.* Cambridge University Press, Cambridge, 2000.

Jacek Pozorski and Sourabh V. Apte. Filtered particle tracking in isotropic turbulence and stochastic modeling of subgrid-scale dispersion. *International Journal of Multiphase Flow*, 35(2):118 – 128, 2009. ISSN 0301-9322. doi: http://dx.doi.org/10.1016/j.ijmultiphaseflow.2008.10.005. URL `http://www.sciencedirect.com/science/article/pii/S0301932208001511`.

Axel Probst, Johannes Löwe, Silvia Reuß, Tobias Knopp, and Roland Kessler. Scale-resolving simulations with a low-dissipation low-dispersion second-order scheme for unstructured finite-volume flow solvers. In *53rd AIAA Aerospace Sciences Meeting*, Kissimmee, Florida, January 2015.

Youngchul Ra and Rolf D. Reitz. A vaporization model for discrete multi-component fuel sprays. *International Journal of Multiphase Flow*, 35(2):101 – 117, 2009. ISSN 0301-9322. doi: http://dx.doi.org/10.1016/j.ijmultiphaseflow.2008.10.006. URL `http://www.sciencedirect.com/science/article/pii/S030193220800164X`.

Youngchul Ra and Rolf D. Reitz. A combustion model for ic engine combustion simulations with multi-component fuels. *Combustion and Flame*, 158(1):69 – 90, 2011. ISSN 0010-2180. doi: http://dx.doi.org/10.1016/j.combustflame.2010.07.019. URL `http://www.sciencedirect.com/science/article/pii/S0010218010002075`.

Youngchul Ra and Rolf D. Reitz. A combustion model for multi-component fuels using a physical surrogate group chemistry representation (psgcr). *Combustion and Flame*, 162(10): 3456 – 3481, 2015. ISSN 0010-2180. doi: http://dx.doi.org/10.1016/j.combustflame.2015.05.014. URL `http://www.sciencedirect.com/science/article/pii/S0010218015001522`.

M. Rachner. Die stoffeigenschaften von kerosin jet a-1. DLR-Mitteilung 98-01, DLR - German Aerospace Center, 1998.

M. Rachner, M. Brandt, H. Eickhoff, C. Hassa, A. Bräumer, H. Krämer, M. Ridder, and V. Sick. A numerical and experimental study of fuel evaporation and mixing for lean premixed combustion at high pressure. *Symposium (International) on Combustion*, 26(2):2741 – 2748, 1996. ISSN 0082-0784. doi: http://dx.doi.org/10.1016/S0082-0784(96)80111-1. URL `http://www.sciencedirect.com/science/article/pii/S0082078496801111`.

Michael Rachner and Nicolas Doué. Spraysim documentation - ctm-handbook. Technical report, German Aerospace Center (DLR), 2009.

Michael Rachner, Julian Becker, Christoph Hassa, and Thomas Doerr. Modelling of the atomization of a plain liquid fuel jet in crossflow at gas turbine conditions. *Aerospace Science and Technology*, 6(7):495 – 506, 2002. ISSN 1270-9638. doi: DOI:10.1016/S1270-9638(01)01135-X. URL `http://www.sciencedirect.com/science/article/pii/S127096380101135X`.

A.A. Ranger and J.A. Nicholls. Aerodynamic shattering of liquid drops. *AIAA JOURNAL*, 7 (2):285–290, 1969.

Bastian Rauch. *Systematic Accuracy Assessment for Alternative Aviation Fuel Evaporation Models.* PhD thesis, Faculty of Aerospace Engineering and Geodesy of the University Stuttgart, 2017.

Lord Rayleigh. On the instability of jets. *Proceedings of the London Mathematical Society*, s1-10(1):4–13, 1878. doi: 10.1112/plms/s1-10.1.4. URL `http://plms.oxfordjournals.org/content/s1-10/1/4.short`.

L. Raynal, E. Villermaux, J. C. Lasheras, and E. J. Hopfinger. Primary instability in liquid-gas shear layers. In *11th Symposium on Turbulent Shear Flows*, pages 1–4, Grenoble, France, 1997.

E. Riber, V. Moureau, M. García, T. Poinsot, and O. Simonin. Evaluation of numerical strategies for large eddy simulation of particulate two-phase recirculating flows. *Journal of Computational Physics*, 228(2):539 – 564, 2009. ISSN 0021-9991. doi: 10.1016/j.jcp.2008.10.001. URL `http://www.sciencedirect.com/science/article/pii/S0021999108005238`.

F. L. Sacomano Filho, M. Chrigui, A. Sadiki, and J. Janicka. Les-based numerical analysis of droplet vaporization process in lean partially premixed turbulent spray flames. *Combustion*

Science and Technology, 186(4-5):435–452, 2014. doi: 10.1080/00102202.2014.883207. URL `http://dx.doi.org/10.1080/00102202.2014.883207`.

P. Sagaut. *Large Eddy Simulation for Incompressible Flows: An Introduction*. Scientific Computation. Springer, 2006. ISBN 9783540263449.

P. Sagaut, S. Deck, and M. Terracol. *Multiscale And Multiresolution Approaches in Turbulence*. Imperial College Press, 2006. ISBN 9781860946509.

M. Sanjosé, J.M. Senoner, F. Jaegle, B. Cuenot, S. Moreau, and T. Poinsot. Fuel injection model for euler-euler and euler-lagrange large-eddy simulations of an evaporating spray inside an aeronautical combustor. *International Journal of Multiphase Flow*, 37(5): 514 – 529, 2011. ISSN 0301-9322. doi: DOI:10.1016/j.ijmultiphaseflow.2011.01.008. URL `http://www.sciencedirect.com/science/article/pii/S0301932211000280`.

Thomas Ferdinand Sattelmayer. *Zum Einfluß der ausgebildeten, turbulenten Luft-Flüssigkeitsfilm-Strömung auf den Filmzerfall und die Tropfenbildung am Austritt von Spalten geringer Höhe*. PhD thesis, Universität Karlsruhe, 1985.

H. Schlichting. *Grenzschicht-Theorie*. Verlag G. Braun Karlsruhe, 1965.

R. Schmehl. *Tropfendeformation und Nachzerfall bei der technischen Gemischaufbereitung*. PhD thesis, Universität Karlsruhe, 2004.

Judith C. Segura. *Predictive capabilities of particle-laden large eddy simulation*. PhD thesis, Stanford university, department of mechanical engineering, September 2004.

P. K. Senecal, D. P. Schmidt, I. Nouar, C. J. Rutland, R. D. Reitz, and M. L. Corradini. Modeling high-speed viscous liquid sheet atomization. *International Journal of Multiphase Flow*, 25(6-7):1073 – 1097, 1999. ISSN 0301-9322. doi: DOI:10.1016/S0301-9322(99)00057-9. URL `http://www.sciencedirect.com/science/article/pii/S0301932299000579`.

J. A. Sethian and Peter Smereka. Level set methods for fluid interfaces. *Annual Review of Fluid Mechanics*, 35(1):341–372, 2003. doi: 10.1146/annurev.fluid.35.101101.161105. URL `http://www.annualreviews.org/doi/abs/10.1146/annurev.fluid.35.101101.161105`.

Linda Shafer, Rich Striebich, J. Gomach, and Tim Edwards. Chemical class composition of commercial jet fuels and other specialty kerosene fuels. In *14th AIAA/AHI Space Planes and Hypersonic Systems and Technologies Conference*, 2006. doi: doi:10.2514/6.2006-7972. URL `http://dx.doi.org/10.2514/6.2006-7972`.

B. Shotorban, K.K.Q. Zhang, and F. Mashayek. Improvement of particle concentration prediction in large-eddy simulation by defiltering. *International Journal of Heat and Mass Transfer*, 50(19-20):3728 – 3739, 2007. ISSN 0017-9310. doi: http://dx.doi.org/10.1016/j.ijheatmasstransfer.2007.02.033. URL `http://www.sciencedirect.com/science/article/pii/S0017931007001895`.

Babak Shotorban and Farzad Mashayek. A stochastic model for particle motion in large-eddy simulation. *Journal of Turbulence*, 7(18):1–13, 2006. doi: 10.1080/14685240600595685. URL `http://www.tandfonline.com/doi/abs/10.1080/14685240600595685`.

J-S. Shuen, L-D. Chen, and G. M. Faeth. Evaluation of a stochastic model of particle dispersion in a turbulent round jet. *AIChE Journal*, 29(1):167–170, 1983. ISSN 1547-5905. doi: 10.1002/aic.690290127. URL `http://dx.doi.org/10.1002/aic.690290127`.

H.C. Simmons. The correlation of drop-size distributions in fuel nozzle sprays. part i - the drop-size/volume-fraction distribution. *Journal of Engineering for Power*, 99:309–314, July 1977a.

H.C. Simmons. The correlation of drop-size distributions in fuel nozzle sprays. part ii - the drop-size/number distribution. *Journal of Engineering for Power*, 99:315–319, July 1977b.

W. A. Sirignano and C. Mehring. Review of theory of distortion and disintegration of liquid streams. *Progress in Energy and Combustion Science*, 26(4-6):609 – 655, 2000. ISSN 0360-1285. doi: DOI:10.1016/S0360-1285(00)00014-9. URL `http://www.sciencedirect.com/science/article/pii/S0360128500000149`.

William A. Sirignano. *Fluid Dynamics and Transport of Droplets and Sprays*. Cambridge University Press, Cambridge, 2 edition, 2010. ISBN 9780511806728. doi: 10.1017/CBO9780511806728. URL `https://www.cambridge.org/core/books/fluid-dynamics-and-transport-of-droplets-and-sprays/EEEF907721AE679B11BC62AA59C61DE2`.

N. Slavinskaya, Mehdi Abbasi, T. Kathrotia, and U. Riedel. Reduced mechanism for kerosene combustion. private communication, 2015.

J. Smagorinsky. General circulation experiments with the primitive equations. *Monthly Weather Review*, 91:99, 1963.

Gregory P. Smith, David M. Golden, Michael Frenklach, Nigel W. Moriarty, Boris Eiteneer, Mikhail Goldenberg, C. Thomas Bowman, Ronald K. Hanson, Soonho Song, William C. Gardiner Jr., Vitali V. Lissianski, and Zhiwei Qin. Gri 3.0 mech, 2000. URL `http://www.me.berkeley.edu/gri_mech/`.

M. Sommerfeld and H.-H. Qiu. Detailed measurements in a swirling particulate two-phase flow by a phase-doppler anemometer. *International Journal of Heat and Fluid Flow*, 12(1):20 – 28, 1991. ISSN 0142-727X. doi: 10.1016/0142-727X(91)90004-F. URL `http://www.sciencedirect.com/science/article/pii/0142727X9190004F`.

M. Sommerfeld and H.-H. Qiu. Characterization of particle-laden, confined swirling flows by phase-doppler anemometry and numerical calculation. *International Journal of Multiphase*

Flow, 19(6):1093 – 1127, 1993. ISSN 0301-9322. doi: 10.1016/0301-9322(93)90080-E. URL `http://www.sciencedirect.com/science/article/pii/030193229390080E`.

D.B. Spalding. The combustion of liquid fuels. *Symposium (International) on Combustion*, 4 (1):847 – 864, 1953. ISSN 0082-0784. doi: http://dx.doi.org/10.1016/S0082-0784(53)80110-4. URL `http://www.sciencedirect.com/science/article/pii/S0082078453801104`.

O.T. Stein, G. Olenik, A. Kronenburg, F. Cavallo Marincola, B.M. Franchetti, A.M. Kempf, M. Ghiani, M. Vascellari, and C. Hasse. Towards comprehensive coal combustion modelling for les. *Flow, Turbulence and Combustion*, 90(4):859–884, 2013. ISSN 1386-6184. doi: 10.1007/s10494-012-9423-y. URL `http://dx.doi.org/10.1007/s10494-012-9423-y`.

R. Stickles and J. Barrett. Taps ii combustor final report, continuous lower energy, emissions and noise (cleen) program. Technical report, GE Aviation, 2013.

S. Stolz, N. A. Adams, and L. Kleiser. An approximate deconvolution model for large-eddy simulation with application to incompressible wall-bounded flows. *Physics of Fluids*, 13(4): 997–1015, 2001. doi: http://dx.doi.org/10.1063/1.1350896. URL `http://scitation.aip.org/content/aip/journal/pof2/13/4/10.1063/1.1350896`.

Ken-Ichi Sugioka and Satoru Komori. Drag and lift forces acting on a spherical water droplet in homogeneous linear shear air flow. *Journal of Fluid Mechanics*, 570:155–175, 1 2007. ISSN 1469-7645. doi: 10.1017/S0022112006003065. URL `http://journals.cambridge.org/article_S0022112006003065`.

M. Sussman. A second order coupled level set and volume-of-fluid method for computing growth and collapse of vapor bubbles. *J. Comput. Phys.*, 187:110–136, May 2003. ISSN 0021-9991. doi: 10.1016/S0021-9991(03)00087-1. URL `http://portal.acm.org/citation.cfm?id=795462.795468`.

M. Sussman, K.M. Smith, M.Y. Hussaini, M. Ohta, and R. Zhi-Wei. A sharp interface method for incompressible two-phase flows. *J. Comput. Phys.*, 221:469–505, February 2007. ISSN 0021-9991. doi: 10.1016/j.jcp.2006.06.020. URL `http://portal.acm.org/citation.cfm?id=1224552.1224613`.

Nicholas Syred. A review of oscillation mechanisms and the role of the precessing vortex core (pvc) in swirl combustion systems. *Progress in Energy and Combustion Science*, 32 (2):93 – 161, 2006. ISSN 0360-1285. doi: https://doi.org/10.1016/j.pecs.2005.10.002. URL `http://www.sciencedirect.com/science/article/pii/S0360128505000353`.

J. Tamim and W.L.H. Hallett. A continuous thermodynamics model for multicomponent droplet vaporization. *Chemical Engineering Science*, 50(18):2933 – 2942, 1995. ISSN 0009-2509. doi: http://dx.doi.org/10.1016/0009-2509(95)00131-N. URL `http://www.sciencedirect.com/science/article/pii/000925099500131N`.

F. X. Tanner. *Evaporating Sprays*, chapter 12, pages 263–278. Springer US, Boston, MA, 2011. ISBN 978-1-4419-7264-4. doi: 10.1007/978-1-4419-7264-4_12. URL `http://dx.doi.org/10.1007/978-1-4419-7264-4_12`.

F.X. Tanner. Liquid jet atomization and drop breakup modeling of non-evaporation diesel fuel sprays. *SAE Trans. J. Engines*, 970050:67–80, 1997.

F.X. Tanner. Development and validation of a cascade atomization and drop breakup model for high-velocity dense sprays. *Atomization and Sprays*, 14:211–242, 2004.

R.W. Tate and W.R. Marshall Jr. Atomization by centrifugal pressure nozzles. *Chem. Eng. Prog.*, 49:169?174, 1953.

The MathWorks Inc. *MATLAB version 8.1 (R2013a).* Natick, Massachusetts, USA, 2013.

S. Thomas, A. Esmaeeli, and G. Tryggvason. Multiscale computations of thin films in multiphase flows. *International Journal of Multiphase Flow*, 36(1):71 – 77, 2010. ISSN 0301-9322. doi: DOI:10.1016/j.ijmultiphaseflow.2009.08.002. URL `http://www.sciencedirect.com/science/article/pii/S0301932209001347`.

G. Tomar, D. Fuster, S. Zaleski, and S. Popinet. Multiscale simulations of primary atomization using gerris. *Computers and Fluids*, 39(10):1864–1874, 2010. URL `http://gfs.sf.net/papers/tomar2010.pdf`.

Cameron Tropea. Optical particle characterization in flows. *Annual Review of Fluid Mechanics*, 43(1):399–426, 2011. doi: 10.1146/annurev-fluid-122109-160721. URL `http://www.annualreviews.org/doi/abs/10.1146/annurev-fluid-122109-160721`.

G. Tryggvason, B. Bunner, A. Esmaeeli, D. Juric, N. Al-Rawahi, W. Tauber, J. Han, S. Nas, and Y.-J. Jan. A front-tracking method for the computations of multiphase flow. *Journal of Computational Physics*, 169(2):708 – 759, 2001. ISSN 0021-9991. doi: 10.1006/jcph.2001.6726. URL `http://www.sciencedirect.com/science/article/pii/S0021999101967269`.

S. Ukai, A. Kronenburg, and O.T. Stein. Les-cmc of a dilute acetone spray flame. *Proceedings of the Combustion Institute*, 34(1):1643 – 1650, 2013. ISSN 1540-7489. doi: http://dx.doi.org/10.1016/j.proci.2012.05.023. URL `http://www.sciencedirect.com/science/article/pii/S1540748912000247`.

Luis Valiño. A field monte carlo formulation for calculating the probability density function of a single scalar in a turbulent flow. *Flow, Turbulence and Combustion*, 60(2):157–172, 1998. ISSN 1573-1987. doi: 10.1023/A:1009968902446. URL `http://dx.doi.org/10.1023/A:1009968902446`.

Emmanuel Villermaux. Mixing and spray formation in coaxial jets. *Journal of Propulsion and Power*, 14:807 – 817, 1998. doi: 10.2514/2.5344. URL `http://dx.doi.org/10.2514/2.5344`.

A. Violi, S. Yan, E. G. Eddings, A. F. Sarofim, S. Granata, T. Faravelli, and E. Ranzi. Experimental formulation and kinetic model for jp-8 surrogate mixtures. *Combustion Science and Technology*, 174(11-12):399–417, 2002. doi: 10.1080/00102200215080. URL `http://dx.doi.org/10.1080/00102200215080`.

Bert Vreman, BernardJ. Geurts, N.G. Deen, J.A.M. Kuipers, and J.G.M. Kuerten. Two- and four-way coupled euler?lagrangian large-eddy simulation of turbulent particle-laden channel flow. *Flow, Turbulence and Combustion*, 82(1):47–71, 2009. ISSN 1386-6184. doi: 10.1007/s10494-008-9173-z. URL `http://dx.doi.org/10.1007/s10494-008-9173-z`.

Ville Vuorinen, Harri Hillamo, Ossi Kaario, Martti Larmi, and L. Fuchs. Large eddy simulation of droplet stokes number effects on turbulent spray shape. *Atomization and Sprays*, 20(2): 93–114, 2010. ISSN 1044-5110.

C. Wahl and M. Kapernaum. Report on kerosene validation data. final report G4RD-CT-00075, DLR - German Aerospace Center, 2003.

Q. Wang and K.D. Squires. Large eddy simulation of particle deposition in a vertical turbulent channel flow. *International Journal of Multiphase Flow*, 22(4):667 – 683, 1996. ISSN 0301-9322. doi: http://dx.doi.org/10.1016/0301-9322(96)00007-9. URL `http://www.sciencedirect.com/science/article/pii/0301932296000079`.

J. Warnatz, U. Maas, and R.W. Dibble. *Combustion - Physical and Chemical Fundamentals, Modeling and Simulation, Experiments, Pollutant Formation*. Springer, Berlin Heidelberg, 4 edition, 2006.

K.L. Wert. A rationally-based correlation of mean fragment size for drop secondary breakup. *International Journal of Multiphase Flow*, 21(6):1063 – 1071, 1995. ISSN 0301-9322. doi: 10.1016/0301-9322(95)00036-W. URL `http://www.sciencedirect.com/science/article/pii/030193229500036W`.

Curtis H. Whitson. Characterizing hydrocarbon plus fractions. *Society of Petroleum Engineers Journal*, 23(04), August 1983. doi: http://dx.doi.org/10.2118/12233-PA.

D.C. Wilcox. *Turbulence modeling for CFD*. DCW Industries, Inc., La Canada, CA, 1994.

M. C. Yuen and L. W. Chen. On drag of evaporating liquid droplets. *Combustion Science and Technology*, 14(4-6):147–154, 1976. doi: 10.1080/00102207608547524. URL `http://dx.doi.org/10.1080/00102207608547524`.

A.J. Yule and K. Vamvakoglou. Break-up of a liquid sheet adjacent to a single air stream. In *ILASS Europe 1999 - 15th Annual conference on liquid atomization and spray systems*, Toulouse, France, July 1999.

Hui Zhao, Hai Feng Liu, Jian Liang Xu, and Wei Feng Li. Experimental study of drop size distribution in the bag breakup regime. *Industrial & Engineering Chemistry Research*, 50 (16):9767–9773, 2011. doi: 10.1021/ie200622d. URL `http://pubs.acs.org/doi/abs/10.1021/ie200622d`.

Zurich Airport. Aircraft emission charges zurich airport. Technical report, Zurich Airport, 2010.

Lebenslauf

Persönliche Daten

Name	Georg Eckel
Geburtsdatum	17.07.1980
Geburtsort	Karlsruhe
Staatsangehörigkeit	Deutsch

Schulausbildung

1991–2000	Gymnasium Hemsbach, Baden-Württemberg

Studium

10/2001–04/2009	Universität Stuttgart, Luft- und Raumfahrttechnik
07/2006–03/2007	RMIT Melbourne, Australien

Berufliche Tätigkeit

seit 2009	Wissenschaftlicher Mitarbeiter, Deutsches Zentrum für Luft- und Raumfahrt, Institut für Verbrennungstechnik